AN EXPERIMENTAL STUDY OF DENSE AEROSOL AGGREGATIONS

by

RAJAN DHAUBHADEL

M. S., Tribhuvan University, 2000

AN ABSTRACT OF A DISSERTATION

submitted in partial fulfillment of the requirements for the degree

DOCTOR OF PHILOSOPHY

Department of Physics
College of Arts and Sciences

KANSAS STATE UNIVERSITY
Manhattan, Kansas

2008

Abstract

We demonstrated that an aerosol can gel. This gelation was then used for a one-step method to produce an ultralow density porous carbon or silica material. This material was named an aerosol gel because it was made via gelation of particles in the aerosol phase. The carbon and silica aerosol gels had high specific surface area (200 – 350 m^2/g for carbon and 300 – 500 m^2/g for silica) and an extremely low density (2.5 – 6.0 mg/cm^3), properties similar to conventional aerogels. Key aspects to form a gel from an aerosol are large volume fraction, ca. 10^{-4} or greater, and small primary particle size, 50 nm or smaller, so that the gel time is fast compared to other characteristic times.

Next we report the results of a study of the cluster morphology and kinetics of a dense aggregating aerosol system using the small angle light scattering technique. The soot particles started as individual monomers, ca. 38 nm radius, grew to bigger clusters with time and finally stopped evolving after spanning a network across the whole system volume. This spanning is aerosol gelation. The gelled system showed a hybrid morphology with a lower fractal dimension at length scales of a micron or smaller and a higher fractal dimension at length scales greater than a micron. The study of the kinetics of the aggregating system showed that when the system gelled, the aggregation kernel homogeneity λ attained a value 0.4 or higher. The magnitude of the aggregation kernel showed an increase with increasing volume fraction.

We also used image analysis technique to study the cluster morphology. From the digitized pictures of soot clusters the cluster morphology was determined by two different methods: structure factor and perimeter analysis. We find a hybrid, superaggregate morphology characterized by a fractal dimension of $D_f \approx 1.8$ between the monomer size, ca. 50 nm, and 1 μm and $D_f \approx 2.6$ at larger length scales up to ~ 10 μm. The superaggregate morphology is a consequence of late stage aggregation in a cluster dense regime near a gel point.

AN EXPERIMENTAL STUDY OF DENSE AEROSOL AGGREGATIONS

by

RAJAN DHAUBHADEL

M. S., Tribhuvan University, 2000

A DISSERTATION

submitted in partial fulfillment of the requirements for the degree

DOCTOR OF PHILOSOPHY

Department of Physics
College of Arts and Sciences

KANSAS STATE UNIVERSITY
Manhattan, Kansas

2008

Approved by:

Major Professor
Christopher M. Sorensen

Abstract

We demonstrated that an aerosol can gel. This gelation was then used for a one-step method to produce an ultralow density porous carbon or silica material. This material was named an aerosol gel because it was made via gelation of particles in the aerosol phase. The carbon and silica aerosol gels had high specific surface area (200 – 350 m^2/g for carbon and 300 – 500 m^2/g for silica) and an extremely low density (2.5 – 6.0 mg/cm^3), properties similar to conventional aerogels. Key aspects to form a gel from an aerosol are large volume fraction, ca. 10^{-4} or greater, and small primary particle size, 50 nm or smaller, so that the gel time is fast compared to other characteristic times.

Next we report the results of a study of the cluster morphology and kinetics of a dense aggregating aerosol system using the small angle light scattering technique. The soot particles started as individual monomers, ca. 38 nm radius, grew to bigger clusters with time and finally stopped evolving after spanning a network across the whole system volume. This spanning is aerosol gelation. The gelled system showed a hybrid morphology with a lower fractal dimension at length scales of a micron or smaller and a higher fractal dimension at length scales greater than a micron. The study of the kinetics of the aggregating system showed that when the system gelled, the aggregation kernel homogeneity λ attained a value 0.4 or higher. The magnitude of the aggregation kernel showed an increase with increasing volume fraction.

We also used image analysis technique to study the cluster morphology. From the digitized pictures of soot clusters the cluster morphology was determined by two different methods: structure factor and perimeter analysis. We find a hybrid, superaggregate morphology characterized by a fractal dimension of $D_f \approx 1.8$ between the monomer size, ca. 50 nm, and 1 μm and $D_f \approx 2.6$ at larger length scales up to ~ 10 μm. The superaggregate morphology is a consequence of late stage aggregation in a cluster dense regime near a gel point.

Table of Contents

Table of Contents ..... **v**
List of Figures ..... **xi**
List of Tables ..... **xxi**
Acknowledgements ..... **xxii**
Dedication ..... **xxiii**
Nomenclature and Abbreviation ..... **xxiv**
CHAPTER 1- Introduction **1**
CHAPTER 2- Aerosol Mechanics **7**
2.1. Introduction 7
2.2. Radius of Gyration 8
2.3. Size Distribution 9
2.3.1. Self- similar Size Distribution 9
2.3.2. Log-normal Size Distribution 9
2.4. Properties of Medium Gas 10
2.4.1. Mean Free Path 11
2.4.2. Knudsen Number 11
2.4.3. Reynolds Number 12
2.5. Cunningham Slip Correction Factor 13
2.6. Particle Motion in a Medium 13
2.6.1. External Forces 14
2.6.1.1. Gravitational Force 14
2.6.1.2. Electrostatic Force 15
2.6.1.3. Thermal Force 15
2.6.1.4. Other Forces 16
2.6.2. Drag Force 17
2.6.3. Particle-Particle Interactive Forces 19
2.6.3.1. van der Waals Force 19
2.6.3.2. Repulsive Force between Atoms or Molecules 22
2.6.3.3. Repulsive Force between Particles 22

2.6.3.4. Total Interparticle Force 23
2.6.4. Brownian Motion and the Particle Transport 25
2.6.4.1. Langevin Equation 26
2.6.4.2. Equation of Diffusion 28
2.6.4.3. Diffusion Coefficient 29
CHAPTER 3- Aggregates, Fractals and Aggregation Theory 31
3.1. Introduction 31
3.2. Fractals and Fractal Dimension 32
3.2.1. Fractals 32
3.2.2. Fractal Dimension 35
3.3. Fractal Aggregates and their Growth Models 38
3.3.1. Particle-Cluster Aggregation Model 39
3.3.2. Cluster-Cluster Aggregation Model 41
3.3.2.1. Diffusion Limited Cluster Aggregation (DLCA) 43
3.3.2.2. Reaction Limited Cluster Aggregation (RLCA) 45
3.3.2.3. Ballistic Limited Cluster Aggregation (BLCA) 47
3.4. Kinetic Regimes of Particle Aggregation 49
3.4.1. Continuum Regime 49
3.4.2. Free Molecular Regime 50
3.4.2.1. Epstein Regime 50
3.4.2.2. Ballistic Regime 51
3.5. Relation between Mobility Radius and Radius of Gyration 51
3.6. Volume Fraction 52
3.6.1. Monomer Volume Fraction 52
3.6.2. Cluster Volume Fraction 52
3.7. Nearest Neighbor Separation 53
3.8. Aggregation Kinetics 56
3.8.1. Assumptions in the Mean Field Theory 56
3.8.2. Smoluchowski Equation 57
3.8.3. Aggregation (Coagulation) Kernel 58
3.8.3.1. Aggregation Kernel for Diffusing Particle 59

3.8.3.2. Modification in Aggregation Kernel due to a Force Field 61
3.8.3.3. Aggregation Kernel in Different Regimes of Particle Aggregation 63
3.8.3.3.1. Continuum Regime 63
3.8.3.3.2. Epstein Regime 64
3.8.3.3.3. Ballistic Regime 64
3.8.4. Kernel Homogeneity λ from Scaling Arguments 66
3.8.4.1. Homogeneity for Diffusive Fractal Aggregation 67
3.8.4.2. Homogeneity for Ballistic Aggregation 68
3.8.4.3. Homogeneity for Intermediate Diffusive Fractal Aggregation 68
3.8.5. Analytical Solution of Smoluchowski Equation 69
3.8.5.1. General Homogeneous Kernel Case 69
3.8.5.2. Constant Kernel Case 71
3.9. Self-Preserving Particle Size Distribution 73
3.10. Scaling Solution of Smoluchowski Equation 74
3.11. Evolution of the Moments of the Size Distribution 76
3.12. Particle Size Distribution Dynamics 77
3.13. Aggregation when Dense 80
3.13.1. Gelation 83
3.14. Gravitational Settling 86
3.15. Turbulence Effect on Aggregation 87
CHAPTER 4- Techniques for Studying Aggregation Processes 89
4.1. Introduction 89
4.2. Photon (Light) Scattering 90
4.2.1. Scattering Theories 92
4.2.1.1. Rayleigh Scattering 92
4.2.1.2. Rayleigh-Debye-Gans (RDG) Scattering 94
4.2.1.3. Mie Scattering 96
4.2.2. Scaling Description of the Scattering of a Wave 98
4.2.2.1. Scattering from Fractal Aggregates 104
4.2.3. The Structure Factor 106
4.2.3.1. Small q Behavior 108

4.2.3.2. Large q Behavior 109
4.2.3.2.1. The Best Cutoff Function for Fractal Aggregates 109
4.2.3.3. Structure Factor from The Scattered Intensity 111
4.2.3.3.1. Structure Factor for a Single and an Ensemble of Fractal Aggregates 112
4.2.4. Absolute Scattering by Fractal Aggregates 114
4.2.5. Photon Correlation Spectroscopy (Dynamic Light Scattering) 117
4.3. Image Analysis 122
4.3.1. Structure Factor Method 122
4.3.2. Perimeter Analysis 123
CHAPTER 5- Experimental Study of Cluster Morphology in Dense, Gelling Aerosols 125
5.1. Introduction 125
5.2. Cluster Image Analysis Study 127
5.2.1. Aggregate Structure Determination Methods 129
5.2.2. Results 130
5.2.3. Conclusion 133
5.3. Light Scattering Study 133
5.3.1. Experimental Setup 133
5.3.1.1. The Optical Chamber 134
5.3.1.2. Small Angle Static Light Scattering Setup 137
5.3.1.3. SASLS Setup Calibration 141
5.3.1.4. Light Scattering Data Acquisition 143
5.3.2. Results and Discussion 143
5.3.2.1. Monomer Volume Fraction Measurement 145
5.3.2.2. Interpretation of Light Scattering data with Multiple Scattering Effects 148
5.3.2.3. Observation of Hybrid Morphological Superaggregates 153
5.3.3. Conclusion 159
5.4. Neutron Scattering Study 159
5.4.1. Results and Discussion 163
5.4.2. Conclusion 167

CHAPTER 6- Light Scattering Study of Aggregation Kinetics in Dense, Gelling Aerosols 168

6.1. Introduction 168

6.2. Experimental Setup 171

6.3. Results and Discussion 172

6.3.1. Kinetic Exponent z (and Homogeneity λ) Measurements 173

6.3.2. Aggregation Kernel K 176

6.4. Conclusion 181

CHAPTER 7- Aerosol Gelation: Synthesis of a Novel, Light Weight, High Specific Surface Area Material 182

7.1. Introduction 182

7.2. Carbon Aerosol Gel 184

7.2.1. Experimental Methods 184

7.2.2. Results and Discussion 186

7.2.2.1. Density Measurement 190

7.2.2.2. Specific Surface Areas and Surface Porosity 191

7.2.2.3. Microscopic Structure of the Carbon Aerosol Gel 192

7.2.2.4. Electrical Conductivity of the Carbon Aerosol Gel 198

7.2.2.5. Hydrophobicity of the Carbon Aerosol Gel 199

7.2.2.6. Comparision with a Normal Open Flame Soot 200

7.2.3. Conclusion 200

7.3. Silica Aerosol Gel 201

7.3.1. Experimental Setup 201

7.3.2. Results and Discussion 204

7.3.2.1. Role of the Background Gas 205

7.3.2.2. Premixing and Amount of Silane/Oxidizer in the Background Gas 209

7.3.2.3. Hydrophilic and Hydrophobic Silica Aerosol Gels 210

7.3.2.4. Microscopic Structure of the Silica Aerosol Gel 212

7.3.2.5. Morphology of the Silica Aggregates 215

7.3.3. Conclusion 216

CHAPTER 8- Light Scattering Study of Cluster Dynamics in Dense, Gelling Aerosols 217

8.1. Introduction....217

8.2. Experimental Methods....218

8.3. Results....221

8.4. Conclusion....227

CHAPTER 9- Summary.... 228

Appendix A 230

Appendix B 231

Appendix C 232

Appendix D 234

Appendix E 237

References 240

List of Figures

Figure 1.1: A dispersed system of monomers aggregates due to the Brownian motion of the particles to form clusters. Because of the fractal nature, the nearest neighbor separation between the clusters R_{nn} decreases as the aggregation proceeds with time. Hence R_{nn} eventually becomes a relevant length scale with respect to any given cluster's motion. Finally when the ratio R_{nn}/R_g approaches two, the clusters start touching each other and the system gels. 3

Figure 1.2: Evolution of a dispersed system of aggregating monomers from individual monomeric particle to the gelation. Initially when $R_{nn}/R_g >> 1$ (cluster dilute), normal Brownian diffusion, Diffusion Limited Cluster Aggregation (DLCA) occurs creating fractals with a dimension D_f = 1.8 less than the special dimension d = 3. Eventually when $R_{nn}/R_g \geq 1$ (cluster dense), clusters are not free to Brownian diffuse, instead they jam, percolate and form percolation *superaggregate* with $D_f \approx 2.6$. 5

Figure 2.1: The plots of the attractive, repulsive and the total potential for 20 nm polystyrene particles in water. The zeta potential ψ_0 is taken to be 30 mV and 40 mM of $MgCl_2$ is assumed to be added to the system. The Hamaker constant is taken to be 3.14 k_BT. 25

Figure 2.2: A typical Brownian motion in a 3-d space. This picture has been taken from http://en.wikipedia.org. 26

Figure 3.1: Zooming in to different magnification level reveals more details with a self-similar structure. (a) A fern plant. (b) A Sierpinski Triangle. 33

Figure 3.2: Koch curve shown up to its 4^{th} generation. 34

Figure 3.3: Third generation Koch snow flake. 35

Figure 3.4: Geometrical objects: a line, a square and a cube. (a) Each side is bisected. (b) Each side is divided into three equal parts. A line is a one dimensional, a square is a two dimensional and a cube is a three dimensional object. 36

Figure 3.5: DLA cluster of 3000 monomers on a square lattice (Witten, 1983). 40

Figure 3.6: A computer generated DLCA cluster in 2-*d* system with size L = 128 and 1024 monomers. This cluster was formed at the end of the simulation and contains all the monomers (Kolb et al., 1983). 44
Figure 3.7: Comparison between TEM pictures of gold colloidal clusters with 5000 particles. (a) DLCA cluster with D_f =1.75. (b) Slow RLCA cluster with D_f =2.01 (Weitz et al., 1985). 47
Figure 3.8: A 2-*d* BLCA cluster with 5000 particles simulated on a 400 x 400 lattice (Meakin, 1984b). 48
Figure 3.9: Nearest neighbor separation. (a) Closed packed spheres for which $R_{nn} = 2R_p$. (b) The system is expanded such that $R_{nn} > 2R_p$. (c) Spheres are replaced by fractal aggregates. 55
Figure 3.10: Functionalities of the gel time t_{gel}. 86
Figure 4.1: A typical electromagnetic wave scattering geometry. (a) A vertically polarized beam (along X-axis) falls on a scatterer at postion $\vec{r}$. The scattering plane is the horizontal plane (YZ-plane). (b) The scattering wave vector $\vec{q}$ for a scatter wave on the scattering plane. 91
Figure 4.2: Rayleigh-Debye-Gans scattering. Straight lines separating different scattering regimes shown in this figure are in exaggeration. In reality there are no distinct boundaries between the different regimes. 96
Figure 4.3: The envelopes of the Mie scattered intensity distribution normalized by the forward scattered intensity. The crossovers between three regimes $(qa)^0$, $(qa)^{-2}$ and $(qa)^{-4}$ (Rayleigh, intermediate and Porod regimes) are shown. In the limit $\rho \to 0$ Mie scattering reduces to RDG scattering. 97
Figure 4.4: A sphere of radius R containing N point scatterers uniformly distributed with $2a$ as the nearest neighbor separation. Only the skin layer of thickness l gets illuminated by the incident wave. Thickness l decreases with increase in the phase shift parameter ρ. The dotted circles are q-regions. Only scatterers in one single q-region scatter in phase; scattering from different ones being random. 100
Figure 4.5: Log-log plot of $I(q)$ versus q. The region where the intensity falls with $-D_s$ slope becomes narrower and narrower and finally vanishes as the phase shift

parameter $\rho \to 0$. For the mass dimension $D_m = 3$ and the surface dimension $D_s = 2$, this plot becomes identical to the Mie scattering plot. 104
Figure 5.1: (a) 16.6 liter aluminum chamber with a 23.9 cm internal diameter and a 37.1 cm height. (b) 3.9 liter aluminum chamber with a 12.5 cm internal diameter and a 31.5 cm height. 128
Figure 5.2: (a) TEM picture of soot clusters, note scale bar, (b) structure factor of and (c) perimeter analyses of part (a). The fractal dimension measured is equal to the negative slope of either graph and is found to be ~ 1.80. 131
Figure 5.3: (a) TEM picture of a large soot cluster, note scale bar, (b) structure factor of and (c) perimeter analyses of part (a). The fractal dimension is equal to the slope in the structure factor analysis. The perimeter analysis slope yields the perimeter fractal dimension, 1.44. The mass fractal dimension is found via Eqs. (4.94) to be 2.42. 132
Figure 5.4: The front view of the optical chamber. 134
Figure 5.5: Schematic diagram of the optical chamber. (a) Different components of the optical chamber. (b) Internal dimensions of the central ring which becomes the reaction volume when the components were put together. 135
Figure 5.6: The chart showing the optical chamber filling procedure. 136
Figure 5.7: (a) The schematic diagram of SASLS measurement technique. The lens 1 collects the light scattered at constant angle and focuses at its Fourier plane that is then imaged by the lens 2 on the photodiode detector. The transmitted beam is cleaned by using a tiny reflecting mirror placed at the focus of the lens 1. (b) Schematic diagram of the light scattering from the optical chamber. 138
Figure 5.8: The schematic diagram of SASLS measurement technique. There is one to one correspondence between the pixels of the photodiode detector and the scattering wave vector q associated with the scattering angle θ 140
Figure 5.9: Forward normalized diffraction intensity distribution for a 10 μm single slit. The open circles are the experimental data while the solid line is the theoretical distribution. Since a slit is a one dimensional object the slope (dotted line) with which the intensity drops in the power law regime is -2. 142

Figure 5.10: TEM image of carbon soot monomers prepared by the detonation of a gas mixture of acetylene and oxygen in a closed combustion chamber. The monomers looked more graphitic compare to those from a normal diffusion flame. The monomers had a size distribution with an average radius of 38 nm and a standard deviation of 8 nm. 144

Figure 5.11: Frequency distribution of monomer sizes for 187 randomly chosen monomer images in TEM pictures. Average monomer diameter for this distribution was 76.7 nm (radius 38.3 nm) with a standard deviation of 16.6 nm. 147

Figure 5.12: A graph of albedo ω (Eq. (39)) against the cluster radius of gyration R_g with $3(E/F)/2k_0 = 1$, a typical value for soot fractal aggregates, and λ = 488 nm. Here we used the carbon soot monomer size (radius) a = 38 nm as shown by TEM pictures, and the fractal dimension D_f = 1.8. 148

Figure 5.13: Log-log plot of scattered intensity versus the scattering wave vector q evolving with time when the optical path length for the laser beam through the scattering volume is (a) 10 mm (b) 3 mm and (c) 1.5 mm. The time elapsed when a measurement was taken after the creation of the aerosol is indicated. The effect of multiple scattering becomes larger with increasing optical path length as indicated by a smaller apparent fractal dimension. 150

Figure 5.14: A typical result of the scattering from a system with $f_v = 1.0 \times 10^{-4}$ as a log-log plot of scattered intensity versus scattering wave vector. A hybrid morphology of the clusters with a larger fractal dimension at larger length scale (smaller q values) and smaller fractal dimension at smaller length scale (larger q values) was revealed from these figures. (a) Scattered intensity plot evolving with time. (b) Scattered intensity distribution 60 sec after the creation of the aerosol. The crossover length scale seems to be somewhere between 1.5 to 3.0 μm. (c) Replot of (b) emphasizing the morphological crossover. 155

Figure 5.15: Ultra small-angle neutron scattering (USANS) BT5 instrument with a perfect crystal diffractometer (PCD) for ultra-high resolution measurements. This instrument is located at NIST Center for Neutron Scattering (NCNR). Source: http://www.ncnr.nist.gov. 160

Figure 5.16: Small-angle neutron scattering (SANS) NG7 30 m instrument. This instrument is located at NIST Center for Neutron Scattering (NCNR). Source: http://www.ncnr.nist.gov. 160
Figure 5.17: A photograph of the cylindrical chamber for neutron scattering experiments. The picture was taking after detonating the gas mixture inside using a starter (can be seen in the picture) connected to the spark plug of the chamber. 162
Figure 5.18: The gelled network as a consequence of Brownian aggregation of carbon nanoparticles produced during the explosion of the gas mixture inside the chamber. The network did span the whole volume of the system. 162
Figure 5.19: Combined USANS and SANS result from a collapsed carbon aerosol gel sample. Scattered neutron intensity $I(q)$ is plotted versus the scattering wave vector q. Here one clearly sees several power-law regimes; $\sim q^{-4}$ at low-q indicative of a compact 3-d structure at large length scales formed during collapsing of the aerosol gel; $\sim q^{-1.65}$ at intermediate-q indicative of a mass fractal aggregate; $\sim q^{-3.4}$ at high-q indicative of 3-d monomer structure; and one more $\sim q^{-4}$ at yet higher-q indicative of the internal feature of the monomer structure. 163
Figure 5.20: TEM picture of carbon soot monomers from a closed explosion of acetylene and oxygen mixture. Monomers had graphitic layer planes a few nanometers thick around the surface with their planer orientation parallel to the particle surfaces forming a shell-like structure. 164
Figure 5.21: Combined USANS and SANS result from an unperturbed carbon aerosol gel sample. Scattered neutron intensity $I(q)$ is plotted versus the scattering wave vector q. Here one clearly sees several power-law regimes; $\sim q^{-1.67}$ at intermediate-q indicative of a mass fractal aggregate; $\sim q^{-3.7}$ at high-q indicative of 3-d monomer structure; and one more $\sim q^{-4}$ at yet higher-q indicative of the internal feature of the monomer structure. 166
Figure 6.1: A picture of the static gel network formed inside the optical chamber observed through its glass windows. The upper black layer was due to gravitational settlement. Initially individual ca. 38 nm radius carbon particles grew in size upon Brownian aggregation eventually resulting in formation of a macroscopic

random network in less than 100 sec. A macroscopic anisotropy with vertical strand structures was observed. These strands were the results of the gravitational settling tendency of the giant clusters. 172
Figure 6.2: Growth of cluster radius of gyration with time when $f_v = 2.3 \times 10^{-5}$. The cluster radius of gyration is determined using Guinier analysis of the scattered intensity data. 174
Figure 6.3: A plot of the kinetic exponent z and the homogeneity λ versus the monomer volume fraction f_v. The enhanced aggregation kinetics with increasing f_v was the result of the effect of cluster crowding. 175
Figure 6.4: Figure 8 from the paper by Carpineti et al. (Carpineti et al., 1990) showing evolutions of the radius of gyration (R_G) of the clusters of 130 nm diameter polystyrene colloidal particles as a function of a reduced time $T = tc_o$ for different values of monomer number concentration. The tendency of the curves to roll upward shows the speeding up of the aggregation process at later times. 176
Figure 6.5: An example of the plot of the inverse cluster number density $1/n_2$ versus time t when $f_v = 2.3 \times 10^{-5}$. 179
Figure 6.6: A plot $K(s_2, s_2)$ as a function of the monomer volume fraction f_v. The dashed line shows the theoretical value of K independent of the monomer volume fraction. The theoretical K was computed for a monodisperse aggregating system in continuum regime with Stokes-Einstein diffusion. 180
Figure 7.1: Carbon aerosol gel, density = 2.5 mg/cm^3. 186
Figure 7.2: A series of top view pictures of gravitationally collapsing acetylene aerosol gel in the 24 cm wide 37 cm deep chamber. (a) The gel was found to fill almost to the top 2 minutes after creating the aerosol and 5 seconds after opening the lid. (b) The aerosol gel collapsed somewhat 30 sec after the lid was opened. (c) The gel collapsed by more than half the depth of the chamber 1 min later. Relatively slow collapsing was observed afterwards. (d) 1.5 min later. (e) 2 min later. (f) Gel collapsed completely to about a 2 cm thick layer 20 min later. .. 188
Figure 7.3: TEM pictures of (a) an acetylene aerosol gel (b) an ethylene aerosol gel (c) a propane aerosol gel and (d) an acetylene open flame soot. 193

Figure 7.4: A high resolution TEM pictures of an acetylene aerosol gel. The graphitic layer planes are clearly visible and appear to extend only over the surface of the primary particles of the aerosol gel. 194
Figure 7.5: X-ray diffraction of the compressed carbon aerosol gels and open flame acetylene soot. The vertical lines indicate the positions of the corresponding diffraction peaks. 195
Figure 7.6: Thermal Gravimetric Analysis (TGA) showing less than 1% change in the total mass of the carbon aerosol gels after heating from room temperature up to 600^{o}C. This is an indication of the absence (or negligible presence) of volatile substances in the carbon aerosol gels. 196
Figure 7.7: Energy Dispersive X-ray spectroscopy (EDS) result showing only the peak corresponding to the elemental carbon present in the carbon aerosol gel. 197
Figure 7.8: Log-log plot of conductivity vs density at room temperature for acetylene aerosol gel. Quadratic variation of conductivity with density is observed. The data final point indicated by a star sign is for pure graphite..... 198
Figure 7.9: Almost spherical shaped water droplet, about 2 mm in diameter, sitting on the surface of a crushed carbon aerosol gel. A large contact angle demonstrates the hydrophobic behavior of the carbon aerosol gel..... 199
Figure 7.10: A schematic diagram of the experimental setup for making a silica aerosol gel. .. 202
Figure 7.11: Experimental setup for making Silica Aerosol Gel. Apparatus arrangement under an exhaust hood. Different components are as labeled. 203
Figure 7.12: Silica aerosol gel prepared using oxygen as the oxidizer and nitrogen as a background gas. 204
Figure 7.13: Silica paint scrapped out from the inner walls of the chamber when no background gas was used..... 205
Figure 7.14: View, looking down into the reaction chamber, of (a) light fluffy silica aerosol gel formed when the N_2 gas up to 2.5 atmospheric pressure was used as the background gas and (b) comparatively denser silica aerosol gel formed when the N_2 gas up to 1.5 atmospheric pressure was used as the background gas. 206

Figure 7.15: TEM images of silica aerosol gels prepared using (a) nitrogen and (b) carbon dioxide as the background gas. These images show no significant difference between the two cases. 207
Figure 7.16: TEM picture of Silica aerosol gel prepared using oxygen as the oxidizer and helium as a background gas. 208
Figure 7.17: Dense (13mg/cm^3) bright white silica aerosol gel formed when O_2 was premixed with the background N_2 gas. 209
Figure 7.18: Brown silica aerosol gel prepared when SiH_4/O_2 ratio was more than stoichiometric. 210
Figure 7.19: A picture of a hydrophobic silica aerosol gel taken several months after floating the gel on the top of water. N_2O was used as the oxidizer to prepare this silica aerosol gel. 211
Figure 7.20: Carbon coating on hydrophilic silica aerosol gel turns it into a hydrophobic silica aerosol gel. In the picture is shown a water drop (~ 3mm diameter) sitting on the aerosol gel showing its hydrophobic nature. 211
Figure 7.21: X-ray diffraction patterns for the silica aerosol gel and powdered amorphous silica. Matching of the peaks confirmed the material of the aerosol gel to be definitely silica. Broad peak indicated low degree of crystalline for the silica aerosol gel. 213
Figure 7.22: (a) Electron diffraction pattern from the silica aerosol gel. (b) Electron diffraction pattern from the commercial silica aerogel. The more distinct diffraction pattern for the silica aerosol gel implies that its monomers are more crystalline compare to those of commercial silica aerogel. 214
Figure 7.23: TEM image of the commercial silica aerogel. The monomers, ~10 nm in diameter, do not appear distinctly. 214
Figure 7.24: Combined USANS and SANS result from a collapsed silica aerosol gel sample. Scattered neutron intensity $I(q)$ is plotted versus the scattering wave vector q. One clearly see power-law regimes; ~ $q^{-1.75}$ at intermediate q indicative of a mass fractal aggregate and ~q^{-4} at high-q indicative of 3-d monomer structure. Stronger power law decay of scattered intensity at low-q

can be explained as an artifact of the collapsing of the aerosol gel. Collapsing caused a compact 3-*d* structure to form at large length scales. 215

Figure 8.1: Schematic diagram of the experimental set up for the DLS experiments. Counter propagating beams allowed quick measurements of the intensity correlation at 40^{o} and 140^{o} scattering angles by blocking one beam at a time. 218

Figure 8.2: The characteristic correlation time τ_c for a dilute system of 24 nm diameter polystyrene colloidal particles inside the optical chamber plotted versus the scattering wave vector q. The observed q^{-2} dependence of τ_c verified that the measurements on the scatterers inside the optical chamber were reliable..... 220

Figure 8.3: Field correlation function $g^{(1)}(\tau)$ at q = 8.81 μm^{-1} at various time t after the creation of carbon soot aerosols inside the optical chamber. A quick transition was observed from an exponential to a stretched exponential decay of the correlation function at both q values. Solid lines are the stretched exponential curves fitted. 222

Figure 8.4: Field correlation function $g^{(1)}(\tau)$ at q = 24.20 μm^{-1} at various time t after the creation of carbon soot aerosols inside the optical chamber. A quick transition was observed from an exponential to a stretched exponential decay of the correlation function at both q values. Solid lines are the stretched exponential curves fitted. 223

Figure 8.5: Plot of the decay exponent β and the characteristic correlation time $\tau_c^{'} = \tau_c / \delta^{1/\beta}$ versus time t. The time evolutions in β and $\tau_c^{'}$ were fast such that the saturation values were almost attained by the end of the first 70 sec after the creation of the aggregating aerosol system. 224

Figure 8.6: Plot of the decay exponent β and the characteristic correlation time $\tau_c^{'} = \tau_c / \delta^{1/\beta}$ versus time t. The time evolution in β was fast such that the saturation value was almost attained by the end of the first 60 sec after the creation of the aggregating aerosol system. The characteristic correlation time $\tau_c^{'}$ showed no or negligible evolution. 225

Figure 8.7: Field correlation functions at a certain time t corresponding to 40^{o} and 140^{o} scattering angles plotted versus $\left(\tau / \tau_c^{'}\right)$. The two correlation functions fall under

the same master curve illustrating that the dynamics is well described by a stretched exponential decay of the correlation function (Eq. (8.6)). 226
Figure 8.8: The same correlation functions as in Fig. 8.7 plotted versus the correlation time τ 227

List of Tables

Table 2-1: Reynolds number and flow type. 12
Table 5-1: Monomer Size Distribution Statistics 146
Table 7-1: Aerosol gel densities for numerous synthesis runs obtained for selected fuels. 191
Table 7-2: Listing of the BET results averaged over different runs. The densities are about 10 mg/cm^3, higher than as prepared, due to some crushing during sample preparation. 192

Acknowledgements

Before anything else I would first like to express my deepest gratitude to my thesis advisor Dr. Chris Sorensen. This dissertation could not have been completed without his supervision, encouragement and guidance. He has been like my father patiently educating me throughout my academic program and helping me to develop quality of an independent scientist within myself. He taught me how to approach research problems and the need to be persistent to accomplish any goal. I am equally grateful to Dr. Amit Chakrabarti as well for his stimulating and very helpful suggestions during this work. I not only learned a great deal, but also enjoyed a lot from his style of analysing complex research problems starting with analogical simple problems.

I also thank my research group for the helpful discussions we had. Discussions with colleagues including Flint Pierce and Tahereh Mokhtari have been very useful. I greatly appreciate all of them. I cannot forget to thank Dr. Kennet J. Klabunde for letting me to use BET and XRD facilities in his laboratory in Dept. of Chemistry, KSU. Also thanks to Dr. Dan Boyle for helping me in capturing TEM images of my samples. I would like to express my gratefulness to the NIST Center for Neutron Scattering Research as well for letting me to conduct neutron scattering experiments from our carbon aerosol gel. I also acknowledge NASA and Cabot Corp. for financially supporting the research work presented in this thesis.

I gratefully acknowledge all the members of my committee who have given their time to read this manuscript and also offered valuable advice during my graduate career at KSU.

I thank my parents for their love, support and encouragement throughout my life.

My final but very special thanks go to my loving wife Smriti Shrestha for being a constant source of inspiration. Her support, encouragement, and companionship have turned my struggle through graduate school into a pleasure.

Dedication

To my parents, Govinda and Laxmi, and my wonderful wife, Smriti: for their encouragement and ever lasting love and support.

Nomenclature and Abbreviation

Chapter 1

λ	Kernel homogeneity
Ω	Free volume
d	Euclidean dimension
D_f	Fractal dimension
DLCA	Diffusional limited cluster aggregation
$K(v,u)$	Aggregation kernel
Kn	Knudsen number
P_{stick}	Sticking probability of a particle
R_g	Radius of gyration
R_{gel}	Gel time cluster radius of gyration
RLCA	Reaction limited cluster aggregation
R_{nn}	Nearest neighbor particle separation
SE	Smoluchowski's coagulation rate equation
t	Time
TEM	Transmission Electron Microscope
u	Cluster size (either mass or monomer number)
v	Cluster size (either mass or monomer number)
z	Aggregation kinetic exponent

Chapter 2

α_i	Electronic polarization of the i^{th} particle
χ	Shape parameter
ε	Relative permittivity of a medium
ε_0	Permittivity of the free space
$\in_0$	Lennard-Jones potential well depth
η	Dynamic fluid viscosity
λ_D	Debye screening length
λ_g	Mean free path of the medium molecules
μ	Particle mobility
$\rho(\vec{r})$	Mass density
ρ_g	Fluid (medium) mass density
ρ_p	Particle mass density
ρ_{pni}	Molecule number density in the i^{th} particle
σ_g	Geometric standard deviation of particle size distribution
σ_i	Radius of the i^{th} atom or molecule
ψ_o	Surface or zeta potential of a particle

B	Electrical mobility
C_c	Cunningham slip correction factor
C_D	Coefficient of drag force
d	Characteristic dimension of an object
D	Diffusion coefficient
d_g	Diameter of a medium molecule
d_{gm}	Geometric mean particle diameter
d_p	Particle diameter
E	Electric field
F_D	Drag force
f_{dg}	Drag coefficient
F_{th}	Thermophoresis
g	Acceleration due to gravity
H	Hamaker constant
h	Vertical height
I_i	Ionization potential of the i^{th} particle
$\vec{J}$	Particle flux
k_g	Thermal conductivity of a medium
Kn	Knudsen number
k_p	Thermal conductivity of a particle
m_p	Mass of a particle
n	Particle number concentration
n_g	Number density of the medium molecules
P	Pressure
q	Charge on a particle
$\vec{r}$	Distance vector
R	Radius of an aerosol particle
Re	Reynolds number
Re_f	Flow Reynolds number
Re_p	Particle Reynolds number
R_g	Radius of gyration
T	Absolute temperature
t	Time
v_p	Relative velocity of a particle
V_p	Volume of a particle
v_{pgrav}	Particle gravitational settling velocity
v_{pt}	Terminal velocity of a particle
v_{pth}	Thermophoresis particle velocity
$W(r)$	Potential energy of a particle
x	Scaled separation

Chapter 3

α	p - λ

β	Correction factor in the aggregation kernel
β_i	Characteristic inertial response time of the i^{th} particle
$\in$	Energy dissipation per unit medium fluid mass
Φ	Potential function
$\phi(x)$	Self-preserving or scaled size distribution
γ	Diffusivity or mobility exponent
γ_c	Critical diffusivity exponent
η	Dynamic fluid viscosity
φ	Random number
λ	Kernel homogeneity
λ_p	Persistence length of a particle
μ	$\mu + \nu = \lambda$
μ	Particle mobility
ν	$\mu + \nu = \lambda$
ν	Kinematic viscosity of the medium
ρ	Cluster mass density
ρ_g	Medium mass density
ρ_p	Density of a monomer
τ	An exponent $\omega = (2-\tau)z$
Γ	RMS Velocity gradient in an isotropic turbulence
ω	An exponent $\omega = (2-\tau)z$
Ω	Free volume
$\psi(x)$	Scaling function
ζ	An exponent
a	Monomer radius
A	Normalization constant in the scaled size distribution
A_c	Collision cross sectional area
A_{ij}	Collision cross sectional area
BLA	Ballistic limited aggregation
BLCA	Ballistic limited cluster aggregation
c_{ij}	Particle equipartition relative velocity
D	Diffusion coefficient
d	Euclidean dimension
D_E	Epstein diffusion coefficient
D_f	Fractal dimension
DLA	Diffusion limited aggregation
DLCA	Diffusional limited cluster aggregation
D_{max}	Maximum diffusion coefficient of any cluster in the system
D_{SE}	Einstein diffusion coefficient
$\vec{F}$	Force
f_{cpv}	Close packed volume fraction
f_v	Monomer volume fraction
f_{vc}	Cluster volume fraction
f_{vp}	Particle volume fraction

$g(x)$	Scaling function
$I_i(K,\phi)$	A notation given to a complex integration
$\vec{J}$	Particle flux
$\bar{k}$	Mean particle size
$K(v,u)$	Aggregation kernel
k_B	Boltzmann coefficient
Kn	Knudsen number
Kn_D	Diffusional Knudsen number
k_0	A prefactor
l_k	Kolmogorov length scale
m	Medium molecular mass
m_i	i^{th} moment of the scaling distribution
M_i	i^{th} moment of the size distribution
m_p	Mass of a particle
N	Number of monomers in a cluster
n	Particle number concentration
n_0	Initial particle concentration
n_c	Total cluster number concentration
$n_{cluster}$	Monomer number density in a cluster
$n_{col}(t)$	Total collision rate
n_m	Monomer number concentration
n_{system}	Monomer number density in a system
P_{stick}	Sticking probability of a particle
R	Particle size (radius)
r	Radial distance
$\dot{r}$	Relative velocity of a particle
R_g	Radius of gyration
R_{gel}	Gel time cluster radius of gyration
RLA	Reaction limited aggregation
RLCA	Reaction limited cluster aggregation
R_m	Mobility radius of a cluster
R_{nn}	Nearest neighbor particle separation
R_p	Perimeter radius
s_p	Mean particle size
T	Absolute temperature
t	Time
t_c	Characteristic Time
t_{gel}	Gel time
u	Cluster size (either mass or monomer number)
v	Cluster size (either mass or monomer number)
$\vec{v}_d$	Particle drift velocity
$\bar{v}(t)$	Mean cluster size at time t
v_T	Cluster terminal velocity
x	v/s_p Scaled size of a cluster
y	v/s_p Scaled size of a cluster

z	Aggregation kinetic exponent

Chapter 4

$\delta(\vec{r}-\vec{r}_i)$	Dirac delta function
ϕ	Polar angle
λ	Wavelength
μ_n	n^{th} cumulant
θ	Scattering angle on the scattering plane (Azimuthal angle)
ρ	Phase shift parameter = $2ka\lvert m-1\rvert$
σ_{scat}	Total scattering cross section
σ_{absp}^{agg}	Total scattering cross section for an aggregate
σ_{absp}^{mon}	Total scattering cross section for a monomer
$d\sigma_{scat}/d\Omega$	Differential scattering cross section
$\frac{d\sigma_{scat}^{agg}}{d\Omega}$	Differential scattering cross section for an aggregate
$\frac{d\sigma_{scat}^{mon}}{d\Omega}$	Differential scattering cross section for a monomer
τ	Correlation time
τ_c	Characteristic correlation time
$\overline{\tau_c^{-1}}$	Average inverse characteristic correlation time
ξ	Characteristic length
A and B	Instrumental factors
a	Monomer radius
A	Normalization constant in $g(r)$
a	Spacing distance between point scatterers in a particle
a	Spherical particle radius
C	A constant of proportionality in scaling relation for the structure factor
c_0	A constant
c_i	Amplitude of the decay rate for the i^{th} particle
C_p	Polydispersity factor of the ensemble
D	Diffusion coefficient
d	Spatial dimension
$\overline{D}$	Scattered intensity weighted average diffusion coefficient
D_f	Fractal dimension
D_m	Mass dimension
D_p	Perimeter fractal dimension
$\overline{D}_R$	Mean rotational diffusion coefficient for a system
D_s	Surface dimension
$E(m)$	Imaginary part of $\left[(m^2-1)/(m^2+2)\right]$

$\vec{E}(t)$	Scattered electric field at time t
$F(m)$	$\left\|(m^2-1)/(m^2+2)\right\|^2$
f_v	Monomer volume fraction
$g^{(1)}(\tau)$	Field correlation function
$g^{(2)}(\tau)$	Intensity correlation function
$G(kR_g)$	$\left(1+\frac{4}{3D_f}k^2R_g^2\right)^{-D_f/2}$
$g(r)$	Auto correlation function
$h(r/\xi)$	Cutoff function in $g(r)$
$I(q)$	Scattered intensity per unit solid angle at q
$I(q)/I(0)$	Scattered intensity normalized by forward scattering
$I(t)$	Scattered intensity at time t
I_0	Incident intensity
I_f	Mean scattered intensity from a diffusing scatterer
I_s	Static scattering from a static structure in the scattering volume
I_{scat}	Scattered intensity per unit solid angle
k	Wave vector
k_0	A prefactor
L	Size of the square mesh in an image analysis
l	Thickness of the illuminated region on a scattering particle
m	Relative refractive index of a scatterer
m_i	i^{th} moment of the scaling distribution
M_i	i^{th} moment of the size distribution
N	Number of monomers in a cluster
n	Number of scatterer per unit scattering volume
N	Total number of point scatterers in a particle (sphere or cluster)
$N(L)$	Number of square meshes of size L covering the picture of a cluster
$n(N)$	Cluster size distribution
$n(\vec{r})$	Density function of a scattering system
N_q	Total number of scatterers in a q-region
n_q	Total number q-regions in a system
N_s	Number of point scatterers on a surface
$P(\Delta\vec{r}(\tau),\tau)$	Gaussian probability distribution
q	Scattering wave vector
R	Particle size (radius)
R_c	Characteristic size
R_g	Radius of gyration
R_{g2}	Radius of gyration of the average cluster size $\langle N\rangle = s_2$
R_{gz}	z-average radius of gyration
$\vec{r}_i$	Position of the i^{th} particle
$\vec{r}(t)$	Position vector of a scatterer at time t
$S(q)$	Structure factor

s_2	2nd moment mean cluster size
SANS	Small Angle Neutron Scattering
SASLS	Small Angle Static Light Scattering
SAXS	Small Angle X-ray Scattering
$S_{eff}(q)$	Effective structure factor for an ensemble of clusters
SEM	Scanning Electron Microscope
t	Time
TEM	Transmission Electron Microscope
USANS	Ultra Small Angle Neutron Scattering
V_{scat}	Volume of a scattering particle
x	Ratio of I_s and I_f

Chapter 5

α	Conversion factor for the photodiode detector
γ	Diffusivity exponent
λ	Wavelength
θ	Scattering angle
σ_t	Maximum tensile stress in a window
τ	Cluster size distribution exponent
τ_{absp}	Absorption coefficient
τ_{ext}	Extinction coefficient
τ_{scat}	Scattering coefficient
ω	Albedo
a	Monomer radius
b	The width of a single slit
d	Window diameter
d	Spatial dimension
D_f	Fractal dimension
D_f^*	Apparent fractal dimension
D_p	Perimeter fractal dimension
$E(m)$	Imaginary part of $[(m^2 - 1)/(m^2 + 2)]$
f	Focal length of a lens
$F(m)$	$\left\|(m^2-1)/(m^2+2)\right\|^2$
f_v	Monomer volume fraction
$I(q)$	Scattered light intensity at wave vector q
I_0	Incident intensity
I_T	Transmitted intensity
k	Wave number of the incident wave
k_0	A prefactor
l	A length on the photodiode detector
l	Optical path length of a beam through the system

L	Size of the square mesh in an image analysis
m	Relative refractive index of a scatterer (monomer)
$N(L)$	Number of square meshes of size L covering the picture of a cluster
NCNR	NIST Center for Neutron Scattering Research
P	Pressure
q	Scattering wave vector
R_g	Radius of gyration
R_{gel}	Gel time cluster radius of gyration
R_{gz}	z-average radius of gyration
R_{nn}	Nearest neighbor particle separation
$S(q)$	Structure factor
SANS	Small Angle Neutron Scattering
SASLS	Small Angle Static Light Scattering
$S_{eff}(q)$	Effective structure factor for an ensemble of clusters
S_i	Object distance from a lens
S_o	Image distance from a lens
t	Window thickness
t	Time
TEM	Transmission Electron Microscope
t_{gel}	Gel time
t_{set}	Gravitational settling time
USANS	Ultra Small Angle Neutron Scattering
XRD	X-ray diffraction
z	Aggregation kinetic exponent

Chapter 6

λ	Kernel homogeneity
τ_{absp}	Absorption coefficient
ω	Albedo
Ω	Free volume
a	Monomer radius
A_c	Collision cross sectional area
A_s	Cluster's surface area
D	Diffusion coefficient
d	Spatial dimensional
D_f	Fractal dimension
$E(m)$	Imaginary part of $\left[(m^2-1)/(m^2+2)\right]$
f_v	Monomer volume fraction
K	Aggregation kernel
k_0	A prefactor
m	Relative refractive index of a scatterer (monomer)
m_i	i^{th} moment of the scaling distribution

M_i	i^{th} moment of the size distribution
N	Number of monomers in a cluster
n_2	Average cluster number density
n_c	Total cluster number concentration
n_m	Monomer number concentration
P_2	Polydispersity index
$\dot{r}$	Relative velocity of a particle
R_c	A characteristic length
R_g	Radius of gyration
R_{gz}	z-averaged radii of gyration
R_{nn}	Nearest neighbor particle separation
s_2	2nd moment mean cluster size
SASLS	Small Angle Static Light Scattering
t	Time
z	Aggregation kinetic exponent

Chapter 7

a	Monomer radius
BET	Brunauer-Emmett-Teller
d	Spatial dimensional
D_f	Fractal dimension
EDS	Energy Dispersive X-ray spectroscopy
f_v	Monomer volume fraction
HEL	Higher Explosion Limit
K	Aggregation kernel
LEL	Lower Explosion Limit
MF	Melamine/formaldehyde
MSDS	Material Safety Data Sheet
$n_{cluster}$	Monomer number density in a cluster
NCNR	NIST Center for Neutron Scattering Research
n_{system}	Monomer number density in a system
q	Scattering wave vector
RF	Resorcinol-formaldehyde
R_{gel}	Gel time cluster radius of gyration
SANS	Small Angle Neutron Scattering
STP	Standard temperature and pressure
TEM	Transmission electron microscopy
TEOS	Tetraethoxysilane
TGA	Thermal Gravimetric Analysis
t_{gel}	Gel time
TMOS	Tetramethoxysilane
USANS	Ultra Small Angle Neutron Scattering
XRD	X-ray diffraction

Chapter 8

β	Decay exponent
δ	An exponent
ϕ_0	$\phi(\tau = 0)$
λ	Wavelength
τ	Correlation time
τ_c	Characteristic correlation time
$\tau_c^{'}$	Characteristic correlation time
A and B	Instrumental factors
D	Diffusion coefficient
DLS	Dynamic Light Scattering
$g^{(1)}(\tau)$	Field correlation function
$g^{(2)}(\tau)$	Intensity correlation function
I_f	Mean scattered intensity from a diffusing scatterer
I_s	Static scattering from a static structure in the scattering volume
PAD	Pulse amplifier and discriminator
PMT	Photomultiplier tube
q	Scattering wave vector
x	Ratio of I_s and I_f

Chapter 9

λ	Kernel homogeneity
λ	Wavelength
DLCA	Diffusional limited cluster aggregation
f_v	Monomer volume fraction
K	Aggregation kernel
s_2	2^{nd} moment mean cluster size
SASLS	Small Angle Static Light Scattering
z	Aggregation kinetic exponent

CHAPTER 1- Introduction

Aggregation of particles has always remained a very important phenomenon in physics, biology and material science (Lin et al., 1989). Formation of cloud and rain drops, atmospheric aerosol particles, fractal formation, sol-gel transition, etc. are some examples where the aggregation process plays a vital role. Much deeper understanding of the structure of particle aggregates and the kinetics of their formation is the key to explain and control many complex but important phenomena in many different fields including biomedical science, material science and industry. During the last two and half decades people have used TEM pictures, confocal microscopy, photon correlation spectroscopy, and light, x-ray and neutron scattering techniques to study aggregation of colloids and aerosols which are common in nature and important for our technology (Bushell, et al, 2002).

Available literature indicates that the past studies are mostly limited to systems with low particle (or cluster) concentration. Although aggregation in such a system has been well understood, our knowledge of aggregation in systems with large particle (or cluster) concentration is still vague. Understanding the aggregation in concentrated system is important because the dense state of dispersed particulate matter is common in nature. Earlier works from our laboratory (see below) have observed indications of enhanced aggregation and morphological crossover in dense aggregating system. A need of more work to gain deeper understanding of dense aggregation has motivated the research reported in this thesis.

The morphology and aggregation kinetics in systems with low particle concentration have been extensively studied experimentally, theoretically and with computer simulations (Family and Landau, 1984, Cai, et al, 1995, Carpineti, et al, 1990, Jullien and Botet., 1987, Kolb, et al, 1983, Lin, et al, 1989, Meakin, 1983, Meakin, 1988,Meakin, 1992, Meakin, 1999, Schaefer and Martin, 1984, Sorensen and Roberts, 1997, Vicsek, 1989, Weitz and Oliveria, 1984). We will describe a system as dilute when the average cluster-cluster separation is very large compared to the cluster size and we will call this situation *cluster dilute*. Then the average cluster-cluster

separation is not a relevant length scale. Advancement in this area of research took a major step after Forrest and Witten (Forrest and Witten, 1979) first put forward a mathematical description of aggregates using the fractal concept developed by Mandelbrot (Mandelbrot, 1977). Such an aggregation in dilute systems has been well represented by a model called diffusion limited cluster-cluster aggregation (DLCA) (Kolb, et al, 1983, Meakin, 1983).

Smoluchowski's coagulation rate equation (SE) has been successfully used to determine the evolving aggregation kinetics during the aggregation process of non-equilibrium systems with low particle concentration (Smoluchowski, 1917), i.e. the SE can well describe the DLCA process. SE is based on a mean-field theory which can predict system behaviours only in the limit of spatially uncorrelated binary cluster collisions. Systems with low particle concentration are always in this limit. In mean field theory the thermodynamic fluctuations are assumed unimportant.

For a dilute system where particles undergo Brownian diffusional motion (Knudsen number Kn <<1), the aggregation process, based on the sticking probability (P_{stick}), is either *diffusion limited cluster aggregation* (DLCA) when $P_{stick} = 1$, or *reaction limited cluster aggregation* (RLCA) when $P_{stick} << 1$ (Meakin, 1992, Vicsek, 1989). Both DLCA and RLCA processes lead to the formation of fractal structures whose density decreases as the number of monomers in aggregate increases. This property of a fractal aggregate is a consequence of its fractal dimension D_f which is less than the spatial dimensional d.

As the system continuously evolves, the available volume for the cluster to diffuse (free volume) decreases and hence the nearest neighbor cluster separation R_{nn} eventually becomes a relevant length scale with respect to any given cluster's motion (see Fig. 1.1). We call this case the *intermediate regime*. Later in time, the clusters can grow large enough such that they start developing a connectivity network among themselves. Such systems are near the gel point. In this extreme, *cluster dense* limit, the distance between extended edges of the cluster become comparable to the *persistence length* (the distance over which a cluster moves effectively in a straight line). This makes the aggregation kinetics different in the cluster dense regime compare to the cluster dilute regime and thus results clusters with different morphology.

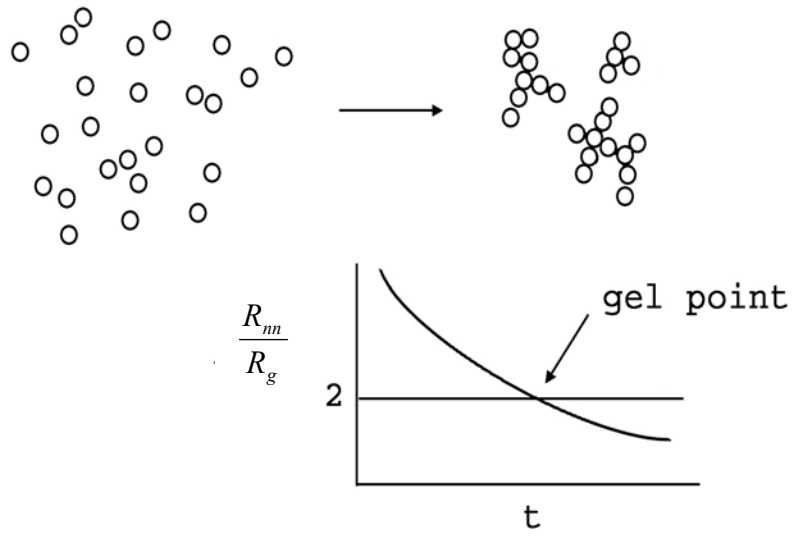

Figure 1.1: A dispersed system of monomers aggregates due to the Brownian motion of the particles to form clusters. Because of the fractal nature, the nearest neighbor separation between the clusters R_{nn} decreases as the aggregation proceeds with time. Hence R_{nn} eventually becomes a relevant length scale with respect to any given cluster's motion. Finally when the ratio R_{nn}/R_g approaches two, the clusters start touching each other and the system gels.

Very few simulations (Fry et al., 2002, Gimel et al., 1995, Hasmy and Jullien, 1996, Kolb and Herrmann, 1985, Rottereau et al., 2004) and almost no experimental studies (Dhaubhadel et al., 2006, Kim et al., 2006, Sorensen et al., 2003) are found in literature that study aggregation from the dilute regime up to the cluster dense regime. Previous simulation studies of aggregation were limited in time and/or system size (however, see below) with smaller volume fractions so that the cluster dense regime was not attained. Also most of the previous experimental attempts were limited to smaller monomer volume fractions such that the time the system would have taken to transit from cluster dilute to cluster dense was much longer than the typical experimental observation time.

Previous computer simulations of aggregation with Brownian dynamics (Fry et al., 2002) from our laboratory have shown that the cluster motion evolves from cluster dilute limit DLCA (Brownian) to cluster dense, ballistic motion as the system crossed over from the cluster dilute to the cluster dense regime. The *kinetic exponent z* in the power-law cluster growth with time *t*, i.e.

$R_g \sim t^{z/D_f}$, was found to continuously evolve from 1 to 2 and the *kernel homogeneity* λ, which is related to the cluster growth kinetics and the resulting cluster size distribution, concomitantly evolved from 0 to 0.5. Kinetic exponent $z = 1$ and homogeneity $\lambda = 0$ during the early dilute stage of the aggregation process were as expected for DLCA. For a ballistic-type aggregation, where the aggregating clusters move along straight paths between successive collisions with speed determined by the equipartition of energy, z was 2 and λ was 0.5. Both parameters z and λ were found to be universal functions of the *free volume* Ω, which is the volume not occupied by the growing clusters. The cluster crowding was found to be the only reason for the enhanced aggregation kinetics.

In related simulation studies (Fry et al., 2004), it has also been shown that near the gel point the aggregates become so crowded that they percolate to form $D_f \approx 2.6$ aggregates. It has been shown (Stauffer and Aharony, 1985) that the clusters formed by a percolation process have a fractal dimension of 2.6, larger than DLCA value. Each of these $D_f \approx 2.6$ aggregates is found to be built with dilute limit $D_f \approx 1.8$ aggregates when analyzed at smaller length scales. Such clusters have been named as *superclusters* or *superaggregates*. The crossover in the fractal dimension occurs at a critical or ideal gel point cluster size R_{gel}, which is the average cluster size when R_{nn} / R_g drops to two. Fig. 1.2 shows the evolution of a dispersed system of aggregating monomers from individual monomeric particle to the gelation.

Gimel et al. (Gimel et al., 1995, Rottereau et al., 2004) have also recognized the crossover process to be explainable by static percolation theory. From their extensive computer simulation study, they found that systems undergoing the DLCA process eventually become cluster dense and finally gel irrespective to their monomer volume fraction provided the system size tends to infinity. This crossover occurs at a characteristic size which is determined by the overlap of the clusters and decreases with increasing monomer volume fraction. Also the sol-gel transition occurs at a well defined time. They observed strong modifications in both the cluster size distribution and the mass fractal dimension as the aggregation process crosses over from cluster dilute regime to cluster dense regime. They found that the characteristic of the space filling network of clusters is the same whether it is a result of a dynamic DLCA process or a static percolation process. They also observed a transition in the fractal dimension from that expected

for DLCA to that expected for percolation. They found dilute limit DLCA fractal dimension of 1.8 at smaller length scales and percolating cluster fractal dimension of 2.5 at larger length scales. All these results are in support of our simulation results.

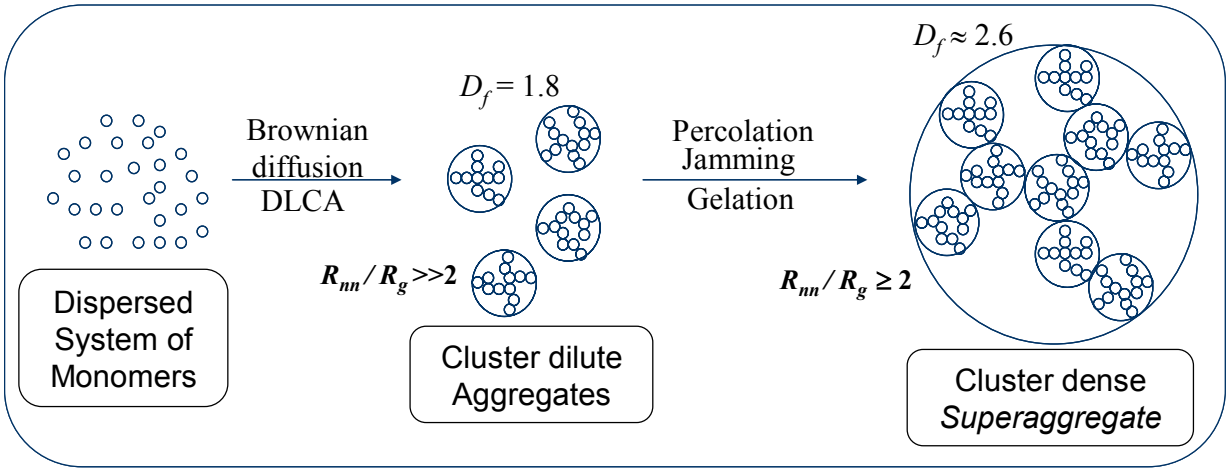

Figure 1.2: Evolution of a dispersed system of aggregating monomers from individual monomeric particle to the gelation. Initially when $R_{nn}/R_g >> 1$ (cluster dilute), normal Brownian diffusion, Diffusion Limited Cluster Aggregation (DLCA) occurs creating fractals with a dimension $D_f = 1.8$ less than the special dimension $d = 3$. Eventually when $R_{nn}/R_g \geq 1$ (cluster dense), clusters are not free to Brownian diffuse, instead they jam, percolate and form percolation *superaggregate* with $D_f \approx 2.6$.

Other simulation studies on dense systems have found a fractal dimension intermediate between that for DLCA clusters and percolation clusters (Herrmann and Kolb, 1986, Kolb and Herrmann, 1985). Hasmy et al. (Hasmy et al., 1997) reported that there is a critical volume fraction for a system to gel and the gel time for a gelling system is system size dependent. This is in contradiction to the results of Gimel et al. (Gimel et al., 1995, Rottereau et al., 2004). Lushnikov (Lushnikov, 2005) did a theoretical study of the formation of a gel in a disperse system wherein binary coagulation alone governs the temporal changes in the particle size distribution. However, his study is based on the assumption that the aggregation kernel is

proportional to the product of masses of aggregating particles, i.e., $K(v,u) = 2vu$, which is a case with homogeneity $\lambda = 2$. He also considered the SE to work through the aggregation process and reported on the exact solution of this model of non Brownian kernel for a finite total mass of the coagulating system.

In this work we present experimental results of a study of aerosol fractal aggregate growth kinetics and morphology as the system evolves from cluster dilute to dense. Carbon particle aerosols were created inside a closed chamber and their kinetics and morphology were studied using a small angle light scattering technique and image analysis technique. We will show that our experimental results are consistent with previous simulation results from our laboratory described above.

We will also show that dense aggregating aerosol systems gel to produce materials having unprecedentedly low densities, high surface areas as well as other useful novel properties. We have named such materials as *aerosol gels*. We present descriptions on aerosol gels made via gelation of carbon and silica nanoparticles.

We have segmented this thesis in various chapters. After this short "Introduction" chapter 1, we present the basic physics behind the aerosol mechanics in chapter 2. Chapter 3 presents the theoretical basis on fractals and aggregation mechanism. Different techniques for studying aggregation processes including the non-invasive light scattering technique are described in chapter 4. We present our experimental results in chapters 5 through 8. Finally we give a brief summary of our work in chapter 9.

CHAPTER 2- Aerosol Mechanics

2.1. INTRODUCTION

A dispersion of solid or liquid particles in gaseous medium because of their thermal energy or convection currents is called an *aerosol*. They are formed from different mechanisms like the atomization of solids and liquids, gases to particle conversion and the resuspension of powders (breaking up of aggregates) through the action of vibration or gas currents. Common examples of aerosols are smoke coming out from combustion of any organic material, mist, fume, etc. Smoke consists of black carbon soot particles and has become a serious concern in atmospheric pollution. Aerosol particles cover wide size range from 1 nm to 0.1 mm. Aerosol particles created directly from gases to particle conversion are relatively much smaller than those from resuspension. Any size above 0.1 mm sediments quickly because of the gravitational force. Smaller aerosol particles normally undergo Brownian motion while larger ones are affected primarily by gravitational and inertial forces. Since this thesis concerns the study of solid particle aggregation, we mainly focus on solid aerosol particles.

Although liquid aerosol particles are spherical in shape because of the surface tension, solid aerosol particles can have quite complex shape. They usually come with variety of shape such as crystalline, fibrous, rough spherical, random aggregates, etc. However, to avoid the complexity that can involve solid aerosol particles they are mostly treated as spherical in the development of many basic aerosol mechanics theory as well as in many different aerosol studies including ones using light scattering technique. The sizes of irregularly shaped aerosol particles can be represented by different equivalent diameters depending on the measurement technique. Some of such equivalent diameters are discussed below.

Mobility equivalent diameter: It is the diameter of a sphere with the same mobility as the particle in being measured.

Aerodynamic equivalent diameter: It is the diameter of a standard density ($1 g/cm^3$) sphere having the same gravitational settling velocity as the particle in question.

Stokes diameter: It is the diameter of a sphere with the same density and settling velocity as the particle in question.

Mass equivalent diameter: It is the diameter of a sphere without voids made by compressing the particle in question.

Volume equivalent diameter: It is the diameter of a sphere with equal volume as the particle in question.

Diffusion equivalent diameter: It is the diameter of a standard density sphere with the same rate of diffusion as the particle in question.

2.2. RADIUS OF GYRATION

An aerosol particle can be a random aggregation of further tinier particles known as *monomers* (also known as *primary particles* in some literature). The size of such an aggregate or cluster is well represented by a measure called the *radius of gyration* R_g. It is a root mean square radius weighted by the aggregate mass density $\rho(\vec{r})$ and is given as

$$R_g = \sqrt{\frac{\int_0^\infty r^2 \rho(\vec{r}) d\vec{r}}{\int_0^\infty \rho(\vec{r}) d\vec{r}}} \quad . \tag{2.1}$$

Here the vector $\vec{r}$ is the distance vector from the center of mass of the aggregate. The denominator in Eq. (2.1) is equal to the total mass of the aggregate. The radius of gyration for a sphere of radius R with constant mass density will then simply be $R_g = \sqrt{3/5}R$. The morphology of random aggregates can be characterized by the fractal dimension. The random aggregate formation process and their morphology are discussed in detail in following chapters.

2.3. SIZE DISTRIBUTION

A collection of aerosol particles is a thermodynamically non-equilibrium system. The particles undergo Brownian dynamics and stick with each other, usually irreversibly, upon collision. Further the starting monomers themselves may not be all of the same size. Thus aerosol particles are normally polydisperse, i.e. they are composed of particles with many different sizes. Hence we talk about the number density of particle per unit diameter range, d_p to $d_p + d(d_p)$, i.e. $n(d_p)$. Different size distribution functions have been used to fit the experimental data on polydisperse aerosol particles. *Self-similar* and *log-normal size distributions* are the ones which are well able to match the experimental data.

2.3.1. SELF- SIMILAR SIZE DISTRIBUTION

This size distribution is called self-similar because the function can be scaled such that it becomes time invariant, i.e., the shape of the distribution does not change with time. It is now well known that diffusion process results in self-similar size distribution asymptotically. Self-similar size distribution is also independent of the starting size distribution of the aggregating particles. The time invariant transformation for the particle size distribution is based on the assumption that the fraction of the particles in a given size range is a function only of particle size (= monomer number for non-coalescing particles) normalized by the average particle size. This size distribution is discussed more in coming chapters.

2.3.2. LOG-NORMAL SIZE DISTRIBUTION

Most aerosol particle size distribution often have positively skewed peak. Log-normal function can approximately fit such positively skewed distribution with long tail at large sizes. The $n(d_p)$ in terms of log-normal function, with d_{gm} and σ_g as geometric mean and geometric standard deviation respectively, is given as

$$n(d_p) = \frac{1}{d_p \ln(\sigma_g)\sqrt{2\pi}} \exp\left[-\frac{1}{2}\left(\frac{\ln(d_p / d_{gm})}{\ln(\sigma_g)} \right)^2 \right] \tag{2.2}$$

where

$$\ln\left(d_{gm}\right)=\frac{\sum_i n_i \ln\left(d_i\right)}{\sum_i n_i} \tag{2.3}$$

and

$$\ln\left(\sigma_g\right)=\sqrt{\frac{\sum_i n_i\left[\ln\left(d_i / d_{gm}\right)\right]^2}{\sum_i n_i}}\,. \tag{2.4}$$

For log-normal distribution the geometric mean diameter is equal to the median diameter, i.e., $d_{gm} = d_{50}$, where d_{50} is the median diameter. Also the geometric standard deviation is such that $\sigma_g = \frac{d_{84.1}}{d_{50}} = \frac{d_{50}}{d_{15.9}}$. The geometric standard deviation being a ratio is a dimensionless quantity.

2.4. PROPERTIES OF MEDIUM GAS

Aerosol particles, in general, are suspended in a gaseous medium. These aerosol particles are being constantly bombarded from all possible directions by a large number of medium molecules. The mechanics of these aerosol particles are highly influenced by the motion and the intrinsic properties of the medium gas as well as the interaction between the medium molecules and the aerosol particles themselves. The trajectory that an aerosol particle follows is a function of the aerosol particle size and the medium molecule number density. The trajectory can vary from a Brownian type to a ballistic type depending on the relative aerosol particle size compare to the intermolecular distance of the medium (see section 3.4.). Besides, the flow of the medium also has a great effect on the behaviour of aerosol particles; especially on their aggregation mechanism (see section 3.15.). Here we list the following very important intrinsic properties of medium and the aerosol system.

2.4.1. MEAN FREE PATH

It is defined as an average distance that a medium molecule has to travel before it collides with next random medium molecule. For a medium with molecular diameter d_g and molecular number density n_g the mean free path λ_g can be expressed as

$$\lambda_g = \frac{1}{\sqrt{2}\pi d_g^2 n}. \tag{2.5}$$

For a gas at 293 K [20^{o}C] and under 101 kPa (1 atmospheric pressure) pressure the mean free path is 66.4 nm. Using kinetic theory for gas we can see from Eq. (2.5) that $\lambda_g \propto \frac{1}{gas\ pressure\,(P)}$ when the temperature is held constant.

2.4.2. KNUDSEN NUMBER

Knudsen number Kn is the parameter which determines the type of motion of the aerosol particles in the medium. It is a measure of mean free path of the medium relative to the aerosol particle radius *R* as

$$Kn = \frac{\lambda_g}{R}. \tag{2.6}$$

For an aerosol particle to undergo diffusive motion it requires $\lambda_g << R$, i.e., $Kn << 1$. This regime of aerosol particle motion, where they diffuse with Brownian motion, is known as *continuum regime*. On the other hand if $\lambda_g >> R$, i.e., $Kn >> 1$, the aerosol particles can undergo ballistic or diffusive motion between successive collisions of two aerosol particles depending on the particle nearest neighbor separation and the persistence length of the particles (discussed in section 3.4.2.). Such regime of particle motion is known as *free molecular regime*. The intermediate range of Knudsen number approximately $0.1 < Kn < 10$, is usually referred to as the *transition or slip flow regime*.

2.4.3. REYNOLDS NUMBER

What happens to the aerosol particles in the system depends greatly on medium fluid flow pattern. The aerosol particles tend to follow the fluid flow. However, occasionally their motion deviates from that of fluid flow when there are changes in direction and velocity or various external forces. The fluid flow can be distinguished as laminar or turbulent with help of a dimensionless parameter known as Reynolds number *Re*. It is a macroscopic fluid property which represents the ratio of the inertial force of the fluid to the frictional force of the fluid moving over the surface. Reynolds number governs the flow to be laminar or turbulent and is given as

$$\mathrm{Re} = \frac{\rho_g v_r d}{\eta} \tag{2.7}$$

where ρ_g is the fluid density, v_r is the relative velocity between the fluid and a surface, η is the dynamic fluid viscosity and d is a characteristic dimension of the object, such as the diameter of an aerosol particle.

Reynolds number is classified into two types: *flow Reynolds number* Re_f and *particle Reynolds number* Re_p. Flow Reynolds number is defined when fluid flows in a tube while particle Reynolds number is define when fluid flows around a particle. For Re_f the characteristic dimension d in Eq. (2.7) is replaced by the tube diameter d_t while for Re_p it is replaced by the particle diameter d_p. Table 2-1 lists the values of Re_f and Re_p for laminar, transition and turbulent flow types.

Table 2-1: Reynolds number and flow type.

Flow type	Flow Reynolds number Re_f	Particle Reynolds number Re_p
Laminar	< 2100	< 1
Transition	2100 – 4000	1 – 1000
Turbulent	> 4000	> 1000

2.5. CUNNINGHAM SLIP CORRECTION FACTOR

When the Knudsen number $Kn << 1$, an aerosol particle feels strong resistance to its motion due to a large number of medium molecules impinging on its surface. The particle thus shows Brownian motion. On the other hand when $Kn >> 1$, there is small resistance to the particle motion and hence its motion is free molecular type. However, if the regime of aerosol particle motion is in between continuum and free molecular, i.e. Knudsen number is approximately $0.1 < Kn < 10$, the particles experience slip by the medium molecules. Thus the particle is also said to be in *slip flow regime*.

Continuum is the most general regime of particle motion which can occur in both aerosol and colloidal systems. Many theories for particle motion in a medium have been developed for this continuum regime. These theories can be extended to slip flow regime and free molecular regime as well by introducing a correction factor that accounts for the effect of slip. This correction factor is known as *Cunningham slip correction factor* C_c and is empirically given as (Allen and Raabe, 1985)

$$C_c = 1 + Kn\left[\alpha + \beta \exp\left(-\gamma / Kn\right)\right]. \tag{2.8}$$

For air medium at NTP with λ_g = 66.4 nm the parameters α = 1.142, β = 0.558 and γ = 0.999 for solid particles (Allen and Raabe, 1985) and α = 1.207, β = 0.440 and γ = 0.596 for oil droplets (Rader, 1990).

The Cunningham slip correction factor C_c = 1 in the continuum regime. Its value increases with decreasing particle size in other regimes of particle motion. In a gas medium at NTP and for 1.0 μm particle $C_c \approx 1.15$. C_c increases rapidly with decreasing size for particles less than 1 μm.

2.6. PARTICLE MOTION IN A MEDIUM

The motion of a particle in a medium is influenced by three types of forces. These forces are external forces (gravitational, electrostatic, etc.), medium resistance or drag force and interactive force between the particles (van der Waals attractive force, electrostatic force or their combination). The third type of force is mostly responsible for the aggregating behaviour of the

particles but contribute negligibly to the uniform particle motion compare to the first two types of forces. Analysis of uniform motion of particles is useful for aerosol study since aerosol particles attain uniform motion almost instantly in most cases. The difference between particles and gas molecules trajectories forms the basis for many aerosol particle size measurement techniques.

2.6.1. EXTERNAL FORCES

When particles come under influence of an external force, they start moving along the force field direction. The migration velocity in the force field is particle size dependent, a fact that is exploited by most aerosol-size spectrometers for particle size discrimination. Different common external forces are discussed below.

2.6.1.1. Gravitational Force

Gravitational force is inevitable and its effect in particle motion becomes significant when the particles are bigger than few hundred nanometres. The effective gravitational force is directly proportional to the relative density of the particles as

$$F_{grav} = \left(\rho_p - \rho_g\right) V_p g \tag{2.9}$$

where g is the gravitational acceleration, ρ_p is the density and V_p is the volume of the particle. Hence gravitational force can be balanced by matching the density of particles with that of the medium fluid. However, this is possible only in cases of colloidal systems since buoyancy for aerosol particles is usually almost negligible.

For atmosphere, gravity has a major role in cleaning air polluting aerosol particles. If we assume a stirred system of particles undergoing gravitational settling with a constant settling velocity v_{pgrav} initially spread up to a height h, the particle number concentration $n(t)$ at any time t decreases exponentially with a characteristic time of h/v_{pgrav} as

$$n(t) = n_0 \exp\left(-\frac{v_{pgrav} t}{h}\right). \tag{2.10}$$

Here n_0 is the initial particle number concentration. Here the system is assumed to be monodisperse as for polydisperse case the situation is much more complicated.

2.6.1.2. Electrostatic Force

This type of force exists only for systems with charged particles when an electric field is applied across the system. Most aerosol particles are found to carry a little or large amount of electrostatic charge, which may be continually transferred between particles or gained or lost, depending on a number of external factors. The charge on particles influences their behaviour. Electrostatic force becomes more significant as particle size decreases since gravitational force is a volume dependent quantity. For highly charged particles, the electrostatic force can be several orders of magnitude greater than the gravitational force. If E be the applied electric field and q be the charge on the particle then the electrostatic force qE accelerates the particle until it gets balanced by the drag force (see next section) when the particle attains the terminal velocity v_{pT}. Then for a particle following Stoke's law,

$$qE = -\frac{v_{pT}}{B} \tag{2.11}$$

where $B = 1/3\pi\eta d_p$ is the electrical mobility of the particle. This equation can be used to find the unknown charge on the particle or its terminal velocity.

2.6.1.3. Thermal Force

This type of force on a particle arises when a temperature gradient is established in the system and is known as *thermophoresis*. A particle experiences stronger bombardment of the medium molecules on its surface facing towards the higher temperature side than on the other surface. This drives the particles from a hotter to a colder region and hence heated surfaces tend to remain clean, while relatively cool surfaces tend to collect particles. Thermophoresis F_{th} varies quadratically with the particle size d_p for particles smaller than the mean free path of the medium molecules λ_g as

$$F_{th} = -\frac{P\lambda_g d_p^2 \nabla T}{T} \qquad \text{for} \qquad d_p < \lambda_g . \tag{2.12}$$

Here P is the medium (gas) pressure, T is the absolute temperature and ∇T is the thermal gradient. Also the thermophoresis velocity v_{pth} of a particle is given as (Waldmann and Schmitt, 1966)

$$v_{pth} = -\frac{0.55\eta \nabla T}{\rho_g T} \qquad \text{for} \qquad d_p < \lambda_g . \tag{2.13}$$

For larger particles, i.e., $d_p > \lambda_g$, the thermal force is given as

$$F_{th} = -\frac{9\pi\eta^2 d_p H \nabla T}{2\rho_g T} \qquad \text{for} \qquad d_p > \lambda_g \tag{2.14}$$

and the velocity v_{pth} is (Brock, 1962)

$$v_{pth} = -\frac{3\eta C_c H \nabla T}{2\rho_g T} \qquad \text{for} \qquad d_p > \lambda_g . \tag{2.15}$$

The coefficient H in Eqs. (2.14) and (2.15) is given as

$$H \cong \left(\frac{1}{1 + 6\lambda_g / d_p} \right) \left(\frac{k_g / k_p + 4.4\lambda_g / d_p}{1 + 2k_g / k_p + 8.8\lambda_g / d_p} \right) \tag{2.16}$$

where k_g and k_p are thermal conductivity of the medium (gas) and the particle respectively.

2.6.1.4. Other Forces

Very small particles approach the behavior of the gas molecules, i.e., they diffuse readily, have small inertia, and can be affected by thermal pressure, light pressure and radiation pressure. A concentration gradient in the surrounding gas can also produce a force on a particle. The particle motion produced by these forces is called *thermophoresis*, *photophoresis* or *diffusiphoresis*, depending on the type of gradient.

Photophoresis involves particle motion under the influence of asymmetric light absorption within a particle. Photophoresis closely resembles thermophoresis since illumination of a particle heats up one side of the particle as well as gas molecules nearby that push the particle toward the colder side. Illumination can also produce radiation pressure whereby the stream of photons exerts a force on the particle. Radiation pressure results from a direct momentum transfer by the deflection and absorption of the light.

If there is a gradient in the particle number concentration, a diffusion force called diffusiophoresis can be defined that moves the particles from the high concentration to the low concentration region. It is often the dominant motive force for particles smaller than about 0.2 μm diameter.

2.6.2. DRAG FORCE

Under application of an external force the particles accelerate through the medium molecules. The particles have to overcome the resistance to their motion which they feel as more medium molecules impinge on their front surface than on their back surface. This resistance to the applied external force is the drag force. The drag force increases as the particles accelerate and almost instantly the accelerating external force gets balance. The drag force is thus like a frictional force and can be expressed in the following form.

$$F_D = -\frac{C_D}{C_c}\frac{\rho_g}{2}\frac{\pi d_p^2}{4}v_p^2 . \tag{2.17}$$

Here v_p is the velocity of the particle relative to the medium and C_D is a coefficient known as *drag coefficient*. The negative sign indicates that the force acts in direction opposite to that of the motion. One can note from Eq. (2.17) that the drag force is proportional to the cross sectional area of the moving particle. The drag coefficient is a strong function of the flow regime and takes the following forms for different flow regimes (Hinds, 1998).

$$C_D = \frac{24}{\mathrm{Re}_p} \qquad \text{for} \quad \mathrm{Re}_p < 1.0 \qquad \text{(Laminar flow)}$$

$$C_D = \frac{24}{\mathrm{Re}_p}\left[1 + 0.15\,\mathrm{Re}_p^{0.687}\right] \qquad \text{for} \quad 1 < \mathrm{Re}_p < 1000 \qquad \text{(Transition flow)}. \qquad (2.18)$$

$$C_D = 0.44 \qquad \text{for} \quad 1000 < \mathrm{Re}_p < 2.0 \times 10^5 \qquad \text{(Turbuelnt flow)}$$

If the particles are irregular shaped instead of spherical, a correction factor called a dynamic shape factor χ can be introduced in Eq. (2.17) as

$$F_D = -\frac{1}{\chi}\frac{C_D}{C_c}\frac{\rho_g}{2}\frac{\pi d_p^2}{4}v_p^2. \qquad (2.19)$$

Inclusion of this factor in the equation allows one to calculate the desired parameter while characterizing complex particle shapes by a single dimension.

For a spherical particle in laminar flow and continuum regime, the drag force Eq. (2.17) simplifies to

$$F_D = -3\pi\eta d_p v_p. \qquad (2.20)$$

Here we have used Eq. (2.18) and Eq. (2.7). Eq. (2.20) is also familiar as *Stokes's law*. Stokes arrived to this equation solving the *Navier-Stokes equations* after simplifying assuming that the inertial forces are negligible compare to the viscous forces and that the fluid is incompressible.

For free molecular regime where *Kn* >> 1 and considering laminar flow for spherical particles Eq. (2.17) can be simplified and the drag force can be rewritten as

$$F_D = -\frac{1}{3}\pi\delta\,\rho_g v_g d_p^2 v_p. \qquad (2.21)$$

To derive Eq. (2.21) from Eq. (2.17) the medium viscosity is assumed to be (Fuchs, 1964)

$$\eta = 0.251\delta\rho_g v_g \lambda_g \qquad (2.22)$$

where $\delta = (1 + \alpha\pi/8)$ with $0 \leq \alpha \leq 1$ is a factor which determines the way the gas molecules rebound from the surface of the particle (Fuchs, 1964). Also v_g is the root mean square thermal velocity of the medium molecules.

2.6.3. PARTICLE-PARTICLE INTERACTIVE FORCES

Unlike medium (gas) molecules, particles in a system tend to adhere to form clusters. The interactive force between particles is orders of magnitude smaller than other external forces. The most common interactive forces between particles are a relatively short range attractive force known as the *van der Waals force* and a long range electrostatic force (if particles are charged). Aerosol particles are normally assumed to be neutral. In case of colloidal system it is possible to create double layers of counterions on each colloidal particle such that these particles on approaching interact leading to repulsion. Competition between the attractive van der Waals and the repulsive double layer forces has been described by DLVO (Derjaguin, Landau, Verwey and Overbeek) theory.

2.6.3.1. van der Waals Force

The van der Waals force between any two particles is a result of induction of complementary electric dipoles on the approaching particles, even when these particles are electrically neutral and are non-polar, and is weak compare to a chemical bond. More specifically this force has its basis on quantum mechanical intermolecular force which has an attractive part and sometimes a repulsive part. The attractive part consists of three distinct contributions: 1) the electrostatic interaction between charges, permanent dipoles, quadrupoles or other higher multipoles, 2) the electrostatic induction (polarization) which is the interaction between a permanent multipole on one molecule with and induced multipole on another, and 3) the *London* or *dispersion force* that arise from the attractive force between momentary dipoles (or better multipoles) in molecules without permanent multipole moments. There is a significant chance that there is an instantaneous dipole in an electrically neutral atom or molecule because electrons move randomly within more probable areas as given by quantum theory in the structure of an atom or molecule. These instantaneous dipoles of approaching two atoms or molecules

interact in such a way as to produce an attractive (usually, but sometimes repulsive if the atoms or molecules are of different types) potential between themselves.

The London force makes the most significant contribution to the total and thus can be approximated for the van der Waals force between atoms or molecules. Quantum mechanical perturbation theory is used to find the energy involved in London interaction for two atoms or spherical small molecules as

$$W(r) = -\frac{C_{vdw}}{r^6} \tag{2.23}$$

where

$$C_{vdw} = -\frac{3}{2}\frac{\alpha_1\alpha_2}{(4\pi\varepsilon_0)^2}\frac{I_1 I_2}{(I_1 + I_2)} \tag{2.24}$$

with

$$\alpha_i \approx 4\pi\varepsilon_0\sigma_i^3 \,. \tag{2.25}$$

In Eq. (2.23) r is the center to center distance of the atoms or molecules and C_{vdw} is a constant which depends on the nature of atoms or molecules involved and the medium they contained in. Also in Eqs. (2.24) and (2.25) ε_0 is free space permittivity, and I_i, α_i and σ_i are ionization potential, electronic polarizability and radius for i^{th} atom or molecule respectively. Single ionization potential has been assumed for each involved atom or molecule while deriving Eq. (2.23).

The London force between two aerosol (or colloidal) particles can be calculated by integrating the London forces of all the atoms or molecules in one particle with all the atoms or molecules with the other. This procedure can be carried out for finding the force between a particle (any shape) and a flat surface or between two flat surfaces as well. The net interaction energy between two particles at distance r apart will be

$$W(r) = \iint -\frac{C_{vdw}\rho_{pn1}\rho_{pn2}}{r^6} dV_1 dV_2 \tag{2.26}$$

where ρ_{pni} is the number density of molecules in i^{th} particle with volume V_i. Assuming the particles to be spherical with the same size and material, and scaling the distance between particle centers by the particle diameter σ ($x = r/\sigma$), the integration simplifies to

$$W(x) = -\frac{H}{12}\left[\frac{1}{x^2-1} + \frac{1}{x^2} + 2\ln\left(1-\frac{1}{x^2}\right)\right]. \tag{2.27}$$

Here H is a constant known as the *Hamaker constant* and its value depends on the material property of the particles as

$$H = \pi^2 C_{vdw} \rho_{pn}^2 . \tag{2.28}$$

Typical values for the Hamaker constants of condensed phases, whether solid or liquid, are about 10^{-19} J for interaction across vacuum (Israelachvili, 1992). Metallic particles tend to have higher H while hydrocarbons take smaller values.

London van der Waals interaction dies rapidly with increasing particle-particle separation and becomes negligible when the surface to surface separation is few percent of the particle diameter. For two interacting particles of material 1 dispersed in a medium of material 2, the relative Hamaker H_{1221} constant can be given as (Israelachvili, 1992)

$$H_{1221} = \left(\sqrt{H_{11}} - \sqrt{H_{22}}\right)^2 \tag{2.29}$$

where H_{ii} is the Hamaker constant for pair interaction between particles of material i.

The London van der Waals force as a function of the particle separation r can be calculated by taking the negative gradient of the potential energy as

$$F_{vdw} = -\frac{\partial W(r)}{\partial r}. \tag{2.30}$$

2.6.3.2. Repulsive Force between Atoms or Molecules

In atomic or molecular interaction a strong repulsive force arises when the electron clouds start overlapping. This repulsion increases much more sharply with decreasing separation compare to the attractive van der Waals force. However, its range is much shorter than that of van der Waals force. Hence interacting atoms or molecules find equilibrium at a certain separation corresponding to a minimum interaction energy. The repulsive potential energy can be describe by

$$W(r) = A\left(\frac{\sigma}{r}\right)^n \tag{2.31}$$

where n is a positive integer and A is a constant.

If $n \to \infty$ is assumed the repulsive force becomes infinity when $r < \sigma$ and zero when $r > \sigma$. Such a potential is known as the *hard sphere potential*. A more realistic repulsive potential is given by the repulsive term in the *Lennard-Jones potential* (see next section) for which $n = 12$. This r^{-12} repulsive potential has been widely used because it represents a realistic sharp repulsive interaction with decreasing separation and also because it gives mathematically convenient forms for the equilibrium position and binding energy.

2.6.3.3. Repulsive Force between Particles

A mathematical model of hard sphere repulsive potential is generally assumed for particles (aerosols or colloids) to avoid overlapping of the particles. If the aerosol particles are charged the regular electrostatic (coulombic) force also becomes active. In case of similarly charged colloidal particles, repulsion due to double layer of counterions also plays a major role in the total repulsive force. Double layer repulsion between two similarly charged surfaces in a solvent containing counterions and electrolyte ions originates from the entropic (osmotic) pressure and not electrostatic (Israelachvili, 1992). Double layer repulsion behaves like screened electrostatic repulsion and hence the interaction energy is Yukawa type given as

$$W(x) = J\frac{e^{-\kappa(x-1)}}{x} \tag{2.32}$$

where

$$J = \pi\varepsilon\varepsilon_0\sigma\psi_0^2 \tag{2.33}$$

and

$$\kappa = \sigma / \lambda_D \,. \tag{2.34}$$

In Eqs. (2.32), (2.33) and (2.34) x is the particle-particle separation scaled with the particle diameter, ε is the relative permittivity of the medium, ε_0 is the absolute permittivity, ψ_0 is the *surface* or *zeta-potential* of the particles and λ_D is called the *Debye screening length*. λ_D is only a function of the liquid medium properties. λ_D of aqueous solution is

$$\lambda_D = \frac{b}{\sqrt{Salt\ molarity}} \tag{2.35}$$

where at b is a constant for a given salt. Its value at 25^{o}C is given for various electrolytes as

b = 0.304 nmM$^{1/2}$ for 1:1 electrolytes (NaCl, KOH, etc.)

b = 0.176 nmM$^{1/2}$ for 2:1 or 1:2 electrolytes ($MgCl_2$, Na_2SO_4, etc.)

b = 0.152 nmM$^{1/2}$ for 2:2 electrolytes ($MgSO_4$, $CuSO_4$, etc.).

2.6.3.4. Total Interparticle Force

The total interactive force between particles is the sum of attractive and repulsive components. The best model of the potential energy for this total force between interacting atoms or molecules is given by the *Lennard-Jones potential* as

$$W(r) = 4 \in_0 \left[\left(\frac{\sigma'}{r}\right)^{12} - \left(\frac{\sigma'}{r}\right)^{6}\right] \tag{2.36}$$

where $\in_0$ is the Lennard-Jones potential well depth and σ' is the separation such that $W(\sigma') = 0$. The first term in Eq. (2.36) is repulsive term (Eq. (2.31) with $n = 12$) and the second term is attractive London van der Waals potential (Eq. (2.23)). The minimum possible energy $W = -\in_0$ occurs at $r = 1.12\sigma'$. One can notice in Eq. (2.36) that at large separation only the London van der Waals term survives, i.e., $W(r>>\sigma') \cong -4\in_0 (\sigma'/r)^6$ as expected.

The potential energy for the total force in case of aerosol particles is the sum of London van der Waals potential (Eq. (2.27)) and the hard sphere potential. The coulombic potential is should also add in case of charged aerosol particles.

In colloidal system with particle carrying similar charges the potential energy for the total force is modelled by DLVO (Derjaguin, Landau, Verwey and Overbeek) potential which is the sum of double layer repulsion potential (Eq. (2.32)) and the London van der Waals potential (Eq. (2.27))

$$W(x) = J\frac{e^{-\kappa(x-1)}}{x} - \frac{H}{12}\left[\frac{1}{x^2-1} + \frac{1}{x^2} + 2\ln\left(1-\frac{1}{x^2}\right)\right]. \tag{2.37}$$

The repulsive, attractive and the total potential terms in Eq. (2.37) are plotted in Fig. (2.1) for 20 nm polystyrene particles in water. The repulsive term decays and become negligible faster than the attractive term. If the Hamaker constant H is too larger or J is too low then the double layer repulsion can be neglected. Increasing J (due to an increase in ε, ψ_0 or σ) makes the repulsion stronger and hence the probability ($\propto \exp(-W_{peak}/k_BT)$) that a particle can overcome the repulsive barrier decreases. An increase in screening constant κ can shield coulomb repulsion significantly. At intermediate J values a shallow secondary minimum can exist in which particles can possibly exist in a metastable state (Victor and Hansen, 1984). Once a particle overcomes the repulsive barrier W_{peak} it falls all the way on the potential curve until it hits the surface of the other particle where it then experiences hard sphere potential.

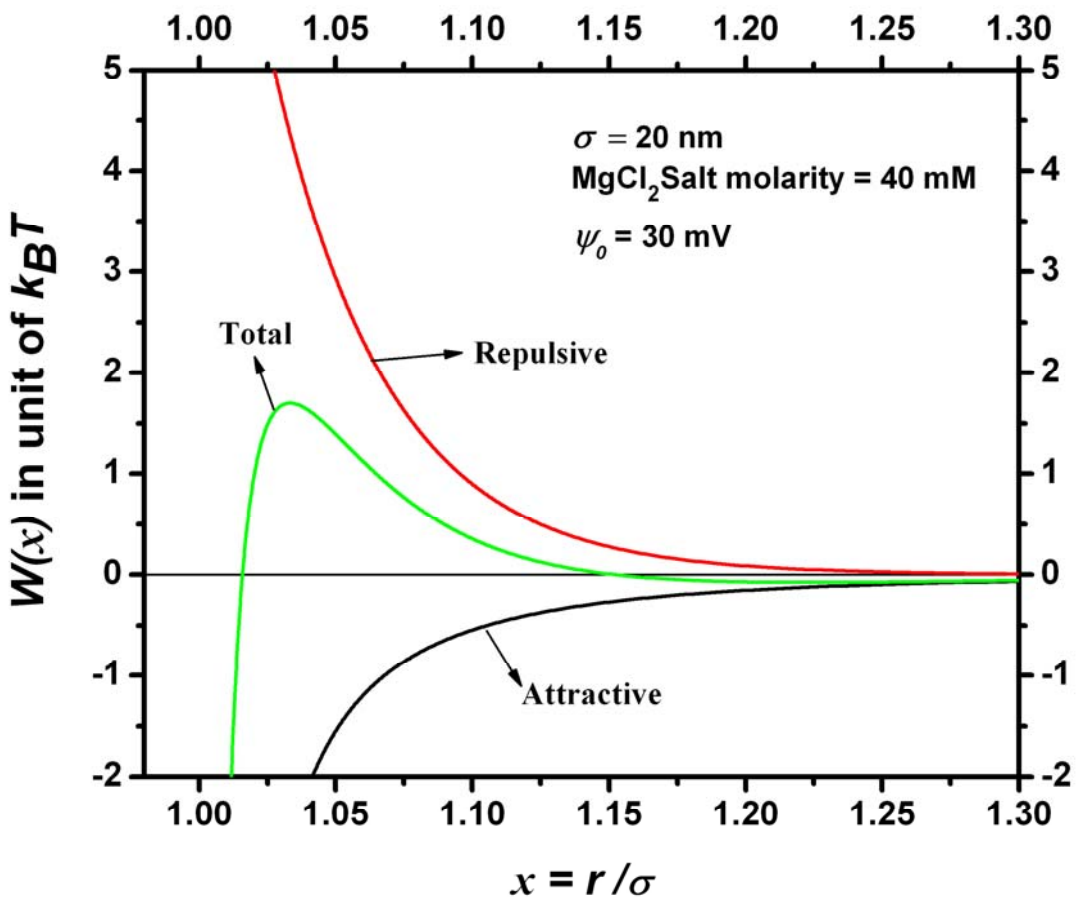

Figure 2.1: The plots of the attractive, repulsive and the total potential for 20 nm polystyrene particles in water. The zeta potential ψ_0 is taken to be 30 mV and 40 mM of $MgCl_2$ is assumed to be added to the system. The Hamaker constant is taken to be 3.14 k_BT.

2.6.4. BROWNIAN MOTION AND THE PARTICLE TRANSPORT

Particles floating in a non-flowing medium exhibit a haphazard motion caused by random variations in the continuous bombardment of the surrounding medium molecules on the particle surface. This kind of motion was first reported by a botanist named Robert Brown in 1827 and now is known as *Brownian motion* or *random walk* (Fig. 2.2). This irregular motion results in a net transport of particles from a high to a low concentration region and the process is known as *diffusion*. Diffusion is a complete statistical process characterized by the particle *diffusion*

coefficient D. The larger the value of *D*, the more vigorous the Brownian motion and the more rapid the particle transport in a concentration gradient. Diffusion coefficient *D* is a function of the particle size, the temperature and the nature of the medium. Knudsen number *Kn* also plays an important role in determining how particles diffuse in a medium.

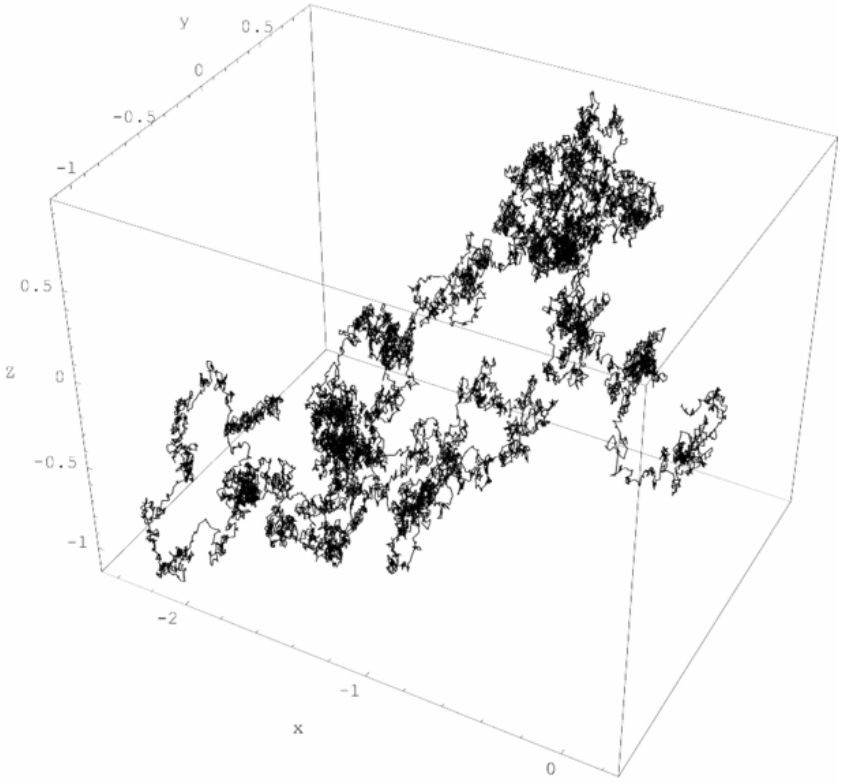

Figure 2.2: A typical Brownian motion in a 3-*d* space. This picture has been taken from http://en.wikipedia.org.

2.6.4.1. Langevin Equation

Complete understanding of the Brownian motion and diffusion is necessary for a complete understanding of the behaviour of the dispersed particles in a medium. In statistical physics, Brownian motion can be described by a *Langevin equation* which is a stochastic differential equation. Most cases potential remains constant. For the simplest case where particles are not acted upon by any other force except the one due to the medium molecular bombardment, the equation of motion (Langevin equation) for a particle of mass m_p and velocity $\vec{v}_p(t)$ is

$$m_p \frac{d\vec{v}_p}{dt} = -f_{dg}\vec{v}_p + \vec{\xi}(t). \tag{2.38}$$

The first term in Eq. (2.38) is the velocity dependent drag force (see Eq. (2.19)) with f_{dg} as the drag coefficient. Drag coefficient $f_{dg} = 6\pi\eta R$ if the Stoke's law is applicable. The second term $\vec{\xi}(t)$ is the stochastic thermal force due to the momentum exchange during a series of impacts of the fluid molecules on the particle surface. The stochastic force fluctuates rapidly and has no time and space correlation with itself no matter how small the time or space interval is. Thus this force is zero for ensemble average or time average, i.e. $<\vec{\xi}(t)>$ = 0. Using vector tricks (1) $\vec{r}\cdot\vec{v}_p = 1/2(dr^2/dt)$ and (2) $\vec{r}\cdot(d\vec{v}_p/dt) = 1/2(d^2r^2/dt^2) - v_p^2$ where $\vec{r}(t)$ is the position vector, Eq. (2.38) can be rewritten as

$$\frac{d^2r^2}{dt^2} + \frac{f_{dg}}{m_p}\frac{dr^2}{dt} = 2v_p^2 + \frac{1}{m_p}\vec{r}\cdot\vec{\xi}\,. \tag{2.39}$$

Now denoting the constant factor f_{dg}/m_p by $1/\tau$ and taking an ensemble average of Eq. (2.39) we find

$$\frac{d^2<r^2>}{dt^2} + \frac{1}{\tau}\frac{d<r^2>}{dt} = 2<v_p^2>. \tag{2.40}$$

Here we assumed that $<\vec{r}\cdot\vec{\xi}>=0$ because in general we expect no correlation between $\vec{r}(t)$ and $\vec{\xi}(t)$. After long enough time the particles reach thermal equilibrium with the medium molecules and then $<v_p^2>$ can be replaced by its equipartition value $3k_BT/m_p$, where k_B is the Boltzmann constant. The differential equation then can be solved for $<r^2>$as

$$<r^2>=\frac{6k_BT\tau^2}{m_p}\left[\frac{t}{\tau} - \left\{1-\exp\left(-\frac{t}{\tau}\right)\right\}\right]. \tag{2.41}$$

The constant of integration is chosen such that at t = 0 both $<r^2>$ and its first time-derivative vanish. In the limiting case $t \to 0$, Eq. (2.41) reduces to

$$< r^2 > \cong \frac{3k_B T}{m_p} t^2 = < v_p^2 > t^2 \tag{2.42}$$

i.e.,

$$\vec{r}(t) = \vec{v}_p t \,. \tag{2.43}$$

This is as expected for very small time scale. On the other hand at large time scale Eq. (2.41) reduces to

$$< r^2 > \cong \frac{6k_B T \tau}{m_p} t = \frac{6k_B T}{f_{dg}} t = 6k_B T \mu \, t \,. \tag{2.44}$$

Here $\mu = 1/f_{dg}$ is known as the *particle mobility*. This equation proves that the origin of Brownian displacement is the random fluctuating forces arising from the non-exhausting irregular motion of the medium molecules.

2.6.4.2. Equation of Diffusion

It has been observed that the rate of particle transport (particle flux J) from the high to the low concentration is proportional to the concentration gradient ∇n. Thus

$$\vec{J} = -D \nabla n(\vec{r}, t). \tag{2.45}$$

where D is a proportionality constant known as the *diffusion constant*. This relationship is also known as the *Fick's first law of diffusion*.

The continuity theorem, which arises due to the conservation of the total number of diffusing particles, suggests that

$$\frac{\partial n(\vec{r}, t)}{\partial t} + \nabla \cdot \vec{J} = 0 \,. \tag{2.46}$$

Using of Eq. (2.45), Eq. (2.46) reduces to

$$\frac{\partial n}{\partial t} = D\nabla^2 n = D\left(\frac{\partial^2}{\partial^2 x} + \frac{\partial^2}{\partial^2 y} + \frac{\partial^2}{\partial^2 z}\right)n\,. \tag{2.47}$$

This equation is known as the *Fick's second law of diffusion*.

2.6.4.3. Diffusion Coefficient

The one dimensional form of Fick's second law of diffusion can be written as

$$\frac{\partial n(x,t)}{\partial t} = D\frac{\partial^2 n(x,t)}{\partial^2 x}\,. \tag{2.48}$$

The solution for Eq. (2.48) can be obtained from Fourier transforms. Considering $n(k,t)$ as the spatial Fourier transform of $n(x,t)$, we obtain,

$$\frac{\partial n(k,t)}{\partial t} = -Dk^2 n(k,t). \tag{2.49}$$

The solution for this differential equation is

$$n(k,t) = C\exp\left(-Dk^2 t\right). \tag{2.50}$$

We assume the particles to start diffusing from $x = 0$ at $t = 0$. This makes $n(x,0) = \delta(x)$, i.e., $n(k,0) = 1$, so the constant of integration $C = 1$. Now inverting the Fourier transform in Eq. (2.50)

$$n(x,t) = \frac{1}{2\pi}\int_{-\infty}^{\infty} n(x,t)e^{-ikx}\,dk$$
$$n(x,t) = \frac{1}{2\pi}\int_{-\infty}^{\infty} \exp\left(-Dk^2 t\right)e^{-ikx}\,dk$$

gives

$$n(x,t) = \frac{1}{\sqrt{4\pi Dt}}\exp\left(-\frac{x^2}{4Dt}\right). \tag{2.51}$$

This distribution of the particle concentration in one dimensional space implies

$$< x^2 >= 2Dt \, . \tag{2.52}$$

For particle concentration distribution in 3-d space we have $<r^2> = <x^2> + <y^2> <z^2> = 3 <x^2>$. Hence

$$< r^2 >= 6Dt \, . \tag{2.53}$$

Comparing Eq. (2.53) with Eq. (2.44) we find the expression for the diffusion coefficient as

$$D = k_B T \mu \, . \tag{2.54}$$

This equation gives the relation between the particle mobility and the diffusion.

A better understanding of the particle diffusion is essential to the more accurate prediction of the related problem of Brownian controlled coagulation. The understanding of how particles diffuse is essential to the continued development of particle sizing by dynamic light-scattering techniques. The Brownian motions of the particles give rise to phase modulations of the scattered light, which cause changes in the frequency spectrum. By measuring and analysing these modulations, the distribution of the Brownian velocities, and, hence the diffusion coefficient, may be determined.

CHAPTER 3- Aggregates, Fractals and Aggregation Theory

3.1. INTRODUCTION

A dispersed system of a large number of finely divided particles in a medium (gas or liquid) is under a non-equilibrium condition which can be at least partially relieved by aggregation (Family and Landau, 1984, Jullien and Botet, 1987, Meakin, 1988). Aggregation drives particles to become part of a whole as a consequence of van der Waals interparticle interaction (Family and Landau, 1984, Carpineti et al., 1990, Jullien and Botet, 1987, Kolb et al., 1983, Meakin, 1983, Meakin, 1988, Meakin, 1999, Schaefer and Martin, 1984, Weitz and Oliveria, 1984). The particles diffuse randomly due to the continuous bombardment of the thermally agitating medium molecules. The diffusive motion is independent of the detailed chemical nature of the system (Lin et al., 1989). Aggregation, an inevitable process, usually results due to the net attractive interacting potentials between the particles and is irreversible for relatively strong attractions. Aggregation of particles has always remained as a very important phenomenon in physics, biology and material science (Liu, 2006). Formation of cloud and rain drops, atmospheric aerosol particles, fractal formation, sol-gel transition, etc. are some examples where the aggregation process plays a vital role. Brownian motion is the most important one among others, like fluid shear and differential settling, in driving the aggregation process (Family and Landau, 1984, Jullien and Botet, 1987, Meakin, 1988). Much deeper understanding of the structure of particle aggregates and the kinetics of their formation is the key to explain and control many complex but important phenomena in many different fields including biomedical science, material science and industry. For example, control and prevention of different diseases like cataract, mad cow, etc. need basic understanding of protein aggregation mechanism (Jacob, 1999, Krebs et al., 2007, Tsai, 2005).

By controlling the particle interaction it is possible to aggregate non-coalescing particles with a variety of microstructures ranging from ordered two-dimensional, three-dimensional nanocrystal superlattices (Lin et al., 1999, Lin et al., 2001, Murray et al., 1995), and fractal-like aggregates to percolated network structures (Meakin, 1999, Seaton and Glandt, 1987). Stronger van der Waals interaction usually leads to the formation of fractal aggregates as a consequence of an irreversible process for non-coalescing particles. Controlled aggregation of particles can hence lead to formation of novel materials.

In the discussion following we refer "particle" to non-coalescing particles or clusters of particles unless otherwise stated.

3.2. FRACTALS AND FRACTAL DIMENSION

During an aggregation process, non-coalescing solid particles come together and connect on contact usually to form ramified self-similar complex structures known as *aggregates* or *clusters*. A proper mathematical description of such a complex structures of random aggregates has been possible after Mandelbrot first introduced the concepts of *fractals* and *fractal geometry* (Mandelbrot, 1977) in his work published during 1970's. He coined the name *fractals* for complex self-similar structures. Fractals are found in the nature in form of structures of wide varieties of objects ranging from microscopic aggregates of nanoparticles to clusters of galaxies. We talk about fractals and their properties in more detail in the following section.

3.2.1. FRACTALS

Fractals are the complex naturally occurring or artificial structures with a self-similarity feature, i.e. their shape is scale independent. Mathematical fractals have infinite detail with identical appearance at all levels of magnifications (Fig. 3.1). However, in the real world this is almost impossible. In the physical world all structures which show self-similar behavior for a wide range of length scales are approximated as fractals. Such approximated fractals behave as real fractals in the range between certain lower and upper cut-off magnification levels. A few examples of such naturally occurring fractals are coastlines, tree structure, branching of

bronchioles in lungs, lightning bolt structure, cloud's silver linings and surfaces, fern plant, microscopic clusters of nanoparticles such as soot, etc.

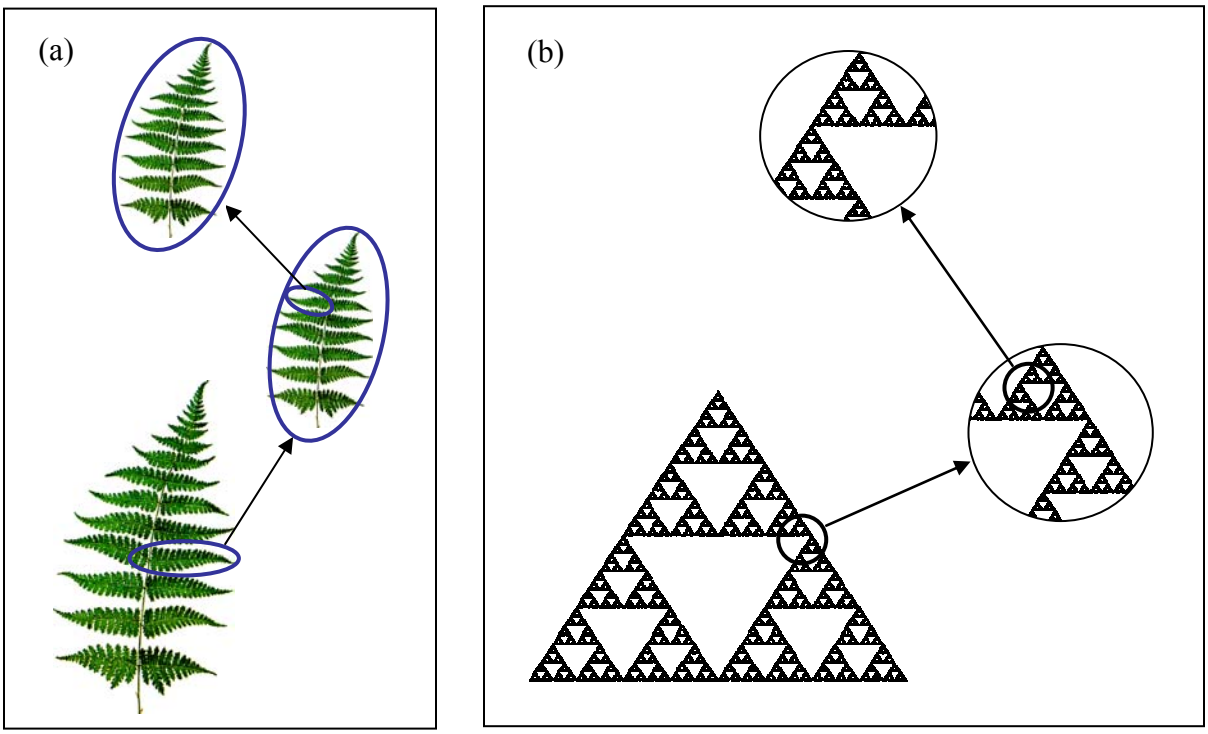

Figure 3.1: Zooming in to different magnification level reveals more details with a self-similar structure. (a) A fern plant. (b) A Sierpinski Triangle.

When we zoom in on a coastline, we start seeing more and more detail, and this keeps going for a range of length scale orders of magnitude larger. The length of a coastline looks longer and longer as we more and more zoom in on the map since the length measurement step size (ruler size) depends on the level of magnification. The coastline length grows without bound. Hence coastlines behave as fractals. A power law relationship is observed between the measured length of a coastline and the length of the step size. The use of the concept of fractal geometry can predict the lengths of a coastline at different magnification levels. Every estimate, however, would be lower than the true length.

One among many classical examples of fractals is the *Koch curve*. Such a curve can be generated by infinite number of iterations of a procedure involving division of a straight line into three equal segments and replacement of the central segment with two other segments of the same length inclined at a 60^o angle to each other. One end of a segment joins with one end of another segment (Fig. 3.2). Koch snowflake is another form of Koch curve which can be obtained by starting with an equilateral triangle and generating Koch curve on each side (Fig. 3.3). As in the case of the coastline length problem, the length of a Koch curve also follows a power law relationship. We can see looking carefully at first few generations of Koch curve that its length increases by a factor of 4/3 at next higher generation. The length of the n^{th} generation thus becomes $(4/3)^n$ in the unit of its length when $n = 0$. The length hence becomes infinity as n becomes infinitely large.

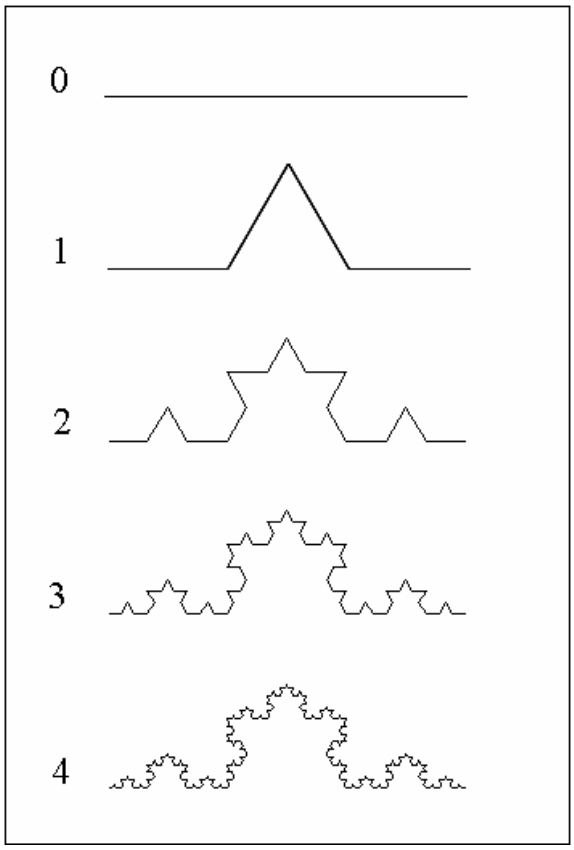

Figure 3.2: Koch curve shown up to its 4^{th} generation.

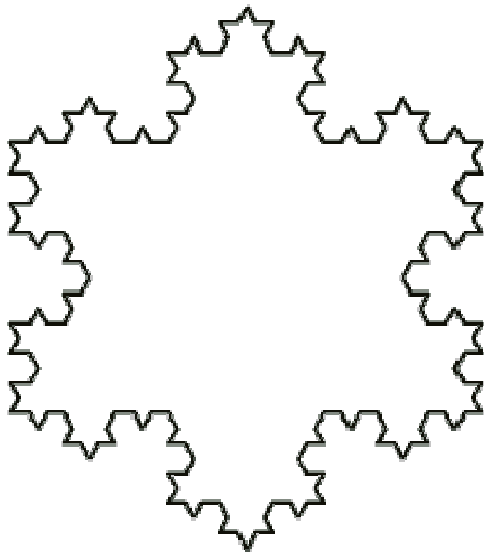

Figure 3.3: Third generation Koch snow flake.

3.2.2. FRACTAL DIMENSION

Fractal geometry has allowed analyzing and describing an incredibly broad range of complex structures found in nature by a simple parameter known as a *fractal dimension*. Before going into more detail on fractal dimension let us discuss about the concept of dimension of an object.

The total number of building units in an object follows a scaling law with the number of times a unit repeats on one side of the object, and the exponent of this scaling law is called the dimension of that object. If d be the dimension of an object then the scaling law gives

$$\text{Number of building blocks} = (\text{Number of segments on one side of the object})^{d}.$$

Let us consider geometric objects like a line, a square and a cube and draw line to bisect each side of these geometric objects (Fig. 3.4a). We end up making 2 segments or blocks for the line, 4 blocks for the square and 8 blocks for the cube.

For the line we must have $2 = 2^{d}$. This implies the dimension $d = 1$ for a line.

For the square we must have $4 = 2^{d}$. This implies the dimension $d = 2$ for a square.

For the cube we must have $8 = 2^{d}$. This implies the dimension $d = 3$ for a cube.

Hence we can predict the mass of a rod with $d = 1$ to double and the mass of an elephant with $d = 3$ to increases by 8 folds when their sizes are doubled. The dimension remains constant for a given object. We can see this by dividing each side of the above objects into three halves instead. We get 3 segments for the line, 9 blocks for the square and 27 blocks for the cube (Fig. 3.4b). This is consistent with a line having $d = 1$ since $3^1 = 3$, a square having $d = 2$ since $3^2 = 9$, and a cube having $d = 3$ since $3^3 = 27$.

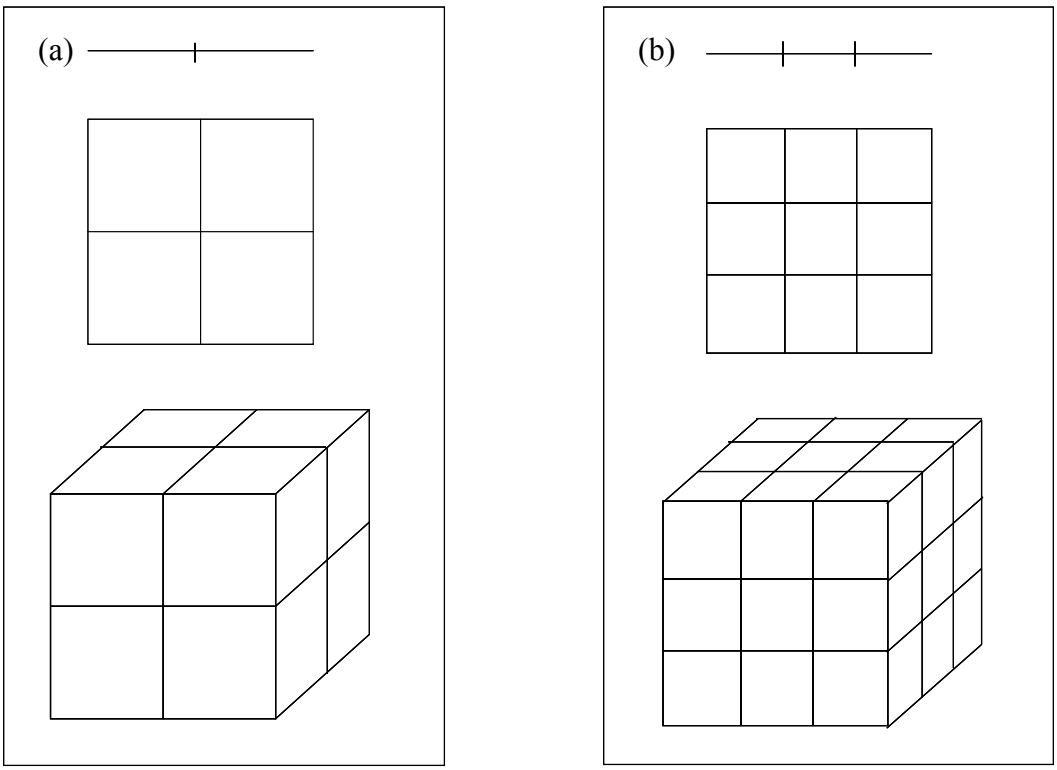

Figure 3.4: Geometrical objects: a line, a square and a cube. (a) Each side is bisected. (b) Each side is divided into three equal parts. A line is a one dimensional, a square is a two dimensional and a cube is a three dimensional object.

Now we return to our discussion of fractal dimension. We explore the dimension of a Koch curve as an example for a fractal. Let us start with the simplest case taking the 1st generation of a Koch curve (Fig. 3.2). It has 4 counts of basic segments and the total length is 3 in units of the

length of a basic segment. If D_f be the dimension of this Koch curve then we must have $3^{Df} = 4$. Thus

$$D_f = \frac{\log(4)}{\log(3)} = 1.26\,. \tag{3.1}$$

Let us now consider the n^{th} generation Koch curve. The count of basic segments will be 4^n and the length will be 3^n in unit of the length of a basic segment. We must have $(3^n)^{Df} = 4^n$. As expected, this implies that for the n^{th} generation Koch curve the dimension D_f is again the same as in Eq. (3.1) for the 1st generation Koch curve. An interesting fact that we observe here is that the dimension for the Koch curve, a fractal, is a non-integer number unlike the integer number dimensions of three, two or one (Euclidian dimension) for most of the things lying around us.

Koch curves are line fractals having no surface area. Since they are not surfaces a dimension of 2 will be too big, and also since they are more than lines or curves a dimension of 1 will be too small. This is the reason they take a non-integer dimension between 1 and 2. Having a non-integer dimension is an important feature of fractal objects.

Now we will give more generalized mathematical definition of a fractal dimension. Consider a fractal embedded in a Euclidian d (2 or 3) dimensional space with a linear size L. If $N(L)$ be the number of d dimensional building blocks of unit size required to cover the fractal structure then the fractal dimension D_f is given by the relation

$$D_f = \lim_{L\to\infty} \frac{\log N(L)}{\log L}\ . \tag{3.2}$$

The linear size length L in Eq. (3.2) is measured in units of the length of the building block.

Talking more precisely the fractal dimension we describe above is actually called the *number fractal dimension*. Likewise we can also define *mass fractal dimension* as mass also scales with the linear size of a fractal. However, for fractals with identical basic units (monodisperse) the number and mass fractal dimensions coincide since here the scaling relations for number and mass differ only by a constant factor of proportionality. In fact, even in the case

of polydisperse basic units, i.e., basic units have a size distribution, the number and mass fractal dimensions are found to be the same (Tence et al., 1986).

3.3. FRACTAL AGGREGATES AND THEIR GROWTH MODELS

The study of fractals and their growth phenomenon is very important. One among many reasons for this being that fractal structures are observed in far-from-equilibrium phenomena which are common in many important fields of science and technology (Vicsek, 1989). Physicists working in different areas of research have commonly recognized fractal patterns in their experiments. Understanding the fractal growth phenomena creates the possibility of gaining insight into extremely basic questions in the field of statistical mechanics regarding the theory of critical points where phase transition and percolation occur (Stanley and Ostrowsky, 1986) in equilibrium systems.

The self-similar random structures developed during the aggregation process of non-coalescing particles are started to be known as *fractal aggregates* after Mandelbrot (Mandelbrot, 1977) coined the term fractal to give mathematical description of self-similar disordered structures. The particles undergoing aggregation process are known as *monomers* or *primary particles*. Aggregation process can be homogeneous, i.e. aggregation between particles of similar type, or heterogeneous, i.e. aggregation between different types of particles. Further the particles can be of equal size (*monodisperse*) or of different sizes (*polydisperse*). Aggregation of similar particles represents an important class of growth phenomena. Aggregation may take place particle by particle, or the aggregates may also be actively playing role joining together to form larger clusters during their motion.

Fractal aggregation being a chaotic and complex growth process, it is impossible to predict the resulting patterns and forms. With the introduction of the fractal concept it has become possible to characterize the complex rugged structures by simple parameter known as fractal dimensions. A simple fractal scaling law can give the number of monomers N contained by a fractal aggregate with radius of gyration R_g as

$$N = k_0 \left(R_g / a \right)^{D_f} . \tag{3.3}$$

Here the prefactor $k_0 \approx 1.3$ for DLCA (Cai et al., 1995, Sorensen and Roberts, 1997) and a is the monomer size (radius).

Fractal growth during a particle aggregation process involves many factors, and it is usually difficult to predict which factor plays a relevant role in determining the structure of the growing object (Vicsek, 1989). Advancement in this area of fractal aggregation and growth process took a major step after Forrest and Witten (Forrest and Witten, 1979) first put forward a mathematical description of aggregates using the fractal concept developed by Mandelbrot (Mandelbrot, 1977). Different computer models have been developed to detect the most relevant factor. These models simplify the problem and study the effects of only a few of the factors in the absence of the perturbation from others. Such computer models have played an important role in the development of understanding of the fractal aggregation phenomenon.

In the following subsections we will describe two of the aggregation models which have been successful to receive considerable attention among physics and other scientific community. These are the particle-cluster aggregation model (Witten and Sander, 1981) and the cluster-cluster aggregation model (Kolb et al., 1983, Meakin, 1983). These models assume the aggregating system to be dilute. This means the monomer number density or the monomer volume fraction (the fraction of the system volume occupied by the total monomers) is very small such that the cluster-cluster separation always remains much larger than the cluster size (more discussion on *dilute* and *dense system* will be given later). The major difference between these two models is that in case of the first one a cluster can only aggregate with another particle while in the latter case a cluster can aggregate with both another particle and another cluster. In both models the particles usually follow Brownian trajectories (random walk) in a Euclidean space and binary collisions between two particles unite them irreversibly.

3.3.1. PARTICLE-CLUSTER AGGREGATION MODEL

Particle-cluster aggregation model is based on the assumption that single monomers keep adding up to a growing cluster. If the single monomers follow Brownian diffusional paths before crashing into the growing cluster, then the process is *diffusion limited aggregation* (DLA). DLA model has been first introduced by and Sander in 1981 (Witten and Sander, 1981) putting

forward a computer simulation related to the above mentioned process. DLA process starts with a stationary seed monomer and grows by capturing, one at a time, randomly diffusing monomers launched far from the growing cluster in an Euclidean space.

Fig. 3.5 shows a DLA cluster made up of 3000 monomers on a square lattice (Witten, 1983). This figure clearly demonstrates the random branching and self-similar structure of a cluster resulting from the DLA process. Analysis of a variety of mass/length scaling relationship for computer simulated DLA clusters, they are found to have a fractal dimensionality of $D_f \sim 1.70$ in two dimensional space while $D_f \sim 2.53$ is observed in three dimensional space (Meakin, 1983a, Meakin, 1983b). This model has been successfully used in explaining structures observed in a wide variety of physical processes including colloidal aggregation (Witten and Sander, 1981), dielectric breakdown (Sawada et al., 1982), diffusion-limited electrodeposition (Léger et al., 1999), and viscous fingering in porous materials (Bogoyavlenskiy, 2001).

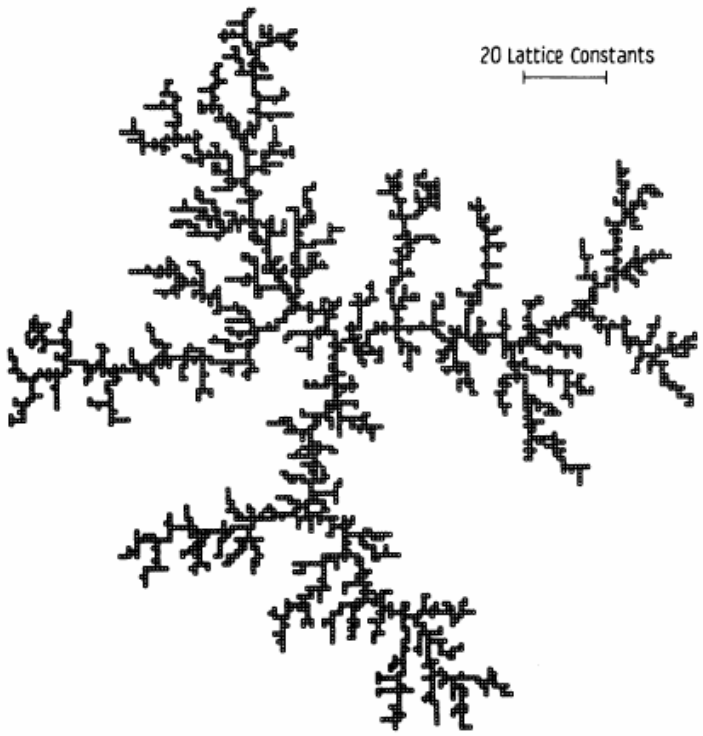

Figure 3.5: DLA cluster of 3000 monomers on a square lattice (Witten, 1983).

If the monomers in DLA model, instead of undergoing diffusive motion, move in a straight line (ballistic) trajectory before colliding with the growing cluster, then the process is called *ballistic limited aggregation* (BLA). DLA model has also been modified to give next model called *reaction limited aggregation* (RLA). The probability that a diffusing monomer sticks irreversibly with the growing cluster upon collision far less than unity gives rise to RLA process. Although DLA, BLA and RLA models have similarities, the cluster structures they generate show different morphological behavior.

Although the DLA model can explain different diffusion limited growth processes in physical systems, it is an unrealistic process in most cases of aerosol and colloidal aggregation since it ignores the aggregation of clusters themselves. Immobile growing clusters are rarely observed in aerosol and colloidal systems. More realistic model known as *diffusion limited cluster aggregation* (DLCA) for aerosol and colloidal aggregation has been proposed and well accepted by the scientific community. In DLCA model both clusters of monomers and monomers are allowed to diffuse around. More discussion follows in next subsection.

3.3.2. CLUSTER-CLUSTER AGGREGATION MODEL

Since the DLA model is limited in describing most of the aerosol and colloidal aggregation processes, it was necessary to develop a more complete aggregation model. Meakin (Meakin, 1983) and Kolb et al. (Kolb et al., 1983) simultaneously but independently developed other aggregation model in which both clusters of monomers and individual monomers are mobile. In this model, both monomers and clusters move in the embedding d-dimensional Euclidean space, and whenever binary collision (two-particle collision) occurs, the colliding particles (monomers or clusters) irreversibly and rigidly unite and continue to move in the space as a single entity. This process continues until only one giant cluster containing all the monomers of the system remains behind. Such an aggregation model is known as *cluster-cluster aggregation model*.

In cluster-cluster aggregation model, the properties of the clusters and their growth kinetics are directly affected by the kind of motion the particles exhibit. Usually the particles are made to follow Brownian trajectories. However, the particles can also be made to take ballistic trajectories during cluster-cluster aggregation process. To explain the aggregation mechanism

and cluster structures observed in real experimental system, two major types of cluster-cluster aggregation models, with particles undergoing random motion, have been developed based on the sticking probability between monomers and/or between clusters. These models are *diffusion-limited cluster aggregation* (DLCA) and *reaction-limited cluster aggregation* (RLCA) (Meakin, 1992, Vicsek, 1989).

A sticking probability between monomers and/or between clusters equal to one leads to DLCA while that significantly less than one gives rise to RLCA. This sticking probability is analogous to the probability that a particle will overcome the potential barrier it feels in the vicinity of another particle in a real aggregating system. The shape of the interaction potential between two particles determines the nature of cluster-cluster aggregation. If this potential barrier is strong, then the aggregation is RLCA type, otherwise it is DLCA type. In the case of cluster-cluster aggregation with particles following straight line path the sticking probability is held unity and the model is known as *ballistic limited cluster aggregation* (BLCA).

In both DLCA and RLCA models particles show diffusive motion. This means the position of a particle at a given time is uncorrelated with its position at any other time. The space and time of collision between two particles is thus unpredictable. The aggregation process in these models lead to the formation highly ramified and loopless structures exhibiting fractal properties. The density of such a cluster decreases as the number of monomers in the cluster increases. This property of a fractal aggregate is a consequence of its fractal dimension D_f which is less than the spatial dimension d.

The morphology and aggregation kinetics in systems with low particle concentration (dilute systems where the average cluster-cluster separation is very large compared to the average cluster size) have been extensively studied experimentally, theoretically and with computer simulations (Family and Landau, 1984, Cai et al., 1995, Carpineti et al., 1990, Jullien and Botet, 1987, Kolb et al., 1983, Lin et al., 1989, Meakin, 1983, Meakin, 1988, Meakin, 1992, Meakin, 1999, Schaefer and Martin, 1984, Sorensen and Roberts, 1997, Vicsek, 1989, Weitz and Oliveria, 1984). During the last two and half decades people have used TEM pictures, confocal microscopy, photon correlation spectroscopy, and light, X-ray and neutron scattering techniques to study aggregation of colloids and aerosols which are common in nature and important for our

technology (Bushell et al., 2002). These studies have found that the clusters generated by computer using cluster-cluster aggregation algorithm and the real aggregates observed in many experiments have very similar fractal scaling.

The cluster-cluster aggregation models DLCA and RLCA are quite successful in representing the aggregation process in the most common real aggregating systems of particles where the ratio of the mean free path of the medium molecules to the diffusing particle radius, which we define as the Kundsen number *Kn*, is far less than one. Even though most of the real cluster-cluster aggregation processes are more complex these simple models can be successfully used to study the structure of aggregates and the dynamics of their formation. For example, DLCA and RLCA models, in which clusters are held fixed in rotational orientation to simplify the problem, describe quite well processes such as the aggregation of very small particles and clusters in flames and dilute systems of colloidal particle aggregation.

We give further discussion on DLCA, RLCA and BLCA in the following subsections.

3.3.2.1. Diffusion Limited Cluster Aggregation (DLCA)

Diffusion limited aggregation is a dilute limit particle cluster aggregation model in which the aggregation process continues by randomly picking a particle (monomer or cluster) and moving it with certain probability by the monomer diameter distance in a random direction. Such randomly diffusing particle in *d*-dimensional (usually $d = 2$ or 3) space permanently stick with another particle in the space at the point of contact as soon as they touch each other (Jullien and Botet, 1987, Kolb et al., 1983, Meakin, 1983, Meakin, 1988, Vicsek, 1989). Fig. 3.6 show a computer generated DLCA cluster, from Kolb et al. (Kolb et al., 1983), in 2 dimensional space showing the branching structure.

In DLCA model the diffusion coefficient *D* is assumed to be a function of the number of monomers in the cluster *N* as

$$D(N) \propto N^{\gamma}. \tag{3.4}$$

Here γ is known as diffusivity or mobility exponent. If $\gamma = 0$ is chosen, then the diffusion of a cluster becomes mass independent. DLCA for such clusters is simulated in computer by randomly selecting clusters and moving them by one lattice unit in a randomly chosen direction one at a time. If $\gamma \neq 0$, then a random number φ uniformly distributed in the range $0 < \varphi < 1$ is assigned to a randomly chosen cluster and this cluster is moved only if $\varphi < D/D_{max}$, where D is the diffusion coefficient for the selected cluster and D_{max} is the largest diffusion coefficient for any cluster in the system.

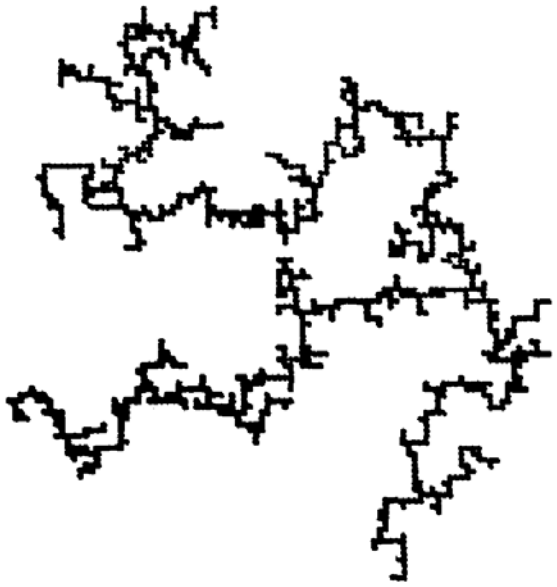

Figure 3.6: A computer generated DLCA cluster in 2-*d* system with size L = 128 and 1024 monomers. This cluster was formed at the end of the simulation and contains all the monomers (Kolb et al., 1983).

For $\gamma < 0$, the DLCA cluster structures are found to have fractal properties with fractal dimensions of about 1.40 – 1.45 in 2-*d* space and 1.75 – 1.80 in 3-*d* space (Meakin, 1992). Theoretical considerations and simulation results have indicated that the fractal dimension D_f of clusters generated using DLCA model are quite insensitive to the mobility exponent γ when $\gamma <$ 0 (Botet, 1985, Meakin, 1992). When $\gamma \rightarrow \infty$, DLCA turns into DLA since at large γ only a single largest cluster will be moving collecting the rest of the individual particles during its

diffusional motion. The fractal dimension of the resulting DLCA clusters increases from ~ 1.75 to ~ 2.50 when the diffusivity exponent γ is increased from a negative to a large positive value (Meakin, 1992). Note here that 2.50 is the fractal dimension for 3-*d* DLA clusters.

In a typical physical system $\gamma \approx -1/D_f$ is expected since the mobility of a cluster in a medium is inversely proportional to its mobility (hydrodynamic) radius R_m which for a fractal aggregate is typically proportional to its radius of gyration R_g. The fractal morphology of DLCA aggregates as having a mass fractal dimension of $D_f \approx 1.8$ when $\gamma < 0$ is in good agreement with experimental results obtained from both dilute limit aggregating systems of aerosol and colloidal particles (Forrest and Witten, 1979, Samson et al., 1987, Sorensen et al., 1992, Weitz and Oliveria, 1984, Zhang et al., 1988). Although being simple, the DLCA model surprisingly provides a complete description of a dilute limit fast aggregating system where the interactive potential between particles has only attractive part. Even in the case where the particles have a repulsive potential barrier, the aggregation process can still be explained by DLCA model if this repulsive barrier height is weak compare to the thermal fluctuation. DLCA is thus an ideal model for understanding complex behavior of aggregating aerosols.

3.3.2.2. Reaction Limited Cluster Aggregation (RLCA)

The main feature of the reaction limited cluster aggregation is the sticking probability P_{stick} upon collision of two aggregating particles going nearly to zero, i.e., $P_{stick} << 1$. Different models for reaction limited cluster aggregation have been developed (Brown and Ball, 1985, Jullien and Kolb, 1984, Kolb and Jullien, 1984, Meakin and Family, 1987, Meakin and Family, 1988). Among these different models, the one proposed by Kolb and Jullien, and Meakin et al. (Kolb and Jullien, 1984, Meakin and Family, 1987, Meakin and Family, 1988) is the modification of the DLCA. The modification is replacing $P_{stick} = 1$ with $P_{stick} << 1$. This RLCA model allows the investigation of not only the morphology of the clusters but also the kinetic and dynamic properties. RLCA is also sometimes known as *chemically limited cluster-cluster aggregation* in literature.

As DLCA model this RLCA model also considers only a dilute limit aggregating system where the monomer concentration tends to zero. Since the sticking probability is too small in

RLCA model, a particle (cluster or monomer) has to encounter other particles a large number of times until it finally can aggregates permanently with one of the particles. At early times during the aggregation process there are only small clusters. This increases the probability that a particle will diffuse away from another particle without coming in contact again if it does not aggregate upon the first collision. This makes the aggregation process too slow. Larger clusters are formed at later times. These big clusters, while close to each other, will touch each other many times as there are many ways for them to get linked.

RLCA model has been found successful in explaining complex real aggregating systems of particles (Aubert and Cannell, 1986, Lin et al., 1989, Schaefer and Martin, 1984) where the interacting potential function of the particles has a comparatively long range repulsive barrier in addition to the van der Waals attractive term. Such potential function mostly occurs in colloidal particles. The repulsive barrier between colloidal particles usually develops due to the double layer repulsion which behaves like screened electrostatic repulsion.

The tiny sticking probability in RLCA model requires the particles to come in contact a large number of times before they can stick together. This is analogous to several trials of the particle to overcome a small but relevant repulsive potential barrier before they can aggregate in real systems. Thermal fluctuations help particles to overcome the repulsive barrier. The particles spend some time in selecting the minimum energy configuration from all possible bonding configurations between pairs of particles. Once a particle overcomes the repulsive barrier it falls all the way on the potential curve until it hits the surface of the other particle and forms a permanent bonding.

RLCA clusters in 3-*d* space are found to be more compact compared to DLCA clusters and are characterized by a higher fractal dimension of $D_f \sim 2.10$ (Fry, 2003, Gonzalez, 1993, Lin et al., 1990, Weitz et al., 1985). Fig. 3.7 shows a comparison between gold colloidal cluster grown with DLCA and RLCA mechanism. This picture has been taken from work of Weitz et al. (Weitz et al., 1985). Higher fractal dimension makes RLCA clusters more dense as seen in Fig. 3.7.

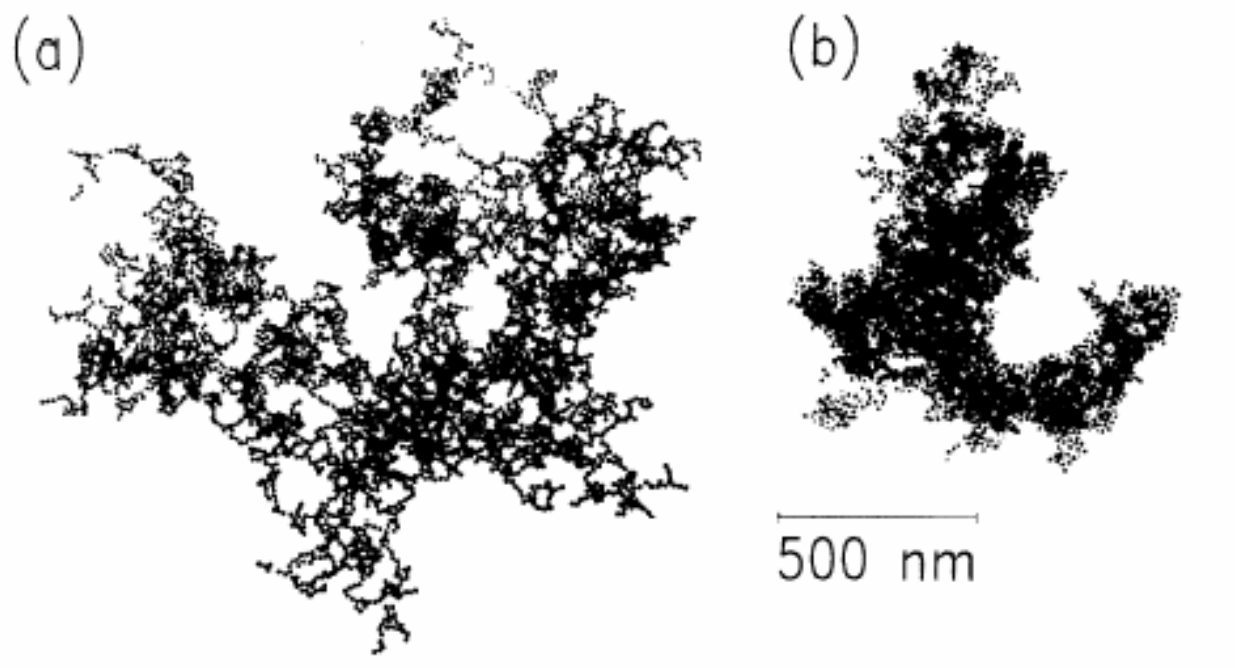

Figure 3.7: Comparison between TEM pictures of gold colloidal clusters with 5000 particles. (a) DLCA cluster with D_f=1.75. (b) Slow RLCA cluster with D_f=2.01 (Weitz et al., 1985).

The aggregation kinetics in RLCA, besides being slow, is found to produces higher degree of polydisperse cluster size distribution (Fry, 2003, Sorensen and Wang, 1999). The cluster growth is found to follow exponential law with time at early stage (Lin et al., 1990, Martin et al., 1990, Weitz et al., 1985) which may crossover to a power law growth at the later stages (Broide and Cohen, 1990, Fry, 2003).

3.3.2.3. Ballistic Limited Cluster Aggregation (BLCA)

Aggregation models in which particles follow linear trajectories (ballistic motion), but in random direction, have also been developed (Hasmy, 1999, Meakin and Donn, 1988, Meakin, 1984a, Mulholland et al., 1988, Sutherland and Goodarzn, 1971). The model, which is quite similar DLCA except that the clusters move along linear paths instead of Brownian path between collisions, is known as *ballistic limited cluster aggregation* (BLCA). Since the particles move in straight line BLCA becomes a fast process compare to DLCA.

BLCA model can explain the aggregation process in a real system for which the Knudsen number is too high. The straight line trajectories of the particles mimic the particle motion in an extremely tenuous gaseous medium with adequately low pressure. For such system the particles continue to move in a straight line path for a distance longer that its own size.

Fig. 3.8 shows a BLCA cluster formed at the end of a 2-*d* computer simulation (Meakin, 1984b). BLCA clusters are found to be somewhat compact compared to DLCA clusters (compare Fig. 3.6 and Fig. 3.8). BLCA clusters have slightly different morphologies compared to those of DLCA, the fractal dimension in 3-*d* being ~ 1.95 (Hasmy, 1999, Meakin and Donn, 1988, Meakin, 1984a, Mulholland et al., 1988). The fractal dimensionality is not sensitive to rotation of the clusters prior to a collision but is sensitive to the impact parameter (Meakin, 1984a).

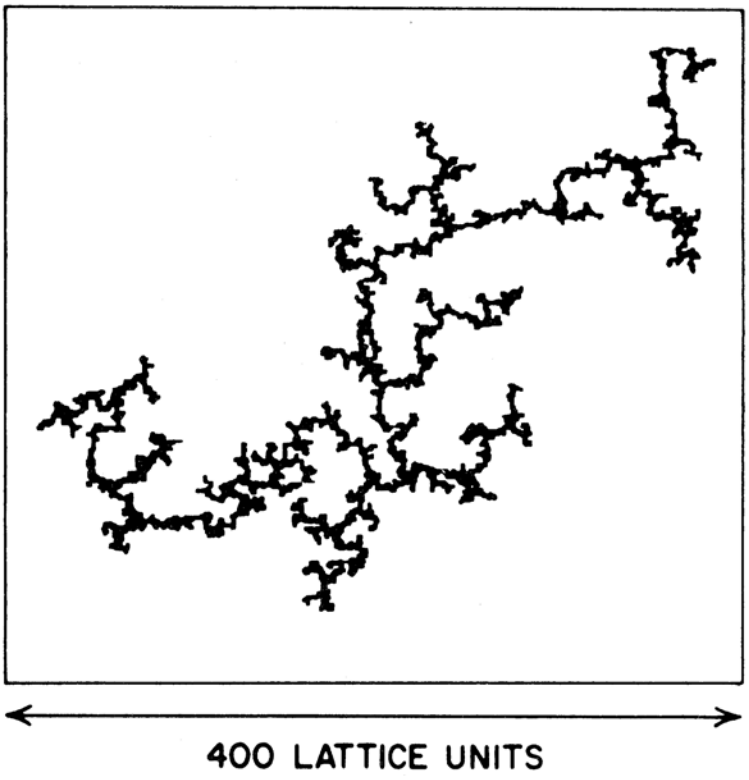

Figure 3.8: A 2-*d* BLCA cluster with 5000 particles simulated on a 400 x 400 lattice (Meakin, 1984b).

3.4. KINETIC REGIMES OF PARTICLE AGGREGATION

The morphology, kinetics and size distribution of an aggregating system are largely influenced by the type of kinetic regime in which the particle aggregation occurs. The embedding fluid determines the regime of particle motion. For example, particles move in straight line trajectories and aggregation process results in denser clusters with $D_f \sim 1.95$ if the particle size is far smaller than the mean free path of the medium molecules. The kinetic regimes of particles are governed mainly by the Knudsen number *Kn*. On the basis of *Kn* the kinetic regimes of aggregating particles are broadly classified into (1) *continuum regime* and (2) *free molecular regime*. However, there is also a third kinetic regime which has a significant effect in kinetics of particle aggregation (Oh and Sorensen, 1997, Pierce, 2007, Wang and Sorensen, 2001). This regime is called *Epstein regime*. We discuss these regimes separately in the following subsections.

3.4.1. CONTINUUM REGIME

If the Kundsen number $Kn << 1$, then the particles follow Brownian trajectories, and the system is said to be in continuum regime. The diffusion constant for the particles in this regime is given by the Stokes-Einstein diffusion coefficient

$$D_{SE} = k_B T / 6\pi\eta R_m \tag{3.5}$$

where R_m is the mobility radius of the diffusing particle, k_b is the Boltzmann constant, T is the absolute temperature of the system and η is the shear viscosity of the medium fluid.

In this regime the mean free path of medium molecules is much greater than the size of a particle, i.e., the medium is dense, and thus the particles undergo Brownian motion. Colloids practically always have Stokes-Einstein type of diffusion and hence are always in continuum regime. Aerosols also lie in the continuum regime if medium gas pressure is large enough.

The dilute limit particle aggregation in continuum regime can be well described by either DLCA or RLCA models depending upon the strength of the repulsive potential barrier between the interacting particles (Aubert and Cannell, 1986, Forrest and Witten, 1979, Lin et al., 1989,

Samson et al., 1987, Schaefer and Martin, 1984, Sorensen et al., 1992, Weitz and Oliveria, 1984, Zhang et al., 1988).

3.4.2. FREE MOLECULAR REGIME

Particles are said to be in the free molecular regime if the mean free path of the medium molecules is much larger compare to the particle size. In other words the Knudsen number $Kn >> 1$ for a free molecular regime. A particle motion in the free molecular regime will appear diffusive if the particles are allowed to move over a length scales larger than the particle separation between two successive particle collisions. Otherwise it is ballistic type. The diffusive or ballistic type of motion of particles is determined by a parameter called the particle *persistence length* λ_p, which is the average distance over which a particle moves effectively in a straight line (Meyer, 1983). Following two sub regimes of particle aggregation can be classified on the basis of the particle persistence length for a dilute limit system.

3.4.2.1. Epstein Regime

In many cases, when the mean free path of the medium molecules is greater than the size of the aggregating particles, there may be a situation such that the particles still exhibit diffusional motion between two successive particle-particle collisions. Such a situation is possible when the particle persistence length λ_p is smaller than the nearest neighbor particle separation R_{nn} for a dilute system. This regime of particle aggregation is known as *Epstein regime*.

Unlike the continuum regime, where particles experience a drag force proportional to the particle size, the moving particles experience a drag force proportional to the square of the particle size in this regime. The diffusion coefficient for Epstein regime (D_E) is thus inversely proportional to the square of the particle size as (Seinfeld, 1986),

$$D_E = \left[\frac{8\rho_g}{3}\left(\frac{2\pi}{mk_BT}\right)^{1/2}\left(1+\frac{\alpha\pi}{8}\right)\right]^{-1}\frac{1}{R_m^2} \tag{3.6}$$

where ρ_g is the medium mass density, m is the medium molecular mass, and the accommodation coefficient $0 \leq \alpha \leq 1$ is a factor which determines the way the gas molecules rebound from the surface of the particle (Fuchs, 1964).

3.4.2.2. Ballistic Regime

We call the aggregating system to be *ballistic regime* when the persistence length λ_p is much larger than the average particle separation. The particles loose their diffusive motion in this regime since they collide with another before they can diffuse. The particles thus trace straight line paths between two successive collisions. The average relative speed of the clusters is assumed to be given by the equipartition theorem.

The dilute limit aggregation process for the particle aggregation in free molecular regime has been understood by using the BLCA model (Hasmy, 1999, Meakin and Donn, 1988, Meakin, 1984a, Mulholland et al., 1988).

3.5. RELATION BETWEEN MOBILITY RADIUS AND RADIUS OF GYRATION

The Stokes-Einstein and Epstein diffusion coefficient assume a diffusing particle to be spherical. These diffusion coefficients can be generalized to use for fractal aggregates by replacing the radius with that of an equivalent sphere. This equivalent radius of an aggregate is known as the *mobility radius* and is denoted by R_m. The radius of gyration R_g of an aggregate with monomer size a has a direct relationship with the mobility radius R_m as

$$R_m = \beta\, a\, N^x \tag{3.7}$$

where β is a constant of proportionality and N is the total number of monomers in the cluster.

For the continuum regime it has been found that the $R_m \sim R_g$ for N far greater than one making the exponent $x = 1/D_f$ (Pusey et al., 1987, Rogak and Flagan, 1992, Wang and Sorensen, 1999). But the single particle limit of $R_m = 1.29 R_g$ must approach as $N \rightarrow 1$. For the Epstein

regime, the exponent x has been reported to be 0.44 ± 0.03 with β = 0.99 ± 0.02 (Wang and Sorensen, 1999) for $D_f \approx 1.75$. For this regime Eq. (3.7) gives the correct $N \to 1$ limiting value.

3.6. VOLUME FRACTION

The number and volume concentration of the particles (monomers or clusters) participating in an aggregating system have significant influence in the aggregation mechanism and the resulting cluster size distribution. The aggregation models described above are for dilute limit systems where the particle number and volume concentration tend to zero during the whole aggregating process. Uncorrelated binary collisions between particles are assumed in all DLCA, RLCA and BLCA aggregation models. The volume concentration of particles is more widely recognized as the *volume fraction* in the literature. We discuss volume fraction for monomers and clusters under following subsections.

3.6.1. MONOMER VOLUME FRACTION

The *monomer volume fraction* is the fraction of the system volume occupied by the monomers. It is a fixed quantity for a given system and is denoted by f_v. In most of the cases the monomers can be assumed to be spherical to avoid complication. The monomer volume fraction f_v for a system with n_m monomer number concentration is given by,

$$f_v = \frac{4}{3}\pi a^3 n_m \tag{3.8}$$

where a is the monomer radius.

3.6.2. CLUSTER VOLUME FRACTION

The *cluster volume fraction* f_{vc} is the fraction of the system volume occupied by the clusters. Unlike monomer volume fraction, cluster volume fraction is a growing quantity in an aggregating system. The cluster volume fraction f_{vc}, which is initially identical to the monomer volume fraction, increases with time because of the growing clusters with a fractal dimension D_f

less than the spatial dimension d of the system. The mass density ρ of the cluster thus decreases as they grow.

Let R_p be the perimeter radius of an equivalent sphere for a cluster with radius of gyration R_g. The total volume of such clusters in the system is thus $\frac{4\pi}{3}\sum R_p^3$. To express f_{vc} in terms of R_g we first find the relation between R_p and R_g. In the definition $R_g^2 = \int_0^{R_p} \rho(\vec{r}) r^2 d\vec{r} \Big/ \int_0^{R_p} \rho(\vec{r}) d\vec{r}$, we assume cluster isotropy and use the power law mass density function $\rho \propto r^{D_f - 3}$ to get $R_g^2 = \int_0^{R_p} r^{D_f-3} r^4 dr \Big/ \int_0^{R_p} r^{D_f-3} r^2 dr$. Further simplification gives

$$R_p = \sqrt{\frac{D_f + 2}{D_f}}\ R_g\,. \tag{3.9}$$

Hence the cluster volume fraction f_{vc} can be given for a system with volume V as

$$f_{vc} = \frac{4\pi}{3}\left(\frac{D_f + 2}{D_f}\right)^{3/2} \frac{\sum R_g^3}{V}. \tag{3.10}$$

Late during aggregation process the cluster volume fraction f_{vc} may increase greater than unity until the system gels. The increasing f_{vc} during an aggregation process is the key phenomenon responsible for the gelation of a system. We will return back to the discussion of a gelling system in coming sections.

3.7. NEAREST NEIGHBOR SEPARATION

Nearest neighbor separation denoted by R_{nn} is the mean separation between particles in a system. R_{nn} is very important parameter since its value determines if an aggregating system is in dilute regime or else. As has been already mentioned several times, the aggregation models described above explain only aggregation in dilute systems. A system is said to be dilute only if R_{nn} is much greater than the average particle size R. Below we derive relations for R_{nn} with the

particle volume fraction f_{vp}, the particle number concentration n and the particle radius of gyration R_g.

Let us consider an ideal case of close packed monodisperse system of spheres with radius R_p (Fig. 3.9a). Let the close packed volume fraction be f_{cpv} (in a 3-d space, the maximum possible $f_{cpv} = \pi/\sqrt{18} \approx 0.74$ for the hexagonally closed packed system). The nearest neighbor separation (center to center) is $R_{nn} = 2R_p$ and the particle volume fraction is $f_{vp} = f_{cpv}$. Now assume this system to expand symmetrically in all direction (Fig. 3.9b). R_{nn} now becomes greater than $2R_p$ while f_{vp} drops below f_{cpv}. The new particle volume fraction f_{vp} is given as

$$f_{vp} = f_{cpv}\left(\frac{2R_p}{R_{nn}}\right)^3 . \tag{3.11}$$

Rearranging Eq. (3.11) for R_{nn} we get

$$R_{nn} = 2R_p\left(\frac{f_{cpv}}{f_{vp}}\right)^{1/3} . \tag{3.12}$$

Using $f_{vp} = \frac{4}{3}\pi R_p^3\, n$, where n is the particle number concentration, Eq. (3.12) reduces to

$$R_{nn} = 2\left(\frac{3}{4\pi} f_{cpv}\right)^{1/3} \frac{1}{\sqrt[3]{n}} . \tag{3.13}$$

The spherical particles in the system are now replaced by fractal aggregates each having N number of monomers, D_f fractal dimension and R_g radius of gyration equivalent to that of the initial spherical particle (Fig. 3.9c). The particle number density n in Eq. (3.13) becomes the cluster number density n_c. In the limiting case where the monomer numbers in a cluster $N \to 1$, n_c coincides with the monomer number density n_m in the system. The quantities n_c and n_m are related as

$$n_c = \frac{n_m}{N} . \tag{3.14}$$

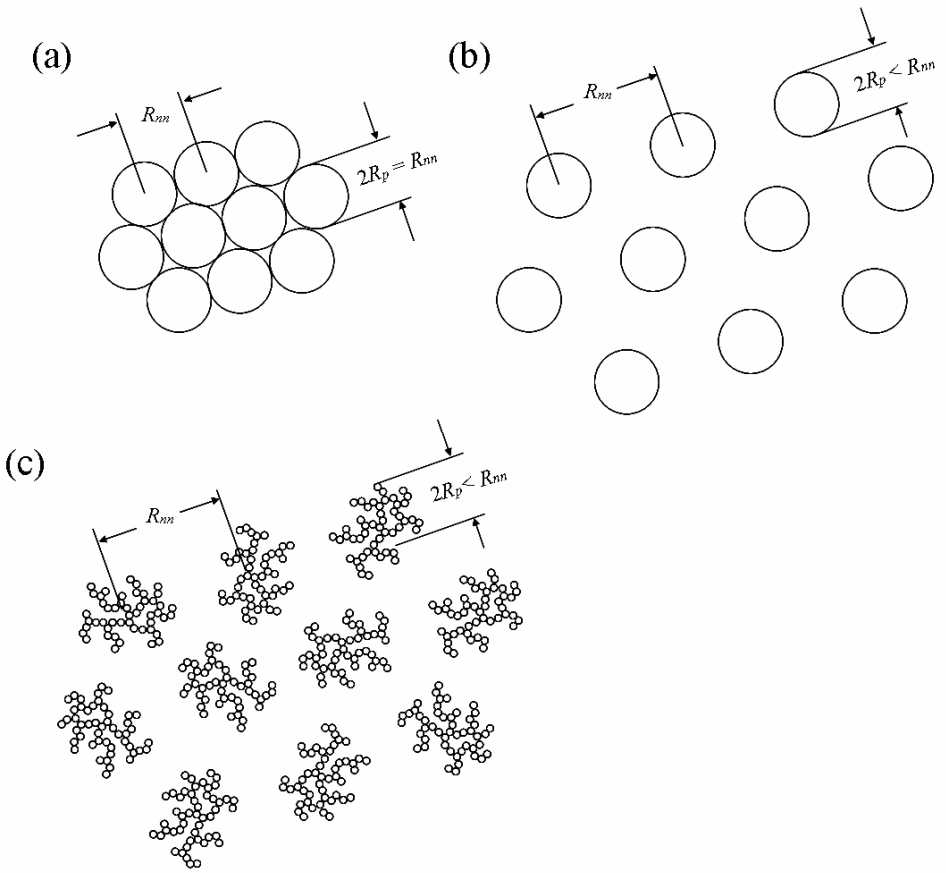

Figure 3.9: Nearest neighbor separation. (a) Closed packed spheres for which $R_{nn} = 2R_p$. (b) The system is expanded such that $R_{nn} > 2R_p$. (c) Spheres are replaced by fractal aggregates.

Using Eqs. (3.3) and (3.8), we can rewrite Eq. (3.14) in terms of the monomer volume fraction f_v and the cluster radius of gyration R_g as

$$n_c = \frac{3f_v}{4\pi k_0}\frac{a^{D_f-3}}{R_g^{D_f}}. \tag{3.15}$$

The nearest neighbor separation thus becomes

$$R_{nn} = 2\left(\frac{f_{cpv}}{f_v}\frac{k_0}{a^{D_f-3}}\right)^{1/3} R_g^{D_f/3}. \tag{3.16}$$

Hence

$$R_{nn} \propto n^{-1/3} \propto R_g^{D_f/3}. \tag{3.17}$$

Eq. (3.17) shows that the nearest neighbor cluster separation R_{nn} increases with increasing R_g following a power law. However, the cluster surface to surface separation decreases as clusters grow because of the fractal nature of the clusters.

3.8. AGGREGATION KINETICS

The information that the fractal dimension can provide is limited only to the geometrical properties of a single cluster in an aggregating system. The measurement of the fractal dimension alone is thus insufficient for complete characterization of the aggregation process. For example, DLA and percolating clusters in three dimensions have roughly the same fractal dimensionality, yet they have a completely different structure. It is thus very important also to understand the kinetics of the aggregation process and the resulting cluster size distribution to fully characterise an aggregation phenomenon.

A dispersed system of particles is usually unstable. The initial monomers in such a system coagulate into dimers, dimers into trimers or quadramers and so on. The rate of aggregation depends on the collision frequency, the sticking probability and also on the strength of the external field. In 1917 Marian von Smoluchowski (Smoluchowski, 1917) introduced a mathematical expression to give the fundamental description of the time evolution of the particle concentration. His description of time evolving particle concentration is based on the mean field theory which ignores the fluctuations in aggregation phenomenon. This expression is now known as the mean field *Smoluchowski Equation* (SE). Much of our understanding of aggregation kinetics is based on this mean field SE.

3.8.1. ASSUMPTIONS IN THE MEAN FIELD THEORY

The following are the basic assumptions in the mean field theory of Smoluchowski equation.

1. The space dependence of the particle concentration of a given size is neglected and is assumed to be represented by its spatial average.

2. The aggregation kernel or the reaction rate for the particles of two given sizes *i* and *j* is the same for any two particles of the same sizes *i* and *j*.

3. The system is sufficiently dilute such that the aggregation rate between two given particles of certain sizes is uninfluenced by the activity of other clusters.

3.8.2. SMOLUCHOWSKI EQUATION

Smoluchowski's coagulation rate equation (SE) is an infinite set of coupled non-linear integrodifferential which has been successfully used to determine the evolving aggregation kinetics during the aggregation process of non-equilibrium systems with low particle concentration (Smoluchowski, 1917), i.e. SE can well describe cluster-cluster processes. SE is based on a mean-field theory which can predict system behaviours only in the limit of spatially uncorrelated binary cluster collisions. Systems with low particle concentration are always in this limit. In mean field theory the thermodynamic fluctuations are assumed unimportant. For a continuous cluster size distribution with cluster number density $n(v,t)$ of size v (mass or monomer number) at time t, SE is given as,

$$\frac{\partial n(v,t)}{\partial t} = \frac{1}{2}\int_0^v K(v-u,u)n(v-u,t)n(u,t)du - n(v,t)\int_0^\infty K(v,u)n(u,t)du\,. \tag{3.18}$$

The first term on the r.h.s. of this equation is responsible for the gain while the second term for the loss of clusters of size v at time t during the collision and sticking process of the clusters. The factor ½ is necessary in the gain term to account for the double counting of a collision during the integration. Also $K(v,u)$ is the aggregation kernel which describes the rate of clustering between particles of size v and size u. SE can be solved analytically for many different functional forms of the aggregation kernel. However, for many physical situations the kernel is a homogeneous function (Dongen and Ernst, 1985, Friedlander, 2000),

$$K(cv,cu) = c^{\lambda} K(v,u) \tag{3.19}$$

where λ is the degree of the kernel homogeneity, such that a scaling solution exists for the SE.

For an aggregating system with a discrete cluster size distribution Eq. (3.18) takes the following form

$$\frac{\partial n(v,t)}{\partial t} = \frac{1}{2}\sum_{u=1}^{v-1} K(v-u,u)n(v-u,t)n(u,t) - n(v,t)\sum_{u=1}^{\infty} K(v,u)n(u,t)\,. \tag{3.20}$$

If the aggregation kernel remains constant being independent of particle size, i.e. $K(v,u) = K$ (a constant), Eq. (3.20) further reduces to

$$\frac{\partial n(v,t)}{\partial t} = \frac{1}{2}K\sum_{u=1}^{v-1} n(v-u,t)n(u,t) - Kn(v,t)\sum_{u=1}^{\infty} n(u,t)\,. \tag{3.21}$$

Taking sum over all v in Eq. (3.21) we get time derivative of the total cluster number density n_c as

$$\frac{dn_c}{dt} = -\frac{1}{2}Kn_c^2\,. \tag{3.22}$$

3.8.3. AGGREGATION (COAGULATION) KERNEL

The aggregation kernel $K(v,u)$ in SE governs the aggregation kinetics in a system of aggregating particles. It describes the aggregation rate and ultimately determines the characteristic particle size distribution. For coagulating particles of any sizes v and u, $K(v,u)$ is time independent. However, this parameter depends on the collision interaction among the particles, viz., sticking probability of particles upon collision, type of particle motion (diffusive, shear flow, gravitational settling, etc.), sizes of the interacting particles, etc.

We will limit our discussion to only homogeneous kernels for spontaneous thermal coagulation of uncharged particles. Below we derive an expression for $K(v,u)$.

3.8.3.1. Aggregation Kernel for Diffusing Particle

Let us consider a system in which monodisperse spherical particles of radius R_j are in Brownian motion around a particle with radius R_i. The particle number density is n. We choose a coordinate system to fix the particle R_i at the origin. Assuming spherical isotropy the diffusion equation, $\partial n/\partial t = D\nabla^2 n$, can be written as

$$\frac{\partial n(r,t)}{\partial t} = D\frac{1}{r}\frac{\partial^2}{\partial r^2}(r\,n). \tag{3.23}$$

We set the boundary conditions as

$$\begin{aligned} n &= 0 \qquad \text{at} \quad r = R_i + R_j \quad \text{and for all} \quad t \\ n &= n_0 \qquad \text{at} \quad r > R_i + R_j \quad \text{and} \quad t = 0 \end{aligned} \quad . \tag{3.24}$$

Particle number concentration at $r = R_i + R_j$ vanishes means the fixed particle R_j behaves as a perfect absorber. This means that initially non-interacting particles suddenly experience a strong attractive potential at $r = R_i + R_j$. The solution of Eq. (3.23) can be given as (Friedlander, 2000)

$$n(r,t) = n_0\left[1 - \frac{(R_i + R_j)}{r}\left\{1 - erf\left(\frac{r - (R_i + R_j)}{2\sqrt{Dt}}\right)\right\}\right]. \tag{3.25}$$

At steady state, i.e., when $t \to \infty$, Eq. (3.25) reduces to

$$n(r, t \to \infty) = n_0\left[1 - \frac{(R_i + R_j)}{r}\right] \tag{3.26}$$

which, as expected, is the solution of $\partial n/\partial t = 0$.

Now we find the total collision rate of particles R_i on the particle R_j. The total collision rate $n_{col}(t)$ is determined by the flux ($J = -D(\partial n/\partial r)_{r=R_i+R_j}$) of particles R_i on the particle R_j as

$$n_{col}(t) = -4\pi(R_i + R_j)^2 J$$
$$n_{col}(t) = 4\pi(R_i + R_j)n_0 D\left[1 + \frac{(R_i + R_j)}{\sqrt{\pi D t}}\right]. \tag{3.27}$$

Once the steady state is achieved ($t \to \infty$), Eq. (3.27) reduces to

$$n_{col}(t) = 4\pi D(R_i + R_j)n_0 . \tag{3.28}$$

We assume that a system reaches steady state almost instantly for the systems we study.

We can generalize Eq. (3.28) for a system in which there are more than one R_j particle, and both R_i and R_j particles are under Brownian motion. The diffusion coefficient D is replaced by D_{ij} which describe the relative motion of the particles. Let n_i and n_j be the number concentration for particles R_i and R_j respectively. Hence the collision rate per unit volume is given by

$$n_{col}(t) = 4\pi D_{ij}(R_i + R_j)n_i n_j . \tag{3.29}$$

The relative diffusion coefficient between two particles ($D_{ij} = <\left(r_i - r_j\right)^2 > / 2t$) can be expressed in terms of the individual particle diffusion coefficients as

$$D_{ij} = \frac{< r_i^2 >}{2t} + \frac{< r_j^2 >}{2t} - \frac{< r_i r_j >}{2t} . \tag{3.30}$$

We can set $< r_i\, r_j > = 0$ for dilute systems where particles move independent to each other. Hence we see

$$D_{ij} = D_i + D_j . \tag{3.31}$$

We can directly compare Eq. (3.29) with the SE (Eq. (3.18) or (3.20)). This comparison yields

$$K(i, j) = 4\pi\left(D_i + D_j\right)(R_i + R_j) . \tag{3.32}$$

The factor ($D_i + D_j$) in Eq. (3.32) depends on the transport properties of the clusters while the other factor ($R_j + R_j$) is the geometric term depending on the cluster structure.

The aggregation kernel given by Eq. (3.32), though derived for spherical particles, can also be approximated for fractal aggregates using radii of gyration R_g as the representation of the cluster radii. Fractal clusters have ill defined radius and R_g gives the best estimate of their size. The aggregation kernel given by Eq. (3.32) is for pure Brownian aggregation in dilute system where particles move independent of each other and stick together with unity probability upon collision.

3.8.3.2. Modification in Aggregation Kernel due to a Force Field

If particles experience a force field in a Brownian aggregating system, Eq. (3.32) needs a modification to give correct aggregation kernel. Let $\vec{v}_d$ be the drift velocity due to the force $\vec{F}$ and μ be the particle mobility. The particle flux at any distance r from the center is then given by

$$\vec{J}(\vec{r},t) = -D\nabla n(\vec{r},t) + \vec{v}_d n(\vec{r},t). \tag{3.33}$$

The quantity $\vec{v}_d$ in Eq. (3.33) is related to the force $\vec{F}$ and mobility μ as $\vec{v}_d = \mu\vec{F}$. Also the mobility μ is related to the diffusion coefficient D as $D = k_B T\mu$. The force $\vec{F}$ can be expressed in terms of its potential function as $\vec{F} = -\nabla\Phi(\vec{r})$. Now using these relations and assuming spherical symmetry, Eq. (3.33) and be rewritten as

$$J = -D\left(\frac{\partial n}{\partial r} + \frac{n}{k_B T}\frac{\partial \Phi}{\partial r}\right). \tag{3.34}$$

Eq. (3.34) is used to find the total collision rate $n_{col}(t)$ of diffusing particles with radius R_i on the particle with radius R_j fixed at the origin. We can let $R_i + R_j = r$ for arbitrary values of R_i and R_j. The collision rate $n_{col}(t)$ is then given as

$$\begin{aligned} n_{col}(t) &= -4\pi r^2 J \\ n_{col}(t) &= 4\pi r^2 D\left(\frac{\partial n}{\partial r} + \frac{n}{k_B T}\frac{\partial \Phi}{\partial r}\right). \end{aligned} \tag{3.35}$$

Eq. (3.35) can be solved for n to get the following solution

$$n(r,t) = n_0 \exp\left[-\frac{\Phi(r)}{k_B T}\right] + \frac{n_{col}(t)}{4\pi D}\exp\left[-\frac{\Phi(r)}{k_B T}\right]\int_{\infty}^{r}\frac{\exp[\Phi(r')/k_B T]}{r'^2}dr'. \tag{3.36}$$

Now we use the boundary condition of $n = 0$ at $r = R_i + R_j$ in Eq. (3.36) and rearrange it to solve for $n_{col}(t)$ as

$$n_{col}(t) = \frac{4\pi D\, n_0 (R_i + R_j)}{W} \tag{3.37}$$

where W is the factor given by

$$W = (R_i + R_j)\int_{R_i+R_j}^{\infty}\exp[\Phi(r')/k_B T]/r'^2\, dr'. \tag{3.38}$$

Eq. (3.37) is now generalized for a system in which all particles are under Brownian motion. The collision rate per unit volume is given by

$$n_{col}(t) = \frac{4\pi D_{ij}(R_i + R_j) n_i n_j}{W} \tag{3.39}$$

where n_i and n_j be the number concentration for particles R_i and R_j respectively.

Comparison of Eq. (3.39) with the SE yields

$$K(i,j) = \frac{4\pi(D_i + D_j)(R_i + R_j)}{W}. \tag{3.40}$$

The aggregation kernel given by Eq. (3.40) reduces to the Brownian aggregation kernel (Eq. (3.32)) as expected in the absence of the perturbing force (i.e., $\Phi = 0$). The factor W, which can be called the correction factor, determines the speed of the aggregation process. If a repulsive force field, for which Φ is positive, exists, the correction W (Eq. (3.38)) is greater than unity and hence $K(i,j)$ is smaller resulting in slower aggregation. This explains why RLCA process is slower than DLCA process. The correction factor $W(\Phi > 0)$ gives the particle-particle sticking probability P_{stick} as $P_{stick} = 1/W$. On the other hand, for an attractive force field ($\Phi < 0$), W becomes smaller than unity and hence the aggregation is faster.

3.8.3.3. Aggregation Kernel in Different Regimes of Particle Aggregation

Depending on the type of aggregation regime (continuum, Epstein or ballistic), the nature of the motion of particles will be different. Diffusive motions in continuum and Epstein regimes, and straight line motion in free molecular ballistic regime will result in a different aggregation kernel. Even both continuum and Epstein regimes have diffusive motions the aggregation kernel is still different due to the difference in the diffusive nature in these regimes. Different aggregation kernel may result in different aggregation kinetics and cluster morphology in an aggregating system.

3.8.3.3.1. Continuum Regime

For the continuum regime, $K(i,j) = 4\pi(D_i + D_j)(R_i + R_j)$ (Eq. (3.32)) can be used to determine the aggregation kernel. The diffusion constant D for the continuum regime ($Kn << 1$) is Stokes-Einstein type given by $D_{SE} = k_B T / 6\pi\eta R_m$ (Eq. (3.5)). Note here $D_{SE} \propto R_m^{-1}$ relation between the diffusion constant and the mobility radius of the diffusing particle. For fractal aggregates of a size i (mass or monomer number), the sphere radius R_i in Eq. (3.32) is replaced by the cluster radius of gyration R_{gi} which is again nearly equal to its mobility radius R_{mi} if the system is in continuum regime (see section 3.5.). The kernel $K(i,j)$ for the aggregation of fractal clusters of sizes i and j in the continuum regime then becomes

$$\begin{aligned} K(i,j) &\approx \frac{2}{3}\frac{k_B T}{\eta}\left(\frac{1}{R_{gi}} + \frac{1}{R_{gj}}\right)(R_{gi} + R_{gj}) \\ &= \frac{2}{3}\frac{k_B T}{\eta}\left(i^{-1/D_f} + j^{-1/D_f}\right)(i^{1/D_f} + j^{1/D_f}) \end{aligned} \quad . \tag{3.41}$$

This form of $K(i,j)$ can also be used for spherical coalescing particles when the radius of gyration R_{gi} is replaced by the perimeter radius R_p and the fractal dimension D_f is replaced by the spatial dimension d.

3.8.3.3.2. Epstein Regime

The aggregation kernel in this regime can also be determined using Eq. (3.32). However, the diffusion coefficient is now given by Epstein diffusion coefficient D_E for which $D_E \propto R_m^{-2}$. The diffusion coefficient for Epstein regime is given by $D_E = \left[\left(8\rho_g/3\right)\left(2\pi/mk_BT\right)^{1/2}\left(1+\alpha\pi/8\right)\right]^{-1} R_m^{-2}$ (Eq. (3.6)). The aggregation kernel $K(i, j)$ for particles of sizes i and j in the Epstein regime then becomes

$$K(i,j) = \frac{12}{\rho_g(8+\alpha\pi)}\left(\frac{\pi mk_BT}{2}\right)^{1/2}\left(\frac{1}{R_{mi}^2}+\frac{1}{R_{mj}^2}\right)(R_i + R_j). \tag{3.42}$$

For spherical coalescing particles R_{mi} and R_i are identical. However, the mobility radius R_{mi} for a fractal cluster goes as $R_m = \beta\, a\, N^x$ with β = 0.99 ± 0.02 and x = 0.44 ± 0.03 (Wang and Sorensen, 1999) in Epstein regime unlike in continuum regime. The radius R_i for a fractal cluster of a size i is approximated by its radius of gyration R_{gi}. We can not use perimeter radius R_p because it is not well defined for fractal objects. The kernel $K(i, j)$ for fractal aggregates in the Epstein regime then becomes

$$\begin{aligned} K(i,j) &\approx \frac{12}{\rho_g(8+\alpha\pi)}\left(\frac{\pi mk_BT}{2}\right)^{1/2}\left(\frac{1}{R_{mi}^2}+\frac{1}{R_{mj}^2}\right)(R_{gi}+R_{gj}) \\ &= \frac{12}{\rho_g(8+\alpha\pi)}\left(\frac{\pi mk_BT}{2}\right)^{1/2} a^{-1}k_0^{-1/D_f}\left(i^{-0.88}+j^{-0.88}\right)\left(i^{1/D_f}+j^{1/D_f}\right) \end{aligned}. \tag{3.43}$$

3.8.3.3.3. Ballistic Regime

In free molecular ballistic regime, where particles move in a straight line between successive collisions, the aggregation kernel can be determined by the relative mean velocity c_{ij} between colliding particles and their collision cross sectional area A_{ij} as

$$K(i,j) = c_{ij}A_{ij}. \tag{3.44}$$

The relative mean velocity c_{ij} for colliding particles with masses m_{pi} and m_{pj} can be described in terms of the kinetic theory of gases. The particle behave like giant gas molecules and thus c_{ij} can be expressed as

$$c_{ij} = \sqrt{\frac{8k_B T}{\pi}\left(\frac{1}{m_{pi}} + \frac{1}{m_{pj}}\right)}. \tag{3.45}$$

Collision between particles is assumed to be hard sphere collision where the collision cross section is independent of the particle velocity. The collision cross sectional area A_{ij} for these particles is then given as

$$A_{ij} = \pi(R_i + R_j)^2. \tag{3.46}$$

Eq. (3.32) has also been modified using a correction factor β to get $K(i,j)$ for the ballistic regime as (Seinfeld, 1986)

$$K(i,j) = 4\pi\left(D_i + D_j\right)(R_i + R_j)\beta. \tag{3.47}$$

The correction factor β is related to the diffusive Knudsen number Kn_D which is the ratio of the particle persistence length in the medium to the particle radius. β approaches unity when both Kn and Kn_D tend to zero. In the ballistic regime, where the particle persistence length becomes larger than the particle nearest neighbor separation, both Kn and Kn_D >> 1, and β takes the following form

$$\beta \approx 1/2Kn_D. \tag{3.48}$$

The diffusive Knudsen number Kn_D can be given as

$$Kn_D = \frac{2(D_i + D_j)}{c_{ij}(R_i + R_j)}. \tag{3.49}$$

With Eqs. (3.48) and (3.49), Eq. (3.47) is identical to Eq. (3.44). Also, use of Eq. (3.45) for c_{ij} gives

$$K(i,j) = \sqrt{8\pi k_B T}\left(\frac{1}{m_{pi}} + \frac{1}{m_{pj}}\right)^{1/2} (R_i + R_j)^2 . \tag{3.50}$$

If the particles are fractal aggregates the radius R_i is replaced by the cluster radius of gyration R_{gi}. Hence the kernel $K(i, j)$ for fractal aggregates in the ballistic regime becomes

$$K(i,j) = \sqrt{\frac{6k_B Ta}{\rho_p}}\, k_0^{-2/D_f}\left(\frac{1}{i} + \frac{1}{j}\right)^{1/2} (i^{1/D_f} + j^{1/D_f})^2 . \tag{3.51}$$

Here ρ_p is the mass density of each monomer in a cluster.

3.8.4. KERNEL HOMOGENEITY λ FROM SCALING ARGUMENTS

For many physical situations the kernel in the SE is a homogeneous function (Dongen and Ernst, 1985, Friedlander, 2000) as $K(cv, cu) = c^{\lambda} K(v,u)$ (Eq. (3.19)). A scaling solution exists for the SE for such a homogeneous kernel. The parameter λ, known as *kernel homogeneity*, is a very important parameter involved in the size distribution for an aggregating system (Dongen and Ernst, 1985). λ also plays an important role in the aggregation kinetics (Fry et al., 2002, Wang and Sorensen, 2001) through the kinetic exponent $z = (1- \lambda)^{-1}$, which describes the asymptotic behavior of the cluster number concentration $n_c \sim t^{-z}$ (see section 3.8.5.).

The homogeneity λ for different particle aggregation regimes can be determined by the scaling argument of the aggregation kernel K. We have seen that the aggregation K is proportional to the flux of particles towards the given particle. So we can write

$$K \propto A_c \dot{r} \tag{3.52}$$

where A_c is the collision cross sectional area and $\dot{r}$ is the relative velocity for the colliding particles. Here we are assuming the simplest case where the aggregating system has sufficiently narrow size distribution such that we can approximate all particles to have the same size.

For fractal clusters the collision cross sectional area A_c is proportional to the square of the cluster radius of gyration R_g for all regimes of cluster aggregation (Oh and Sorensen, 1997). In terms of the number of monomers N in a cluster, A_c can hence be given as

$$A_c \propto N^{2/D_f} . \tag{3.53}$$

3.8.4.1. Homogeneity for Diffusive Fractal Aggregation

Now if the clusters are undergoing diffusive motion (as in the cases of continuum and Epstein regimes) the relative cluster velocity $\dot{r}$ is given by $\dot{r} = D/R_c$ where D is the diffusion constant and R_c is a characteristic length scale with respect to the given aggregate's motion. For a dilute system with very low particle number density the only characteristic length scale is the size of the cluster itself. Hence for fractal aggregation we can write

$$\dot{r} \propto D/R_g \propto DN^{-1/D_f} . \tag{3.54}$$

We know that the diffusion of particles behave differently in different aggregation regimes. We generalize the diffusion coefficient D to be a function of the number of primary particles (monomers) N in the cluster as $D \propto N^{\gamma}$ (Eq. (3.4)). Here γ is called diffusivity exponent.

Use of Eqs. (3.53) and (3.54) along with Eq. (3.4) in Eq. (3.52) gives

$$K \propto N^{\gamma+1/D_f} . \tag{3.55}$$

Comparing Eq. (3.55) with the kernel $K \propto N^{\lambda}$ for the aggregating system with clusters of the same size N, we see that the kernel homogeneity λ is

$$\lambda = \gamma + \frac{1}{D_f} \qquad (\text{for diffusive clusters}) . \tag{3.56}$$

We now use Eq. (3.56) to find the homogeneity λ for continuum and Epstein regimes. For continuum regime we have $\gamma = -1/D_f$ (since $D \propto 1/R_g \propto N^{-1/Df}$). Hence for continuum regime

$$\lambda = 0 \qquad (\text{for continuum regime}) . \tag{3.57}$$

For Epstein regime we have $D_f \approx 1.75$ and $D \propto R_g^{-2} \propto \left(N^{0.44\pm0.03}\right)^{-2}$ (Wang and Sorensen, 1999). Hence $\gamma \approx$ -0.88 ± 0.06 for this regime. This gives the homogeneity for Epstein regime as

$$\lambda \approx -0.31 \mp 0.06 \qquad (\text{for Epstein regime}). \tag{3.58}$$

3.8.4.2. Homogeneity for Ballistic Aggregation

We now again return back to Eq. (3.52) to find the aggregation kernel for clusters moving ballistically. The particle mean velocity can be given by the equipartition theorem in this regime. Thus,

$$\dot{r} \propto 1/\sqrt{N}\,. \tag{3.59}$$

Use of Eqs. (3.53) and (3.59) in Eq. (3.52) yields

$$K \propto N^{2/D_f - 1/2}\,. \tag{3.60}$$

Hence for ballistic aggregation regime we have the homogeneity λ as

$$\lambda = \frac{2}{D_f} - \frac{1}{2} \qquad (\text{for ballistic regime}). \tag{3.61}$$

Using D_f = 1.95 for ballistic regime (Hasmy, 1999, Meakin and Donn, 1988, Meakin, 1984a, Mulholland et al., 1988) we find

$$\lambda = 0.53 \qquad (\text{for ballistic regime}). \tag{3.62}$$

3.8.4.3. Homogeneity for Intermediate Diffusive Fractal Aggregation

In many situations an aggregating system evolves and no longer remains dilute (Bibette et al., 1992, Kumar and Douglas, 2001, Sorensen et al., 1998). This means that the cluster nearest neighbor separation starts becoming comparable to the size of the cluster itself. This is possible because of the cluster fractal dimension D_f is smaller than the dimension d of the space in which the aggregation process is occurring. We will discuss more on dense aggregating system in

coming sections. Here we compute the homogeneity for system in which clusters are diffusing but the relevant length scale R_c involved in the relative cluster velocity $\dot{r} = D/R_c$ is the nearest neighbor separation $R_{nn} \propto R_g^{D_f/d} \propto N^{1/d}$ (Eq. (3.17)) instead of the cluster radius R_g. Being neither dilute nor dense, this regime of cluster aggregation is named as the *intermediate regime* (Pierce et al., 2006).

The new dependence of $\dot{r}$ on N for the intermediate regime becomes

$$\dot{r} \propto N^{\gamma - 1/d}. \tag{3.63}$$

Here the fact $D \propto N^{\gamma}$ has been used. Finally, using Eqs. (3.53) and (3.63) in Eq. (3.52) and we find

$$\lambda = \frac{2}{D_f} + \gamma - \frac{1}{d} \tag{3.64}$$

as the relation for the homogeneity at the intermediate aggregation regime. Appropriate choice for the value of the diffusivity exponent γ in Eq. (3.65) will return continuum or Epstein intermediate regime.

3.8.5. ANALYTICAL SOLUTION OF SMOLUCHOWSKI EQUATION

As has already been discussed the aggregation kernel is a homogeneous function for many physical situations. We solve Smoluchowski equation for the following two cases of a general homogeneous kernel and a constant kernel. We will derive an expression for the particle number density evolution with time. We will also see that we can solve the SE for a spectrum of particle size distribution in the case of a constant kernel.

3.8.5.1. General Homogeneous Kernel Case

Here we solve the SE considering a general homogeneous kernel constant in time. We consider the simplest case where all the particles are of nearly the same size. If N be the number

of primary particles (monomers) in each particle at any time t, then the aggregation kernel $K(N,N)$ is

$$K(N,N) = N^{\lambda} K(1,1) . \tag{3.65}$$

Here $K(1,1)$ is the aggregation kernel for primary particles and remains constant. Note that if the aggregation kernel $K(N,N)$ is Brownian type, then the homogeneity $\lambda = 0$ and the aggregation kernel becomes a constant as (see Eq. (3.41))

$$K(N,N) = 8k_B T/3\eta . \tag{3.66}$$

Now the SE (Eq. (3.20)) for monodisperse particles with the number concentration n is

$$\frac{dn(N,t)}{dt} = -K(N,N)n^2(N,t) . \tag{3.67}$$

Using Eq. (3.65) for $K(N,N)$ in Eq. (3.67) we get

$$\frac{dn}{dt} = -K(1,1)N^{\lambda} n^2 . \tag{3.68}$$

Expressing N in terms of the primary particle number concentration n_m and the particle concentration n ($N = n_m/n$), Eq. (3.68) becomes

$$\frac{dn}{dt} = -n_m K(1,1)n^{2-\lambda} . \tag{3.69}$$

Solving Eq. (3.69) we get

$$n(t) = n_m \left(1 + \frac{t}{t_c}\right)^{-\frac{1}{1-\lambda}} \tag{3.70}$$

where $t_c = \left[(1-\lambda)n_m K(1,1)\right]^{-1}$ is the characteristic time for decreasing the total particle number density decreases by half, and is usually very small for large n_m (Russel et al., 1999). The

exponent $1/(1-\lambda)$ in Eq. (3.70) determines the aggregation speed and is known as the *kinetic exponent* denoted by z, i.e.

$$z = \frac{1}{1-\lambda}. \tag{3.71}$$

Using values of the homogeneity λ (see section 3.8.4.), the kinetic exponent z are found as $z = 1$ for continuum regime, and for fractal aggregation $z \approx 0.76$ and 2.13 for Epstein and ballistic regimes, respectively.

From Eq. (3.70) we can see that N scales with time at $t >> t_c$ as

$$N \sim t^{z}. \tag{3.72}$$

This implies that the radius of gyration R_g of fractal clusters scales with t as

$$R_g \sim t^{z/D_f}. \tag{3.73}$$

This power law growth for fractal aggregates continues until the cluster nearest neighbor separation R_{nn} become a relevant length scale (see following sections).

3.8.5.2. Constant Kernel Case

The SE with a constant K can be analytically solved for the discrete size distribution. This equation with a constant aggregation kernel K is given by Eq. (3.21) as

$$\frac{\partial n(k,t)}{\partial t} = \frac{1}{2} K \sum_{i+j=k} n(i,t) n(j,t) - K n(k,t) \sum_{j=1}^{\infty} n(j,t) \qquad \text{(Eq. (3.21))}$$

where particles of sizes i and j unite to give a particle of size k. For monomers the first term in Eq. (3.21) vanishes and can be written in terms of the total particle number density n_c as

$$\frac{\partial n(1,t)}{\partial t} = -K n(1,t) n_c \tag{3.74}$$

whose solution is

$$n(1,t) = n_m\left(1+\frac{t}{t_c}\right)^{-2}. \tag{3.75}$$

Here $t_c = 2/n_m K$ is the characteristic time when the total particle number density n_c becomes $n_m/2$. Likewise the solution for dimmers is

$$n(2,t) = n_m\left(\frac{t}{t_c}\right)\left(1+\frac{t}{t_c}\right)^{-3}. \tag{3.76}$$

Generalizing the solution for *k*-mer, we find

$$n(k,t) = n_m\left(\frac{t}{t_c}\right)^{k-1}\left(1+\frac{t}{t_c}\right)^{-(k+1)}. \tag{3.77}$$

Eq. (3.77) is the complete solution for the discrete size distribution at any time *t* as the aggregation process continues in a coagulating system with a constant (in time) and size independent aggregation kernel (Friedlander, 2000).

A constant aggregation kernel *K* also yields a very simple rate equation for the total cluster number density n_c. Taking sum over all *k* in Eq. (3.21) we obtain the rate of change in the total cluster number density n_c as

$$\frac{dn_c(t)}{dt} = -\frac{1}{2}Kn_c^2. \tag{3.78}$$

Solving Eq. (3.78) we get

$$n_c(t) = n_m\left(1+\frac{t}{t_c}\right)^{-1}. \tag{3.79}$$

The exponent of -1 in Eq. (3.79) implies $z = 1$ or $\lambda = 0$, which is expected for an aggregating system with a constant kernel.

3.9. SELF-PRESERVING PARTICLE SIZE DISTRIBUTION

The onset of an aggregation process in a dispersed system of initially monomeric particles results in the evolution of particle size distribution, typically broadening with time. However, under *similarity transformation* for the particle size distribution, the distribution function, after a sufficiently enough long time, approaches an asymptotic form independent of time as well as the starting size distribution. This means the shapes of the rescaled size distribution at any time and initial conditions are identical for a given aggregation kernel. The scaling solution of SE for such a properly rescaled particle size distribution at sufficiently long times is called the *self-preserving* (Friedlander and Wang, 1966, Friedlander, 2000, Lai et al., 1972, Lushnikov, 1973) or *scaling* (Dongen and Ernst, 1985) *size distribution*.

Similarity transformation for particle size distribution is performed to render the distribution at any time as a function of only particle size normalized by the average size at that time. Let us consider the similarity transformation for a continuous size distribution $n(v,t)$ at time t when the particle number density in the system is $n_c(t)$. Let $\phi(x)$ be a function such that at sufficiently large times we can write

$$\frac{n(v,t)}{n_c(t)}dv = \phi(x)dx \tag{3.80}$$

where $x = v/\bar{v}(t)$ is the particle size scaled with the mean size $\bar{v}(t)$ at time t. Both sides of Eq. (3.80) are dimensionless. Rearranging we can get

$$\phi(x) = n(v,t)\frac{n_m}{n_c^2(t)}. \tag{3.81}$$

Since no particle is being added or removed from the system, the dimensionless quantity $\phi(x)$ remains constant and thus is the self-preserving size distribution. We demonstrated this self-preserving nature of the reduced size distribution function $\phi(x)$ using solution of SE with a constant kernel (Eqs. (3.77) and (3.79)). We find (note the change in notation for size from i to v)

$$n(v,t)\frac{n_m}{n_c^2(t)} = \left[\left(1+\frac{1}{t/t_c}\right)^{t/t_c}\right]^{-(k-1)t_c/t} . \tag{3.82}$$

Also we can show (using Eq. (3.77) and (3.79))

$$\frac{t}{t_c} = 1+\frac{n_m}{n_c} = 1+\frac{k}{\bar{k}} . \tag{3.83}$$

Here $\bar{k} = n_m / n_c$ is the mean particle size at time *t*. Now following Eq. (3.81) uses of Eq. (3.83) and the mathematical identity $\lim_{x\to\infty}(1+1/x)^x = e$ in Eq. (3.82) we find the self-preserving size distribution as

$$\phi(x) = e^{-\varsigma} \tag{3.84}$$

where $\varsigma = (k-1)/(\bar{k}+1) \approx k/\bar{k}$ (at large *k* and *t*). We showed here that $\phi(x)$, which is scaling solution of SE at sufficiently long times, is independent of time as it should be.

3.10. SCALING SOLUTION OF SMOLUCHOWSKI EQUATION

For a homogeneous kernel $K(v,u)$ with λ as the degree of homogeneity, the scaling or self-preserving solutions to the SE (Eq. (3.18)) at large reduced sizes *x* ($x = v/s_p$) take the form (Dongen and Ernst, 1985, Friedlander and Wang, 1966, Lai et al., 1972, Lushnikov, 1973, Vicsek and Family, 1984)

$$n(v,t) = M_1 s_p^{-2}\phi(x) \quad . \tag{3.85}$$

In Eq. (3.85) M_i is the i^{th} moment of the size distribution given by

$$M_i = \int_0^\infty v^i n(v,t)dv \tag{3.86}$$

and s_p is one of a class of mean sizes indexed by *p* (a fixed number chosen in accord with experimental convenience, e.g. $p = 2$ is taken for light scattering experiments) and defined by

$$s_p = \frac{M_p}{M_{p-1}}. \tag{3.87}$$

The time dependence enters in Eq. (3.85) only through the mean size s_p. The reduced function $\phi(x)$ is the scaling or self-preserving size distribution, and is given by

$$\phi(x) \approx Ax^{-\lambda} e^{-\alpha x} \qquad x > 1. \tag{3.88}$$

In Eq. (3.88) A and α are some normalization constants which we determine below.

Substituting Eq. (3.85) in Eq. (3.86) and using $x = v/s_p$ we find

$$M_i = M_1 s_p^{i-1} m_i \tag{3.89}$$

where

$$m_i = \int_0^\infty x^i \phi(x) dx \tag{3.90}$$

is the i^{th} moment of the scaling distribution. Conservation of total mass (or volume or monomer numbers) of the particles impose $m_1 = 1$ (Eq. (3.89)). Using Eq. (3.88) Eq. (3.90) can be rewritten in terms of the Gamma function $\Gamma(x)$ as

$$m_i = A\alpha^{\lambda-1-i}\Gamma(i+1-\lambda). \tag{3.91}$$

The normalization constant A is determined by using the fact that $m_1 = 1$ as

$$A = \alpha^{2-\lambda} / \Gamma(2-\lambda). \tag{3.92}$$

Again applying Eq. (3.89) in Eq. (3.87) we find

$$m_p = m_{p-1}. \tag{3.93}$$

One needs to be careful that the index p can take only one predetermined value. Applying Eq. (3.91) in Eq. (3.93) we determine the value of α in Eq. (3.88) as

$$\alpha = p - \lambda \,. \tag{3.94}$$

3.11. EVOLUTION OF THE MOMENTS OF THE SIZE DISTRIBUTION

Knowledge on the moments of the particle size distribution is required for a correct interpretation of the light scattering experimental data since light scattering probes intensity weighted moments of the cluster size distribution. The scattered intensity is proportional to the volume (or number of monomers) of the scattering particle. The i^{th} moment of a particle size distribution is given by Eq. (3.86). We get the rate of change of the i^{th} moment from the SE (Eq. (3.18)) multiplying it by v^i and integrating over all v to yield

$$\frac{dM_i(t)}{dt} = \frac{1}{2}\int_0^\infty\int_0^\infty \left[(v+u)^i - v^i - u^i\right] K(v,u)n(v,t)n(u,t)dvdu \,. \tag{3.95}$$

For the homogeneous kernel ($K(cv,cu) = c^\lambda K(v,u)$) and the scaling solution for the size distribution (Eq. (3.85)), Eq. (3.95) can be written in the form

$$\frac{dM_i(t)}{dt} = M_1^2 s_p(t)^{i+\lambda-2} I_i(K,\phi) \tag{3.96}$$

where

$$I_i(K,\phi) = \frac{1}{2}\int_0^\infty\int_0^\infty \left[(x+y)^i - x^i - y^i\right] K(x,y)\phi(x)\phi(y)dxdy \,. \tag{3.97}$$

The time dependence comes in r.h.s. of Eq. (3.96) only through the mean size s_p. We define the mean size taking $p = 2$. For $i = 2$ Eq. (3.96) then becomes

$$\frac{dM_2(t)}{dt} = M_1^2 s_2(t)^\lambda I_2(K,\phi) \,. \tag{3.98}$$

Making use of $s_p = M_2/M_1$, Eq. (3.98) is rewritten as

$$\frac{1}{s_2(t)^\lambda}\frac{ds_2(t)}{dt} = M_1 I_2(K,\phi) \,. \tag{3.99}$$

We can integrate Eq. (3.99) for $\lambda \neq 1$ to obtain

$$s_2(t) = s_2(0)\left[1 + \frac{t}{t_c}\right]^z \tag{3.100}$$

where $z = 1/(1 - \lambda)$ is the kinetic exponent and

$$t_c = \frac{z\, s_2(0)^{1/z}}{M_1 I_2(K,\phi)} \tag{3.101}$$

is the characteristic coagulation time. As can be seen in Eq. (3.101) t_c depends on the kernel homogeneity and the mean size, the total mass of the aggregating particles.

Substituting the mean size s_p in Eq. (3.96) with the one given by Eq. (3.100) we can solve for the i^{th} moment of the size distribution as

$$M_i(t) = M_i(0)\left[1 + \frac{t}{t_c}\right]^{(i-1)z} \tag{3.102}$$

with

$$M_i(0) = M_1 \frac{I_i(K,\phi)}{I_2(K,\phi)} \frac{s_2(0)^{i-1}}{(i-1)}. \tag{3.103}$$

3.12. PARTICLE SIZE DISTRIBUTION DYNAMICS

The time dependence statistics of particle concentrations of different sizes in an aggregating system is of interest to understand the evolution of the system. The particle size distribution $n(v,t)$ gives the concentration of particles of a given size v at a given time t. Vicsek and Meakin et al. (Meakin et al., 1985, Vicsek and Family, 1984) investigated the resulting cluster size distribution in a DLCA process by using computer simulation. Meakin et al. found that the cluster diffusivity exponent γ ($D(N) \propto N^{\gamma}$) has a strong influence on the cluster size distribution dynamics (Meakin et al., 1985) and described the cluster size distribution by the following dynamic scaling of the form

$$n(v,t) \sim t^{-\omega} v^{-\tau} g\left(v/t^{z}\right). \tag{3.104}$$

Here ω and τ are some constants, z ($\bar{v}(t) \sim t^{z}$) is the kinetic exponent, and $g(x)$ is a scaling function.

Alternatively Eq. (3.104) can also be presented in the form (Meakin et al., 1985, Vicsek and Family, 1984)

$$n(v,t) \sim v^{-2} \psi\left(v/t^{z}\right) \tag{3.105}$$

where

$$\psi(x) = x^{2-\tau} g(x). \tag{3.106}$$

Mass conservation, i.e., $n_m = \int_0^\infty v\, n(v,t) dv$ = constant in time, requires

$$\omega = (2-\tau) z. \tag{3.107}$$

The parameters ω, z and τ are functions of the diffusivity exponent γ. For a physical system ω, z are positive quantities and thus $\tau < 2$ has to be satisfied. When γ is less than some critical value γ_c, $\tau = 0$ has been found.

The scaling function $g(x)$ in Eq. (3.104) also depends on the diffusivity exponent γ. For $\gamma < \gamma_c$, $g(x)$ decays exponentially for both $x << 1$ and $x >> 1$. However, for $\gamma > \gamma_c$, $g(x)$ becomes a constant function at $x << 1$, and becomes $<< 1$ at $x >> 1$ (Meakin et al., 1985).

The diffusivity exponent γ dependence is introduced in the DLCA cluster size distribution due to the differences in ways the clusters diffuse at different γ. When $\gamma > 0$, smaller clusters show sluggish motion, and relatively many smaller clusters do not get chance to involve in the aggregation process. The number of clusters thus monotonously decreases for increasing size in the resulting size distribution. On the other hand when $\gamma < 0$, smaller clusters are more actively involve in the aggregation process. The resulting size distribution is thus bell-shaped with only few small and very large clusters in the system.

The crossover from the monotonically decreasing to the bell-shaped cluster size distribution occurs at $\gamma = \gamma_c$. Meakin et al. (Meakin et al., 1985) found from their simulations that $\gamma_c \approx -0.27$ for 2-*d* DLCA process and $\gamma_c \approx -0.5$ for 3-*d* DLCA process. For a real system of particles in continuum regime, the diffusion constant $D \propto$ (hydrodynamic radius R_m)$^{-1}$. Thus for real systems diffusing in continuum regime (where $R_m \propto R_g$) the diffusivity exponent $\gamma = -1/D_f$. In real 3-*d* DLCA systems, the fractal dimension of the clusters $D_f \approx 1.80$ and hence $\gamma = -1/D_f \approx -0.56$. This value of γ is close to the value of γ_c for 3-*d* DLCA process.

van Dongen and Ernst (Dongen and Ernst, 1985) have also described the cluster size distribution of the following scaling form

$$n(k,t) = M_1 \bar{k}^{-2} \phi(k/\bar{k}) . \tag{3.108}$$

Their description is based on the behavior of the homogeneous kernel $K(ci, cj) = c^{\lambda} K(i, j)$ characterized by two exponents μ and ν such that

$$K(j >> i) \sim i^{\mu} j^{\nu} \qquad (\mu + \nu = \lambda) . \tag{3.109}$$

The homogeneous kernel is classified into three classes based on the relative sticking probabilities between two large clusters, and between small and large clusters. In class I, $\mu > 0$; in class II, $\mu = 0$; and in class III, $\mu < 0$. The Brownian kernel (Eq. (3.41)) belongs to class III type.

For class I kernel, the aggregation of large clusters with other large clusters is dominant. Aggregation preference is independent of the cluster size for class II kernel, and for class III kernel the aggregation of small clusters to large clusters is preferred. This results in different cluster size distribution dynamics for these three different classes of kernel. The scaling function $\phi(x)$ in Eq. (3.108) at the limit $x >> 1$ takes the following form for all classes with $(\lambda - \mu) < 1$.

$$\phi(x >> 1) \approx A x^{-\lambda} e^{-\alpha x} . \tag{3.110}$$

In the limit $x << 1$ the distribution for classes I and II kernels in non-gelling systems ($\lambda < 1$) exhibit a power law as

$$\phi(x << 1) \sim x^{-\tau} \tag{3.111}$$

where the exponent τ satisfies

$$\tau = 1 + \lambda \qquad \text{for class I kernel} \tag{3.112}$$

and

$$\tau < 1 + \lambda \qquad \text{for class II kernel.} \tag{3.113}$$

For class III kernel, the small x behavior for the distribution function for non-gelling system ($\lambda <$ 1) follows an exponential decay as

$$\phi(x << 1) \sim \exp\left(- x^{-|\mu|}\right). \tag{3.114}$$

The distribution function for class III kernel is bell-shaped thus relatively narrower.

3.13. AGGREGATION WHEN DENSE

Although aggregation in a dilute system (DLCA aggregation) has been well understood, our knowledge of aggregation in dense systems (cluster crowded) is still vague. For dense systems, the aggregating particles start developing the connectivity network among themselves. This can cause the varying mobility of different clusters to have little or no effect in their aggregation mechanism. Hence for dense systems the aggregation kinetics, cluster morphology, cluster dynamics and cluster size distribution are expected to be deviated from those observed for dilute and intermediate systems (Dhaubhadel et al., 2006, Fry et al., 2002, Fry et al., 2004, Gimel et al., 1995, Hasmy and Jullien, 1995, Hasmy and Jullien, 1996, Hasmy, 1999, Kim et al., 2006, Kolb and Herrmann, 1985, Rottereau et al., 2004, Sorensen et al., 2003).

According to the mean field theory the growth kinetics of a cluster radius of gyration follows a power-law in time as $R_g \sim t^{z/D_f}$. As the aggregating system evolves, the cumulated volume fraction occupied by the clusters increases because of the self-similar fractal nature of the cluster structure. With a dimensionality $D_f < d$, the growth kinetics causes the aggregates to

occupy a greater fraction of the available space with time. The ratio of the mean cluster nearest neighbor separation R_{nn} (Eq. (3.17)) to the cluster size R_g decreases with time as

$$R_{nn} / R_g \sim t^{-z(d-D_f)/dD_f} . \tag{3.115}$$

When the ratio R_{nn} / R_g approaches two, the aggregates in the system no longer encounter each other in a spatially uncorrelated manner but instead the neighboring aggregates jam together to form a volume-spanning network (Dhaubhadel et al., 2006, Kim et al., 2006, Sorensen et al., 2003). The details of the evolution from cluster dilute to cluster dense and to gel are largely unknown since aggregation of finely divided matter has been studied typically for only dilute systems (Gimel et al., 1995, Hasmy and Jullien, 1995, Hasmy, 1999). We define "*cluster dilute*" and "*cluster dense*" as when the ratio R_{nn} / R_g is large or small, respectively. This transition of an aggregating system from dilute flocculation regime to dense interconnected regime has been reported in some limited literature (Dhaubhadel et al., 2006, Fry et al., 2002, Fry et al., 2004, Gimel et al., 1995, Hasmy and Jullien, 1995, Hasmy and Jullien, 1996, Hasmy, 1999, Kim et al., 2006, Kolb and Herrmann, 1985, Rottereau et al., 2004, Sorensen et al., 2003).

Very few simulations (Fry et al., 2002, Gimel et al., 1995, Hasmy and Jullien, 1996, Kolb and Herrmann, 1985, Rottereau et al., 2004) and almost no experimental studies (Dhaubhadel et al., 2006, Kim et al., 2006, Sorensen et al., 2003) are found in literature which study aggregation from the dilute regime up to the cluster crowded regime. Previous simulation studies of aggregation were limited in time and/or system size (however, see below) with smaller volume fractions so that the cluster dense regime was not attained. Also most of the previous experimental attempts were limited to smaller monomer volume fractions such that the time the system would have taken to transit from cluster dilute to cluster dense was much longer than the typical experimental observation time.

Previous computer simulations of aggregation with Brownian dynamics in our laboratory (Fry et al., 2002) have shown that the cluster motion evolved from cluster dilute limit DLCA (Brownian) to cluster dense, ballistic motion as the system crossed over from the cluster dilute to the cluster dense regime. It was found that the kinetic exponent z continuously evolved from 1 to 2 and the kernel homogeneity λ, which is related to the cluster growth kinetics and the resulting

cluster size distribution, concomitantly evolved from 0 to 0.5. Kinetic exponent z = 1 and homogeneity λ = 0 during the early dilute stage of the aggregation process were as expected for DLCA. For a ballistic-type aggregation, where the aggregating clusters move along straight paths between successive collisions with speed determined by the equipartition of energy, z was 2 and λ was 0.5. Both parameters z and λ were found to be universal functions of the free volume Ω, which is the volume not occupied by the growing clusters. The cluster crowding is found to be the only reason for the enhanced aggregation kinetics.

Some other simulation studies have also given an indication of a crossover from the DLCA value of the fractal dimension to a larger value as the sol evolves from the cluster dilute case to the gel (Fry et al., 2004, Gimel et al., 1995, Hasmy and Jullien, 1996, Kolb and Herrmann, 1985, Rottereau et al., 2004). A recent large-scale, three dimensional, off-lattice diffusion-limited cluster-cluster computer simulation from our laboratory (Fry et al., 2004) have also shown that near the gel point the aggregates become so crowded that they percolate to form $D_f \approx 2.6$ aggregates.

Gimel et al. (Gimel et al., 1995, Rottereau et al., 2004) have also recognized the crossover process to be explainable by static percolation theory. From their extensive computer simulation study, they found that systems undergoing the DLCA process eventually become cluster dense and finally gel irrespective to their monomer volume fraction provided the system size tends to infinity. This crossover occurs at a characteristic size which is determined by the overlap of the clusters and decreases with increasing monomer volume fraction. Also the sol-gel transition occurs at a well defined time. They observed strong modifications in both the cluster size distribution and the mass fractal dimension as the aggregation process crosses over from cluster dilute regime to cluster dense regime. In their simulation studies, Gimel et al. (Gimel et al., 1995, Rottereau et al., 2004) used the mean field Smoluchowski Equation approach to describe the cluster aggregation kinetics in the early dilute state, but the connectivity network of the fractals during the gelation of the system has been explained in terms of the percolation theory. The DLCA and percolation clusters are characterized by the scaling size distribution exponents of 0 and 2.18, respectively. They found that the characteristic of the space filling network of clusters is the same whether it is a result of a dynamic DLCA process or a static percolation process. They also observed a transition in the fractal dimension from that expected for DLCA to that

expected for percolation. They found dilute limit DLCA fractal dimension of 1.8 at smaller length scales and percolating cluster fractal dimension of 2.5 at larger length scales. All these results are in support of our simulation results.

Other simulation studies on dense systems have found a fractal dimension intermediate between that for DLCA clusters and percolation clusters (Herrmann and Kolb, 1986, Kolb and Herrmann, 1985). Hasmy et al. (Hasmy et al., 1997) reported that there is a critical volume fraction for a system to gel and the gel time for a gelling system is system size dependent. This is in contradiction to the results of Gimel et al. (Gimel et al., 1995, Rottereau et al., 2004). Lushnikov (Lushnikov, 2005) did a theoretical study of the formation of a gel in a disperse system wherein binary coagulation alone governs the temporal changes in the particle size distribution. However, his study is based on the assumption that the aggregation kernel is proportional to the product of masses of aggregating particles, i.e., $K(v,u) = 2vu$, which is a case with homogeneity $\lambda = 2$. He also considered the SE to work through the aggregation process and reported on the exact solution of this model of non-Brownian kernel for a finite total mass of the coagulating system.

3.13.1. GELATION

A form of aerosol gelation was first reported by Lushnikov and coworkers (Lushnikov et al., 1990). The gel was formed in the presence of an electric field which enhanced aggregation of solid particles along field lines. Subsequently our laboratory has reported gelation of soot in laminar diffusion flames (Kim et al., 2006, Sorensen et al., 1998). Simulations (Fry et al., 2004, Gimel et al., 1995, Gimel et al., 1999, Hasmy and Jullien, 1996) imply that any system of particles undergoing aggregation can form a gel if the combining particles do not coalesce, and if the time to reach the gel point is shorter than other time scales that can deter gel formation. Non-coalescence is necessary so that the aggregating particles will form a non-dense (ramified) fractal aggregate with fractal dimension, D_f, less than the spatial dimension, d. When $D_f < d$, the average cluster separation to cluster size ratio falls with time during aggregation until the separation equals the size. Then the clusters jam together to form a gel.

A reasonable approximation for when the particulate system gels is when the monomer or primary particle number density in the average cluster $n_{cluster}$ is equal to the primary particle number density in the entire system n_{system}, i.e.,

$$n_{cluster} = n_{system} . \tag{3.116}$$

For a fractal aggregate (cluster) the number of primary particles N of radius a in a cluster of radius R_g is approximately $N \approx (R_g / a)^{D_f}$. Then the primary particle number density in the cluster in three dimensional space is

$$\begin{aligned} n_{cluster} &\approx N \Big/ (4\pi R_g^3 / 3) \\ &= (3/4\pi) R_g^{D_f - 3} \Big/ a^{D_f} \end{aligned} . \tag{3.117}$$

The system primary particle number density is related to the particulate volume fraction f_v by

$$f_v = \frac{4\pi}{3} a^3 n_{system} . \tag{3.118}$$

Then Eqs. (3.117), (3.118) and (3.119) yield the size of the cluster at the gel point

$$R_{gel} \approx a \, f_v^{\frac{1}{D_f - 3}} . \tag{3.119}$$

For Diffusion Limited Cluster Aggregation (DLCA) with D_f =1.8 this is

$$R_{gel} \approx a f_v^{-5/6} . \tag{3.120}$$

The gel time is the time for a cluster to grow to R_{gel}. Kinetics of growth are governed by the Smoluchowski Equation which in its simplest form is $\frac{dn_c}{dt} = -\frac{1}{2} K n_c^2$ (Eq. (3.22)). The long time solution to Eq. (3.22) is

$$n_c(t) \approx (Kt)^{-1} . \tag{3.121}$$

The cluster and primary particle number densities are related by

$$n_{system} = N\, n_c\,. \tag{3.122}$$

n_{system} is a constant and N and n_c vary with time. The gel time can be found by setting the number of primary particles per cluster N to its value at the gel point through $N \approx (R_g / a)^{D_f}$ and Eq. (3.119) as

$$N_{gel} \approx f_v^{\,D_f/(D_f-3)}\,. \tag{3.123}$$

Then combining Eqs. (3.119), (3.122), (3.123) and (3.124) one can find the gel time as

$$t_{gel} \approx \frac{4}{3}\pi K^{-1} a^3 f_v^{\,-3/(3-D_f)}\,. \tag{3.124}$$

For D_f=1.8 Eq. (3.124) becomes

$$t_{gel} \approx \frac{4}{3}\pi K^{-1} a^3 f_v^{\,-2.5}\,. \tag{3.125}$$

Eq. (3.125) was derived under the assumptions of spherical clusters, all the same size, with no interpenetration. Despite these caveats, it has the important implication that if a is small and f_v is large, i.e., if there is a lot of finely divided matter, the system will gel fast. Moreover, the functionalities on a and f_v are very strong. Eq. (3.125) is plotted in Fig. 3.10. For the aggregation constant K the Brownian kernel value for air at STP is used, $K = 3\times10^{-10}$ cm^3/s. Fig. 3.10 shows that an aerosol can gel quickly, 100 s or less, if $a \sim 10$ nm and $f_v \sim 10^{-4}$. Coarser aerosols at lower f_v have huge gel times and essentially never gel because other factors, e.g., gravitational setting, occur first.

The conditions for rapid gel formation, $f_v \geq 10^{-4}$ and a ~10 nm, can be obtained with rapid, gas phase reaction. Any gas at STP if converted directly to a solid will yield a solid f_v of about 10^{-3} (recall that gases are about 1,000 times less dense than the condensed phase). Rapid reactions from the gas to the solid phase will drive the system deep into a supersaturated regime. Thus rapid and uniform nucleation to small particles will occur. This is what we did to form carbon aerosol gels.

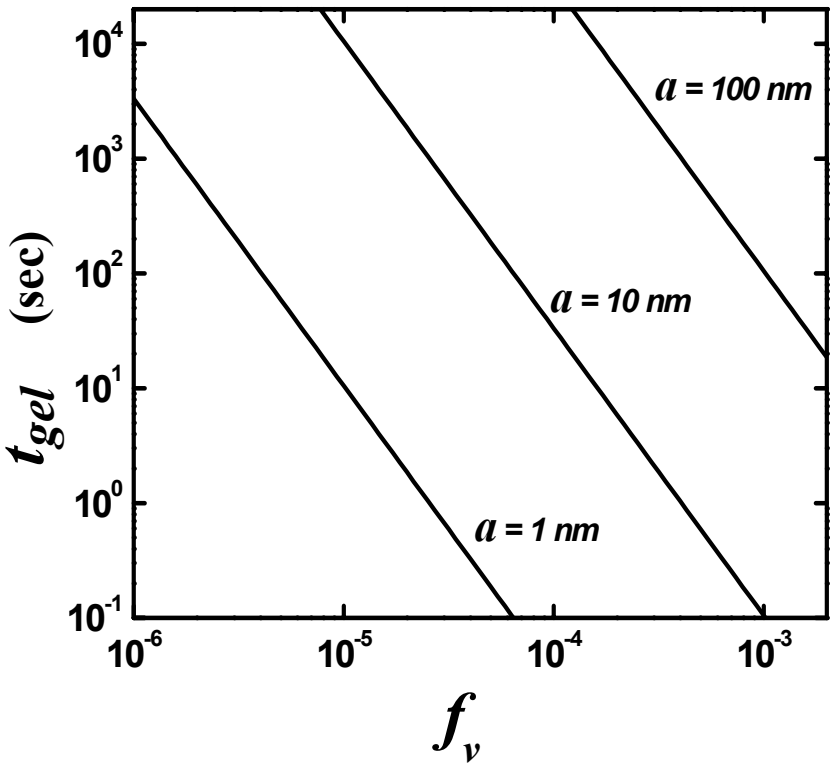

Figure 3.10: Functionalities of the gel time t_{gel}.

3.14. GRAVITATIONAL SETTLING

The particles in an aggregating system continuously settle down due to the gravity if the buoyancy is not matched. The settling behavior depends on the fractal dimension of the clusters. Let us consider a cluster having a mobility radius R_m and N monomers, each of size a and density ρ_p, moving in a medium with density ρ_g and viscosity η. When the gravitational force is balanced by the drag force, the cluster attains the terminal settling velocity v_t. Usually v_t is small and thus the cluster motion is laminar. We can write

$$6\pi\eta R_m v_T = \frac{4}{3}\pi a^3 N(\rho_p - \rho_g)g \tag{3.126}$$

where g is the acceleration due to the gravity. For continuum regime we have $R_m \sim R_g$ (see section 3.5.). Using $N = k_0\left(R_g/a\right)^{D_f}$ (Eq. (3.3)) the terminal settling velocity v_t can then be given as

$$v_T \approx \frac{2a^3(\rho_p - \rho_g)g}{9\eta} k_0 \left(\frac{R_g}{a}\right)^{D_f - 1} . \tag{3.127}$$

Settling removes the heavier (bigger) clusters for the aggregating system. This is the reason why systems with small volume fractions are not gelling. The gel time for such system is much longer than its characteristic settling time. In the absence of settling we expect all aggregating system to gel provided the aggregation is allowed for sufficiently long time.

3.15. TURBULENCE EFFECT ON AGGREGATION

Turbulence creates a relative motion between particles due to shear (*shear aggregation*) or due to unequal particle sizes hence different inertias or velocities (*inertial aggregation*). This enhances the aggregation process especially if the particles are submicron or larger sized but still much smaller than the smaller eddies of the turbulence. In turbulence, energy is transformed from the largest eddy at the beginning of the turbulent field, where the energy is mostly kinetic, to smaller ones at later times. For smallest eddies the motion is random in direction due to the thermal energy gained by the medium molecules during the viscous dissipation of the energy. For higher Reynolds numbers the viscous dissipation occurs at much smaller length scales. The length scale of the smallest eddy is known as the Kolmogorov length scale l_k and can be given in terms of the rate of energy dissipation per unit medium fluid mass $\in$, and the kinematic viscosity of the medium ν as

$$l_k = \left(\nu^3/\in\right)^{1/4} . \tag{3.128}$$

The root mean square velocity gradient in case of an isotropic (independent of direction) turbulence can be characterized by (Friedlander, 2000)

$$\Gamma = \frac{2}{15}\left(\frac{\in}{\nu}\right)^{1/2}. \tag{3.129}$$

Saffman and Turner (Saffman and Turner, 1956) have found the aggregation kernel $K(i,j)$ for turbulent shear aggregation between two coalescing particle with unequal radii R_i and R_j as

$$K(i,j) = 1.3\left(\frac{\in}{\nu}\right)^{1/2}(R_i + R_j)^3. \tag{3.130}$$

Saffman and Turner (Saffman and Turner, 1956) have also found the aggregation kernel $K(i,j)$ for turbulent inertial aggregation assuming the distribution of the relative velocities between the aggregating particles to follow a Gaussian form as

$$K(i,j) = 5.7\left(\frac{\in^3}{\nu}\right)^{1/4}(R_i + R_j)^2\left|\frac{1}{\beta_i} - \frac{1}{\beta_i}\right|. \tag{3.131}$$

In Eq. (3.131) $\beta^{-1} = m_p / f_{dg}$, where m_p is the mass and f_{dg} is the drag coefficient for the particle. β gives the characteristic inertial response time of the particles to the changes in the medium flow.

Since collision process is independent of fractal nature of aggregating clusters, Eqs. (3.131) and (3.132) can also be used for fractal aggregation using radius of gyration as the measure of the cluster size. Comparing the turbulent and diffusion (Brownian or Epstein) kernels we find the aggregation to be much faster for the turbulent kernels due to their higher power dependence on the particle size.

CHAPTER 4- Techniques for Studying Aggregation Processes

4.1. INTRODUCTION

It is very important to understand both the morphology of fractal aggregates and the kinetics of their formation. A number of techniques and different aggregation models have been developed for the study of the aggregation mechanism in past few decades. A direct approach of 2 dimensional (using transmission electron microscope TEM, scanning electron microscope SEM and high magnification light microscope) and 3 dimensional (using confocal microscope) image analyses of a single cluster, to investigate the geometrical structure, have been widely reported in literature. Other *in situ* techniques include small angle static light scattering SASLS, small angle X-ray scattering SAXS, and (ultra) small angle neutron scattering (U)SANS. Photon (light or X-ray) correlation spectroscopy is another technique for the *in situ* measurement of the dynamic structure factor of the aggregating system. These are powerful and sophisticated techniques based on the scattering phenomenon of photon or neutron from the aggregating particles. These techniques, being able to probe and give the measurement instantly without perturbing the aggregating system, have gained more popularity in the scientific community (Beaucage, 1996, Freltoft et al., 1986, Glatter, 1982, Guinier et al., 1955, Schaefer and Keefer, 1986, Schmidt, 1995, Sorensen, 2001).

Experimental techniques, however, have limitations. There are problems associated with the overlapping of monomers in 2-*d* projected images of 3-*d* clusters. Photon and neutron scattering can be used only for particles of certain size range. No important information can be extracted from the scattering pattern for bigger or smaller particles. Besides, in real experiment a large number of factors, e.g., temperature, polydispersity in monomer size and shape, their charging effects, their interaction with the medium fluid molecules, properties of the medium fluid, etc., are in direct involvement in the aggregation process. It is almost impossible to isolate these different factors involved in the real aggregation process. Here comes the importance of

Computer simulations where we can idealize the aggregating system with precise control over every factor. Computer simulations using different aggregation models have contributed significant inputs in understanding the complex process.

In this chapter we discuss the theory behind the techniques we used in the study of the reported work, viz., photon (light) scattering and image analysis techniques.

4.2. PHOTON (LIGHT) SCATTERING

When an electromagnetic wave falls on an object, one may think of the atoms or molecules of that object to absorb and promptly reemit radiations (Bohren and Huffman, 1983, Hulst, 1981, Kerker, 1969). The reemission of radiation can be at the same or different wavelength. Scattering with no change in wavelength is called *elastic scattering* and otherwise called *inelastic scattering* (Jackson, 1998). For the scattering technique we describe here, no or negligible change in the wavelengths (elastic or quasi-elastic scattering) is assumed. The superposition of the reemitted electromagnetic waves by all the atoms or molecules of the object forms a distinct scattered intensity pattern (Hecht, 2002). It is possible to extract information on the geometry of the scatterer (size and dimension) from its scattering pattern. From the behavior of evolving scattering pattern we can obtain information on the kinetics of an aggregating system as well.

The scattering behavior of any object is also dependent on the polarization state of the incident radiation. The light sources for laboratory scattering studies are usually polarized along vertical direction. The detectors are designed to detect far field scattered intensity on a horizontal line perpendicular to both the incident beam and its polarization direction (for 1-*d* detector), or on a vertical plane perpendicular to the incident beam (for 2-*d* detector). We thus limit our discussion to only scattering of a polarized incident radiation. Fig. 4.1 shows the geometry of a typical scattering system. A vertically polarized beam (along X-axis) with wave vector $\vec{k}_i$ incidents from negative Z-axis on a scatterer at position $\vec{r}$. Scattering occurs and one of the scattered ray with wave vector $\vec{k}_s$ travels along a direction (θ, $\phi = \pi/2$) as shown in the figure. In laboratory, the scattered intensity measurements are generally confined on or close to the scattering plane (YZ-plane) where ϕ is equal or very close to $\pi/2$.

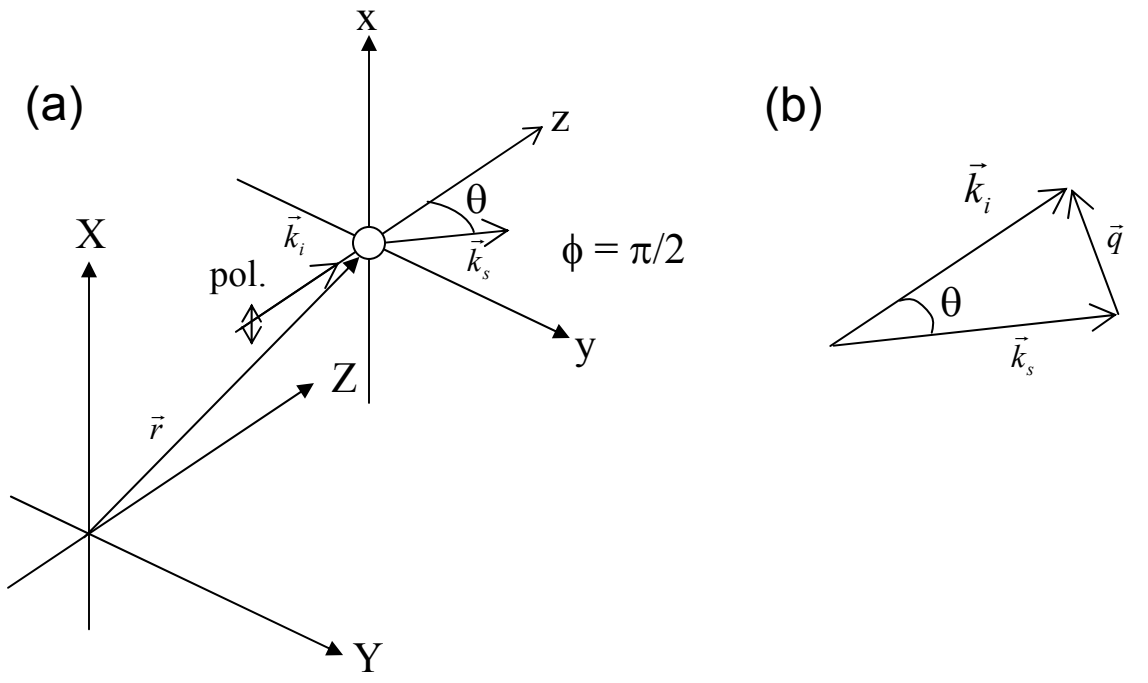

Figure 4.1: A typical electromagnetic wave scattering geometry. (a) A vertically polarized beam (along X-axis) falls on a scatterer at postion $\vec{r}$. The scattering plane is the horizontal plane (YZ-plane). (b) The scattering wave vector $\vec{q}$ for a scatter wave on the scattering plane.

For elastic scattering we have

$$\left|\vec{k}_i\right| = \left|\vec{k}_s\right| = k = 2\pi / \lambda \tag{4.1}$$

where λ is the wavelength of the radiation. The magnitude of the *scattering wave vector* $\vec{q}$ (Fig. 4.1(b)), which is the difference between the incident and the scattered wave vectors ($\vec{q} = \vec{k}_i - \vec{k}_s$), then becomes

$$q = \frac{4\pi}{\lambda}\sin\left(\frac{\theta}{2}\right). \tag{4.2}$$

In scattering experiments, the parameter q is very important because its inverse q^{-1} has a dimension of length and hence represents the probe length (Sorensen, 2001). We can see definite scattering patterns emerging when the intensity scattered from a particle of radius R is plotted in logarithmic scales versus qR rather than the scattering angle θ (Sorensen and Fischbach, 2000).

The next important parameter for scattering of radiation is the dimensionless ratio of the scatterer length scale and the incident wavelength λ. If a be the radius of a spherical scatterer we may define the size parameter as

$$ka = \frac{2\pi}{\lambda} a \,. \tag{4.3}$$

4.2.1. SCATTERING THEORIES

Depending on the relative size of a spherical particle compare to the incident wavelength (size parameter ka), different theories have been developed to explain the scattering patterns. We will describe Rayleigh, Rayleigh-Debye-Gans, and Mie scattering theories in the following subsections subsequently.

4.2.1.1. Rayleigh Scattering

The scattering of electromagnetic radiation can be explained by *Rayleigh scattering theory* when the size parameter $ka << 1$, i.e., the scatter is much smaller than the wavelength λ. The scatterer being very small, all subvolumes of the scatterer reradiate in phase. This results in the scattering amplitude to become proportional to the scatterer's volume, and hence the detector detects scattered intensity going as the square of the scatterer's volume. Light scattering by gas molecules is an example of Rayleigh scattering since gas molecules are far smaller than any wavelength in the light spectrum.

The differential scattering cross section $d\sigma_{scat}/d\Omega$, which is the power scattered per unit solid angle Ω per unit incident intensity I_0, for Rayleigh scattering on the scattering plane is given by

$$\frac{d\sigma_{scat}}{d\Omega} = k^4 a^6 F(m) \tag{4.4}$$

where m is the relative refractive index of the material of the scatterer and

$$F(m) = \left| \frac{m^2 - 1}{m^2 + 2} \right|^2 . \tag{4.5}$$

The intensity scattered per unit solid angle ($I_{scat} = I_0 \, d\sigma_{scat} / d\Omega$) will then be

$$I_{scat} = I_0 k^4 a^6 F(m) . \tag{4.6}$$

The angular independence of I_{scat} in Eq. (4.6) indicates isotropic Rayleigh scattering in all direction on the scattering plane. The k^4 factor in Eq. (4.6) shows a strong dependence in the wavelength λ; smaller wavelengths being scattered a lot more. This briefly explains why sky has blue color in day time.

Let us consider a case when there is a uniform distribution of n scatterers per unit volume. The total scattered intensity per unit solid angle I_{scat} will then be

$$I_{scat} \propto n a^6 = n a^3 a^3 \propto n V_{scat} V_{scat} . \tag{4.7}$$

Here V_{scat} is the volume of the scatterer. Mass conservation will require nV_{scat} to be constant. Hence we find

$$I_{scat} \propto V_{scat} . \tag{4.8}$$

Eq. (4.8) shows that the scattered intensity for a system of scatterers is proportional to the volume of each scatterer. If this system is an aggregating system the scattered intensity will increase linearly with the increasing volume of each scatterer. This effect is known as the *Tyndall effect*.

The total scattering cross section σ_{scat} is obtained by integrating Eq. (4.4) over whole solid angle. One must include the factor $sin^2\phi$ in Eq. (4.4) to account for the differential scattering cross section at points other than those on the scattering plane. After integration we obtain

$$\sigma_{scat} = \frac{8\pi}{3} k^4 a^6 F(m). \tag{4.9}$$

Besides scattering, particles also absorb a part of the incident radiation if the refractive index has an imaginary part. The absorption cross section of a Rayleigh particle is given as

$$\sigma_{absp} = -4\pi k a^3 E(m) \tag{4.10}$$

where $E(m)$ is the imaginary part of $\left[(m^2-1)/(m^2+2)\right]$, i.e.,

$$E(m) = \mathrm{Im}\left(\frac{m^2-1}{m^2+2}\right). \tag{4.11}$$

Real m makes $E(m) = 0$, hence no absorption occurs.

4.2.1.2. Rayleigh-Debye-Gans (RDG) Scattering

Rayleigh-Debye-Gans (RDG) scattering theory describes the scattering of radiation by any particle when the phase shift of the incident wave across the particle is almost the same as the phase shift incurred across the particle diameter distance through the medium. The difference in these phase shifts, which is denoted by ρ and known as the *phase shift parameter*, should thus be such that

$$\rho = 2ka|m-1| < 1. \tag{4.12}$$

For arbitrary sized scatterer Eq. (4.12) will be satisfied on the condition

$$|m-1| << 1. \tag{4.13}$$

Hence tiny refractive index and phase shift parameter are the required conditions for RDG scattering for an arbitrarily sized scatterer.

The RDG approximation considers a scattering system as a set of independent, non-interacting Rayleigh scattering elements (Bohren and Huffman, 1983, Kerker, 1969). In RDG

limit all scatterers, whether inside the sphere or on its surface, are assume to experience the same incident field. This means there is no internal (within a single scattering cluster) multiple scattering. All scatterers throughout the volume of the scattering particle actively participate in non-zero angle scattering.

The differential scattering cross section for a RDG particle $(d\sigma_{scat}/d\Omega)_{RDG}$ in terms of that for Rayleigh particle $(d\sigma_{scat}/d\Omega)_{Ray}$ can be given as

$$\left(\frac{d\sigma_{scat}}{d\Omega}\right)_{RDG} = \left(\frac{d\sigma_{scat}}{d\Omega}\right)_{Ray}\left[\frac{9}{(qa)^6}\{\sin(qa) - qa\cos(qa)\}^2\right]. \tag{4.14}$$

Eq. (4.14) indicates that RDG scattering converges to Rayleigh scattering in the limit $qa \to 0$ (See appendix A). The scattered intensity normalized by forward scattering intensity $I(q)/I(0)$ can be derived from Eq. (4.14) as

$$\frac{I(q)}{I(0)} = \frac{9}{(qa)^6}\left[\sin(qa) - qa\cos(qa)\right]^2. \tag{4.15}$$

The scattered intensity at small scattering angles, where $qa \to 0$, can be given by the Rayleigh scattering intensity. The scattering intensity hence remains constant over this small forward scattering angular range which is know as *Rayleigh regime*. At larger angles Eq. (4.15) indicates a power law decrease in the envelope bounding the scattering intensity curve. The plot of Eq. (4.15) in logarithmic scales (Fig. 4.2) illustrates these features. The envelope of the normalized intensity curve remains constant (unity) as long as $qa < 1$ and becomes $9(qa)^{-4}$ when $qa > 1$. The regime where the scattered intensity follows $(qa)^{-4}$ law is called *Porod regime* (Guinier et al., 1955, Porod, 1951).

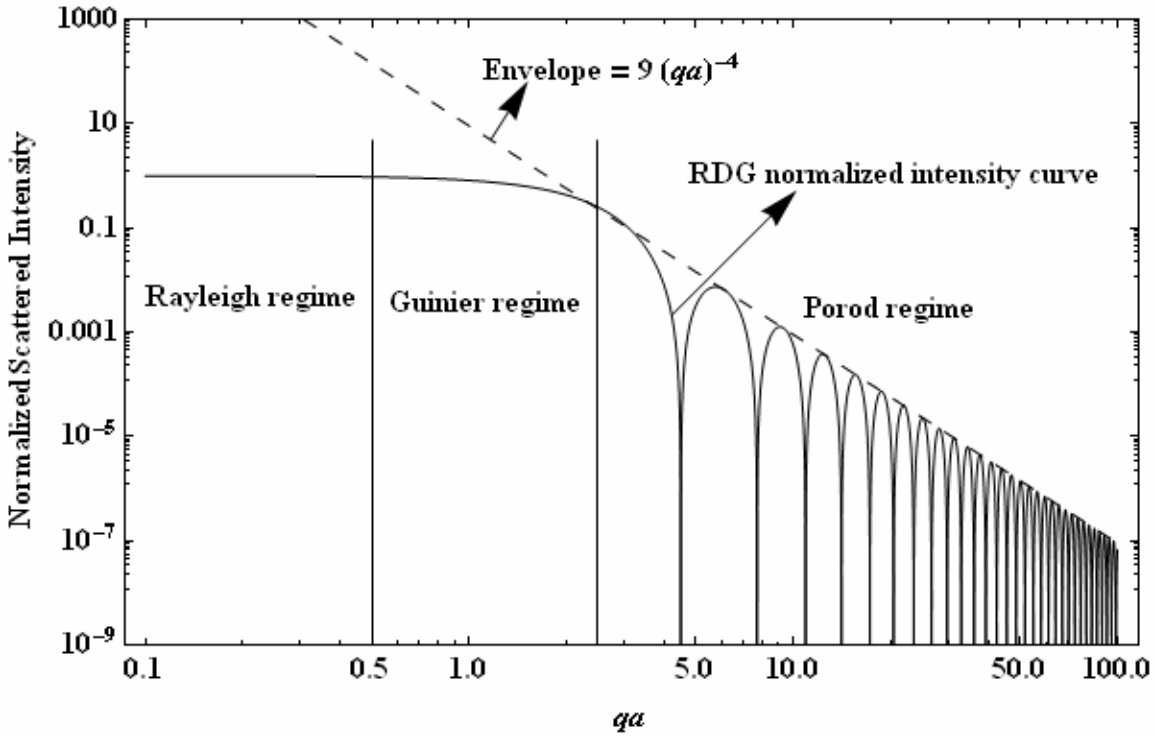

Figure 4.2: Rayleigh-Debye-Gans scattering. Straight lines separating different scattering regimes shown in this figure are in exaggeration. In reality there are no distinct boundaries between the different regimes.

4.2.1.3. Mie Scattering

Both Rayleigh and RDG scattering theory cannot explain the scattering from a particle with a finite arbitrary size and refractive index. Scattering from such particles can, however, be understood by direct solving of Maxwell's equations which is a quite complex task. In 1908 Gustav Mie published a complete analytical solution of Maxwell's equations for the scattering of a plane electromagnetic radiation by a homogeneous particle with the simplest spherical geometry (Born and Wolf, 1999) made up of optically linear dielectric material.

The Mie solution represents a general scattering solution in the sense that it simplifies to Rayleigh scattering in the limit of the size parameter $ka \to 0$, and to RDG scattering in the limit of the size parameter $\rho \to 0$. Hence we can consider both Rayleigh and RDG scattering as the special cases for the *Mie scattering*.

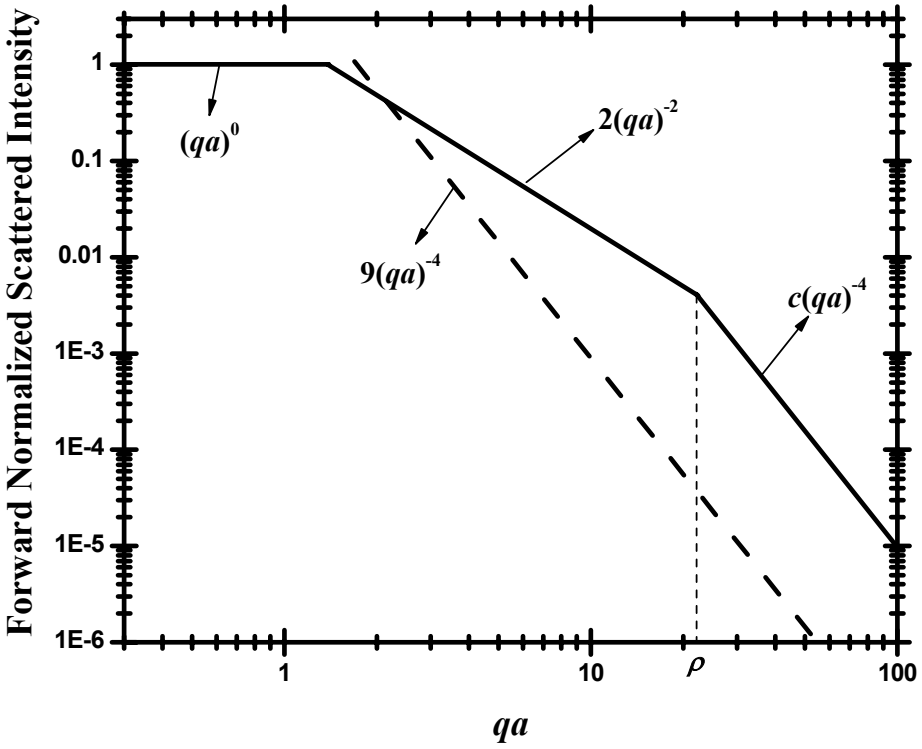

Figure 4.3: The envelopes of the Mie scattered intensity distribution normalized by the forward scattered intensity. The crossovers between three regimes $(qa)^0$, $(qa)^{-2}$ and $(qa)^{-4}$ (Rayleigh, intermediate and Porod regimes) are shown. In the limit $\rho \to 0$ Mie scattering reduces to RDG scattering.

The Mie solutions are quite complex involving sums over associated Legendre polynomials with coefficients that involve Ricatti-Bessel and Hankel functions. Consequently physical interpretation of Mie solutions is obscured by their mathematical complexities. Despite these complexities Sorensen and co-workers (Berg et al., 2005, Sorensen and Fischbach, 2000, Sorensen and Shi, 2000, Sorensen and Shi, 2002) have given easy physical interpretations by plotting the scattered intensity versus the scattering wave vector, rather than the scattering angle. They observed universal features and gave straight forward description of the angular dependence of the Mie scattering. Considering only the envelope of the scattering curve and

ignoring the glory, they found three power law regimes in Mie scattering. For scattering intensity normalized by forward scattered intensity, these three regimes are such that

$$I(q)/I(0) = (qa)^0 \qquad \text{for} \quad qa < 1 \tag{4.16a}$$

$$I(q)/I(0) \sim 2(qa)^{-2} \qquad \text{for} \quad 1 < qa < \rho \tag{4.16b}$$

$$I(q)/I(0) = c(qa)^{-4} \qquad \text{for} \quad qa > \rho \tag{4.16c}$$

where the coefficient c in Eq. (4.16c) is such that $c > 9$. The crossover from $(qa)^{-2}$ to $(qa)^{-4}$ regime (intermediate to Porod regime) has been empirically found to occur at $qa = \rho$. The RDG limit is revealed from the Mie scattering curve as $\rho \to 0$ with the intermediate $(qa)^{-2}$ regime vanishing and the coefficient c approaching 9. Fig. 4.3 illustrates all these features. Berg et al. (Berg et al., 2005) also plotted the Mie scattering intensity from an arbitrarily sized sphere normalized by the Rayleigh scattering from the same sphere and found that the normalized forward intensity decreases as ρ^{-2} as ρ increases above unity.

4.2.2. SCALING DESCRIPTION OF THE SCATTERING OF A WAVE

Now we describe the scaling approach of the scattering from an arbitrary system of scatterers as given by Sorensen (Sorensen, 2001). This scaling approach has its basis on the comparison between the scattering length scale given by q^{-1}, and the various length scales in the scattering system such as the scatterer size. This scaling approach can also be extended to neutron scattering because of the neutron's dual (particle and wave) nature. Single scattering is assumed, which is a good assumption for light scattering from a low density system so that the effective refractive index is low, e.g. fractal aggregates. For X-ray and neutron scattering a low refractive index is usually prevalent. The scaling approach not only simplifies the interpretation of the scattering data and understanding of the scattering process but also unifies many possible experimental systems such as dense sphere, fractal aggregates of spherical monomers, and ensembles of aggregates in a scattering volume, under the same concept of a 'Scattering System'.

Consider a system of N point scatterers in d dimensional space; the i^{th} scatterer being at the position $\vec{r}_i$. The scattering intensity as a function of q can be given as

$$I(q) \propto \left| \sum_{i=1}^{N} \exp\left(i\vec{q}.\vec{r}_i\right) \right|^2 = \sum_{i=1}^{N}\sum_{j=1}^{N} \exp\left\{i\vec{q}.(\vec{r}_i - \vec{r}_j)\right\}. \tag{4.17}$$

The length scale q^{-1} measures the extent the scatterers within which scatter in phase (constructive interference). The scattering from these N scatterers will be in close phase in the case of all N scatterers lying within a separation of q^{-1} of each other, i.e., $q.(\vec{r}_i - \vec{r}_j) < 1$ for all i and j. The total scattered amplitude will then be proportional to N making total scattered intensity proportional to N^2. On the other hand if $q.(\vec{r}_i - \vec{r}_j) > 1$ for any i and j, then the scattering from the N scatterers will be at random phase rendering the total scattered amplitude to be proportional to $\sqrt{N}$ and the total scattered intensity to be proportional to N.

Scattering of a wave occurs at all directions because of the fluctuations in the density of the scatterers. No contribution to the scattering will occur at non-zero scattering angles from the part of the scatterer for which there is no density fluctuation. This is a consequence of *Ewald-Oseen extinction theorem* (Hecht, 2002). With this in mind, let our system of N scatterers be uniformly arranged (uniform density) in a spherical region of radius R with $2a$ as the nearest neighbor separation. We assume every scatterer experiences the same incident field, whether inside the sphere or on its surface. Let ρ be the phase shift parameter for this sphere. Because of Ewald-Oseen extinction, the interior of the sphere does not contribute to the scattering in non-zero angles. We greatly simplify our analysis by assuming the field inside the sphere as localized to the surface layer with depth l as shown in Fig. 4.4. We call this layer as the *active region*. We expect l to decrease with increase in the phase shift parameter ρ. Sorensen and Fischbach (Sorensen and Fischbach, 2000) have empirically found the relationship between l and ρ as $l \sim R/\rho$.

Now we envision the sphere to be covered throughout its volume by imaginary spheres of radius q^{-1} as shown in Fig. 4.4. We refer such imaginary spheres as *q-regions*. If there be n_q *q-*

regions active in the scattering process, and each q-region contain N_q scatterers, the total scattering from the sphere then becomes

$$I(q) \propto n_q N_q^2 . \tag{4.18}$$

This is because the scatterers in separate q-regions scatter randomly while all N_q scatterers in each q-region scatter in phase since $q.(\vec{r}_i - \vec{r}_j) \leq 1$ for all i and j within that q-region. Here we really mean only the envelope of the scattered intensity curve when we say intensity.

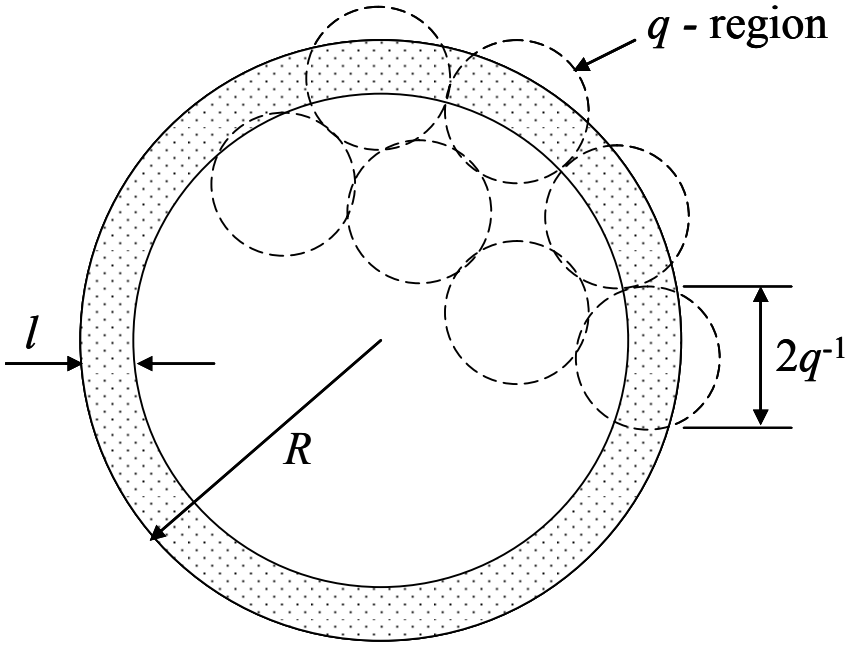

Figure 4.4: A sphere of radius R containing N point scatterers uniformly distributed with $2a$ as the nearest neighbor separation. Only the skin layer of thickness l gets illuminated by the incident wave. Thickness l decreases with increase in the phase shift parameter ρ. The dotted circles are q-regions. Only scatterers in one single q-region scatter in phase; scattering from different ones being random.

We now evaluate the scattered intensity $I(q)$ in terms of the scattering wave vector q, sphere radius R, and the total number of scatterers N at different sizes of q-region as followings.

Case I: $q^{-1} > R$ or $q < R^{-1}$

In this case we find $n_q = 1$ and $N_q \propto N$. Eq. (4.18) then yields

$$I(q) \propto N^2 . \tag{4.19}$$

Eq. (4.19) means the scattered intensity remains constant for $q < R^{-1}$.

Case II: $R > q^{-1} > l$ or $R^{-1} < q < l^{-1}$

In this case the number of q-regions active in the scattering process is equal to the number of q-regions required to cover the surface of the sphere of radius R. Thus we have

$$n_q = R^{D_s} / (q^{-1})^{D_s} = (qR)^{D_s} \tag{4.20}$$

where D_s is the surface dimension.

Next, the number of scatterer in each q-region N_q is roughly equal to the product of the scatterer number density in the sphere, the cross sectional area of the q-region and the depth of the active region, i.e.,

$$N_q \propto \left(N / R^{D_m}\right)\left(q^{-1}\right)^{D_s} l \propto N\, q^{-D_s} R^{-D_m} . \tag{4.21}$$

Here D_m is the mass dimension.

Now using Eqs. (4.20) and (4.21) in Eq. (4.18) we find the total scatting intensity as

$$I(q) \propto N^2 q^{-D_s} R^{-2D_m + D_s} \propto N^2 \left(qR\right)^{-D_s} . \tag{4.22}$$

If the phase shift parameter $\rho \to 0$ then $l \to \infty$. This makes the whole volume of the sphere the active region. Hence N_q in such case will be the product of the scatterer number density in the sphere and the volume of the q-region as

$$N_q = \left(N/R^{D_m}\right)\left(q^{-1}\right)^{D_m} = N(qR)^{-D_m} \tag{4.23}$$

and the total scattering intensity will become

$$I(q) \propto N^2 (qR)^{-2D_m + D_s} . \tag{4.24}$$

Case III: $l > q^{-1} > a$ or $l^{-1} < q < a^{-1}$

The number of q-regions actively involved in the scattering process in this case is also equal to the number of q-regions required to cover the surface of the sphere of radius R in consideration. Thus n_q is again given by Eq. (4.20). However, since every q-region on the surface is within the active region, the number of scatterer in each q-region N_q becomes equal to the product of the scatterer number density in the sphere and the volume of the q-region. Hence N_q can be given by Eq. (4.23). The total scattering intensity for this case will then the same as that given by Eq. (4.24).

Case IV: $q^{-1} < a$ or $q > a^{-1}$

In this case each q-region will contain only one point scatterer. This means all the scatterers in the sphere reradiate in random phases. Only the point scatterers on the surface of the sphere contribute to the scattering. Hence the total scattering intensity is given by

$$I(q) \propto N_s \tag{4.25}$$

where N_s is the number of point scatterers on the surface.

Below we summarize all four cases described above.

$$I(q) \propto \begin{cases} N^2 & \text{when} \quad q < R^{-1} \\ N^2 (qR)^{-D_s} & \text{when} \quad R^{-1} < q < l^{-1} \\ N^2 (qR)^{-2D_m + D_s} & \text{when} \quad l^{-1} < q < a^{-1} \\ N_s & \text{when} \quad q > a^{-1} \end{cases} . \tag{4.26}$$

Fig. 4.5 graphically illustrate Eq. (4.26). Here the scattered intensity $I(q)$ is plotted against the scattering wave vector q in double logarithmic scales. The intensity is constant until $q < R^{-1}$.

Beyond $q = R^{-1}$, the scattered intensity decreases monotonically with a slope of $-D_s$ until $q < l^{-1}$. Afterwards the intensity falls with a slope of $-(2D_m\text{-}D_s)$ as long as $q < a^{-1}$. The region where the intensity falls with $-D_s$ slope becomes narrower and narrower as the phase shift parameter ρ becomes smaller and smaller. This region finally vanishes when $\rho \to 0$. The reason being the illumination of the entire volume of the sphere from the incident wave since $l \to \infty$ as $\rho \to 0$.

Eq. (4.26) is more general. Let us consider a specific example when the spatial dimension $d = 3$. Then we have the mass dimension $D_m = 3$ and the surface dimension $D_s = 2$. Eq. (4.26) then reduces to

$$I(q) \propto \begin{cases} N^2 & \text{when} \quad q < R^{-1} \\ N^2 (qR)^{-2} & \text{when} \quad R^{-1} < q < l^{-1} \\ N^2 (qR)^{-4} & \text{when} \quad l^{-1} < q < a^{-1} \\ N_s & \text{when} \quad q > a^{-1} \end{cases} . \tag{4.27}$$

We find Eq. (4.27) to describe Mie scattering pattern discussed in section 4.2.1.3. We have initial Rayleigh regime $(qR)^0$ until $q < R^{-1}$ followed by the intermediate regime $(qR)^{-2}$ for $R^{-1} < q < l^{-1}$. Porod regime follows next for $l^{-1} < q < a^{-1}$. This intermediate regime vanishes when $\rho \to 0$ revealing RDG scattering. In real experimental situations points scatterers are atoms or molecules behaving as dipoles. Experimental q (using light, X-ray or neutron) has limitations. Even q can approach atomic or molecular separation, the scattered intensity will be immeasurably small. Hence $q > a^{-1}$ region is experimentally non-accessible.

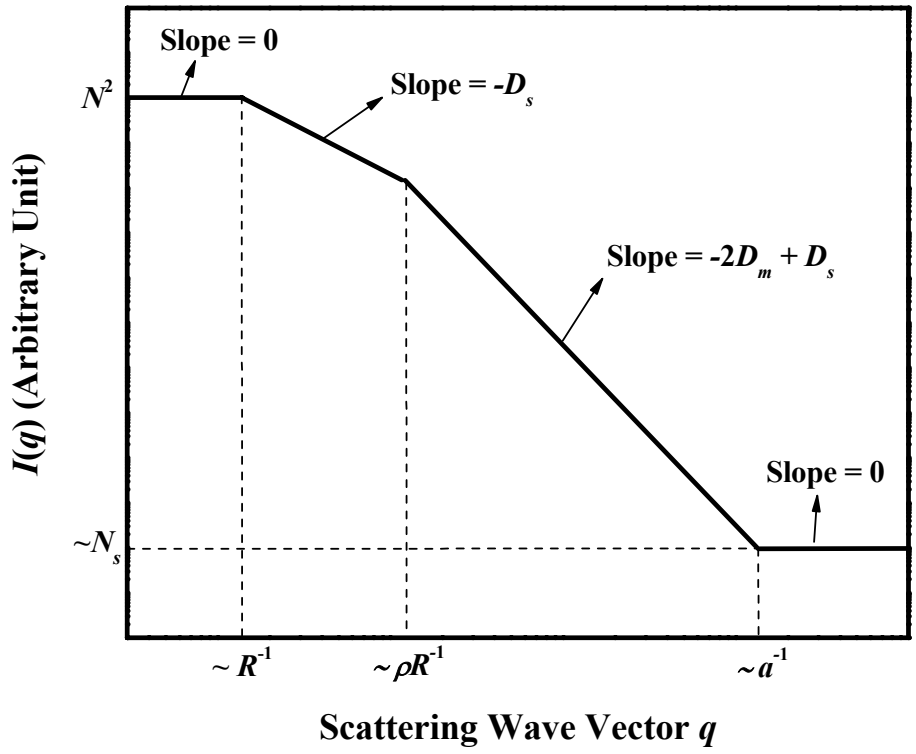

Figure 4.5: Log-log plot of $I(q)$ versus q. The region where the intensity falls with $-D_s$ slope becomes narrower and narrower and finally vanishes as the phase shift parameter $\rho \to 0$. For the mass dimension $D_m = 3$ and the surface dimension $D_s = 2$, this plot becomes identical to the Mie scattering plot.

4.2.2.1. Scattering from Fractal Aggregates

We can extend above scaling description of scattering to explain the scattering from fractal aggregates as well. A fractal aggregate with radius of gyration R_g is composed of N monomers such that $N = k_0 \left(R_g / a \right)^{D_f}$ (Eq. (3.3)). These monomers are typically few tens of nanometers in size and thus are Rayleigh scatterers of optical and other longer wavelengths. We can consider the monomers as dipoles or point scatterers at length scales larger than the monomer size.

When the fractal dimension D_f is less than 2, all monomers are essentially on the surface and hence all of them are active scatterers. The phase shift parameter $\rho \approx 2kR_g f_v |m-1|$, where f_v is the monomer volume fraction in the aggregate and m is the relative refractive index of a monomer, decreases and finally becomes less than unity with increasing R_g. This is RDG limit where all scatterers throughout the volume of the scattering particle actively participate in non-zero angle scattering. When the fractal dimension D_f is greater than 2, the fractal aggregate becomes dense making the phase shift parameter $\rho >> 1$. The scattering in such case occurs only from the monomers in a thin layer with thickness R_g / ρ at the surface of the aggregate. However, mass D_m and surface D_s fractal dimensions are equal for both DLCA and percolating clusters in all spatial dimensions (Strenski and Kirkpatrick, 1991), and are simply called the fractal dimension D_f . The scaling argument hence yield the total scattered intensity for a fractal aggregate as

$$I(q) \propto \begin{cases} N^2 & \text{when} \quad q < R_g^{-1} \\ N^2 \left(qR_g\right)^{-D_f} & \text{when} \quad R_g^{-1} < q < a^{-1} \end{cases} . \tag{4.28}$$

Here we use the radius of gyration R_g as the radius of the scattering system because it gives the best representation of the size of fractal aggregates with ill defined boundaries. The radius of gyration is a good choice also because it comes naturally in the mathematical derivation of the structure factor for a scatterer which we present in next section.

In Eq. (4.28) if q increases beyond a^{-1}, monomers will start scattering in random phases. Now the point scatterers are the atoms or molecules of the monomers. The scattering intensity then behaves like Mie or RDG scattering depending on the phase shift parameter for the monomer.

Besides not be able to provide details on the interference ripples in the scattered intensity the scaling approach has other limitation as well. It is unable to give the details of the crossover from one scattering regime to another. However, it can describe the general features of wave scattering from a variety of system and helps one in developing physical intuition for scattering process.

4.2.3. THE STRUCTURE FACTOR

The *structure factor* is an extremely useful tool in interpreting the pattern in light, X-ray or neutron scattering experiments. The structure factor gives a mathematical description of the structure of an object or a system, i.e., how the fundamental units (e.g., atoms or molecules in crystals and monomers in fractal aggregates) are arranged in a system. The interference ripples in scattering patterns reflects the structure of the fundamental units in the scattering system. This directly relates the structure factor to the scattering pattern. The knowledge of the structure factor is thus very important for anyone who does scattering research.

Let us consider a system with N fundamental units. Since we are relating the structure factor with the scattering pattern, we will term these fundamental units as scatterers. These scatterers scatter wave in phase or out of phase as been described in section 4.2.2. The mathematical definition of the structure factor for this system is then given in terms of the scattering wave vector $\vec{q}$ as

$$S(\vec{q}) = N^{-2}\left|\sum_{i=1}^{N} e^{i\vec{q}.\vec{r}_i}\right|^2 . \tag{4.29}$$

This q-space description of the structure factor comes from the fact that it is both the absolute square of the Fourier transform of the *density function* (number of scatterers per unit volume) and the Fourier transform of the *density autocorrelation function* of the system, which we will show next.

The density function $n(\vec{r})$ of the scattering system can be given in terms of the Dirac delta function $\delta(\vec{r} - \vec{r}_i)$ as

$$n(\vec{r}) = \frac{1}{N}\sum_{i=1}^{N} \delta(\vec{r} - \vec{r}_i) \tag{4.30}$$

where $\vec{r}_i$ is the position vector of the i^{th} scatterer. This expression allows us to write

$$\sum_{i=1}^{N} e^{i\vec{q}.\vec{r}_i} = N\int_{-\infty}^{\infty} e^{i\vec{q}.\vec{r}}\, n(\vec{r})d\vec{r} . \tag{4.31}$$

Now we use Eq. (4.31) back in Eq. (4.29) to get the structure factor as the absolute square of the Fourier transform of the density function as

$$S(\vec{q}) = \left| \int_{-\infty}^{\infty} e^{i\vec{q}.\vec{r}}\, n(\vec{r})\, d\vec{r} \right|^2 . \tag{4.32}$$

The r.h.s. of Eq. (4.32) is the power spectrum and hence equal to the Fourier transform of the autocorrelation function of $n(\vec{r})$. The l.h.s. of this equation, which is the structure factor $S(\vec{q})$, is thus equal to the Fourier transform of the autocorrelation function of the density function $n(\vec{r})$. If we denote this autocorrelation function by $g(\vec{r})$ we can write

$$S(\vec{q}) = \int_{-\infty}^{\infty} e^{i\vec{q}.\vec{r}}\, g(\vec{r})\, d\vec{r} . \tag{4.33}$$

From its definition the autocorrelation function $g(\vec{r})$ of $n(\vec{r})$ is

$$g(\vec{r}) = \int_{-\infty}^{\infty} n(\vec{r}'-\vec{r})\, n^*(\vec{r}')\, d\vec{r}' . \tag{4.34}$$

Here * sign denotes complex conjugate. However, our system is real and isotropic. This allows us to restate Eq. (4.34) as

$$g(r) = \int_{-\infty}^{\infty} n(\vec{r}-\vec{r}')\, n(\vec{r}')\, d\vec{r}' . \tag{4.35}$$

The isotropic nature of the system also makes $S(\vec{q}) = S(q)$ besides making $g(\vec{r}) = g(r)$. Hence Eq. (4.33) becomes,

$$S(q) = \int_{-\infty}^{\infty} e^{i\vec{q}.\vec{r}}\, g(r)\, d\vec{r} . \tag{4.36}$$

Solid angle integration can be done (see appendix B) in Eq. (4.37) assuming $\vec{q}$ direction as the Z-axis to yield

$$S(q) = 4\pi \int_{-\infty}^{\infty} g(r) \frac{\sin(qr)}{qr} r^2 dr \,. \tag{4.37}$$

We now use Eq. (4.37) to investigate both small and large q behaviors of the structure factor.

4.2.3.1. Small q Behavior

We define q to be small when the product $qR_g < 1$. In such case we can approximate the Taylor expansion of sin (qr) as

$$\sin(x) \approx x - \frac{x^3}{3!} \,. \tag{4.38}$$

Use of this expansion in Eq. (4.37) yields

$$\begin{aligned} S(q) &\approx 4\pi \int_{-\infty}^{\infty} r^2 g(r) dr - 4\pi \int_{-\infty}^{\infty} g(r) \frac{(qr)^2}{6} r^2 dr \\ &= 4\pi \int_{-\infty}^{\infty} r^2 g(r) dr - \frac{q^2}{3} 2\pi \int_{-\infty}^{\infty} r^4 g(r) dr \end{aligned} \,. \tag{4.39}$$

The first term on r.h.s. of Eq. (4.39) is unity since $g(r)$ is normalized (see appendix C). Also the radius of gyration R_g can be given in terms of the autocorrelation function g(r) as (appendix D)

$$R_g^2 = 2\pi \int_{-\infty}^{\infty} r^4 g(r) dr \,. \tag{4.40}$$

Eq. (4.39) thus takes the form

$$S(q) \approx 1 - \frac{1}{3}(qR_g)^2 \,. \tag{4.41}$$

Eq. (4.41) is known as the *Guinier equation* (Guinier et al., 1955, Teixeira, 1986). This equation is extremely useful since it directly relates the system size with its structure factor through only the scattering wave vector.

4.2.3.2. Large q Behavior

We call q to be large when $qR_g > 1$. Unlike in the case of the small q limit, the knowledge of density autocorrelation function $g(r)$ should be explicit to study the large q behavior of the structure factor. The functional forms for $g(r)$ are different for fractals and compact objects. This results in different behavior of the structure factor at large q for these two kinds of object. Here we present discussion on the structure factor of fractals as these are of more interest to us.

The general form for the density autocorrelation function of a fractal aggregate can be given by (Teixeira, 1986)

$$g(r) = Ar^{D_f - d} h(r/\xi)\,. \tag{4.42}$$

Here A is the normalization constant and d is the spatial dimension. Also $h(r/\xi)$ is a cutoff function with a characteristic length $\xi \sim R_g$. It describes how the power law of $g(r)$, i.e. $r^{D_f - d}$ is cut off by decreasing faster than $r^{D_f - d}$ as r approaches R_g. Such a cutoff function appearing in the structure factor of a compact object, e.g. a solid sphere, behaves like a step function. However, for fractal aggregates the cutoff function should be a fast but not an abrupt function.

4.2.3.2.1. The Best Cutoff Function for Fractal Aggregates

A number of cutoff functions have been proposed in literature. The exponential cutoff is one among some most used ones. Freltoft et al. (Freltoft et al., 1986), Berry and Percival (Berry and Percival, 1986), and Teixeira (Teixeira, 1986) used this cutoff function to calculate $S(q)$ for fractal aggregates. This cutoff function is given by

$$h(r/\xi) = e^{-r/\xi} \tag{4.43a}$$

where

$$\xi^2 = \frac{2R_g^2}{D_f(D_f + 1)}\,. \tag{4.43b}$$

Mountain and Mulholland (Mountain and Mulholland, 1988) numerically calculated the following cutoff function from simulated DLCA clusters.

$$h(r/R_g) = e^{-c(r/\xi)^{2.5}} . \tag{4.44}$$

This cutoff function is close to a Gaussian type.

Hurd and Flower (Hurd and Flower, 1988) proposed a cutoff derived from the overlap volume of the fractal aerosol aggregates as

$$\begin{aligned} h(r/\xi) &= \left(\frac{4}{3}\pi\xi^2\right)\left(1+\frac{r}{4\xi}\right)\left(1-\frac{r}{2\xi}\right)^2 \qquad \text{for} \quad r < 2\xi \\ &= 0 \qquad\qquad\qquad\qquad\qquad\qquad\qquad\quad \text{for} \quad r > 2\xi \end{aligned} \tag{4.45a}$$

where

$$\xi^2 = \frac{(D_f+2)(D_f+5)}{2D_f(D_f+1)} R_g^2 . \tag{4.45b}$$

Likewise Nelson (Nelson, 1989) proposed a Gaussian cutoff function as a better representation of the autocorrelation function for fractal aggregates. This cutoff function is given by

$$h(r/R_g) = e^{-(r/\xi)^2} \tag{4.46a}$$

where

$$\xi^2 = \frac{4R_g^2}{D_f} . \tag{4.46b}$$

Sorensen et al. (Sorensen et al., 1992) later compared all proposed cutoff functions and structure factors considering light scattering data from soot fractal aggregates in flames. They found that structure factor derived from the autocorrelation function with Gaussian cutoff gave the best fits to the experimental data when the aggregate polydispersity effect was included. They argue that real aggregating systems are always polydisperse and thus fitting of the

experimental data with the single cluster structure factor, which yields exponential cutoff function as the best fit, does not make any sense.

4.2.3.3. Structure Factor from The Scattered Intensity

Let us consider a system with an isotropic distribution of N point scatterers actively scattering a wave. We assume that every scatterer in the system experiences the same incident field. The total scattered intensity from this system can then be given by Eq. (4.17). From this equation we can see the scattered intensity normalized by forward scattering $I(q = 0)$ is

$$\frac{I(q)}{I(0)} = N^{-2}\left|\sum_{i=1}^{N}\exp\left(i\vec{q}.\vec{r}_i\right)\right|^2 . \tag{4.47}$$

Also the structure factor for this system can be given by Eq. (4.29). Comparing Eqs. (4.17), (4.29) and (4.47) we find

$$S(q) = \frac{I(q)}{I(0)} \propto N^{-2}\, I(q) . \tag{4.48}$$

Here we have assumed $S(\vec{q}) = S(q)$ in Eq. (4.29) for our isotropic system. The structure factor inferred from the scattered intensity is sometimes termed as *the optical structure factor*.

Eq. (4.48) is true only when all the scatterers in the system are uniformly illuminated by the incident wave, i.e., there is no diminishing of the incident field at any part of the system. In case of diminishing field in the interior part of the system, $I(q)$ in Eq. (4.48) is only surface scattering. $S(q)$ on the r.h.s. of the equation then give the surface structure of the scattering system. The total number of the scatterers N in Eq. (4.48) must also be replace by N_s the total number of scatters on the surface only.

Eq. (4.48) allows us to relate the structure factor with the scaling description of the scattered intensity. Following Eqs. (4.26), we can write

$$S(q) = \begin{cases} 1 & \text{when} \quad q < R_c^{-1} \\ C\left(qR_c\right)^{-2D_m + D_s} & \text{when} \quad R_c^{-1} < q < a^{-1} \end{cases} . \tag{4.49}$$

Here R_c is a characteristic size of the scattering system and C is a proportionality constant which depends on the explicit form of the density autocorrelation form. Also a is the spacing between the point scatterers in the system.

4.2.3.3.1. Structure Factor for a Single and an Ensemble of Fractal Aggregates

For a single fractal aggregate with the radius of gyration R_g, the structure factor at different q-regimes can be given according to Eqs. (4.41) and (4.49) as

$$S(q) = 1, \qquad qR_g << 1 \qquad \text{(Rayleigh regime)} \tag{4.50a}$$

$$S(q) \approx 1 - \frac{1}{3}\left(qR_g\right)^2, \qquad qR_g \leq 1 \qquad \text{(Guinier regime)} \tag{4.50b}$$

$$S(q) = C\left(qR_g\right)^{-D_f}, \qquad qR_g >> 1 \text{ and } qa << 1 \qquad \text{(Power law regime).} \tag{4.50c}$$

Here C is a proportionality constant whose value is found to be close to unity for variety of structure factors including the one with Gaussian cutoff proposed for DLCA and RLCA clusters (Sorensen and Wang, 1999, Sorensen, 2001).

Eqs. (4.50) assume the RDG approximation which considers a scatterer as a set of independent, non-interacting Rayleigh scattering elements. The fractal dimension and also the radius of gyration R_g of a fractal aggregate can directly be read off from the log-log plot of the aggregate structure factor (proportional to the scattered intensity) versus the scattering wave vector q. The beauty about using the optical structure factor is that it is independent of the refractive index of the scatterer and hence D_f and R_g (and hence the kinetic exponent z or the aggregation kernel homogeneity λ) are immune to the uncertainty in the refractive index.

In experimental situations one always encounters the case where there is an ensemble of different-sized aggregates since a finite width cluster size distribution is always a consequence of an aggregation process. This polydispersity causes the shape of the observed structure factor to be different than that of the structure factor of any single cluster in the distribution (Nicolai et al., 1994, Sorensen and Wang, 1999).

The effective structure factor for an ensemble of polydisperse, RDG aggregates can be written as

$$S_{eff}(q) = \frac{\int N^2 n(N) S[q, R_g(N)] dN}{\int N^2 n(N) dN} \tag{4.51}$$

where $n(N)$ is the size distribution, i.e., the number of clusters per unit volume with N monomers per cluster, and $S[q,R_g(N)]$ is the structure factor for an aggregate of size $R_g(N)$. Use of Eqs. (4.50a), (4.50b) and (4.50c) in Eq. (4.51) yields

$$S_{eff}(q) \approx 1, \qquad qR_{gz} << 1 \quad \text{(Rayleigh regime)} \tag{4.52a}$$

$$S_{eff}(q) \approx 1 - \frac{1}{3} q^2 R_{gz}^2, \qquad qR_{gz} \leq 1 \quad \text{(Guinier regime)} \tag{4.52b}$$

$$S_{eff}(q) = CC_p \left(qR_{gz}\right)^{-D_f}, \qquad qR_{gz} >> 1 \quad \text{(Power law regime).} \tag{4.52c}$$

In Eqs. (4.52) R_{gz} is the so-called *z-average radius of gyration* which represents the size averaged over the distribution weighted by the light scattering cross section hence the square of the cluster mass. The z-average radius of gyration R_{gz} can be obtained when one makes use of Eqs. (3.3), (3.86) and (3.89) while deriving Eq. (4.52b) (see appendix E) as

$$R_{gz}^2 = a^2 k_0^{-2/D_f} \frac{M_{2+2/D_f}}{M_2} = a^2 k_0^{-2/D_f} s_2^{2/D_f} \frac{m_{2+2/D_f}}{m_2}. \tag{4.53}$$

Here a is the monomer radius, k_0 is the prefactor in the power law for the number of monomers in a cluster, M_i is the i^{th} moment of the cluster size distribution, s_2 is the mean cluster size derived from the second moment of the cluster size distribution and m_i is the i^{th} moment of the scaling distribution as discussed in chapter 3.

One can notice in Eq. (4.52c) that the coefficient of the power law is modified by the polydispersity factor C_p of the ensemble. Using Eqs. (3.3), (3.86), (3.89) and (4.53) while deriving Eq. (4.52c) (see appendix E) one can find that

$$C_p = \frac{M_1}{M_2}\left(\frac{M_{2+2/D_f}}{M_2}\right)^{D_f/2} = \frac{m_1}{m_2}\left(\frac{m_{2+2/D_f}}{m_2}\right)^{D_f/2} . \tag{4.54}$$

One needs to be careful here to see the difference between the z-average radius of gyration R_{gz} and the radius of gyration R_{g2} of the average cluster size $\langle N \rangle = s_2$. It follows from the power law for the number of monomers in a cluster (Eq. (3.3)) that the mean sized cluster radius of gyration is

$$R_{g2} = a\ k_0^{-1/D_f} s_2^{1/D_f} . \tag{4.55}$$

Eqs (4.53) and (4.55) can be combined to relate R_{gz} and R_{g2} as

$$R_{gz}^2 = R_{g2}^2 \left(\frac{m_{2+2/D_f}}{m_2}\right). \tag{4.56}$$

Further from Eq. (3.93) we have $m_2 = m_1$ for the choice of $p = 2$ (2nd moment of the cluster size distribution) and conservation of mass requires $m_1 = 1$. Hence we find

$$R_{gz}^2 = m_{2+2/D_f} R_{g2}^2 \ . \tag{4.57}$$

4.2.4. ABSOLUTE SCATTERING BY FRACTAL AGGREGATES

Under the approximation of RDG scattering, i.e., no significant intracluster multiple scattering, the differential scattering cross section for an aggregate with N monomers can be given in terms of that for a single monomer as (Sorensen, 2001, Sorensen, 2003)

$$\frac{d\sigma_{scat}^{agg}}{d\Omega} = N^2 \frac{d\sigma_{scat}^{mon}}{d\Omega} S(q) . \tag{4.58}$$

Here the superscript *agg* and *mon* are to distinguish aggregate and monomer differential scattering cross sections respectively. $S(q)$ is the structure factor for the aggregate.

Integration of Eq. (4.58) over all solid angle gives the total scattering cross section for an aggregate. This integration has been approximated by Dobbins and Megaridis (Dobbins and Megaridis, 1991) to give the total scattering cross section as

$$\sigma_{scat}^{agg} = N^2 \sigma_{scat}^{mon} G\left(kR_g\right) \tag{4.59}$$

where

$$G\left(kR_g\right) = \left(1 + \frac{4}{3D_f} k^2 R_g^2\right)^{-D_f/2} . \tag{4.60}$$

This approximation for the total scattering cross section best describes the clusters with $D_f < 2$ among others found in the literature (Sorensen, 2001).

Likewise the total absorption cross section for an aggregate can be related to the absorption cross section for a single monomer as

$$\sigma_{absp}^{agg} = N \sigma_{absp}^{mon} . \tag{4.61}$$

We now use Eq. (4.58) to find the relation for absolute scattered intensity from a system of fractal aggregates. Let I_0 be the incident intensity. The scattered intensity $I(q)$ by a single cluster is then given by

$$I(q) = c_0 I_0 \frac{d\sigma_{scat}^{agg}}{d\Omega} = c_0 I_0 N^2 \frac{d\sigma_{scat}^{mon}}{d\Omega} S(q) \tag{4.62}$$

where c_0 is a constant which depend on the distance and the solid angle subtended by the detector.

Using Eq. (4.4) for the differential scattering cross section for a monomer, Eq. (4.62) becomes

$$I(q) = c_0 I_0 N^2 k^4 a^6 F(m) S(q) . \tag{4.63}$$

Eq. (4.63) gives the scattered intensity by a single cluster. If the scattering system is an ensemble of clusters with a size distribution of $n(N)$, the scattered intensity $I(q)$ is given by

$$I(q) = c_0 I_0 k^4 a^6 F(m) \int_0^\infty N^2 n(N) S(q) dN . \tag{4.64}$$

The constant c_0 in Eq. (4.64) also accounts for the scattering volume. Also the factor $F(m)$ is a function of the monomer relative refractive index given by Eq. (4.5). In terms of the effective structure factor $S_{eff}(q)$ (Eq. (4.51)) and the second moment of the size distribution M_2, Eq. (4.64) can be rewritten as

$$I(q) = c_0 I_0 k^4 a^6 F(m) M_2 S_{eff}(q) . \tag{4.65}$$

In case of a polydisperse system Eq. (4.65) becomes

$$I(q) = c_0 I_0 k^4 a^6 F(m) M_2 \qquad \text{for} \quad qR_{gz} << 1 \tag{4.66a}$$

and

$$I(q) = c_0 I_0 k^4 a^6 F(m) C M_1 k_0 (qa)^{-D_f} \qquad \text{for} \quad qR_{gz} >> 1. \tag{4.66b}$$

Here we have used Eq. (4.52a) to get Eq. (4.66a), and Eqs. (4.52c), (4.53) and (4.54) to derive Eq. (4.66b).

For a monodisperse system for which the cluster number density is n, we have

$$M_2 = \int_0^\infty N^2 n(N) dN = nN^2 . \tag{4.67}$$

Hence for a monodisperse system Eq. (4.65) becomes

$$I(q) = c_0 I_0 k^4 a^6 F(m) n N^2 \qquad \text{for} \quad qR_g << 1 \tag{4.68a}$$

and

$$I(q) = c_0 I_0 k^4 a^6 F(m) nNCk_0 (qa)^{-D_f} \qquad \text{for} \quad qR_z >> 1. \tag{4.68b}$$

Here we have also used Eq. (4.50a) to get Eq. (4.68a), and Eqs. (4.50c) and (3.3) to obtain Eq. (4.68b).

4.2.5. PHOTON CORRELATION SPECTROSCOPY (DYNAMIC LIGHT SCATTERING)

So far we have discussed only the angular distribution of scattered wave at a given instant of time. This is equivalent to the case of scattering by a static (time independent) system. Thus the study of spatial scattered intensity pattern at given instants of time is often known as *static light scattering study*. However, the dynamic properties of the system, e.g. Brownian dynamics, also cause the temporal variation in the scattered intensity. After the invention of coherent light source like the laser, the technique has been developed for studying the dynamic properties of a system based on the analysis of the autocorrelation of the scattered intensity with time at a given scattering angle or a given wave vector q. This technique is called *photon correlation spectroscopy* (PCS) also commonly known as *dynamic light scattering* if the scattered wave is of optical frequency (Berne and Pecora, 2000). This method is also sometimes called *quasi-elastic light scattering* (QELS) since the scattered wave usually has a very small change in frequency compared to the incident frequency (Finsy, 1994).

Let us consider the scattering at an angle θ corresponding to the scattering wave vector q. Also let the field at time t be $\vec{E}(t)$. Following the discussion given in above sections we can say that the scattered field $\vec{E}(t+\Delta t)$ will be at random phase compare to $\vec{E}(t)$, if the scatterer moves a distance comparable to or greater than q^{-1} by the time $t+\Delta t$. Rearrangement of the scatterers will result in the field fluctuation. Temporal correlations found in these fluctuations give us information on the particle (scatterer) dynamics.

The field correlation function $g^{(1)}(\tau)$ for a diffusing particle is

$$g^{(1)}(\tau) = \frac{\left\langle \vec{E}^{*}(t) \cdot \vec{E}(t+\tau) \right\rangle}{\left\langle E^{2}(t) \right\rangle} \tag{4.69}$$

where <…> means a time or equivalently, for ergodic medium, an ensemble average. Here τ is the correlation time. The scattered field $\vec{E}(t)$ is such that

$$\vec{E}(t) = \vec{E}_0 e^{i\vec{q}.\vec{r}(t)}. \tag{4.70}$$

Here $\vec{r}(t)$ is the position vector of the scatterer at time *t*. Eq. (4.69) thus reduces to

$$g^{(1)}(\tau) = \left\langle \exp\left[i\vec{q}.\{\vec{r}(t+\tau) - \vec{r}(t)\} \right] \right\rangle = \left\langle e^{i\vec{q}\cdot\Delta\vec{r}(\tau)} \right\rangle. \tag{4.71}$$

For Brownian dynamics, the motion of the scatterers with the diffusion constant *D* can be described by the Gaussian probability distribution $P\left(\Delta\vec{r}(\tau), \tau\right)$ as

$$P\left(\Delta\vec{r}(\tau), \tau\right) \propto \exp\left\{ -\frac{\Delta r^{2}(\tau)}{4D\tau} \right\}. \tag{4.72}$$

We use Eq. (4.72) to evaluate Eq. (4.71) as following.

$$\begin{aligned} g^{(1)}(\tau) &= \int_{-\infty}^{\infty} \exp\left\{ -\frac{\Delta r^{2}(\tau)}{4D\tau} \right\} e^{i\vec{q}\cdot\Delta\vec{r}(\tau)} d\left(\Delta\vec{r}(\tau)\right) \\ &= \exp\left\{ -q^{2} D\tau \right\} \end{aligned}. \tag{4.73}$$

In experiments we cannot measure field strength $\vec{E}(t)$. Instead we measure the intensity *I*(*t*). We now find the intensity correlation function $g^{(2)}(\tau)$ in terms of the field correlation $g^{(1)}(\tau)$. The intensity correlation function $g^{(2)}(\tau)$ is given by

$$g^{(2)}(\tau) = \frac{\left\langle I(t) I(t+\tau) \right\rangle}{\left\langle I(t) \right\rangle^{2}}. \tag{4.74}$$

If the scattered intensity is measured for a long enough period of $t = 2T$, then

$$\langle I(\mathrm{t})I(t+\tau)\rangle = \underset{T\to\infty}{Lim}\frac{1}{2T}\int_{-T}^{T} I(t)I(t+\tau)dt \tag{4.75}$$

and

$$\langle I(t)\rangle = \underset{T\to\infty}{Lim}\frac{1}{2T}\int_{-T}^{T} I(t)dt\,. \tag{4.76}$$

For homodyne detection, i.e., no scattering from static structure is reaching the detector, $g^{(2)}(\tau)$ can be presented in terms of $g^{(1)}(\tau)$ by the Siegart relation as (Schatzel, 1993)

$$g^{(2)}(\tau) = 1 + \left|g^{(1)}(\tau)\right|^2. \tag{4.77}$$

For a Brownian scatterer Eq. (4.73) can be used in Eq. (4.77) to get

$$g^{(2)}(\tau) = 1 + \exp\left(-\tau/\tau_c\right) \tag{4.78}$$

where $\tau_c = \left(2q^2D\right)^{-1}$ is the characteristic correlation time for the particle with the diffusion coefficient D. At a given q, long characteristic time indicates slow diffusion rate and vice versa. Physically, larger scatterers have longer characteristic time.

Eq. (4.78) is good for a single scatterer or a system of monodisperse scatterer. However, real system is usually characterized by polydispersity in size (and shape) of the scatterers. Hence PCS provides an intensity weighted average decay rate instead of a pure decay rate. The homodyne intensity correlation function for a polydisperse scattering system can thus be given as

$$g^{(2)}(\tau) = 1 + \sum_i c_i \exp\left(-\tau/\tau_{ci}\right) \tag{4.79}$$

where $\tau_{ci} = \left(2q^2D_i\right)^{-1}$ is the characteristic correlation time for the i^{th} particle in the scattering volume. The coefficient c_i is the amplitude of the decay rate for the i^{th} particle such that

$$\sum_i c_i = 1\,. \tag{4.80}$$

Eq. (4.79) (also Eq. (4.77)) represents an ideal case of perfect scattering and detection, which practically hardly can be achieved. Hence we modify Eq. (4.79) by introducing two instrumental factors *A* and *B* as

$$g^{(2)}(\tau) = A + B\sum_i c_i \exp\left(-\tau/\tau_{ci}\right). \tag{4.81}$$

Here *A* and *B* are such that *A* is always greater than *B*. These factors represent signal noise and spatial incoherency in the scattered field at the detector.

If the scattering system is monodisperse the plot of $\ln[\{g^{(2)}(\tau) - A\}/B]$ versus correlation time τ yields a constant slope of τ_c^{-1}. However, for polydisperse scattering system, this plot is no longer a straight line. The degree of non-linearity of the plot gives a measure of the polydispersity of the scattering system. The summation appearing in Eq. (4.81) is approximated with a cumulant fit to simplify the fitting of the experimentally measured correlation function (Koppel, 1972). This cumulant fit is given as

$$g^{(2)}(\tau) \approx A + B\exp\left(-\mu_1\tau + \frac{\mu_2}{2}\tau^2\right) \tag{4.82}$$

where μ_n is the n^{th} cumulant given by

$$\mu_n = \lim_{t\to 0}(-1)^n \frac{d^n}{dt^n}\ln\left[g^{(2)}(\tau) - A\right]. \tag{4.83}$$

Eq. (4.83) gives

$$\mu_1 = \sum_i c_i\left(1/\tau_{ci}\right) \tag{4.84}$$

and

$$\mu_2 = \sum_i c_i\left(1/\tau_{ci}\right)^2 - \left\{\sum_i c_i\left(1/\tau_{ci}\right)\right\}^2. \tag{4.85}$$

The second cumulant μ_2 gives a measure of the polydispersity of the system. Eq. (4.84) also infers that the first cumulant is the average inverse characteristic correlation time $\overline{\tau_c^{-1}}$ for the polydisperse system. If $\overline{D}$ be the scattered intensity weighted average diffusion coefficient, we can write

$$\mu_1 = \overline{\tau_c^{-1}} = 2q^2\overline{D} \,. \tag{4.86}$$

In the above discussion we assumed translational diffusion of the scatterers is dominant and thus is the only responsible factor for the effective intensity fluctuation. This assumption is good for spherically symmetric particles. Also when q^{-1} is greater than the hydrodynamic radius of the scattering particles, the rotation dynamics will bring negligible phase shift in the scattered field. Hence the assumption is also good for such case. However, for other cases rotational diffusion does produce a significant contribution in the decay rate of the correlation function. The first cumulant given by Eq. (4.86) gets modified for these cases as

$$\mu_1 = 2(q^2\overline{D} + \overline{D}_R) \tag{4.87}$$

where $\overline{D}_R$ is the mean rotational diffusion coefficient for the system.

We next discuss on the intensity correlation function for heterodyne detection where the signal reaching the detector also has scattering from static structures in the scattering volume. We return back and use our simple model where rotational effect is negligible. Let I_f be the mean scattered intensity from the diffusing scatterer and I_s be the static scattering from the static structure in the scattering volume. Then the total scattering intensity is

$$\langle I(t)\rangle = I_f + I_s \,. \tag{4.88}$$

The intensity correlation function for heterodyne detection can then be given by (Ren, 1992)

$$g^{(2)}(\tau) = 1 + \left(\frac{1}{1+x}\right)^2 \left|g^{(1)}(\tau)\right|^2 + \frac{2x}{(1+x)^2}\left|g^{(1)}(\tau)\right| \tag{4.89}$$

where x is the ratio of I_s and I_f. When $I_s \to 0$, x approaches zero and hence Eq. (4.89) reduces to Eq. (4.77). We can rewrite Eq. (4.89) to include the instrumental factors A and B as

$$g^{(2)}(\tau) = A + B\phi(\tau) \tag{4.90}$$

where

$$\phi(\tau) = \left(\frac{1}{1+x}\right)^2 \left|g^{(1)}(\tau)\right|^2 + \frac{2x}{(1+x)^2}\left|g^{(1)}(\tau)\right|. \tag{4.91}$$

4.3. IMAGE ANALYSIS

The image of fractal clusters from different types of microscopes (TEM, SEM, optical microscope, etc.) under various magnifications can provide information about the morphology of the clusters. Even though image analysis considers only a single or few of the clusters from the ensemble and hence does not give a statistical average, it is still a popular technique of characterizing cluster structure because of its simplicity.

Image analysis technique involves digitizing the two-dimensional projected image of a cluster and then using this digitized image to find the fractal dimension D_f. There are various methods for finding the fractal dimension D_f. We describe two of the methods, the structure factor and perimeter analysis in the following subsections.

4.3.1. STRUCTURE FACTOR METHOD

The picture to be analysed is digitized to a binary format; pixel is dark if there is material and white if there is none. The structure factor $S(q)$ can then be calculated for the digitized picture of the soot clusters using the following formula

$$S(q) = N^{-2}\left|\sum_{i=1}^{N} e^{i\vec{q}\cdot\vec{r}_i}\right|^2 \tag{4.92}$$

which basically is Eq. (4.29) with N as the total number of dark pixel points in the picture and $\vec{r}_i$ as the position vector of the i^{th} dark pixel. A computer program can be written to read the digitized picture to calculate the structure factor $S(q)$.

The calculated structure factor $S(q)$ is then plotted in double logarithmic scale. The slope with which the curve decreases in this plot in the power law regime gives the measure of the fractal dimension D_f of the pictured cluster (see section 4.2.3.3.1.). Also, Guinier analysis of the plot will give the radius of gyration R_g of the cluster.

4.3.2. PERIMETER ANALYSIS

The perimeter analysis method for finding the fractal dimension D_f of a three-dimensional fractal aggregate involves quantitative perimeter fractal dimension D_p analysis of the two-dimensional projection of a fractal aggregate. D_p describes the number $N(L)$ of square meshes of size L, each of which includes at least one pixel of the fractal aggregate perimeter when the digitized picture of the fractal aggregate is viewed under a grid. $N(L)$ and L are related to D_p as

$$N(L) = cL^{-D_p} \tag{4.93}$$

where c is a constant of proportionality. The slope of a doubly logarithmic regression of $N(L)$ against L is D_p.

Jullien and coworkers (Jullien et al., 1994) found from computer simulations that, in the asymptotic limit of very large aggregates, the perimeter fractal dimension D_p is well defined and varies continuously with the mass fractal dimension of the three-dimensional aggregate. They proposed the following approximate formulae to account for this variation.

$$D_p \approx 1 + (3 - D_f)^{\frac{3}{2}} \qquad D_f \geq 2 \tag{4.94a}$$

$$D_p \approx D_f \qquad D_f < 2\,. \tag{4.94b}$$

When a three-dimensional cluster is projected on a two-dimensional surface, the information on the depth of the cluster is usually lost. However, the cluster fractal dimension D_f

is preserved in the projection provided $D_f < 2$. Even in the case of $D_f > 2$ we can still investigate the morphology of the cluster by the help of the perimeter fractal dimension D_p using Eqs. (4.94). Perimeter analysis method works for clusters with any fractal dimension, i.e. D_f is either greater than or less than two.

CHAPTER 5- Experimental Study of Cluster Morphology in Dense, Gelling Aerosols

5.1. INTRODUCTION

In an aggregation process solid material comes together to form ramified aggregates with a fractal dimension of less than three (Family and Landau, 1984, Jullien and Botet, 1987, Vicsek, 1989). The growth kinetics of a cluster radius of gyration R_g with time t is characterized by a power-law $R_g \sim t^{z/D_f}$ (Eq. (3.73)), where z is a positive number called the kinetic exponent. With a dimensionality D_f less than the spatial dimension d, the growing aggregates occupy a greater fraction of the available space with time and the system crosses over from cluster dilute to cluster dense. Eventually the system gels filling completely the macroscopic volume (Dhaubhadel et al., 2006, Kim et al., 2006, Sorensen et al., 2003). In chapter 3 we have define "*dilute*" and "*dense*" as when the ratio of the mean cluster nearest neighbor separation R_{nn} to the cluster size R_g is large or small, respectively. The ratio R_{nn}/R_g scales in time as $R_{nn}/R_g \sim t^{-z(d-D_f)/dD_f}$ (Eq. (3.115)). When this ratio approaches two, the neighboring aggregates jam together to form a volume-spanning network.

The available literature from the last two decades showed that Brownian aggregation results in DLCA structures with ~1.8 fractal dimension. However, some previous studies have given an indication of a crossover from the DLCA morphology to another morphology with a larger value of the fractal dimension as the sol evolves from the cluster dilute to the cluster dense, eventually leading to the gelation (Dhaubhadel et al., 2006, Fry et al., 2002, Gimel et al., 1995, Hasmy and Jullien, 1996, Kim et al., 2006, Kolb and Herrmann, 1985, Rottereau et al., 2004, Sorensen et al., 2003). The fractal nature of the gel itself is thought to be described by percolation theory which predicts a fractal dimension of $D_f = 2.55$ for the gel network (Stauffer and Aharony, 1985). A recent large-scale, three dimensional, off-lattice diffusion-limited cluster-cluster computer simulation in our laboratory (Fry et al., 2004) has also shown that near the gel

point the aggregates become so crowded that they percolate to form larger clusters characterized by fractal dimensions ~2.6 at larger length scales and ~1.8 at smaller length scales. We have named such clusters as *superclusters* or *superaggregates*. The crossover in the fractal dimension occurs at a critical or ideal gel point cluster size R_{gel}, which is the average cluster size when R_{nn} / R_g drops to two (Fry et al., 2004).

Gimel et al. (Gimel et al., 1995, Rottereau et al., 2004), from their computer simulation studies, also found that the characteristic of the space filling network of clusters is the same whether it is a result of a dynamic DLCA process or a static percolation process. The sol-gel transition occurs at a well defined time and at a characteristic size determined by the overlap of the clusters, which decreases with increasing starting volume fraction. Other simulation studies on dense systems have found a fractal dimension intermediate between that for DLCA clusters and percolation clusters (Herrmann and Kolb, 1986, Kolb and Herrmann, 1985).

In experiments the key aspects of forming superclusters and finally the gelled structure are smaller monomers and larger volume fraction. The gel time $t_{gel} \sim a^3 / f_v^{3/(3-D_f)}$ (see section 3.13.1.) has strong functionalities with the monomer volume fraction f_v and the monomer size a. With smaller monomers and larger monomer volume fraction the gel time can be made short enough such that the perturbation from other forces like gravitation will have least effect in the aggregation process. The resulting material from the gelation phenomenon, which we call as an *aerosol gel* (see chapter 7), has interesting characteristics such as ultra low density, high specific surface area, etc., as those of conventional aerogels synthesized from a completely different process.

Experimental verification of this hybrid morphology of gelling clusters predicted by theory is limited at best. Simulations suggest a *universal* behavior i.e., this should happen in any particulate system when it becomes dense and gels. Previous experiments by many groups on dense colloids have not seen the $D_f \approx 2.6$ superaggregates, perhaps due to fragmentation, reaction limited kinetics, or gravitational settling due to long gel time. There is, however, some indication of the formation of such superaggreates in a recent colloid experiment (Lattuada et al., 2004).

Aerosols, without significant solvent or hydrodynamic effects, are very clean systems, and one would expect them to be ideal model systems to compare with computer simulations. Soot aggregates in laminar diffusion flames can form a macroscopic gel network in the aerosol phase (Sorensen et al., 1998). Subsequent studies of this flame showed soot clusters with a hybrid morphology having a fractal dimension of $D_f \approx 2.6$ for length scales between approximately 1 and 10 μm and a fractal dimension of $D_f \approx 1.8$ for length scales less than 1 μm down to the monomer size (Kim et al., 2004, Kim et al., 2006, Sorensen et al., 2003). These experimental observations of superaggregates in laminar diffusion flames, although very useful, may still be affected by the complexity of the flames. A diffusion flame is a flowing system with both shear and thermophoretic forces. In addition, the laminar flame front becomes very narrow late in the flame, 100 μm or less. Thus, the mechanism for the formation of these superaggregates is uncertain. To determine the *universality* of the superaggregates one must avoid the complexity of the flame aerosol. This is done in our present work by creating aerosols in chambers and allowing them to aggregate in the three dimensional volume.

In this chapter we present experimental results of a study of aerosol fractal aggregate morphology as the system evolves from cluster dilute to dense. We used an image analysis and a *Small Angle Static Light Scattering* (SASLS) techniques for the study. We also present neutron scattering experimental results from a gelled structure of aerosol nanoparticles. This experiment probed the structure of the gelling network of ca. 38 nm carbon soot particles as a consequence of their Brownian aggregation. We will show that the aggregates start showing a dual morphology with smaller D_f at smaller length scale and larger D_f at larger length scale once f_v becomes high enough.

5.2. CLUSTER IMAGE ANALYSIS STUDY

For image analysis purpose we created carbonaceous soot aerosols by exploding of a mixture of a hydrocarbon and oxygen in a closed cylindrical chamber at atmospheric pressure. The explosion was carried out in either one of two different aluminum cylindrical chambers with different sizes. These chambers were strong enough to withstand the shockwave produced during the detonation of the gas mixture with initially up to one atmospheric pressure. The larger

chamber had a 23.9 cm internal diameter and a 37.1 cm height and hence a volume of 16.6 liters (Fig. 5.1a). The second chamber had a 12.5 cm internal diameter and a 31.5 cm height and hence a volume of 3.9 liters (Fig. 5.1b). Results were chamber independent. Acetylene (C_2H_2), Ethylene (C_2H_4) and Propane (C_3H_8) were used as gaseous hydrocarbon fuels.

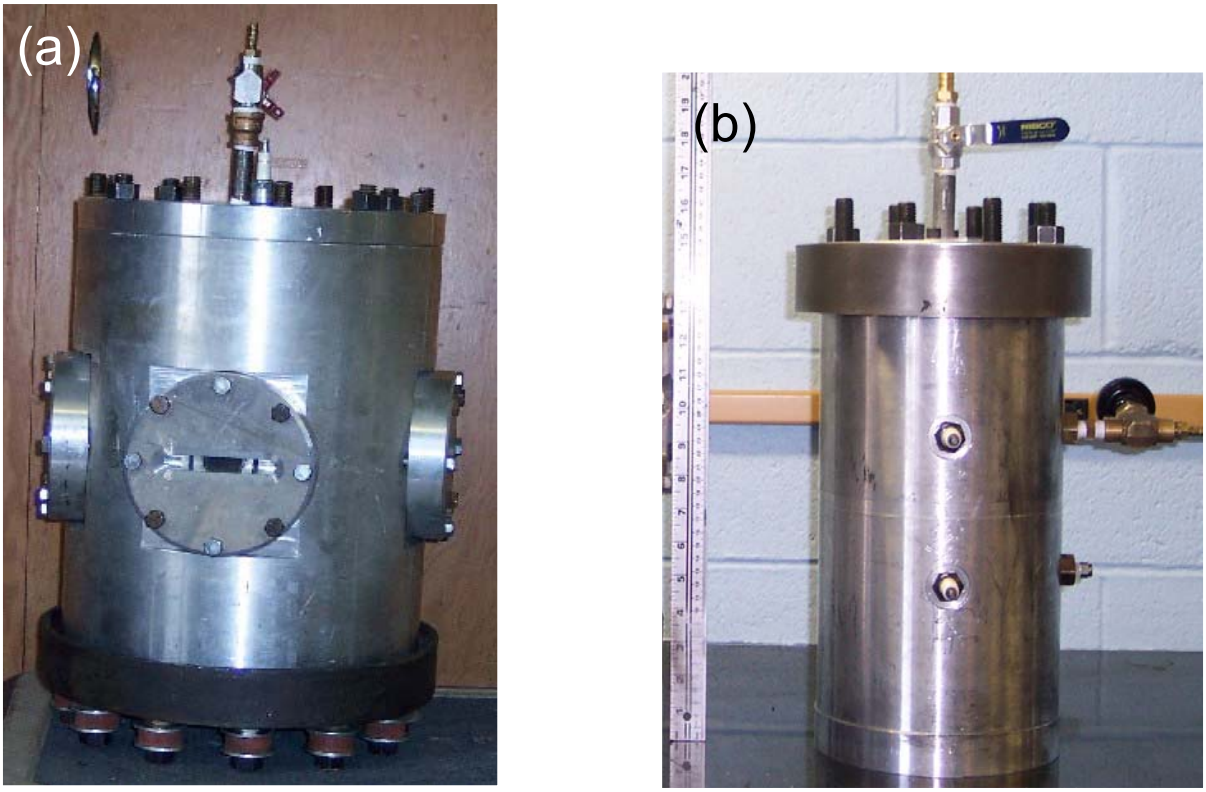

Figure 5.1: (a) 16.6 liter aluminum chamber with a 23.9 cm internal diameter and a 37.1 cm height. (b) 3.9 liter aluminum chamber with a 12.5 cm internal diameter and a 31.5 cm height.

With the hydrocarbon fuels at atmospheric pressure, we could potentially achieve solid carbon volume fractions greater than 10^{-4} (assuming all the hydrocarbon carbon becomes solid carbon). Nanometer sized roughly spherical carbon particles with diameters of ca. 50 nm were produced rapidly during the explosion in a chamber. These particles exhibited Brownian diffusion in the residual gas medium and aggregated over a period of about 15 seconds proceeding from the cluster dilute to cluster dense condition and finally gelled.

After exploding the fuel-oxygen mixture, we waited for several minutes to allow all soot particles to deposit on the inner surface of the chamber. Then the chamber was opened to obtain a dark black fluffy carbon soot layer on the bottom, walls and ceiling of the chamber. This soot layer on the bottom was about 2 cm thick for acetylene and ≤ 3 mm for other hydrocarbon fuels. From a broad perspective this soot is a result of an aerosol gelation process likely involving Brownian motion during the major growth period, then convection and gravitational settling.

5.2.1. AGGREGATE STRUCTURE DETERMINATION METHODS

Carbon soot aggregates were sampled on TEM (transmission electron microscope) grids and light microscope glass slides by inserting them in the chamber through a removable window and holding them horizontally for 30 seconds, 3 to 6 minutes after the explosion. Soot clusters were deposited by gravitational settling on those grids and slides. Two-dimensional projection pictures of the three-dimensional soot were produced by viewing under a TEM and a high-resolution high-magnification light microscope. These pictures were digitized to a binary format (pixel is dark if there is material and white if there is none) and the cluster morphology was determined by two different methods: structure factor and perimeter analysis. These methods have been discussed in section 4.3.

The measured structure factor $S(q)$ was then plotted in double logarithmic scales. The fractal dimension D_f of the analysed cluster slope was measured as the slope with which the curve decreases in the double logarithmic plot. In perimeter analysis we counted the number $N(L)$ of square meshes of size L, each of which includes at least one pixel of the fractal aggregate perimeter when the digitized picture of the fractal aggregate is viewed under a grid. A double logarithmic plot of $N(L)$ versus L was a curve which decreased with a constant slope, equal to the perimeter fractal dimension D_p of the cluster being analysed, with increasing L. We used Jullien and co-workers proposed formulae to extract the cluster mass fractal dimension D_f from the cluster perimeter fractal dimension D_p (Eqs. (4.94)) after confirming their validity by measuring D_p for two-dimensional projections of computer simulated clusters with known fractal dimension.

5.2.2. RESULTS

Two representative examples among the pictures used for the cluster morphology analysis are presented in Figs. 5.2 and 5.3. The structure factor and the perimeter analyses for a picture of the soot on the scale of about 1 μm down to the monomer size (20 nm) are shown in Fig. 5.2. The structure factor analysis measured the fractal dimension as 1.80 while the perimeter analysis gave 1.78, which is consistent. Likewise, Fig. 5.3 gives the structure factor and perimeter analyses for a picture of the soot in the scale from about 1 μm up to the cluster size (50 μm). The fractal dimension is 2.50 according to the structure factor analysis and 2.42 according to the perimeter analysis. Similar results were found with other pictures. The averages over all pictures are $D_f = 1.75 \pm 0.10$ from the monomer size length scale up to 1 μm and $D_f = 2.50 \pm 0.15$ in the cluster size length scale from 1 μm up to 50 μm.

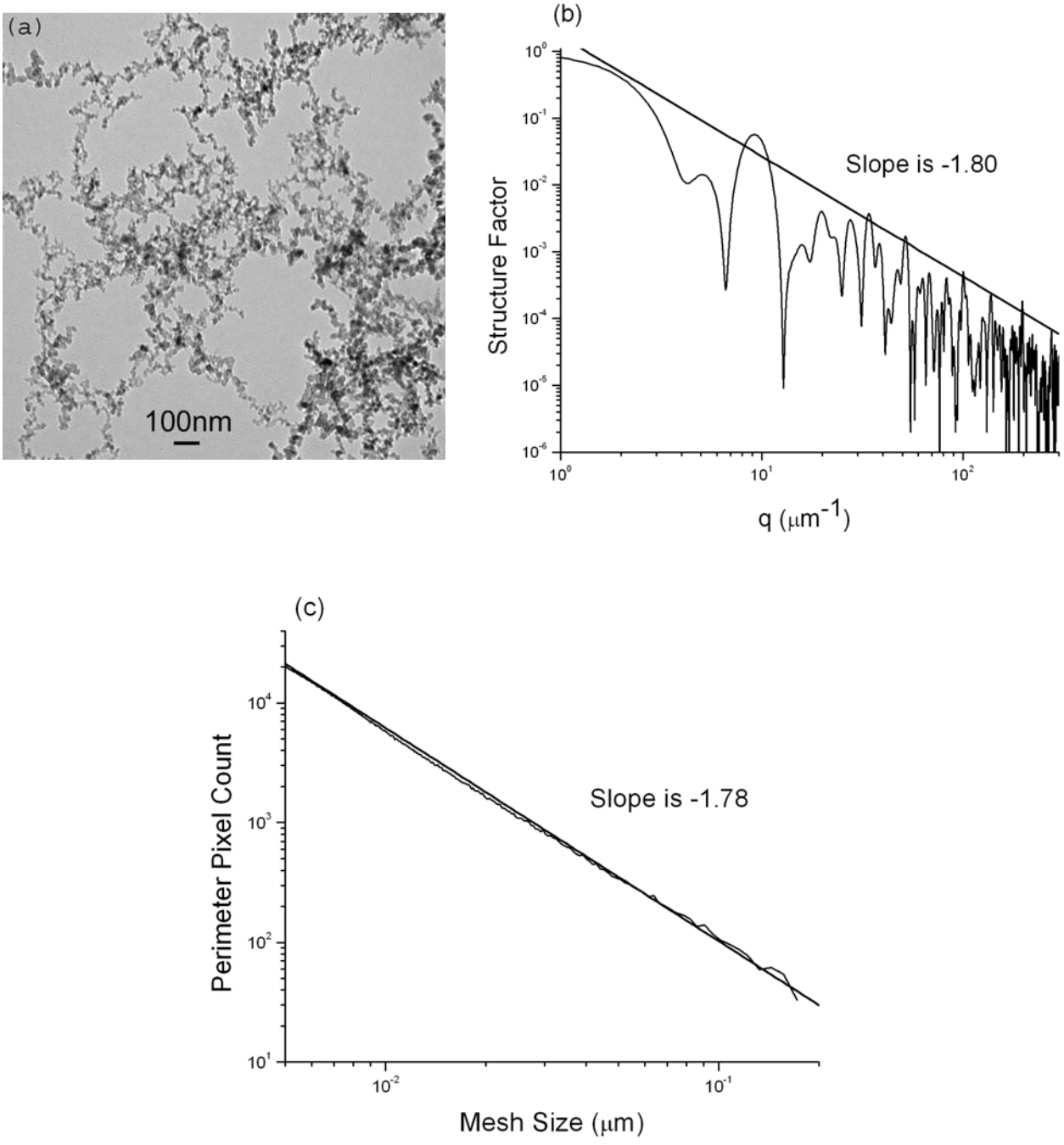

Figure 5.2: (a) TEM picture of soot clusters, note scale bar, (b) structure factor of and (c) perimeter analyses of part (a). The fractal dimension measured is equal to the negative slope of either graph and is found to be ~ 1.80.

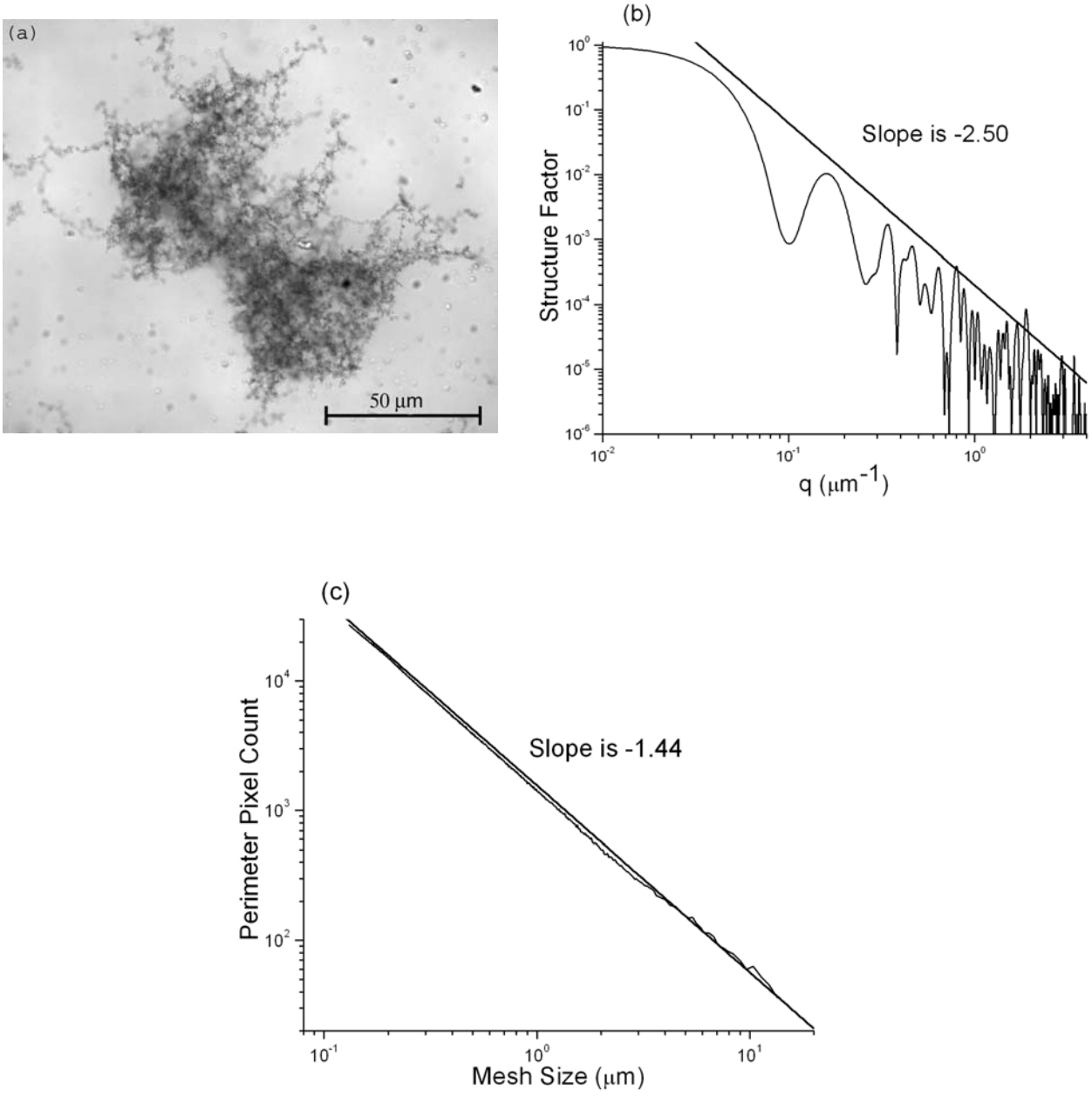

Figure 5.3: (a) TEM picture of a large soot cluster, note scale bar, (b) structure factor of and (c) perimeter analyses of part (a). The fractal dimension is equal to the slope in the structure factor analysis. The perimeter analysis slope yields the perimeter fractal dimension, 1.44. The mass fractal dimension is found via Eqs. (4.94) to be 2.42.

5.2.3. CONCLUSION

In conclusion the cluster morphology of aerosol soot particles was determined from microscopic pictures using both structure factor and the perimeter analyses. The soot clusters were found to have a hybrid morphology characterized by a fractal dimension of 1.75 ± 0.10 over scales from the monomer size of ca. 50 nm up to 1 μm and a fractal dimension of 2.50 ± 0.15 over length scales from ca. 1 μm to 50 μm via both methods of analysis. These results imply that aggregation in the cluster dense regime yields a different morphology than the well known cluster dilute regime. These results also imply universality in superaggregates with hybrid DLCA and percolation morphologies consistent with previous results for gelation in simulations (Fry et al., 2004) and in flames (Kim et al., 2004, Kim et al., 2006, Sorensen et al., 2003).

5.3. LIGHT SCATTERING STUDY

We also used a Small Angle Static Light Scattering (SASLS) technique to study the morphology of the quickly aggregating carbon soot particles rapidly produced during the explosion of a mixture of acetylene and oxygen in an optical chamber. SASLS technique involves measurement of the scattered light intensity $I(q)$ of a vertically polarized laser beam as a function of the scattering wave vector q over a horizontal scattering plane. The measurement of the scattered pattern on the scattering plane against the scattering angle provides the information on the morphology of the scatterer as a function of the length scale.

SASLS is an *in situ* technique providing a powerful tool to probe an aggregating system at length scales of the order of the wavelength of light up to ~100 μm. Further it gives measurements instantly unlike the image analysis technique. The light scattering technique can provide ensemble average cluster size and fractal dimension and also can characterize the kinetics of aggregation.

5.3.1. EXPERIMENTAL SETUP

For SASLS study the carbon nanoparticles were created instantaneously by an explosive detonation of acetylene gas and oxygen mixture inside a closed, cylindrical disk combustion

chamber with circular glass windows on both ends of the cylinder. We discuss on the optical chamber we used and our SASLS setup in following separate subsections.

5.3.1.1. The Optical Chamber

Carbonaceous soot aerosols were created by exploding a mixture (2:1 molar ratio) of acetylene (C_2H_2) and oxygen filled in a closed, aluminium cylindrical disk combustion chamber with circular glass windows on both ends of the cylinder, Fig. 5.4. As shown in Fig. 5.5a this chamber consisted of a 10 mm thick central ring sandwiched between two glass windows 29 mm thick each. Two outer flanges supported the glass windows. The pieces were held together using 6 sets of nuts and bolts. An o-ring in the o-ring groove on each side of the central ring made the central sandwich air-tight. The central ring was also attached with a spark plug and a valve for gas inlet and outlet. The internal space of the chamber, entirely viewable through the glass windows, was 51mm diameter wide and 10mm thick (Fig. 5.5b). The monomer volume fraction f_v could be controlled by the amount of gas mixture in the chamber.

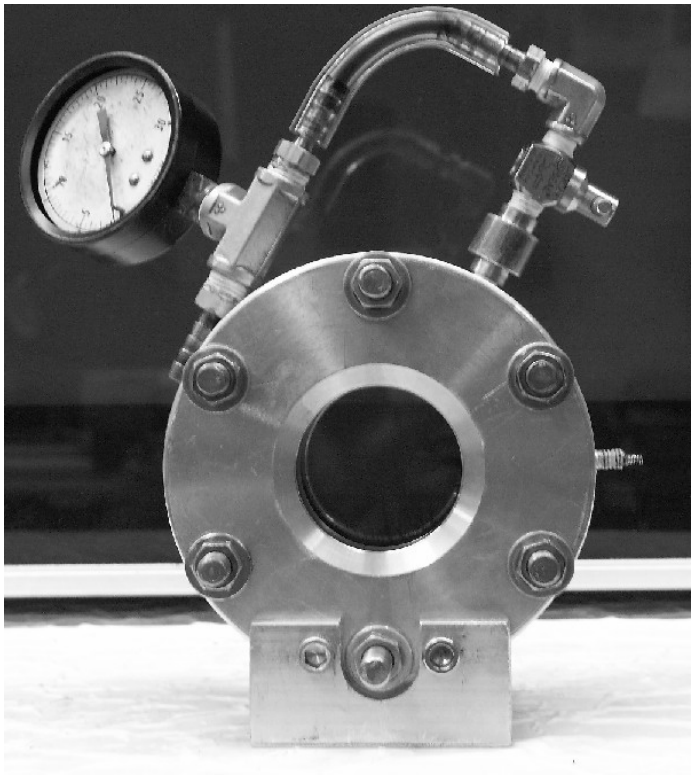

Figure 5.4: The front view of the optical chamber.

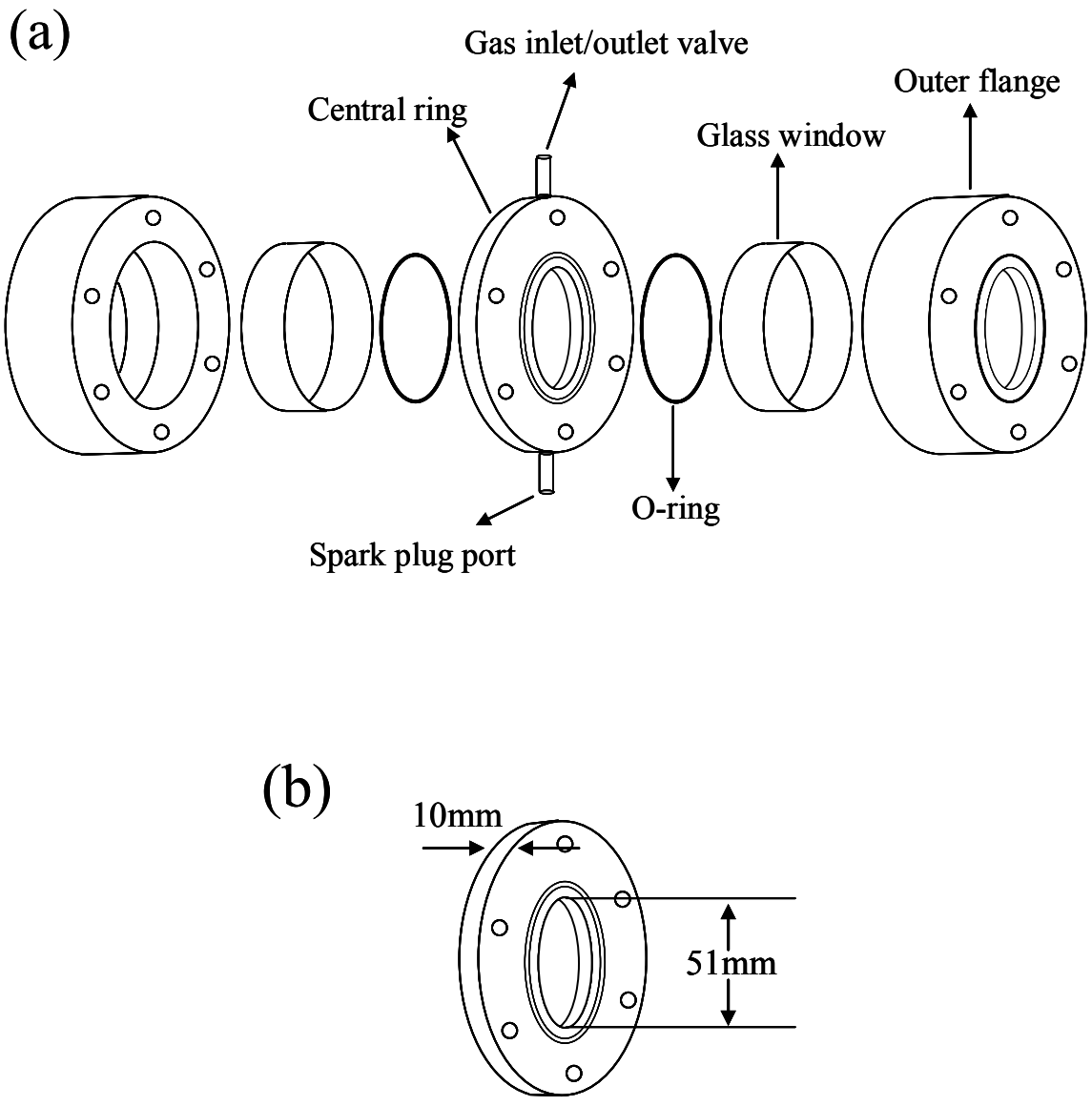

Figure 5.5: Schematic diagram of the optical chamber. (a) Different components of the optical chamber. (b) Internal dimensions of the central ring which becomes the reaction volume when the components were put together.

If the chamber windows were to fail during detonation, high velocity window debris could be produced. However, owing to the small reaction volume ~20 cm^3 and strong glass windows and flanges, the explosions were harmless.

Fig. 5.6 shows the chart of the chamber filling procedure. Acetylene and oxygen gas cylinders with appropriate pressure regulators were connected to two flow meters which were connected to a mixing reservoir. A mixture of two parts of acetylene and one part of oxygen by volume (or moles) was first collected in this mixing reservoir. The flow meters allowed the control over the mixing proportion of the gases. The (optical) chamber was then first evacuated and then back filled with this gas mixture up to a desired pressure. Whenever desired an electric spark was introduced inside the chamber through the spark plug attached to the chamber using a tesla coil. The electric spark ignited the gas mixture, and the detonation resulted in the instant creation of ca. 38 nm sized aggregating carbon soot particles. The chamber was reused after cleaning it using ethanol. The glass windows were carefully cleaned using liquid glass cleaner and also with ethanol making them optically clean.

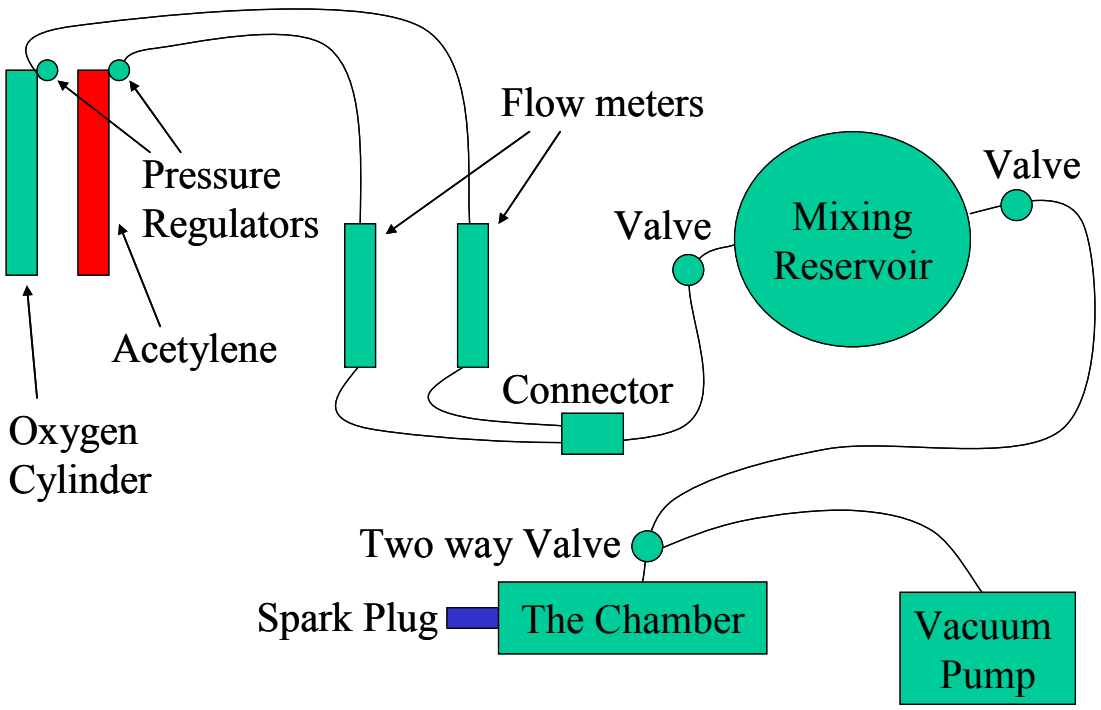

Figure 5.6: The chart showing the optical chamber filling procedure.

5.3.1.2. Small Angle Static Light Scattering Setup

For our experiments we used a home made SASLS device instead of using one available commercially. This home made device was based on that of Ferri (Ferri, 1997). Fig. 5.7a shows a schematic diagram of the light scattering and detection setup. A vertically polarized argon ion laser beam operating at wavelength λ = 488 nm entered normally into the optical chamber through one of its glass windows (Fig. 5.7b). The incident beam intensity was controlled using a Glan-Thompson polarizer before the vertical polarizer. An iris was used to chop any unwanted diffraction caused by the polarisers and other stray light. The scattered light along with unscattered beam left the chamber through the other glass window parallel to the first one. The first lens (lens 1) collected the light scattered at constant angle and focused this at its Fourier plane. The unscattered beam was removed using a tiny mirror (a tiny drill bit cut and polished at 45^{o} at its tip) placed at the axial focus on the Fourier plane. The lens 1 was a biconvex lens positioned with its less convex surface facing towards the scattering system to minimize the possible spherical aberration.

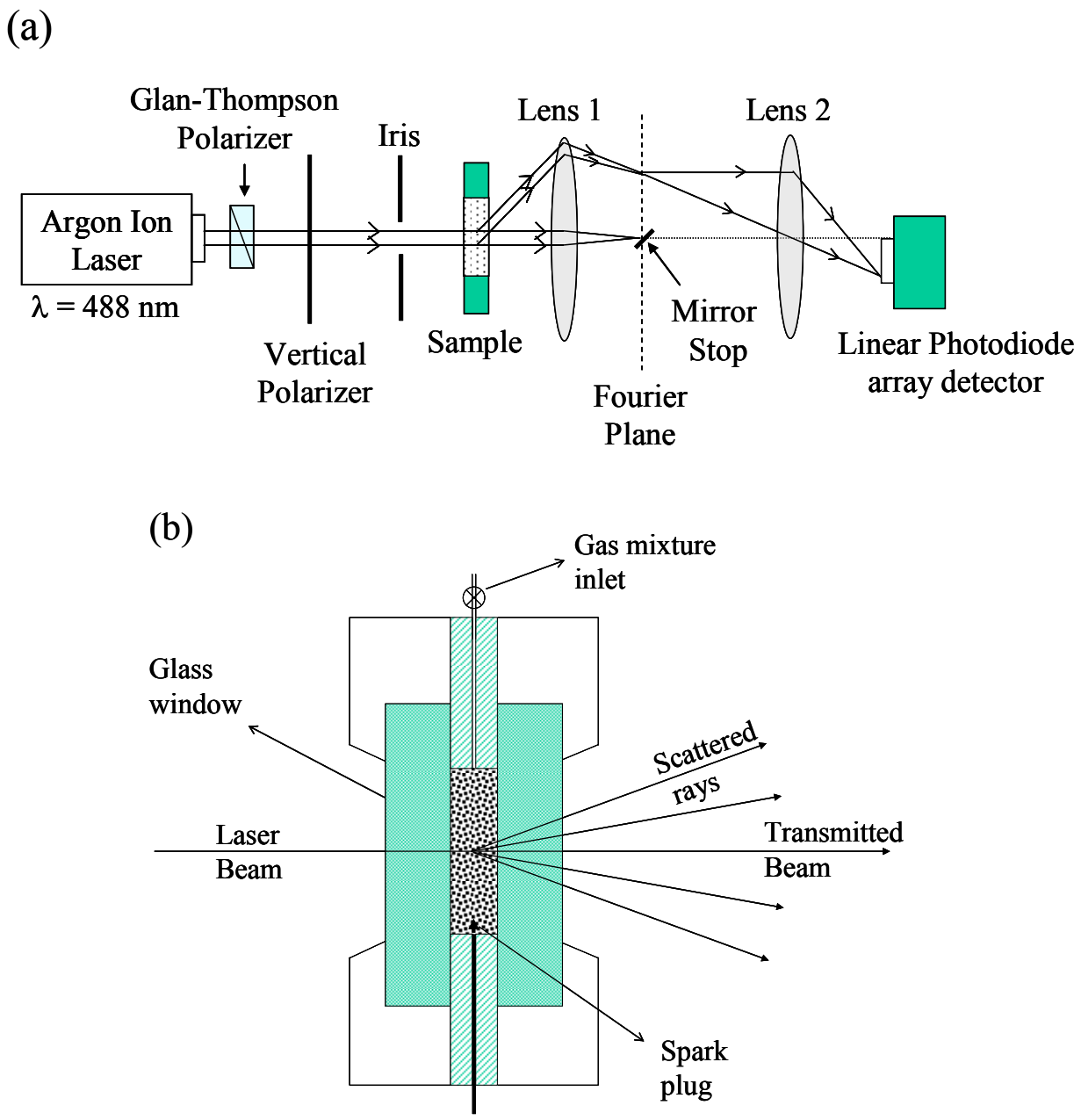

Figure 5.7: (a) The schematic diagram of SASLS measurement technique. The lens 1 collects the light scattered at constant angle and focuses at its Fourier plane that is then imaged by the lens 2 on the photodiode detector. The transmitted beam is cleaned by using a tiny reflecting mirror placed at the focus of the lens 1. (b) Schematic diagram of the light scattering from the optical chamber.

Since the aggregates can grow bigger than 10 μm in size, which corresponds to small q, the measurements were confined to a range of small scattering angles θ. The range was $0.1^o \leq \theta \leq 15^o$ over a horizontal scattering plane, which corresponds to q values in the range 200 $cm^{-1} \leq q \leq 3x10^4$ cm^{-1}. The maximum scattering angle that the device could consider was half the angle subtended by the position of the scatterer on the principle axis to the lens 1 when the device had no vignetting problem.

A second lens (lens 2) imaged the scattering pattern at the Fourier plane onto a horizontal photodiode array (HAMASATSU, S 3902). In absence of the lens 2, clipped data measurement by the detector was possible since the detector had a small and fixed dimension. The photodiode array had 512 pixels (micro photodiodes) each of which was 50 μm wide and 0.5 mm high. The detector has at least three orders of magnitude dynamic range and the maximum sensitivity at the wavelength of 600 nm. The detector, which had a capability of 62.5 kHz pixel readout rate and a 50 ms (20 Hz) integration time, was interfaced with a computer using a National Instruments PCI-6034E data acquisition card (NI part # 778075-01). Frames of data were acquired and recorded; each frame consisting 512 data points with 16-bit resolution.

The position of the lens 2 was selected such that the position of the scattering system became its conjugate point via the lens 1. This arrangement helped in controlling the vignetting problem associated with the lens 2, such that the scattered ray at maximum angle collected by the lens 1 could reach the detector.

The correspondence of the pixels of the photodiode detector to the scattering wave vector q associated with the scattering angle θ can be shown using Fig. 5.8. Using the lens formula $f^{-1} = S_i^{-1} + S_o^{-1}$, the obvious geometrical relation $\tan\theta = R/S_{i1}$ can be rewritten as

$$\tan\theta = \frac{R(S_{o1} - f_1)}{f_1 S_{o1}}. \tag{5.1}$$

Also from simple geometry of the figure we see

$$\frac{R}{r} = \frac{S_{o1}}{(S_{o1} - f_1)}. \tag{5.2}$$

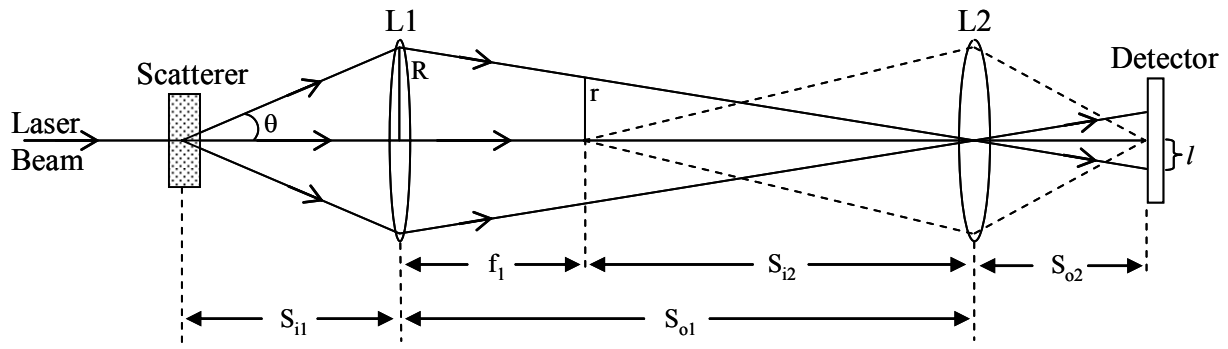

Figure 5.8: The schematic diagram of SASLS measurement technique. There is one to one correspondence between the pixels of the photodiode detector and the scattering wave vector q associated with the scattering angle θ.

Combining Eqs. (5.1) and (5.2) we find

$$\tan\theta = \frac{r}{f_1}. \tag{5.3}$$

Again from the Fig. 5.8 we have

$$\frac{r}{l} = \frac{S_{i2}}{S_{o2}} \tag{5.4}$$

where l is the length of the image of r formed by the lens 2 on the detector. l is directly related to the number of pixels on the photodiode array detector.

The scattering wave vector for a small scattering angle $q \approx 2\pi\theta/\lambda$ can be rewritten using Eqs. (5.3) and (5.4) as

$$q \approx \frac{2\pi}{\lambda}\left(\frac{S_{i2}}{S_{o2}}\frac{l}{f_1}\right). \tag{5.5}$$

Collecting the constant terms in Eq. (5.5) and denoting the collecting by $\alpha = \left(\frac{2\pi}{\lambda}\frac{S_{i2}}{S_{o2}}\frac{1}{f_1}\right)$, this equation becomes

$$q \approx \alpha\, l\,. \tag{5.6}$$

We can call α as the conversion factor. Eq. (5.6) gives one to one correspondence between the pixels of the photodiode detector to the scattering wave vector q at small scattering angles.

5.3.1.3. SASLS Setup Calibration

Calibration process of the SASLS setup involved testing the positions of the lenses and the detector, and finding the conversion factor to convert the number of pixels ($\propto l$) into the scattering wave vector q such that the measured intensity distribution matched closely possible with the known theoretical intensity distribution.

The SASLS device was calibrated by diffracting the laser beam through a 10 μm single slit (Lenox Laser, A-Slit-3/8-Disc-10) placed vertically at the position of the scatterer. The unscattered beam reflecting mirror was removed during the calibration of the setup. The diffraction intensity received by every pixel on the detector was recorded. For every pixel the diffraction intensity was corrected by subtracting background due to the stray light in the "dark" laboratory. Background for every pixel was measured as the intensity, the pixel detected, when the incoming laser was blocked before hitting the scatterer.

We chose the diffraction from a single slit for the calibration purpose because a single slit is a simple diffraction system whose theoretical diffraction intensity distribution $I(q)$ can be given by a simple mathematical relation as

$$I(q) = I(0)\left(\frac{\sin\beta}{\beta}\right)^2 \tag{5.7}$$

where $\beta = (kb / 2) \sin\theta$, with b as the width of the single slit. With small angle approximation, i.e., $\sin\theta \approx \theta$, we can rewrite Eq. (5.6) in the form

$$\frac{I(q)}{I(0)} \approx \left\{\sin\left(\frac{qb}{2}\right) \Big/ \left(\frac{qb}{2}\right)\right\}^2. \tag{5.8}$$

After converting the numbers of pixels (l) into corresponding q values using Eq. (5.6) with some conversion factor α, the measured diffraction intensity distribution normalized by the forward diffraction intensity was plotted versus the scattering wave vector q. The optical components and the conversion factor α were fine tuned to obtain the best possible match between the measured and the theoretical normalized diffraction intensity distributions. Fig. 5.9 shows forward normalized diffraction intensity distribution for one of the best calibrated SASLS setup.

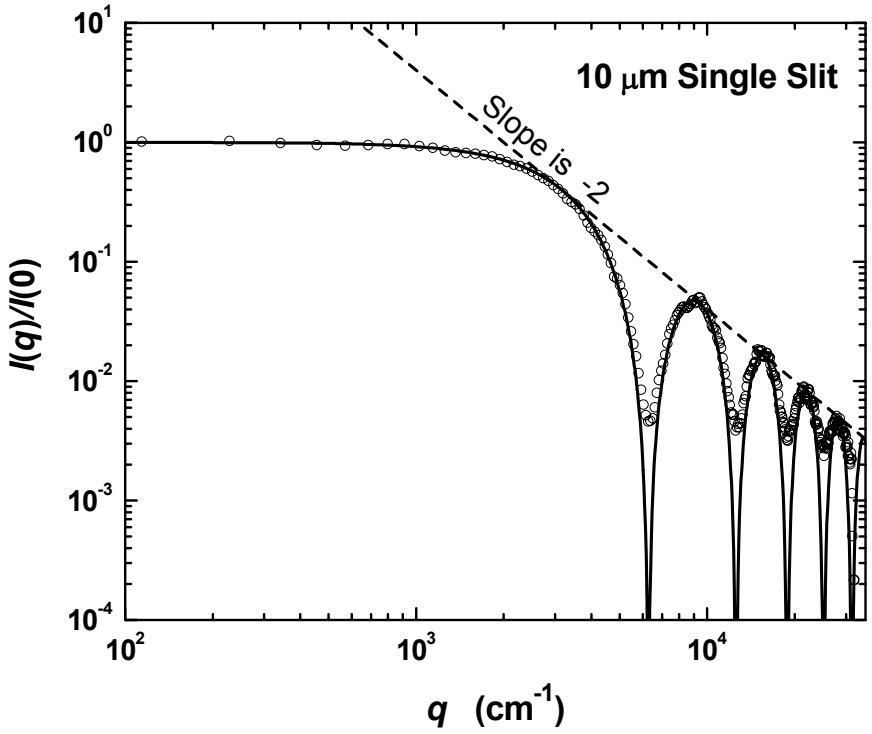

Figure 5.9: Forward normalized diffraction intensity distribution for a 10 μm single slit. The open circles are the experimental data while the solid line is the theoretical distribution. Since a slit is a one dimensional object the slope (dotted line) with which the intensity drops in the power law regime is -2.

It is also possible to calibrate the device using a standard size (e.g. 10 μm) pinhole or aqueous dispersions of standard size (e.g. 9.6 μm) polystyrene latex spheres as the scattering system. However, there are some difficulties. In the case of pinhole diffraction, peak intensities

are too weak making the signal to noise ratio smaller compare to the case of a single slit. In the case of aqueous dispersions of polystyrene latex spheres the intensity falls steeply in the Porod regime with a slope of -4 in the double-logarithmic plot. Further, effects of small polydispersity in the size of the polystyrene spheres are expected. These factors will make the situation difficult to match higher order diffraction peaks to match with the theoretical ones. Despite these difficulties other users of the SASLS setup in our lab have used a pinhole and polystyrene sphere for the calibration purpose (Mokhtari, 2007, Shi, 2001).

5.3.1.4. Light Scattering Data Acquisition

The optical chamber was charged and positioned in the SASLS setup. The gas mixture in the chamber was then exploded at the desired time. A time series light scattering data for the whole range of scattering angles measured by the photodetector array were recorded by the computer starting almost 2 seconds after the creation of the aggregating carbon nanoparticles in the chamber until the system gelled. The residual gas worked as the medium fluid for the diffusion motion of the nanoparticles in the chamber. After gelation, there was no more evolution in the scattering pattern. The stray light background pattern was also measured and subtracted from each measured scattering intensity pattern. The scattered intensity pattern data were acquired for different runs with different monomer volume fraction f_v. The different f_v were achieved by varying the amount of hydrocarbon in the gaseous mixture inside the chamber.

The monomer volume fraction f_v of the aggregating system was determined by measuring both the incident and attenuated beam intensity and calculating the turbidity of the aerosol system using *Beer-Lambert Law*. More discussion on determining the monomer volume fraction is given in the following *Results and Discussion* section. We observed the time evolution of the morphology of the aggregating clusters with different monomer volume fractions.

5.3.2. RESULTS AND DISCUSSION

The scattered light intensity pattern was found to evolve and then stop about 30 to 100 seconds after the aerosol was created during the explosion depending upon the monomer volume fraction f_v. The evolution stopped since the system became static after the gelation. The system

evolved faster with higher f_v. The clusters grew from monomer size ca. 38 nm (measured directly from TEM picture as shown in Fig. 5.10) to $\geq$ 10 microns and finally gelled whenever $f_v \geq 1.0 \times 10^{-4}$. Visual inspection showed that the gel spanned the volume of the scattering chamber. The aerosol gelation process is likely to involve Brownian motion during the major growth period, then convection and minor gravitational settling. We present our light scattering experimental results in the following subsections.

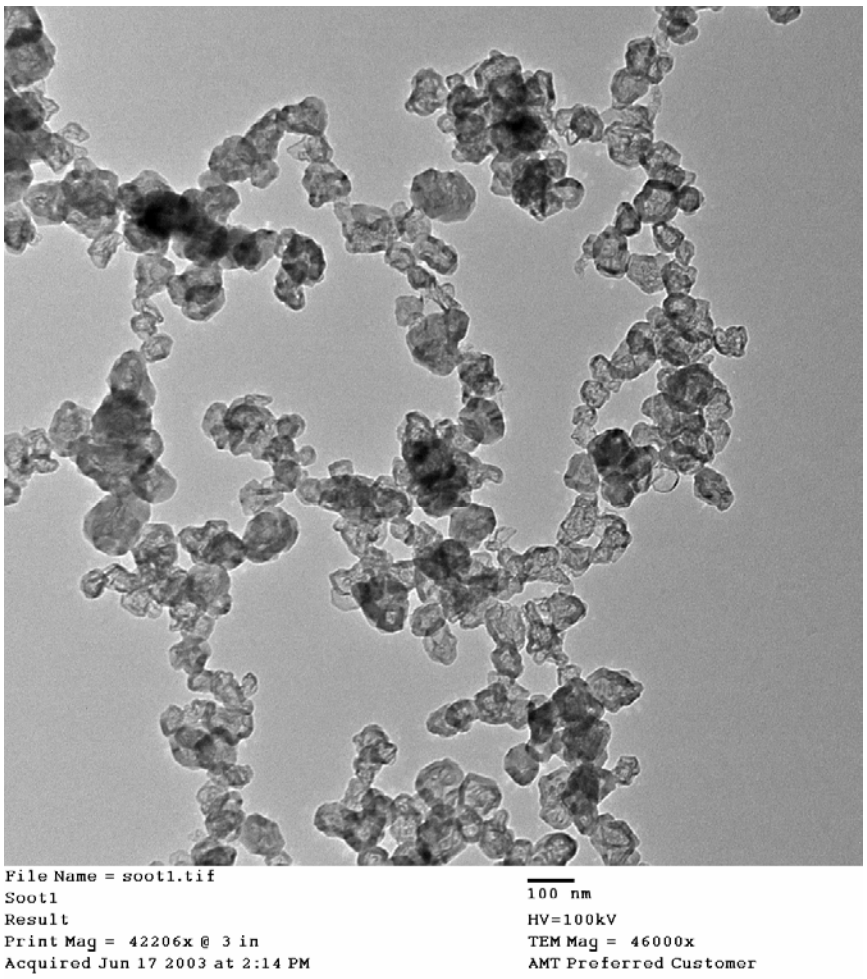

Figure 5.10: TEM image of carbon soot monomers prepared by the detonation of a gas mixture of acetylene and oxygen in a closed combustion chamber. The monomers looked more graphitic compare to those from a normal diffusion flame. The monomers had a size distribution with an average radius of 38 nm and a standard deviation of 8 nm.

5.3.2.1. Monomer Volume Fraction Measurement

Extinction measurements can yield the aggregate monomer volume fraction f_v if the refractive index of the material has an imaginary part. Soot has a complex refractive index, but it is poorly known. Many soot refractive index measurements exist in the literature, and there is little reason to choose one measurement as the best (Bond and Bergstrom, 2006, Sorensen, 2001). Thus the determination of f_v is successful, but ultimately limited by the uncertainty in the refractive index of the soot. Fortunately the refractive index has no influence on the determination of the fractal dimension D_f.

We determined the monomer volume fraction f_v in our aggregating soot system by measuring the absorption coefficient τ_{absp} of the system and then using the relation (Sorensen, 2001)

$$f_v = \tau_{absp} / 3kE(m) . \tag{5.9}$$

Here $k = 2\pi / \lambda$ is the wave number of the incident laser beam, $E(m)$ = Im[$(m^2 - 1)/(m^2 + 2)$] and m is the monomer relative refractive index. The values of $E(m)$ corresponding to the soot refractive indices found in the literature are found to lie in the range 0.19 – 0.37. Here we chose $E(m) = 0.260$, a typical value for a soot system.

Determination of τ_{absp} is not straightforward since a turbidity measurement yields the extinction coefficient τ_{ext} which is the sum of both scattering (τ_{scat}) and absorption (τ_{absp}) coefficients. However, we can extract τ_{absp} from τ_{ext} if we know the albedo $\omega = \tau_{scat} / \tau_{ext}$ of the system (Kerker, 1969). τ_{ext} was determined by measuring both the incident I_0 and transmitted I_T intensities and using Beer-Lambert law

$$I_T = I_0 \exp(-\tau_{ext} l) . \tag{5.10}$$

Here l is the optical path length of the beam through the system. The albedo ω relates τ_{ext} and τ_{absp} as

$$\tau_{absp} = \tau_{ext}(1-\omega)\,. \tag{5.11}$$

The albedo ω for a system of aggregates depends on the refractive index of the monomeric particle, the incident wavelength, the fractal dimension and the radius of gyration of the aggregates and is given by the relation (Sorensen, 2001)

$$\omega = \left[1 + \frac{3}{2}\frac{E(m)}{F(m)}\frac{1}{k_0}(ka)^{D_f-3}\left(\frac{1}{k^2R_g^2} + \frac{4}{3D_f}\right)^{D_f/2}\right]^{-1} \tag{5.12}$$

where $F(m) = |(m^2 - 1)/(m^2 + 2)|^2$, k_0 is the prefactor in Eq. (3.3), a is the monomeric radius and other notations have their usual meanings.

Eq. (5.12) shows that the albedo is governed by the factor $3(E/F)/2k_0$. A typical value of this factor for soot fractal aggregates is equal to 1 (Sorensen, 2001). This implies $E/F = 0.87$ if $k_0 = 1.3$ (for DLCA clusters). We also need to the monomer size a and the fractal dimension D_f to use Eq. (5.12) to determine the albedo ω for a range of cluster radius of gyration R_g. For our system we measured the radius of the carbon monomers directly from the TEM images. Fig. 5.11 shows the frequency distribution of monomer sizes for 187 randomly chosen monomer images in TEM pictures. The average monomer diameter was 76.1 nm (radius 38.3 nm) with a standard deviation of 16.6 nm (see Table 5-1).

Table 5-1: Monomer Size Distribution Statistics.

Average monomer size	76.7 nm
Standard deviation	16.6 nm
Biggest monomer size	118.2 nm
Smallest monomer size	40.9 nm
Monomer count	187

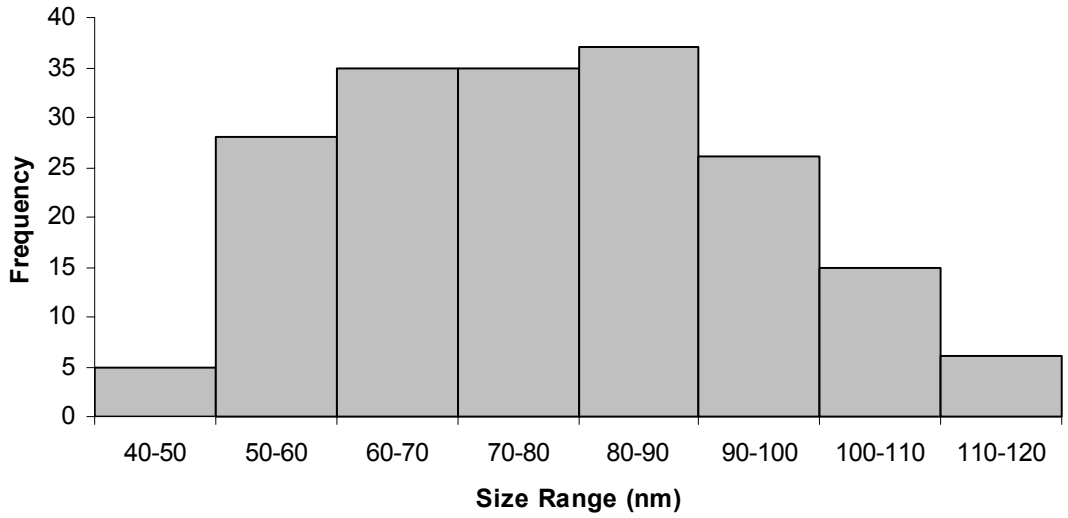

Figure 5.11: Frequency distribution of monomer sizes for 187 randomly chosen monomer images in TEM pictures. Average monomer diameter for this distribution was 76.7 nm (radius 38.3 nm) with a standard deviation of 16.6 nm.

The plot of the albedo ω versus the aggregate size R_g (Fig. 5.12) for our experimental scattering wavelength (λ = 488 nm) with $3(E/F)/2k_0 = 1$ indicates $\omega \approx 0.357$ in the experimentally measured range of R_g. Here we used the carbon soot monomer size (radius) a = 38 nm and the fractal dimension D_f = 1.8 (widely accepted value for DLCA clusters). Further, using the range of E/F values calculated from the soot refractive index values and the fact that in our experiments $R_g > 1$ μm we found $\omega = 0.357 \pm 0.09$. Using this value of ω, the absorption coefficient τ_{absp} was extracted from the extinction coefficient τ_{ext} determined from experimental data using Beer's law (Eq. (5.10)), and hence f_v was measured using Eq. (5.9).

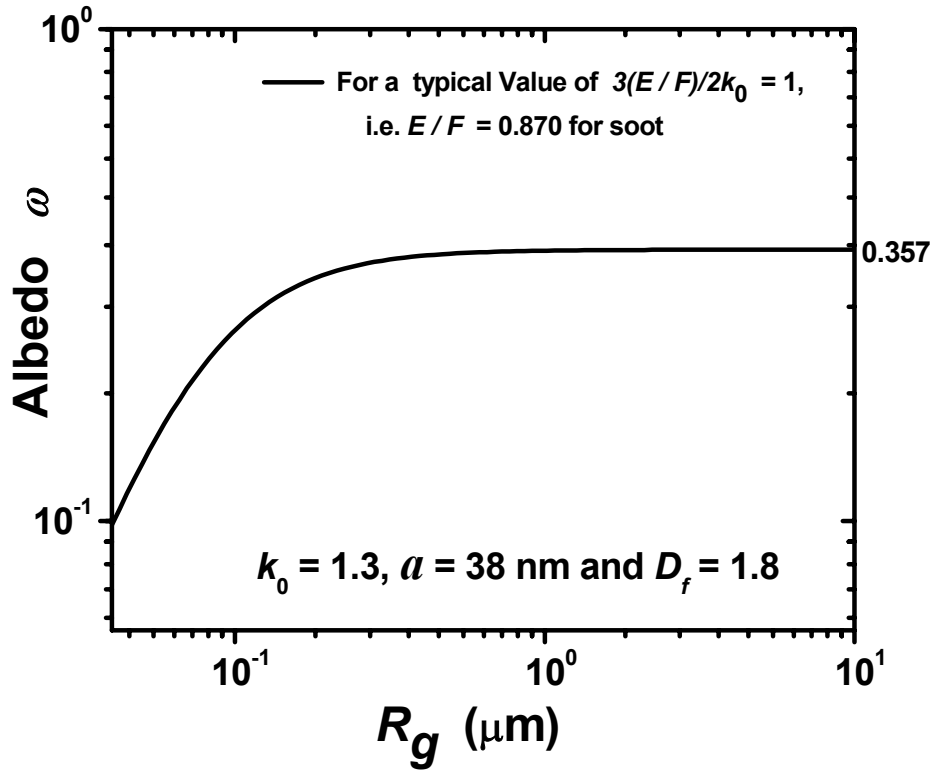

Figure 5.12: A graph of albedo ω (Eq. (39)) against the cluster radius of gyration R_g with $3(E/F)/2k_0 = 1$, a typical value for soot fractal aggregates, and λ = 488 nm. Here we used the carbon soot monomer size (radius) a = 38 nm as shown by TEM pictures, and the fractal dimension D_f = 1.8.

5.3.2.2. Interpretation of Light Scattering data with Multiple Scattering Effects

Under the RDG assumption (see section 4.2.1.2.), the fractal dimension of the evolving aggregates is the magnitude of the slope with which $I(q)$ decreases with increasing q after the initial flat Rayleigh regime on a log-log plot (see section 4.2.2.1.). Here the effect of the form factor of the monomers on the intensity distribution is not important. This is reasonable in our experiment since the soot monomers were of ca. 38 nm radii and hence contributed no effect in the scattering intensity distribution in our scattering angular range.

One problem which hinders the light scattering technique to give the correct fractal dimension measurement is the multiple scattering effect. This effect tends to illuminate the whole scattering angular range uniformly, hence will give an apparent fractal dimension too low (Mokhtari et al., 2005). Previous works (Lattuada et al., 2001, Mokhtari et al., 2005, Urban and Schurtenberger, 1998, Wilcoxon et al., 1987) have shown that multiple scattering effects on the scattered intensity pattern become more serious as the dispersed scattering particle concentration increases, or the optical path length increases, or both. Multiple scattering can become significant for systems with a strong refractive index. Decreasing the optical path length of the laser beam through the aerosol helps to minimize the multiple scattering effects.

To test for the presence of multiple scattering and to decrease its effects, we measured and analysed the scattered intensities $I(q)$ from the aggregating soot system with different optical path lengths at a given volume fraction f_v. We decreased the optical path length by UV curing a small extra glass piece, a disk with diameter 0.63 inch, on the inner side of the glass window facing towards the laser source in the optical chamber. This decreased the optical path length in a small portion of the chamber. Figs. 5.13a, 5.13b and 5.13c show the plot of $I(q)$ versus q, evolving with time, with the optical path lengths 10 mm, 3 mm and 1.5 mm, respectively, keeping the proportion of acetylene and oxygen and the amount of the mixture the same. As is clear from these figures, the magnitude of the slope (apparent D_f) increased from 1.4 to 1.6 as the optical path length decreased from 10 mm to 1.5 mm. We interpret this as a consequence of decreased multiple scattering at small optical path lengths. Our TEM image analyses of the soot clusters at monomer length scales (presented in section 5.2.) had, however, showed that $D_f \approx 1.8$, the DLCA value (Dhaubhadel et al., 2006). The implication was that the expected $D_f = 1.8$ probably would have been revealed if we could further decrease the optical path length below 1.5 mm. Our attempts to scatter light from the system with optical path length lower than 1.5 mm failed since no soot formed in the very thin region during the gas mixture explosion. Hence we confined all our experiments to 1.5 mm optical path length. The multiple scattering effects were also found to grow stronger when the monomer volume fraction f_v was increased above 8×10^{-5}. The apparent fractal dimension hence further decreased below 1.6. We thus need to pay extra attention while determining fractal dimension from light scattering data.

Figure 5.13: Log-log plot of scattered intensity versus the scattering wave vector q evolving with time when the optical path length for the laser beam through the scattering volume is (a) 10 mm (b) 3 mm and (c) 1.5 mm. The time elapsed when a measurement was taken after the creation of the aerosol is indicated. The effect of multiple scattering becomes larger with increasing optical path length as indicated by a smaller apparent fractal dimension.

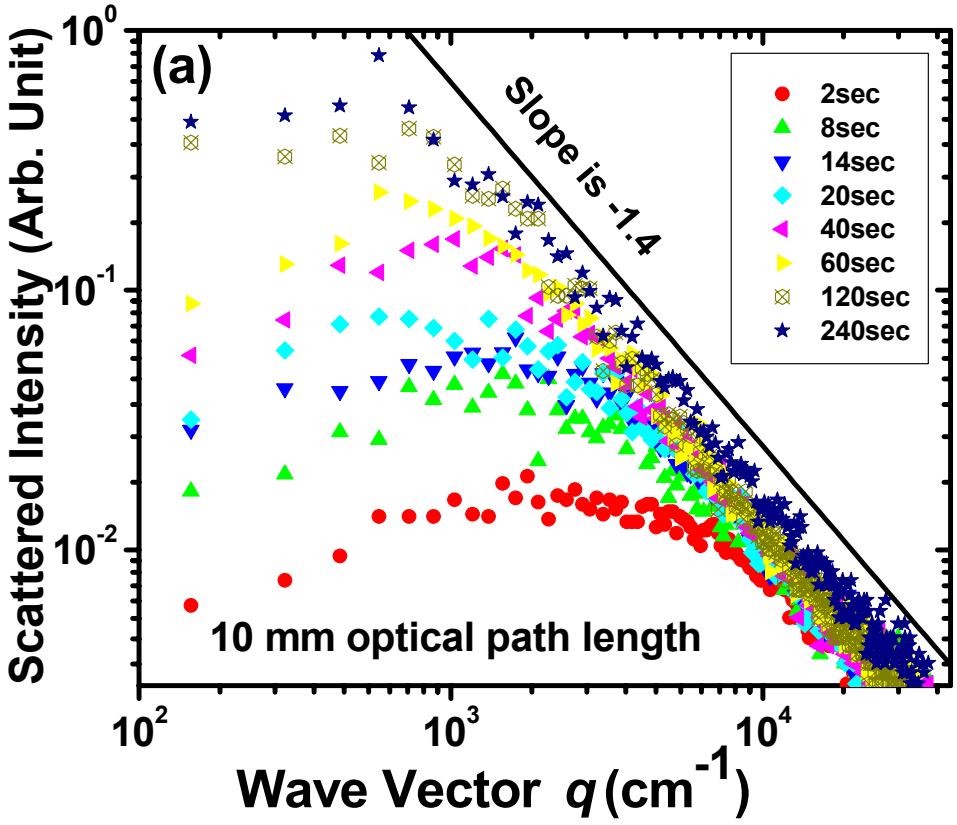
(a)
Slope is -1.4
2sec
8sec
14sec
20sec
40sec
60sec
120sec
240sec
10 mm optical path length
Scattered Intensity (Arb. Unit)
Wave Vector q (cm-1)

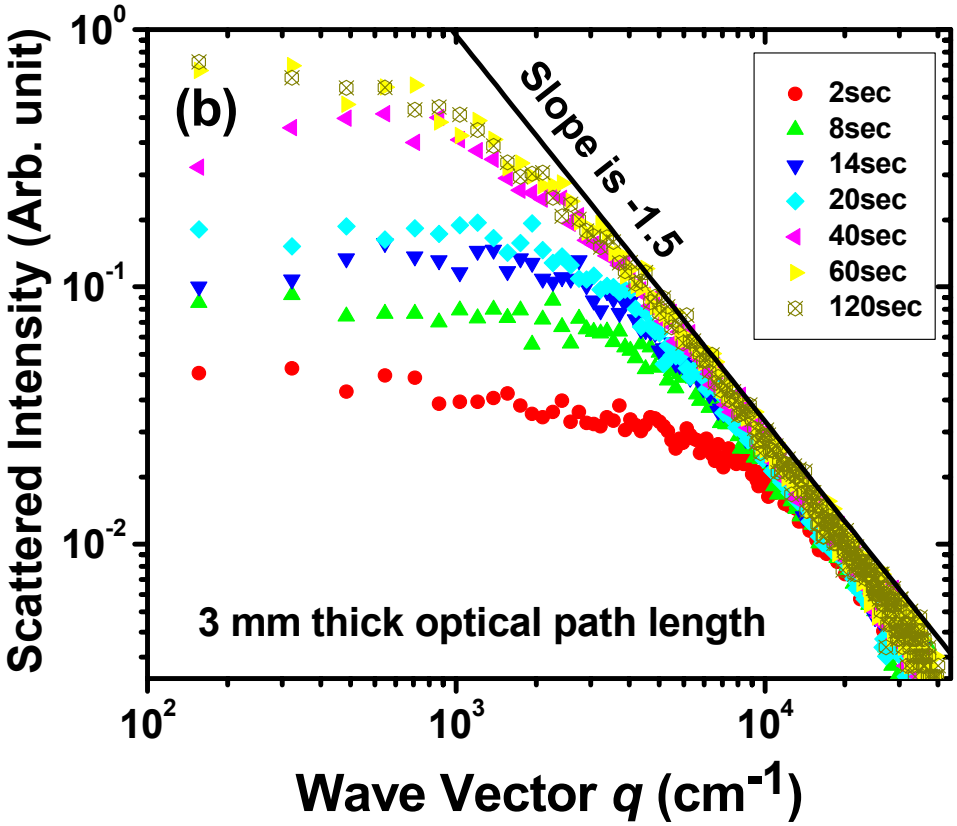
(b)
Slope is -1.5
2sec
8sec
14sec
20sec
40sec
60sec
120sec
3 mm thick optical path length
Scattered Intensity (Arb. unit)
Wave Vector q (cm-1)

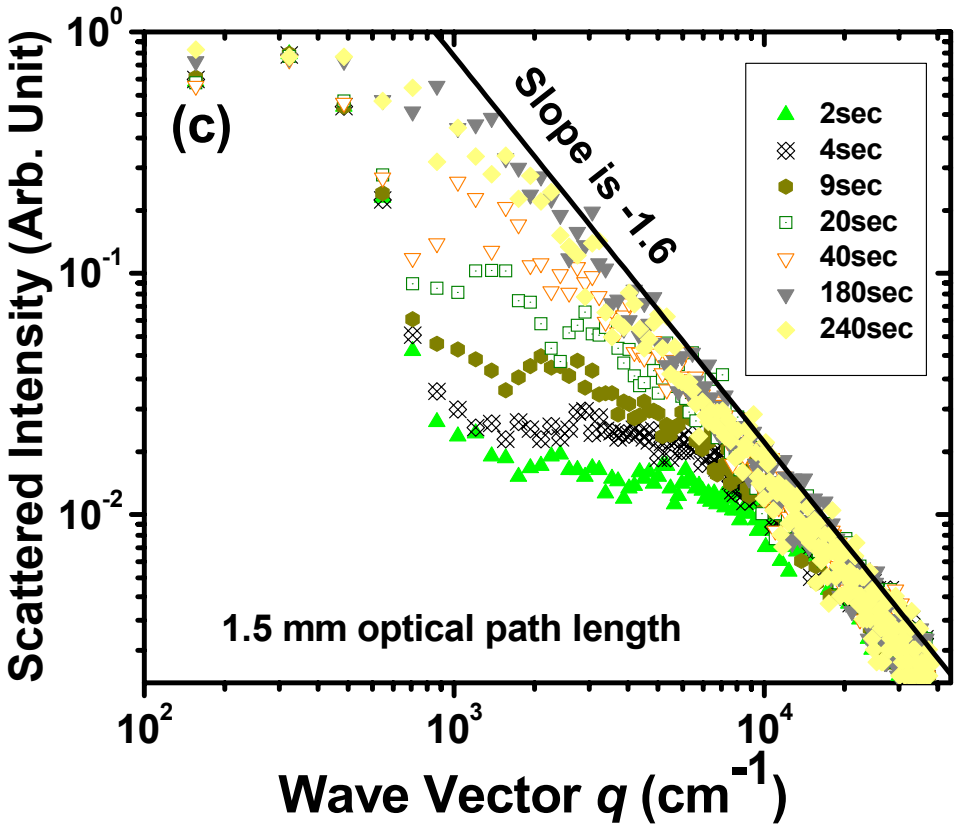
(c)
Slope is -1.6
2sec
4sec
9sec
20sec
40sec
180sec
240sec
1.5 mm optical path length
Scattered Intensity (Arb. Unit)
Wave Vector q (cm-1)
10^0
10^-1
10^-2
10^2
10^3
10^4

5.3.2.3. Observation of Hybrid Morphological Superaggregates

For the monomer volume fraction f_v greater than 8 x 10^{-5}, the experimental scattered intensity (optical structure factor) plots versus the scattering wave vector q in double logarithmic scales showed that at earlier times, when the clusters were about a micron or smaller in size, the intensity dropped with only one slope in the power law regime. However, at later times, when the clusters grew above a micron in size, the optical structure factor plots were characterized by two slopes; a slope with smaller magnitude at q greater than ~10^4 cm^{-1} (i.e. length scales of a micron or smaller) and a slope with larger magnitude at q smaller than ~10^4 cm^{-1} (i.e. length scales greater than a micron). Fig. 5.14a shows a typical result of the scattering from a system with f_v = 1.0 x 10^{-4} evolving with time. The two-slope feature on the optical structure factor plot is more distinct in Fig. 5.14b, which displays only one set of scattering data later in time during the aggregation process. Fig. 5.14c is a replot of data in Fig. 5.14b to emphasize the morphological crossover. In this figure the slope at larger q values has been flattened such that the slope in smaller q shows up if there is any.

These experimental results imply that at earlier time the system was cluster dilute, and the clusters had a unique morphology characterized by a single fractal dimension. The aggregation process was DLCA. At later times, the clusters were grown larger and the system became cluster dense. This resulted in development of clusters with a hybrid morphology characterised by two fractal dimensions; a lower fractal dimension at length scales of a micron or smaller and a higher fractal dimension at length scales greater than a micron (Dhaubhadel et al., 2006, Fry et al., 2004, Sorensen et al., 2003). We use the term *Superaggregate* to mean such a cluster.

From quantitative analysis of our data we found that late in the aggregation when the system became cluster crowded, the larger clusters (superaggregates) in the system had a short-range local structure described by an apparent fractal dimension of 1.45 or less and a long-range overall structure described by an apparent fractal dimension of 2.1 or less. However, we were expecting fractal dimensions of 1.8 at smaller length scales and 2.6 at larger length scales for such superaggregates following previous simulation results from our laboratory (Fry et al., 2004). We contend that the observed lower fractal dimensions were due to multiple scattering effects as explained above in section 5.3.2.2. Besides multiple scattering, the possible extreme

polydispersity in the cluster size among superaggregates might also be the next reason for the apparent lower fractal dimension at lower q. Martin and Ackerson (Martin and Ackerson, 1985) have shown that the extreme polydispersity has influence on the structure factor power law in the cluster dense regime.

Since light scattering probes intensity weighted moments of the cluster size distribution (see section 4.2.3.3.1.), the effective structure factor for an ensemble of polydisperse aggregates is given by Eq. (4.51). Martin and Ackerson (Martin and Ackerson, 1985) showed that the effective structure factor follows

$$S_{eff}(q) \sim q^{-D_f^*}, \qquad qR_{gz} >> 1 \quad \text{and} \quad qa << 1. \tag{5.13}$$

In Eq. (5.13) R_{gz} is the z-average radius of gyration (see section 4.2.3.3.1.), a is the monomer radius and the exponent D_f^* is an apparent fractal dimension due to the size distribution effect in the polydisperse ensemble. Depending greatly on the size distribution exponent τ (see section 3.12.) the apparent fractal dimension D_f^* is such that

$$\begin{aligned} D_f^* &= D_f && \text{if } \tau < 2 \\ D_f^* &= D_f(3-\tau) && \text{if } 2 < \tau < 3 \end{aligned}. \tag{5.14}$$

For a DLCA process for which the cluster diffusivity exponent γ = -1/D_f , the cluster size distribution is characterized by τ = 0 and hence $D_f^* = D_f$ (Meakin et al., 1985). However, once the system crosses over to cluster dense the aggregation process no more remains DLCA type, instead clusters start percolating. Percolation theory (Stauffer and Aharony, 1985) shows that such clusters have a size distribution characterized by τ = 2.18. This renders the apparent fractal dimension $D_f^* \approx 2.1$ in the structure factor analysis of percolating clusters $D_f \approx 2.6$.

The true fractal dimensions of ~1.8 and ~2.6 for such hybrid superaggregates were revealed while analyzing their electron micrographs and high-resolution high-magnification light microscope pictures in our image analysis study presented in section 5.2. (Dhaubhadel et al., 2006).

Figure 5.14: A typical result of the scattering from a system with $f_v = 1.0 \times 10^{-4}$ as a log-log plot of scattered intensity versus scattering wave vector. A hybrid morphology of the clusters with a larger fractal dimension at larger length scale (smaller q values) and smaller fractal dimension at smaller length scale (larger q values) was revealed from these figures. (a) Scattered intensity plot evolving with time. (b) Scattered intensity distribution 60 sec after the creation of the aerosol. The crossover length scale seems to be somewhere between 1.5 to 3.0 μm. (c) Replot of (b) emphasizing the morphological crossover.

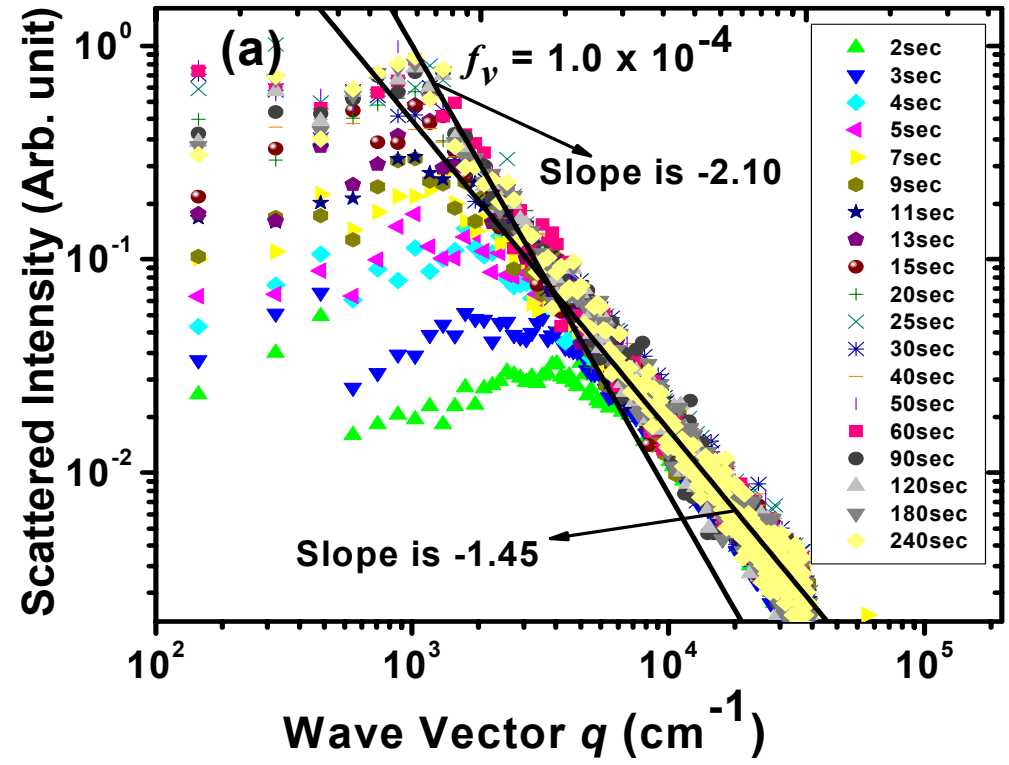
(a)
f_v = 1.0 x 10^{-4}
Slope is -2.10
Slope is -1.45
2sec
3sec
4sec
5sec
7sec
9sec
11sec
13sec
15sec
20sec
25sec
30sec
40sec
50sec
60sec
90sec
120sec
180sec
240sec
Scattered Intensity (Arb. unit)
Wave Vector q (cm^{-1})

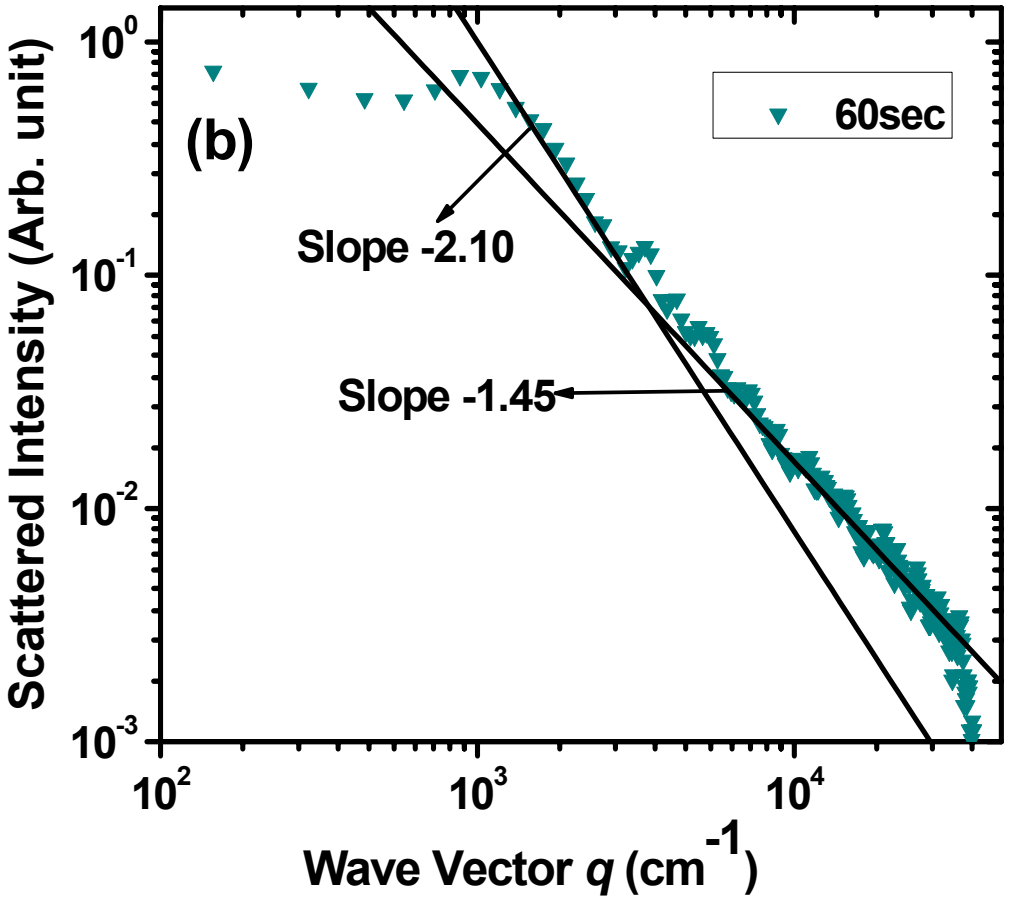
(b)
60sec
Slope -2.10
Slope -1.45
Scattered Intensity (Arb. unit)
Wave Vector q (cm^{-1})

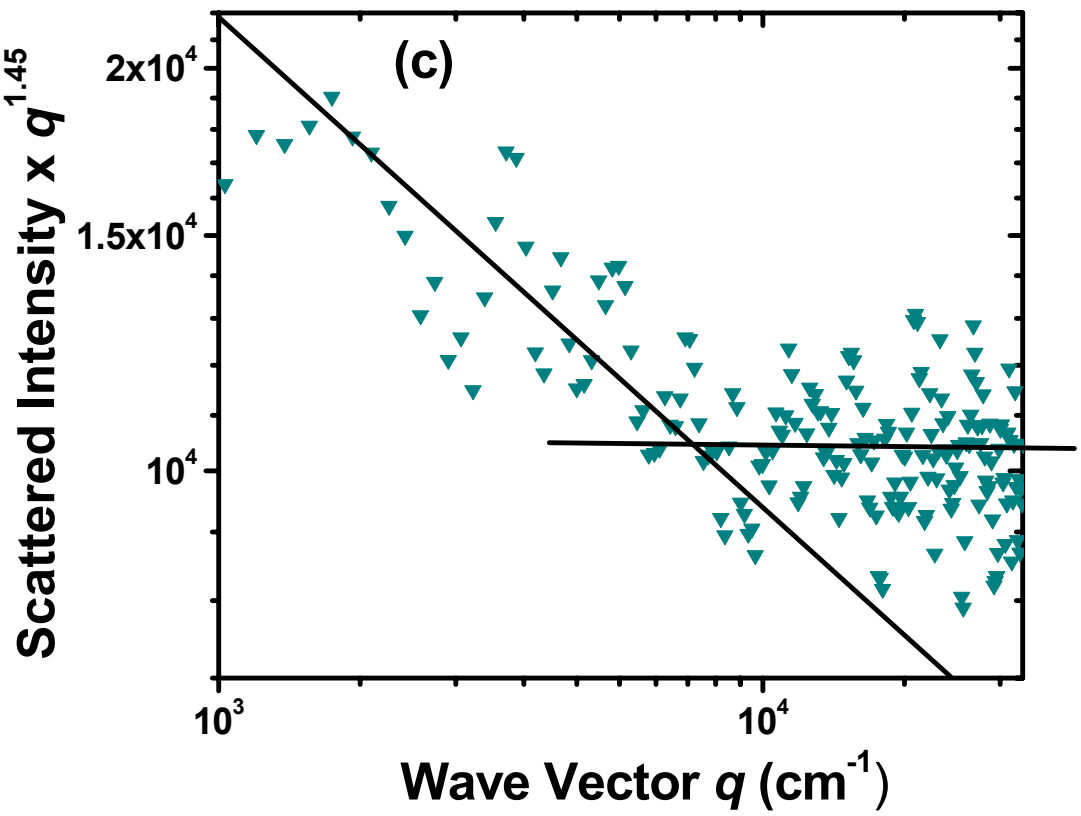
(c)
2x10^4
1.5x10^4
10^4
Scattered Intensity x q^1.45
10^3
10^4
Wave Vector q (cm^-1)

We give the following most plausible explanation for the formation of these $D_f \approx 2.6$ superaggregates. The superaggregates form when the aggregation proceeds beyond a certain critical point in time when the $D_f = 1.8$ DLCA aggregates fill the entire system volume touching each other. The growth process then crosses over to a percolation process that is known to form $D_f = 2.55$ aggregates in three dimensions (Stauffer and Aharony, 1985).

The aggregate radius of gyration R_{gel} at this critical point can be calculated for an ideal system, with monodisperse and spherical clusters, under a reasonable assumption that a particulate system gels when the monomer or primary particle in the average cluster is equal to the primary particle number density in the entire system. With this assumption, we can derive an expression for the gel time radius of gyration for an ideal system as

$$R_{gel} \approx \frac{1}{2} a \, f_v^{1/(D_f - 3)}. \tag{5.15}$$

This R_{gel} can also be called *ideal gel-point radius of gyration* and is expected to be the crossover length scale between the $D_f = 1.8$ and $D_f = 2.6$ regimes. This has been approximately verified from previous computer simulation studies in our laboratory (Fry et al., 2004).

Using Eq. (5.15) we calculated R_{gel} for our system with a = 38 nm and the monomer volume fraction $f_v = 1.0 \times 10^{-4}$ to be ~ 40 μm. However, from the analysis of our light scattering experimental data we found the crossover length scale to be somewhere between 1.5 to 3.0 μm (see Fig. 5.14b). We found such discrepancy between the calculated R_{gel} and the observed crossover length scale for all (limited) monomer volume fractions in our study. The reason behind this discrepancy is not yet resolved but could be the "ideal" assumption while deriving relation for R_{gel} and uncertainty in experimentally determining the monomer volume fraction f_v.

In principle the morphological crossover from $D_f = 1.8$ to $D_f = 2.6$ is expected to occur in any aggregating system once the cluster dense condition is reached regardless of the monomer volume fraction. The only differences a higher volume fraction brings are a faster aggregation process and a shortening of the crossover length scale. However, we could not observe the crossover from lower fractal dimension to higher fractal dimension at monomer volume fractions smaller than 8×10^{-5}. The most likely explanation for this is the faster gravitational settling time

t_{set} compare to the system gel time t_{gel} which is strong function of f_v (Eq. (3.124)). For a slower aggregation process, the aggregating system settles gravitationally before it could attain cluster dense state.

5.3.3. CONCLUSION

By employing the SASLS technique we investigated the morphology and aggregation kinetics of an aggregating aerosol system. We observed a morphological crossover in the aggregating clusters from a homogeneous, DLCA fractal morphology at earlier time to a hybrid superaggregate morphology, DLCA at small scales and percolation at large scales, at later time during the aggregation process. These results consolidated the picture of the evolution of a system of aggregating particles suggested by previous computer simulation results from our laboratory (Fry et al., 2004).

The results reported here were from the study of aggregating carbon nano-particles created by exploding C_2H_2. However, we believe that the reported results should also be true for any dispersed particulate system being independent of the type of material. One among many possibilities of different material aerosols is silica (SiO_2). We can easily create silica nano-particles by exposing silane (SiH_4) to any gaseous oxidizer, e.g. oxygen, nitrous oxide, nitric oxide, etc. A study of aggregating silica nano-particles using SASLS technique will also be interesting as we expect minimum multiple scattering effects because of low refractive index. We may be able to see the real fractal dimension in the scattered light intensity distribution which we didn't see in the case of scattering from soot when the monomer volume fraction and/or optical path length was increased.

5.4. NEUTRON SCATTERING STUDY

We performed *Ultra Small Angle Neutron Scattering* (USANS) and *Small Angle Neutron Scattering* (SANS) experiments to probe the structure of a gelled network of carbon aerosols formed by explosive detonation of acetylene and oxygen mixture. We named such gelled network of aerosols as an *aerosol gel*. We used BT5 and NG7 30 m SANS instruments at NIST Center for Neutron Research (NCNR) for USANS and SANS respectively. Schematic diagrams

of BT5 and NG7 instruments are given in Figs. 5.15 and 5.16, respectively. BT5 and NG7 together could provide q-range of approximately 5 x 10^3 cm^{-1} to 1 x 10^7 cm^{-1} allowing us to probe structure of materials over four orders of magnitude in length scales from few microns down to 10 A^o or less. Unlike light wave, neutron beam could easily penetrate our aerosol gel made up of strongly light absorbing carbon soot particles. This means our system wouldn't have problem of multiple scattering while dealing with neutron beam.

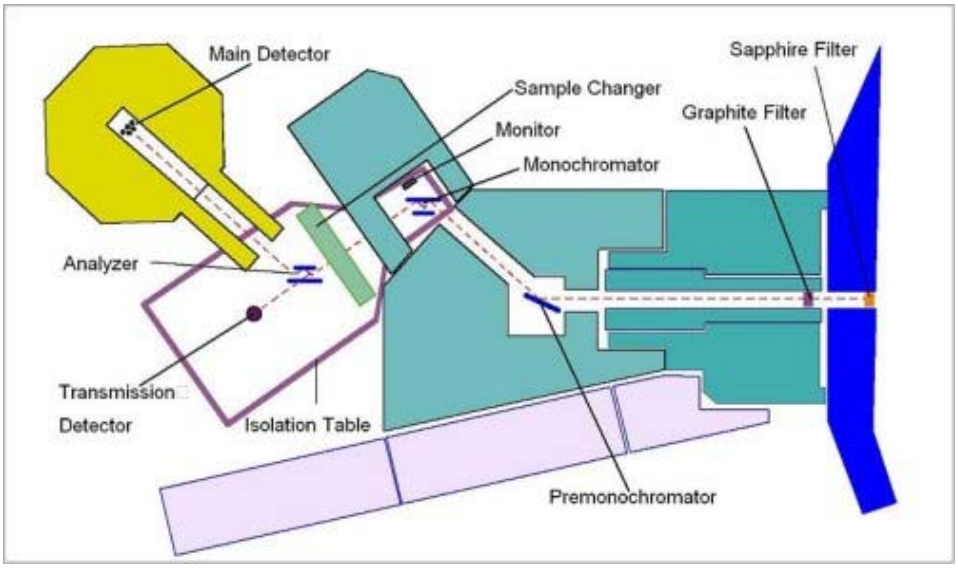

Figure 5.15: Ultra small-angle neutron scattering (USANS) BT5 instrument with a perfect crystal diffractometer (PCD) for ultra-high resolution measurements. This instrument is located at NIST Center for Neutron Scattering (NCNR). Source: http://www.ncnr.nist.gov.

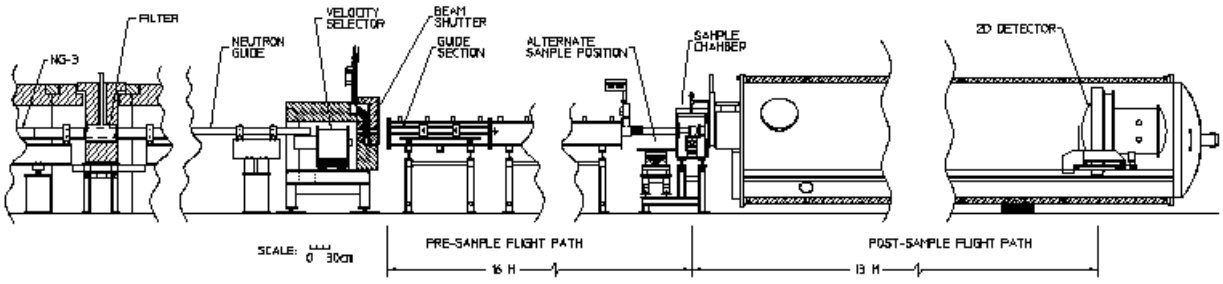

Figure 5.16: Small-angle neutron scattering (SANS) NG7 30 m instrument. This instrument is located at NIST Center for Neutron Scattering (NCNR). Source: http://www.ncnr.nist.gov.

Neutron scattering data were collected for two different samples of the carbon aerosol gel. The first sample was a 1 cm thick collapsed aerosol gel. The second sample was the unperturbed carbon aerosol gel made *in situ* at the instrument site by exploding a gas mixture of acetylene and oxygen (2:1 molar ratio) at one atmospheric pressure inside a closed stainless steel chamber. This was a cylindrical chamber with 3.8 cm internal diameter and 7.3 cm long. It had a 6.35 mm thick quartz window on each end of the cylinder (Fig. 5.17). An aluminum supporting flange held the quartz window against an o-ring at each end of the cylinder making the chamber air tight. The chamber was also equipped with an inlet/outlet valve and a spark plug.

The filling procedure for this chamber was the same as that for the optical chamber as described in section 5.3.1.1. However, the chamber was always filled up to 1 atmospheric pressure for the neutron scattering purpose. After disconnecting the gas source the charged chamber was mounted on the neutron scattering instruments and then the gas mixture in the chamber was ignited remotely using a tesla coil. The neutron scattering data were recorded for a range of q values to probe the as prepared network of carbon aerosol gel. Fig. 5.18 shows a photograph of the gelled network of carbon nanoparticles produced during the explosion of the gas mixture inside the chamber. The network was formed spanning the whole volume of the system as a consequence of Brownian aggregation of carbon nanoparticles in the residual gas medium inside the chamber.

The shockwave caused by the detonation of a gas mixture inside a closed chamber produces high pressure. For a fixed gas mixture pressure, this pressure is proportional to the volume of the chamber. The maximum tensile stress (σ_t) in a window is proportional to

$$\sigma_t \propto \frac{Pd^2}{t^2} \tag{5.16}$$

where P is the pressure produced by shockwave, d is the window exposed diameter and t is the window thickness. If the pressure of the shockwave in our chamber is high enough, the quartz windows will fail producing high velocity debris in the experimental site. We successfully tested the safety factor by performing several detonations at different gas mixture pressure in the chamber in our laboratory before using it at NCNR.

Figure 5.17: A photograph of the cylindrical chamber for neutron scattering experiments. The picture was taking after detonating the gas mixture inside using a starter (can be seen in the picture) connected to the spark plug of the chamber.

Figure 5.18: The gelled network as a consequence of Brownian aggregation of carbon nanoparticles produced during the explosion of the gas mixture inside the chamber. The network did span the whole volume of the system.

5.4.1. RESULTS AND DISCUSSION

USANS and SANS combined data from the 1 cm thick sample of the collapsed carbon aerosol gel are shown in the Fig. 5.19. Here one clearly sees a power-law regime $\sim q^{-1.65}$ at intermediate-q (corresponding to a length scale range of 30 – 350 nm) indicative of a mass fractal aggregate with a fractal dimension D_f = 1.65. Stronger power law of $\sim q^{-4}$ at low-q (corresponding to a length scale of 1.7 μm and higher) was indicative of a compact 3-d structure at large length scales formed during collapsing of the aerosol gel.

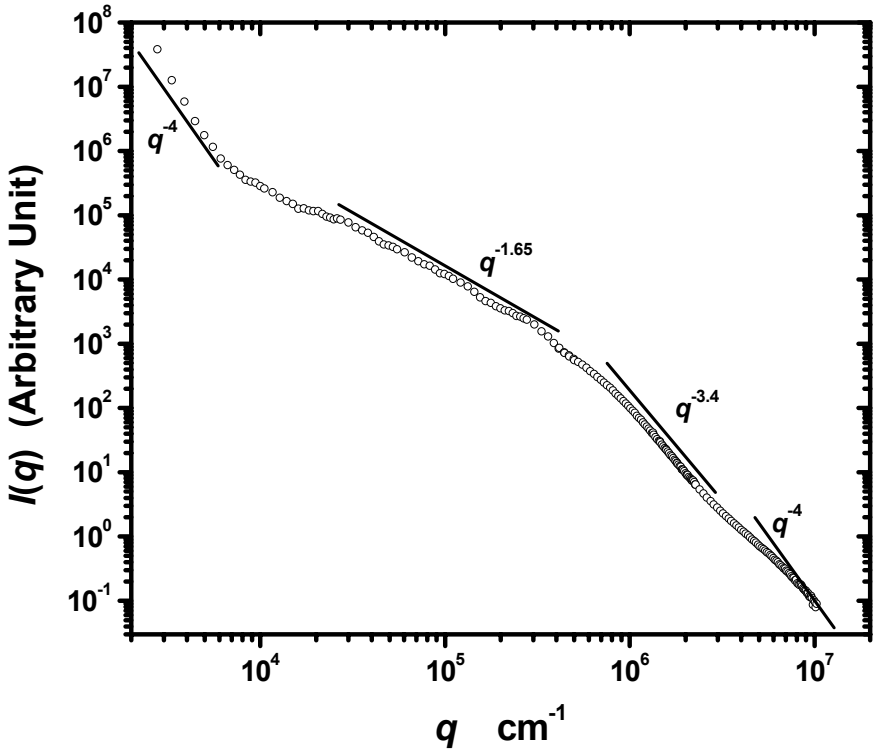

Figure 5.19: Combined USANS and SANS result from a collapsed carbon aerosol gel sample. Scattered neutron intensity $I(q)$ is plotted versus the scattering wave vector q. Here one clearly sees several power-law regimes; $\sim q^{-4}$ at low-q indicative of a compact 3-d structure at large length scales formed during collapsing of the aerosol gel; $\sim q^{-1.65}$ at intermediate-q indicative of a mass fractal aggregate; $\sim q^{-3.4}$ at high-q indicative of 3-d monomer structure; and one more $\sim q^{-4}$ at yet higher-q indicative of the internal feature of the monomer structure.

At high-q (corresponding to a length scale of 10 nm and lower), two other stronger power law regimes were observed. From the TEM image (Fig. 5.20) it appears that the monomers of the aerosol gel had graphitic layer planes a few nanometers thick around the surface with their planer orientation parallel to the particle surfaces forming a shell-like structure. What appears to be encapsulated inside this shell was either voids or amorphous carbon with more random crystallite orientation. From the X-ray diffraction (XRD) patterns (see section 7.2.2.3.) we determined the graphitic layer to be 3 nm thick. The monomer and its internal features thus gave rise to these two stronger power law regimes at high-q.

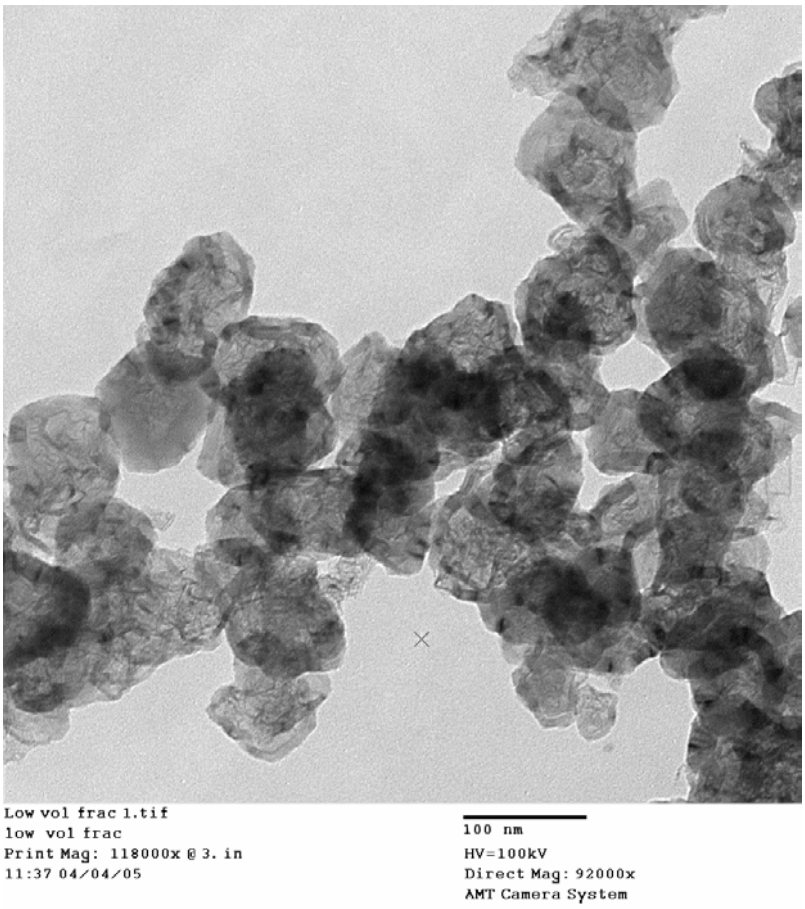

Figure 5.20: TEM picture of carbon soot monomers from a closed explosion of acetylene and oxygen mixture. Monomers had graphitic layer planes a few nanometers thick around the surface with their planer orientation parallel to the particle surfaces forming a shell-like structure.

Among these two power law regimes, the one at larger q (corresponding to a length scale below 1.5 nm) seemed to evolve to $\sim q^{-4}$. This regime was indicative of the monomer's internal feature. Our instrumental limitation in the q-range prevented us from probing deeper into the internal feature. The other power law at smaller q was $\sim q^{-3.4}$, instead of the expected $\sim q^{-4}$ (Porod law), corresponding to the monomer structure. We give the following possible explanation to this deviation from the Porod law. The length scales corresponding to the monomer size and its internal feature size were not well separated in q-space so as to allow the Porod regime to well develop before the influence of the scattering from the internal feature became significant.

The lower mass fractal dimension of D_f =1.65 from the intermediate q-regime compare to the expected DLCA value of D_f =1.80 was surprising as the multiple scattering effect in this case was almost negligible. The high transmission (> 95%) of the neutron beam through the sample eliminated the possibility of multiple scattering. The lowered fractal dimension should only be an apparent and not real since the TEM image analysis had indicated the real fractal dimension to be ~1.75 (see section 5.2.). We attributed this lowered apparent mass fractal dimension to the possible polydispersity in the cluster size distribution (Martin and Ackerson, 1985) with size distribution exponent $\tau \approx 2.08$. Our scattering system was a post gel sample and thus it was not necessary that the clusters at small length scales should still be characterized by the DLCA type size distribution with the exponent $\tau = 0$ (Meakin et al., 1985) in which case the apparent and real fractal dimensions coincide (Martin and Ackerson, 1985). The lowered fractal dimension at small length scales from neutron scattering experiments indicated the possibility of the cluster size distribution to be modified from the DLCA type to a highly polydisperse one during formation of the static gelled network.

The absence of a low-q power law of $q^{-2.6}$ (percolation network) was no surprise as this was the collapsed sample, where ostensibly the largest length scales compress first. Further, it was probable that the crossover length scale could be lying on the extreme end or out of the instrumental range. Unfortunately the minimum q-value we could achieve with USANS instrument was ~5 x 10^5 cm^{-1} which corresponds to a maximum length scale of ~2 μm.

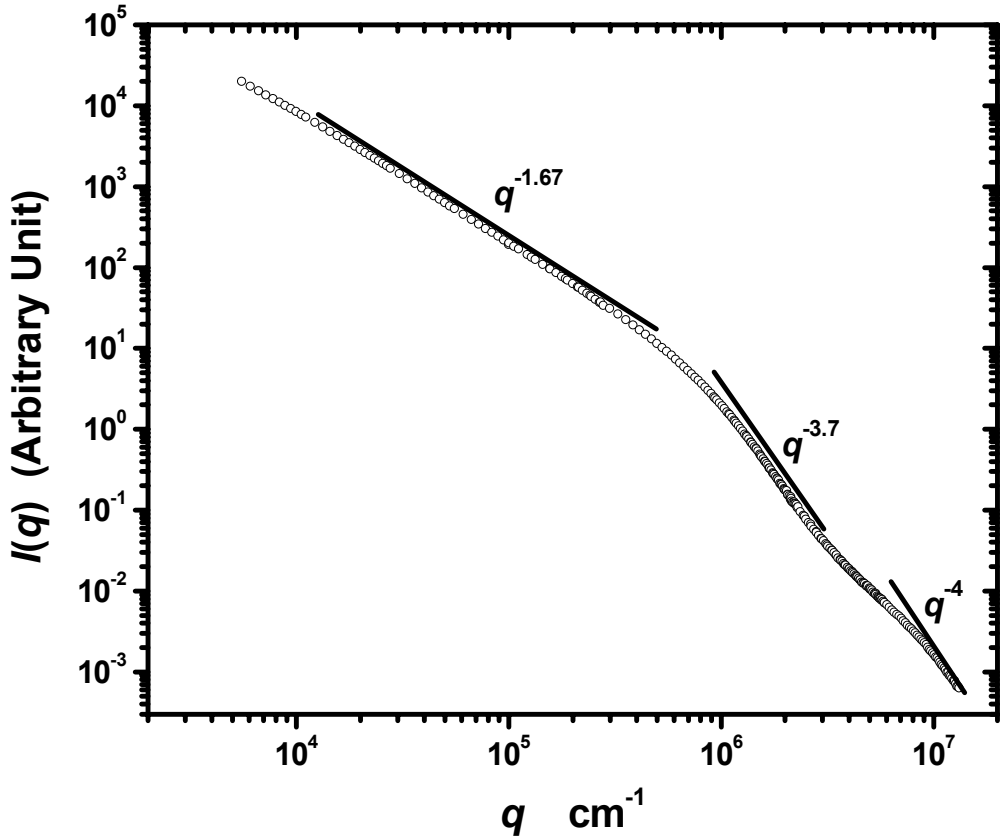

Figure 5.21: Combined USANS and SANS result from an unperturbed carbon aerosol gel sample. Scattered neutron intensity $I(q)$ is plotted versus the scattering wave vector q. Here one clearly sees several power-law regimes; $\sim q^{-1.67}$ at intermediate-q indicative of a mass fractal aggregate; $\sim q^{-3.7}$ at high-q indicative of 3-d monomer structure; and one more $\sim q^{-4}$ at yet higher-q indicative of the internal feature of the monomer structure.

We expected the $\sim q^{-4}$ dependence at low-q to vanish for an as prepared uncollapsed aerosol gel. Fig. 5.21 shows the neutron scattering experimental results for the unperturbed carbon aerosol gel prepared *in situ* at the instrument site. As our expectation the $\sim q^{-4}$ dependence at low-q was absent. We could not find the superaggregate morphology either. This can be explained by the possibility of the crossover length scale to lie outside the instrumental limitation. The apparent small fractal dimension of D_f =1.67 at the intermediate q-values was due to the

polydispersity in the cluster size distribution as has been explained above. We observed the similar q-dependences at high q-values corresponding to the monomer structure and its internal feature as in the case of the collapsed aerosol gel. The similar trends at the intermediate and large q-values for collapsed and unperturbed aerosol gel were not surprising since the collapsing should not affect the structures at smaller length scales.

We were unable to probe the morphology of the system at different time during the aggregation process because the time scale for the system to gel was less than 100 seconds while the neutron scattering instrument took much longer time to collect the scattered neutrons to produce scattering data with reliable statistics.

5.4.2. CONCLUSION

We probed the structure of carbon aerosol gel at a range of length scale from about ~2 μm down to few nanometers. We were able to observe the monomer structure and its internal features at large q-values, and also the fractal nature of the aggregates at smaller q-values. Unfortunately we were unable to observe the superaggregate morphology due to the instrumental limitation in q-range. The lowered apparent fractal dimension observed at small and intermediate q-values gave us new insight in the alteration of the DLCA type to highly polydisperse size distribution characterized by the size distribution exponent $\tau > 2.0$ during the static gel network formation process.

CHAPTER 6- Light Scattering Study of Aggregation Kinetics in Dense, Gelling Aerosols

6.1. INTRODUCTION

Aggregation of particles in aerosols and colloids is a very important phenomenon in physics, biology and material science (Liu, 2006). Aggregation drives particles to become part of a whole as a consequence of van der Waals interparticle interaction (Family and Landau, 1984, Carpineti et al., 1990, Jullien and Botet, 1987, Kolb et al., 1983, Meakin, 1983, Meakin, 1988, Meakin, 1999, Schaefer and Martin, 1984, Weitz and Oliveria, 1984). Brownian motion, fluid shear and differential settling can all cause aggregation (Family and Landau, 1984, Jullien and Botet, 1987, Meakin, 1988). A deep understanding of the structure of particle aggregates and the kinetics of their formation is the key to explain and control many complex but important phenomena in many different fields including biomedical science, material science and industry.

The morphology and aggregation kinetics in systems with low particle concentration have been extensively studied experimentally, theoretically and with computer simulations (Family and Landau, 1984, Cai et al., 1995, Carpineti et al., 1990, Jullien and Botet, 1987, Kolb et al., 1983, Lin et al., 1989, Meakin, 1983, Meakin, 1988, Meakin, 1992, Meakin, 1999, Schaefer and Martin, 1984, Sorensen and Roberts, 1997, Vicsek, 1989, Weitz and Oliveria, 1984). As has been described in previous chapters a system is cluster dilute when the average cluster-cluster separation is very large compared to the cluster size. Then the average cluster-cluster separation is not a relevant length scale. The aggregation kernel K of the Smoluchowski's coagulation rate equation for Brownian particles (particles in the continuum regime) in dilute system is given by Eq. (3.41). The degree of homogeneity λ defined in Eq. (3.19) for Brownian kernel is zero. The kinetic exponent $z = 1/(1-\lambda)$ (Eq. (3.71)) for a dilute Brownian aggregating system is thus unity.

For systems that are not cluster dilute a more general approach of the scaling argument is useful. This approach has been discussed in the section 3.8.4., and we revisit it here. The rate at

which two particles collide, K, is proportional to their relative collision cross-sectional area A_c and relative velocity $\dot{r}$. Thus we can write the aggregation kernel as $K \sim A_c \dot{r}$, consistent with the units of $[L^3/t]$. The relative collision cross-sectional area A_c is the effective area seen by one cluster during its collision with another. Hence it is logical to write $A_c \sim R_g^2$ where R_g is the radius of gyration of a cluster. For the diffusing aggregate the relative velocity goes as $\dot{r} \sim D/R_c$, where D is the diffusion coefficient and R_c is a characteristic length scale with respect to the given aggregate's motion. The diffusion coefficient goes as $D \sim 1/R_g$ in the case of the Stoke-Einstein diffusion. Thus $K \sim R_g/R_c$. Furthermore R_g is the only relevant length scale in the dilute limit. Therefore $R_c \sim R_g$ and $K \sim 1$. Hence in the dilute limit continuum system with Stoke-Einstein diffusion (DLCA limit) K has no size dependence resulting in $\lambda = 0$.

As the system continuously evolves, the available volume for the clusters to diffuse (free volume) decreases and hence the nearest neighbor cluster separation R_{nn} eventually becomes a relevant length scale with respect to any given cluster's motion. We call this case the *intermediate* regime. For a system with an average cluster number density of n_c at any time during aggregation process in d-dimensional space, the nearest neighbor cluster separation goes as $R_{nn} \sim 1/\sqrt[d]{n_c}$. The average cluster number density n_c is related to the average monomer number density in the system n_m and the average number of monomers N in one single cluster as $n_c = n_m/N$. Since n_m is a conserved quantity, R_{nn} can equivalently be expressed in terms of the number of monomers in one cluster N as $R_{nn} \sim N^{1/d}$. Thus at some intermediate time when the free volume is significantly less than the total volume, one can express the aggregation kernel K, considering the fact that $R_g \sim N^{1/D_f}$, as $K \sim N^{\left(\frac{1}{D_f}-\frac{1}{d}\right)}$, which then gives

$$\lambda \sim \frac{1}{D_f} - \frac{1}{d} . \tag{6.1}$$

Here D_f is the cluster fractal dimension. Thus for the intermediate regime, with $D_f = 1.8$ and $d = 3$, Eq. (6.1) yields $\lambda = 0.22$. This behavior has been seen in recent simulation in our laboratory (Pierce et al., 2006).

For very dense systems, the aggregating particles start developing a connectivity network among themselves. Such systems are near the gel point. In this extreme cluster dense limit, the distance between extended edges of the cluster become comparable to the persistence length which is the average distance over which a particle moves effectively in a straight line. Thus the overall cluster motion between collisions is "ballistic-like". The cluster velocity is determined via the equipartition of energy as $\dot{r} \sim N^{-1/2}$. In such a crowded state, a cluster sees the "finger-like" detail of a neighboring fractal aggregate and thus the relative collision cross-sectional area A_c must be replaced by the cluster's surface area A_s in the scaling form of the aggregation kernel, hence from the scaling argument above $K \sim A_s \dot{r}$. Since all the monomeric particles in a fractal cluster are on the surface, the surface area of a cluster goes as the number of monomers in the cluster, i.e. $A_s \sim N$. Thus one finds that $K \sim N^{1/2}$ hence $\lambda = 0.5$ in the cluster dense regime.

Very few simulations (Fry et al., 2002, Gimel et al., 1995, Hasmy and Jullien, 1996, Kolb and Herrmann, 1985, Rottereau et al., 2004) and almost no experimental studies (Dhaubhadel et al., 2006, Kim et al., 2006, Sorensen et al., 2003) are found in literature that study aggregation from the dilute regime up to the cluster dense regime. We have discussed the available previous simulation results in section 3.13.

Previous computer simulations of aggregation with Brownian dynamics (Fry et al., 2002) in our laboratory have shown that the cluster motion evolves from cluster dilute limit DLCA to cluster dense ballistic motion as the system crossed over from the cluster dilute to the cluster dense regime. It was found that the kinetic exponent z continuously evolved from 1 to 2 and the kernel homogeneity λ, which is related to the cluster growth kinetics and the resulting cluster size distribution, concomitantly evolved from 0 to 0.5. Both parameters z and λ were found to be universal functions of the free volume Ω, which is the volume not occupied by the growing clusters. The cluster crowding was found to be the only reason for the enhanced aggregation kinetics.

Here we present experimental results of a study of aerosol fractal aggregate growth kinetics as the system evolves from cluster dilute to dense. Carbon aerosol particles were created inside a closed optical chamber and their kinetics and morphology were studied using a small angle light scattering technique. We will show that our experimental results are consistent with

the simulation pictures described above. The experimental value of the kinetic exponent z increases above its dilute limit value as the monomer volume fraction f_v increases and approaches 0.5. Finally, we present the experimentally determined values of the coagulation rate kernel $K(s_2, s_2)$ at different f_v.

6.2. EXPERIMENTAL SETUP

We used the same small angle light scattering SASLS setup and the optical chamber as for the light scattering study of cluster morphology reported in chapter 5 section 5.3.1. The carbon nanoparticles were created instantaneously by detonating acetylene and oxygen mixture inside the closed cylindrical optical chamber with circular glass windows on both ends of the cylinder. The residual gas worked as the medium fluid for the diffusive motion of the nanoparticles in the chamber. The aggregation process proceeded and resulted in the formation of the gelled network whenever the monomer volume fraction f_v was high enough.

After calibrating the SASLS device (see section 5.3.1.3.), the optical chamber was charged and positioned in the light scattering experimental setup. The gas mixture in the chamber was then exploded at the appropriate time. A time series light scattering data detected by the photodetector array were recorded starting almost 2 seconds after the creation of the aggregating carbon nanoparticles in the chamber until the system gelled. The stray light background pattern was also measured and subtracted from each measured scattering intensity pattern. The scattered intensity pattern data were acquired for different runs with different monomer volume fraction f_v. The different f_v were achieved by varying the amount of hydrocarbon in the gaseous mixture inside the chamber. The monomer volume fraction f_v was determined by measuring the absorption coefficient τ_{absp} of the system as explained in section 5.3.2.1.

We tried minimizing the effect of multiple scattering by decreasing the optical path length through the scattering volume to the lowest possible value of 1.5 mm (see section 5.3.2.2.).

6.3. RESULTS AND DISCUSSION

The scattered light intensity pattern was found to evolve and then stop about 30 to 100 seconds after the aerosol was created during the explosion depending upon the monomer volume fraction f_v. The evolution stopped since the system became static after the gelation. The system evolved faster with higher f_v. The cluster size grew from monomer radius ca. 38 nm to $\geq$ 10 microns and finally gelled whenever $f_v \geq 1.0 \times 10^{-4}$. Visual inspection showed that the gel spanned the volume of the scattering chamber. Fig. 6.1 shows a picture of such a gel network spanning the volume as seen inside the optical chamber through the glass windows.

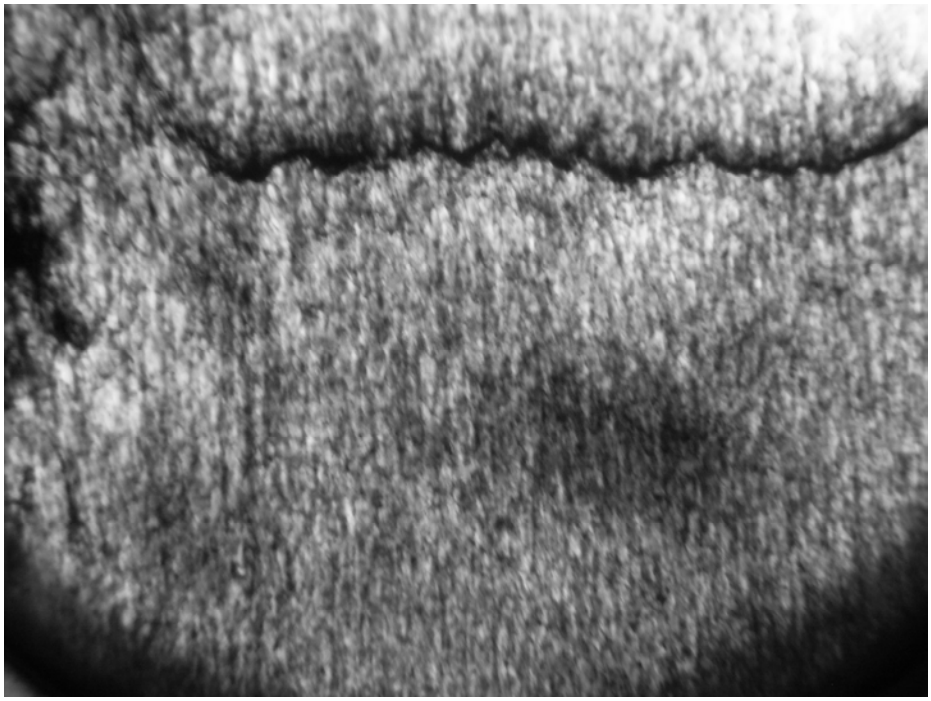

Figure 6.1: A picture of the static gel network formed inside the optical chamber observed through its glass windows. The upper black layer was due to gravitational settlement. Initially individual ca. 38 nm radius carbon particles grew in size upon Brownian aggregation eventually resulting in formation of a macroscopic random network in less than 100 sec. A macroscopic anisotropy with vertical strand structures was observed. These strands were the results of the gravitational settling tendency of the giant clusters.

A monomer volume fraction f_v below 1 x 10^{-5} was of little interest since it never crossed over to cluster dense regime. The monomer volume fraction f_v above 1 x 10^{-4} was too turbid to do any light scattering experiment. Further, very fast aggregation kinetics at higher f_v was difficult to follow using our SASLS detector which hindered us from measuring the kinetic exponent z (and hence the homogeneity λ). Hence the monomer volume fraction f_v we explored in our light scattering experiments was limited in the range extending only between 1 x 10^{-5} and 1 x 10^{-4}. We present our light scattering experimental results in the following subsections.

6.3.1. KINETIC EXPONENT Z (AND HOMOGENEITY λ) MEASUREMENTS

We measured the time evolving cluster sizes R_{gz}, i.e., z-averaged radii of gyration, by a Guinier analysis (Guinier, 1939, Guinier et al., 1955) of the scattered intensity using Eq. (4.52b). We found R_{gz} to increase up to about 10 μm or even higher by the time the system stopped evolving. The slope of a log-log plot of R_{gz} against time t gives the ratio of the kinetic exponent z and the fractal dimension D_f since the radius of gyration R_g scales with time t asymptotically as $R_g \sim t^{z/D_f}$ (Eq. (3.73)). Fortunately the monomer refractive index has no influence on the determination of the kinetic exponent z. Thus with known D_f , z and hence the homogeneity λ (Eq. (3.71)) can be determined. Here we assume that the mean field relation Eq. (3.71) to hold at all time during the aggregation process and for all volume fraction f_v; an assumption substantiated by the simulation study in our laboratory (Fry et al., 2002).

Fig. 6.2 illustrates a typical example of R_{gz} evolving with time, in log-log scale, for an aggregating system with $f_v \approx 2.3$ x 10^{-5}. We used the DLCA value of fractal dimension, i.e., D_f = 1.8, to determine z (and hence λ) from the slope with which R_{gz} evolved with time. These values of z and λ were the mean values accounting for the effects of polydispersity on the light scattering measurement. Fig. 6.3 shows the kinetic exponent z and the homogeneity λ values at different monomer volume fractions f_v. At lower f_v we found $z \approx 1$ (and $\lambda \approx 0$) consistent with the cluster dilute, DLCA case. With increasing monomer volume fraction f_v, z (and λ) was also found to increase up to 1.9 (and λ up to 0.4) indicating the enhanced aggregation kinetics functionality. This increasing value of z (and λ) is consistent with simulation results from our laboratory (Fry et al., 2002) indicating the transition of the aggregating system from cluster

dilute to cluster dense limit. The enhanced aggregation kinetics was the result of the effect of cluster crowding which creates less free volume in which to search for other clusters for the diffusing clusters.

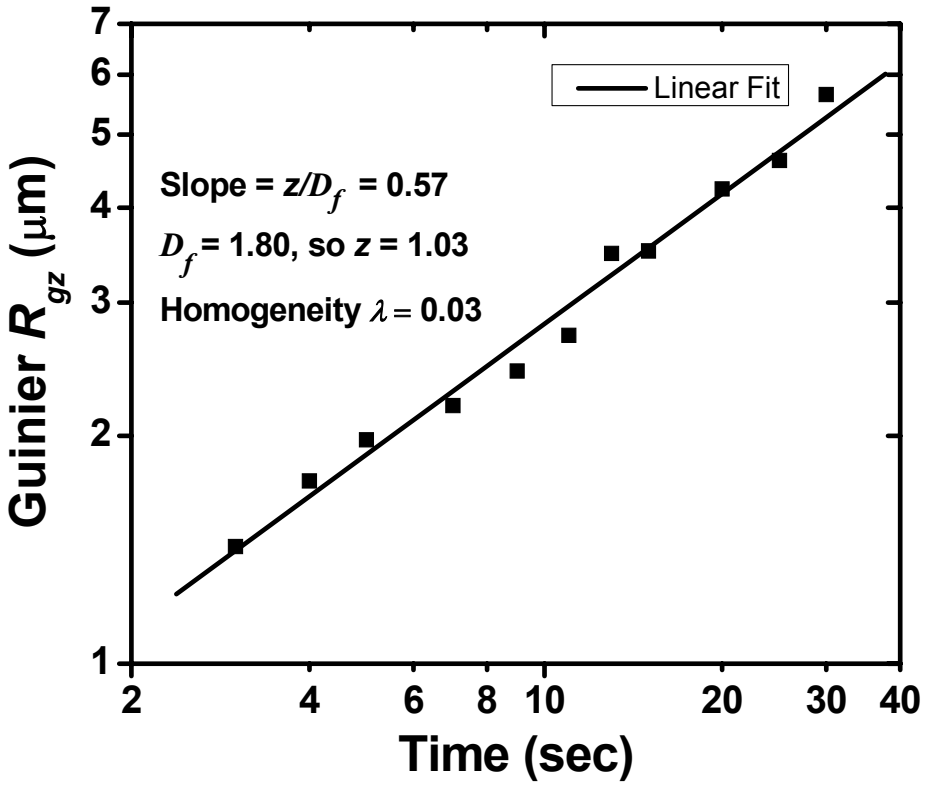

Figure 6.2: Growth of cluster radius of gyration with time when f_v = 2.3 x 10^{-5}. The cluster radius of gyration is determined using Guinier analysis of the scattered intensity data.

Enhanced kinetics has also been reported by Carpineti et al. (Carpineti et al., 1990), without explanation, at later times during the salt induced aggregation of 130 nm diameter polystyrene colloidal particles. They observed enhanced aggregation kinetics later during the aggregation process (see Fig. 6.4). They also found faster growth to occur earlier in time when monomer concentration was increased. Reworking their data, assuming the cluster fractal dimension D_f to be 1.8, we found the kinetic exponent z to increase from 1.3 to 2.2 after the onset of enhanced kinetics. We propose that this enhanced kinetics was the result of the transition of the system from cluster dilute to cluster dense regime.

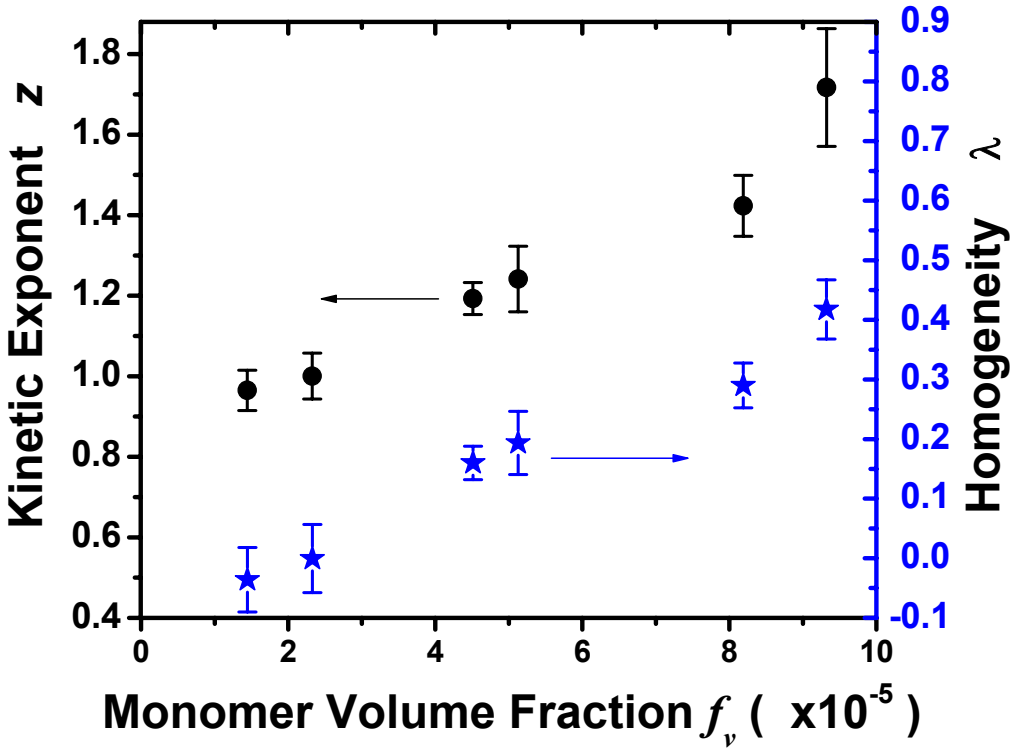

Figure 6.3: A plot of the kinetic exponent z and the homogeneity λ versus the monomer volume fraction f_v. The enhanced aggregation kinetics with increasing f_v was the result of the effect of cluster crowding.

We expect all aggregating systems starting from cluster dilute regime to enter cluster dense regime eventually. However, for systems with small monomer volume fraction f_v, the gravitational settling takes over the aggregation process. The bigger heavier clusters will be removed from an aggregating system as they settle and the cluster dense regime is never achieved. Due to this effect of gravitational settling we had early termination of the aggregation process and hence we were unable to perform any experiment to find $z > 1$ (or $\lambda > 0$) in our aggregating system with lower monomer volume fraction f_v. For the systems with higher f_v the transition from cluster-dilute to cluster-dense regime was so fast (less than few seconds and gelation in 30 sec) that we had difficulty in resolving an increasing trend of z (or λ) from 1 towards 2 (or from 0 towards 0.5).

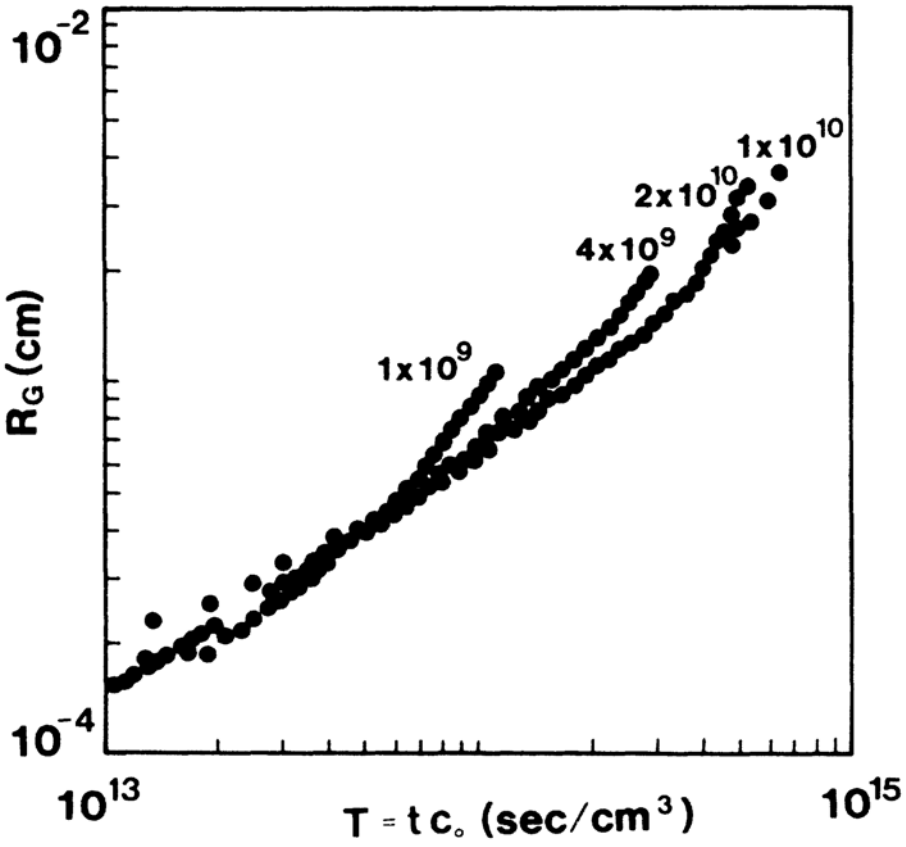

Figure 6.4: Figure 8 from the paper by Carpineti et al. (Carpineti et al., 1990) showing evolutions of the radius of gyration (R_G) of the clusters of 130 nm diameter polystyrene colloidal particles as a function of a reduced time $T = tc_o$ for different values of monomer number concentration. The tendency of the curves to roll upward shows the speeding up of the aggregation process at later times.

6.3.2. AGGREGATION KERNEL K

The aggregation kernel *K* is a function of the medium fluid, the sizes and morphology of the aggregating clusters, and the manner in which the clusters move in the medium. As has been discussed in chapter 3 section 3.8.3., *K* is expected to be independent of the cluster sizes when the clusters undergo dilute regime Brownian aggregation. We determined the magnitude of the aggregation kernel *K* from our SASLS data by measuring the average cluster number density n_2

and using its relation with K. The subscript of 2 in n_2 represents the second moment of size distribution which is naturally involved in the scattered light intensity from the ensemble of scatterers.

The average cluster number density n_2 can be presented in terms of the first moment of the cluster size distribution M_1 and the average cluster size $s_2 = \langle N \rangle$ as

$$n_2 = M_1 / s_2 . \tag{6.2}$$

Using the fact $M_1 = f_v / (4\pi a^3 / 3)$, a being the monomer radius, and expressing s_2 in terms of the z-average radius of gyration R_{gz} and scaled moments of the size distribution m_i as given by Eq. (4.53), we can rewrite Eq. (6.2) as

$$n_2 = \frac{3 f_v}{4\pi k_0 a^{3-D_f} R_{gz}^{D_f}} \left(\frac{m_{2+2/D_f}}{m_2} \right)^{D_f/2} \tag{6.3}$$

where k_0 is the prefactor in the scaling law for the monomer number in a cluster (Eq. (3.3)). DLCA fractal aggregates have $k_0 \approx 1.3$ (Cai et al., 1995, Sorensen and Roberts, 1997). Eq. (6.3) can again be rewritten in terms of the aggregation kernel homogeneity λ using Eqs. (3.91) and (3.94) as

$$n_2 = \frac{3 f_v}{4\pi k_0 a^{3-D_f} R_{gz}^{D_f}} \frac{1}{(2-\lambda)} \left(\frac{\Gamma(3 + 2/D_f - \lambda)}{\Gamma(3-\lambda)} \right)^{D_f/2} . \tag{6.4}$$

We measured the z-average radius of gyration R_{gz} at different times for our evolving aggregating system directly from the light scattering experiments while the monomer radius a was determined from transmission electron microscope images (see section 5.3.2.1.). The cluster number density was then evaluated using Eq. (6.4) considering DLCA fractal dimension $D_f = 1.8$ and homogeneity $\lambda = 0$. We ignored the variation in the homogeneity λ because increasing λ from 0 (for dilute system) to 0.5 (dense system) introduced only ~ 10% change in the cluster number density measurement, and owing to the uncertainty in the monomer volume fraction f_v measurements (see section 5.3.2.1.) this ~10% change was within the uncertainty limit.

To find the relation between the aggregation kernel $K(s_2, s_2)$ and the cluster number density n_2, we modify Eq. (3.98) by multiplying it with $s_2^{-\lambda} K(s_2, s_2)/K(1,1) = 1$ since K is a homogeneous function (Eq. (3.19)). This yields

$$\frac{dM_2(t)}{dt} = M_1^2 P_2 K(s_2, s_2) \tag{6.5}$$

where

$$P_2 = I_2 / K(1,1) \tag{6.6}$$

is the polydispersity index; $P_2 = 1$ for a monodisperse system.

The average cluster size s_2 ($= M_2/M_1$) and the first moment of the cluster size distribution M_1 (total mass or monomer number density) can give a measure of the average cluster number density as

$$n_2 = M_1 / s_2 = M_1^2 / M_2 . \tag{6.7}$$

Using Eq. (6.5) the time derivative of Eq. (6.7) can be given by

$$\frac{dn_2}{dt} = -\left(\frac{M_1}{M_2}\right)^2 \frac{dM_2}{dt} = -n_2^2 P_2 K(s_2, s_2) . \tag{6.8}$$

Thus

$$K(s_2, s_2) = P_2^{-1} \frac{d}{dt}\left(\frac{1}{n_2}\right). \tag{6.9}$$

Using Eq. (6.9) the aggregation kernel $K(s_2, s_2)$ was determined from the rate at which $1/n_2$ evolved with time. We used $P_2 = 1.10$ as the polydispersity index determined numerically for DLCA (Oh and Sorensen, 1997). Fig. 6.5 shows a typical example of the plot of the measured inverse cluster number density $1/n_2$ versus time t for our aggregating system. The

slope of this curve divided by the polydispersity index P_2 gives the value of aggregation kernel $K(s_2, s_2)$ for the equal sized clusters in accordance with Eq. (6.9).

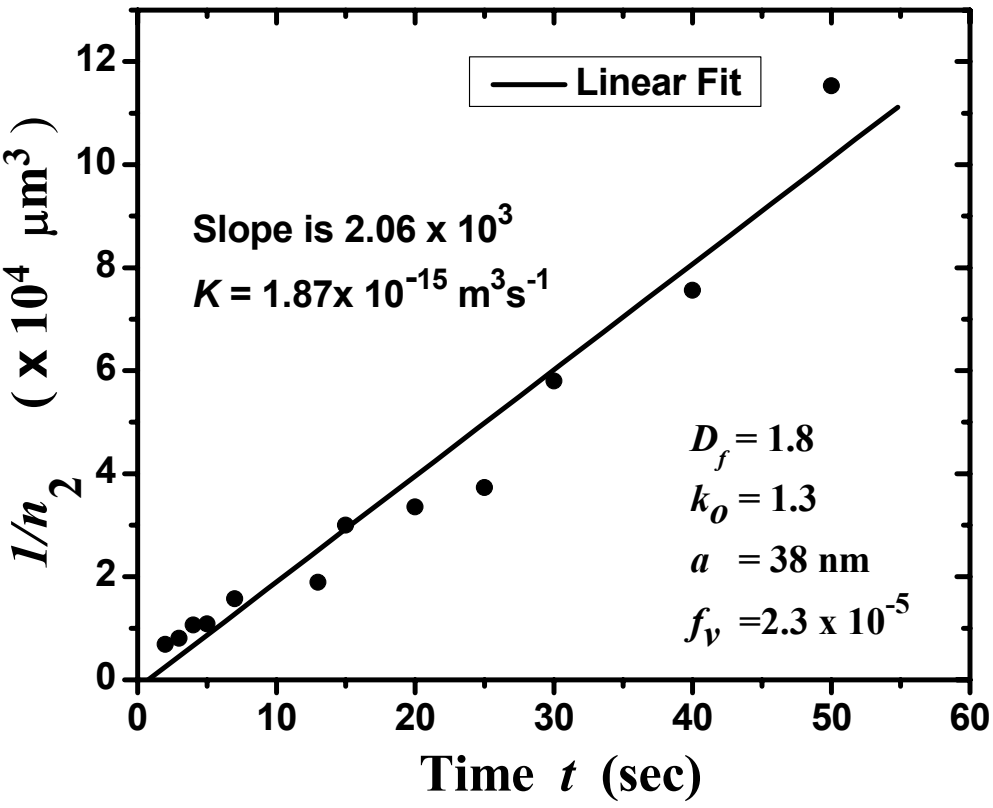

Figure 6.5: An example of the plot of the inverse cluster number density 1/ n_2 versus time t when $f_v = 2.3 \times 10^{-5}$.

Fig. 6.6 gives the values of $K(s_2, s_2)$ as a function of the monomer volume fraction f_v for our carbon soot system. Vertical bars in the plot represent the errors in $K(s_2,s_2)$ due to the error introduced while determining the rate of change of the inverse cluster number density with time. The values of $K(s_2, s_2)$ lay in the range 1.5×10^{-15} to 5.0×10^{-15} m^3/sec and increase slightly with f_v. This indicates the speeding up of aggregation kinetics as f_v was increased. This result is strongly influenced by the soot refractive index value chosen from a broad range of values available in the literature.

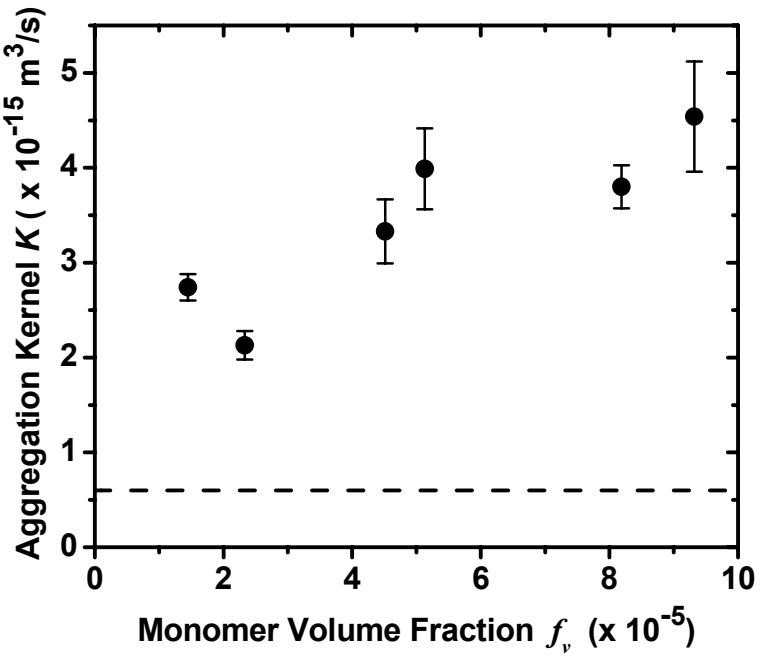

Figure 6.6: A plot $K(s_2, s_2)$ as a function of the monomer volume fraction f_v. The dashed line shows the theoretical value of K independent of the monomer volume fraction. The theoretical K was computed for a monodisperse aggregating system in continuum regime with Stokes-Einstein diffusion.

An uncertainty in the values of $K(s_2,s_2)$ in Fig. 6.6, due to an uncertainty in the soot refractive index, was introduced through an error Δf_v in determining the monomer volume fraction f_v. Using Eqs. (6.4) and (6.9), we derived this uncertainty ΔK in $K(s_2,s_2)$ as

$$\Delta K = \left(\Delta f_v / \bar{f}_v\right)\overline{K}(s_2, s_2)\,. \tag{6.10}$$

Here $\bar{f}_v$ and $\overline{K}$ are the respective averages. The uncertainty Δf_v was caused by uncertainties in $E(m)$ (= Im[$(m^2 - 1)/(m^2 + 2)$]) and the albedo ω (due to an uncertainty in m). From Eqs. (5.9) and (5.11), we derived the following relation for Δf_v.

$$\Delta f_v / \bar{f}_v = \frac{\Delta\omega}{(1-\bar{\omega})} + \frac{\Delta E(m)}{\bar{E}(m)}\,. \tag{6.11}$$

For our soot aggregating system we have $\overline{\omega} = 0.357$, $\Delta\omega = 0.090$, $\overline{E}(m) = 0.260$ and $\Delta E(m) \approx 0.080$ (see section 5.3.2.1.). Hence we found ~ 43% uncertainty in f_v, which propagated into the measurement of $K(s_2,s_2)$ through Eq. (6.10). Thus our measured values of $K(s_2,s_2)$ had an uncertainty of ~ 43%. However, despite this huge uncertainty, our conclusion about the qualitatively increasing trend in the values of $K(s_2,s_2)$ with volume fraction is still reliable.

Fig. 6.6 also shows the comparison of $K(s_2,s_2)$ with the theoretical value (Eq. (3.41)) for a dilute monodisperse system in the continuum regime of a gaseous medium aggregating with Stokes-Einstein diffusion at the room temperature. The theoretical K is independent of the monomer volume fraction. The measured values of $K(s_2,s_2)$ were found to be larger by a factor of 3.5 or higher compare to the theoretical value. The discrepancy can most likely be explained by the assumptions of the system to be dilute and monodisperse aggregating with Stokes-Einstein type diffusion with uncorrelated binary collision while computing the theoretical value of K. For a real system the case is always polydisperse and the assumption of uncorrelated binary collision may no longer hold true especially once the system enters the cluster dense regime.

6.4. CONCLUSION

By employing the SASLS technique we investigated the aggregation kinetics of an aggregating aerosol system at different monomer volume fractions. We found $z \approx 1$ (and $\lambda \approx 0$) consistent with the cluster dilute, DLCA case at lower monomer volume fractions f_v. With increasing monomer volume fraction f_v, z (and λ) was also found to increase up to 1.9 (and λ up to 0.4) indicating the enhanced aggregation kinetics functionality. This result is consistent with simulation results in our laboratory (Fry et al., 2002) indicating the transition of the aggregating system from cluster dilute to cluster dense limit. Our exploration was limited in the monomer volume fraction f_v range extended only between 1×10^{-5} and 1×10^{-4}. This was because gravitational settling was affecting lower f_v systems while higher f_v systems were too turbid for the light scattering purpose. We also found the measured values of $K(s_2,s_2)$ to lie in the range 1.5×10^{-15} to 5.0×10^{-15} m^3/sec and to increase slightly with f_v which indicated the speeding up of aggregation kinetics as f_v was increased.

CHAPTER 7- Aerosol Gelation: Synthesis of a Novel, Light Weight, High Specific Surface Area Material

7.1. INTRODUCTION

Gelation phenomenon in aerosol phase has been first observed in presence of an external electric field (Lushnikov et al., 1990). This gelation is, however, non-spontaneous since external field is required. Subsequently in 1998, Sorensen and coworkers first demonstrated spontaneous superaggregate formation and gelation of soot particles in laminar diffusion flame (Kim et al., 2006, Sorensen et al., 1998). The laminar flame front is thin and complex hence the mechanism for the formation of these superaggregates is uncertain. To avoid the complexity of the flame aerosol we can have a closed chamber system in which aerosols are created instantly and allowed to aggregate. Here we report a novel one-step method to produce porous, low density, high surface area materials via the gelation of non-coalescing nanoparticles in the aerosol phase in such a closed chamber system. We have named these materials *aerosol gels*.

An aerosol system results in gelation if appropriate gelling conditions are established in the system. Aerosol gelation may produce materials having unprecedentedly low densities, high surface areas as well as other useful novel properties. Here we describe aerosol gels made via gelation of carbon and silica nanoparticles. However, our work indicates that any collection of finely divided primary particles with large enough volume fraction can produce an aerosol gel when allowed to aggregate regardless of the chemical composition of the parent primary particles.

For making carbon or silica aerosol gel, the initial aerosol is composed of nanometer sized monomeric particles produced rapidly by exploding any one of a number of precursors to the particles of material with an oxidizer such as oxygen in a closed chamber. The explosive mixture within the chamber is ignited, for example by generation of a spark. These nanometer sized monomeric particles quickly aggregate and then gel to form the aerosol gel.

Aggregation of non-coalescing particles form a ramified structure with a fractal dimension D_f less than the spatial dimension d. Previous simulation studies (Fry et al., 2004, Gimel et al., 1995, Gimel et al., 1999, Hasmy and Jullien, 1996) imply that when $D_f < d$ the average cluster separation to cluster size ratio falls with time during aggregation until the clusters jam together to form a gel. In chapter 3 section 3.13.1., we have derived the time a system takes to gel as

$$t_{gel} \approx \frac{4}{3}\pi K^{-1} a^3 f_v^{-3/(3-D_f)} \qquad \text{(Eq. (3.124))}$$

as well as the cluster radius of gyration at t_{gel} as

$$R_{gel} \approx a\, f_v^{\frac{1}{D_f-3}} \qquad \text{(Eq. (3.119))}$$

under an approximation that the particulate system gels when the monomer number density in the average cluster $n_{cluster}$ is equal to the primary particle number density in the entire system n_{system}. Eq. (3.124) shows a strong functionality of the gel time t_{gel} on the monomer radius a and the monomer volume fraction f_v. A large volume fraction $f_v \geq 10^{-4}$ and a tiny monomer size (a ~10 nm) are required such that the aggregation rate is faster than other characteristic rates such as gravitational settling for a particulate system to gel. The conditions in our chambers are different than this simple example so the details of the gel times will be different, but the important lesson is that aerosols can be made with gel times short enough to be experimentally obtainable.

The properties of the carbon and silica aerosol gels are found to be comparable to those of carbon and silica aerogels respectively. Aerogels represent a very unique and exciting class of solid materials that are generally characterized by a fragile skeletal structure defining highly-accessible, branched mesopores. Aerogels have very unusual properties. For example, carbon aerogels are the first electrically conductive aerogel materials. Also silica aerogels have perhaps the best thermal insulators available, a high transparency that is close to that of glass, and very high specific surface areas. However, the process of making aerogels is complicated. Aerogel production is critically dependent on the liquid-based sol-gel process and, more importantly, the

complex supercritical drying process necessary to remove the gel liquid without damaging the network structure.

Our method of making aerosol gels overcomes the complexities involved in making conventional aerogels. This method of making an aerosol gel is not a wet process and does not require a catalyst. The process yields highly desirable low density, high surface area ramified fractal aggregate gels, while completely avoiding the time consuming and difficult solvent removal steps of the prior art.

In the following subsections we present discussions on the creation of dense carbon and silica aerosols in closed chambers, and the properties of the aerosol gel materials subsequently forming due to dense aerosol aggregation.

7.2. CARBON AEROSOL GEL

In the case of the carbon aerosol gel the initial aerosol is composed of nanometer sized carbon particles produced rapidly by exploding any one of a number of hydrocarbons with oxygen in a closed chamber. The carbon aerosol gels have properties comparable to those of the well-known carbon aerogels prepared by pyrolyzing sol-gel synthesized resorcinol-formaldehyde (RF) or melamine/formaldehyde (MF) precursors via the sol-gel process followed by supercritical drying (Pekala et al., 1994, Reynolds et al., 1996). This carbon aerosol gel is significantly different than ordinary carbon black and soot formed as byproducts during combustion of any hydrocarbon fuel; it is a new material.

7.2.1. EXPERIMENTAL METHODS

The carbon aerosol gel was made by exploding a mixture of a hydrocarbon and oxygen in a chamber at one atmosphere pressure. A conventional spark plug having its electrode within the chamber was used to ignite the mixture; the spark was generated using a Tesla coil coupled to the spark plug. Generation of the spark caused an instantaneous explosion which rapidly produced nanometer-sized (up to about 50 nm) roughly spherical carbon particles, which quickly aggregated to form carbon aerosol gel in the chamber under essentially quiescent conditions. The

explosion was carried out in two different thick walled aluminum cylindrical chambers with different sizes. The larger chamber had a volume of 16.6 liters (Fig. 5.1a); the smaller a volume of 3.9 liters (Fig. 5.1b). The chambers were first evacuated and then back filled with an explosive gas mixture in various proportions between the lower and upper explosive limits (e.g., 2 parts acetylene by volume/1 part oxygen by volume). Precautions were used while setting off the gas mixture in the chamber by standing clear back and using wired remote switch for the Tesla coil. Aerosol gel results were chamber independent.

Methane (CH_4), acetylene (C_2H_2), ethylene (C_2H_4) and propane (C_3H_8) were used as gaseous hydrocarbon fuels. Liquid hydrocarbons used were butane (C_4H_{10}), pentane (C_5H_{12}), hexane (C_6H_{14}) and isooctane (C_8H_{18}) (Gerving, 2004). Butane has highest vapor pressure (1557 mm of Hg at 20^{o}C) and lowest boiling point (-0.5^{o}C), so vaporizes instantly and can be exploded like other gaseous hydrocarbons. Pentane and hexane have vapor pressures of 433 and 131 mm of Hg at 20^{o}C, respectively, and boiling points 36.1 and 68.7^{o}C, respectively. Thus they can be easily vaporized by increasing the temperature slightly and waiting for few minutes, and then can be exploded easily inside the chamber. Isooctane has lowest vapor pressure 41 mm of Hg at 20^{o}C and highest boiling point 99^{o}C and thus is a little harder to deal with. To explode, aerosols of isooctane microdroplets were first prepared by using an ultrasonic nebulizer, which were then sprayed into the chamber filled with oxygen (Gerving, 2004).

There are minimum and maximum limits called Lower Explosion Limit (LEL) and Higher Explosion Limit (HEL) for the mixing proportion of a hydrocarbon fuel and oxygen in order to explode. Material Safety Data Sheet (MSDS) lists the LEL and HEL in terms of the percentage of the fuel in a fuel-air mixture (MSDS (Material Safety Data Sheet), 1970). These LEL and HEL were recalculated to account for a pure oxygen environment and used to prepare the mixture ready for explosion in the chambers. The following chemical reaction was expected to occur ideally during the hydrocarbon and oxygen gas mixture to liberate carbon atoms which quickly nucleated to form namometer sized carbon monomers.

$$a\,C_xH_y + b\,O_2 \rightarrow a \cdot x\,C + 2b\,H_2O\,. \tag{7.1}$$

Here ‘a’ and ‘b’ are coefficients, and ‘x’ and ‘y’ are variables such that 2b = a*y.

After the explosion, the chamber with the aggregating aerosols within was allowed to sit quiescently for several minutes before opening, to allow the aggregating system to gel and settle undisturbed within the chamber.

7.2.2. RESULTS AND DISCUSSION

The chamber was opened several minutes after exploding the fuel-oxygen mixture to obtain a dark black fluffy carbon layer (Fig. 7.1) on the bottom and some lumps here and there clinging on the walls and ceiling of the chamber for all fuels except methane and butane which did not yield a soot. This layer on the bottom was about 2 cm thick for acetylene and ≤ 3 mm for other hydrocarbon fuels in the 16.6 liter chamber. These results seem to imply that the aerosol gel was a result of sedimentation and wall deposition and not the gelation process.

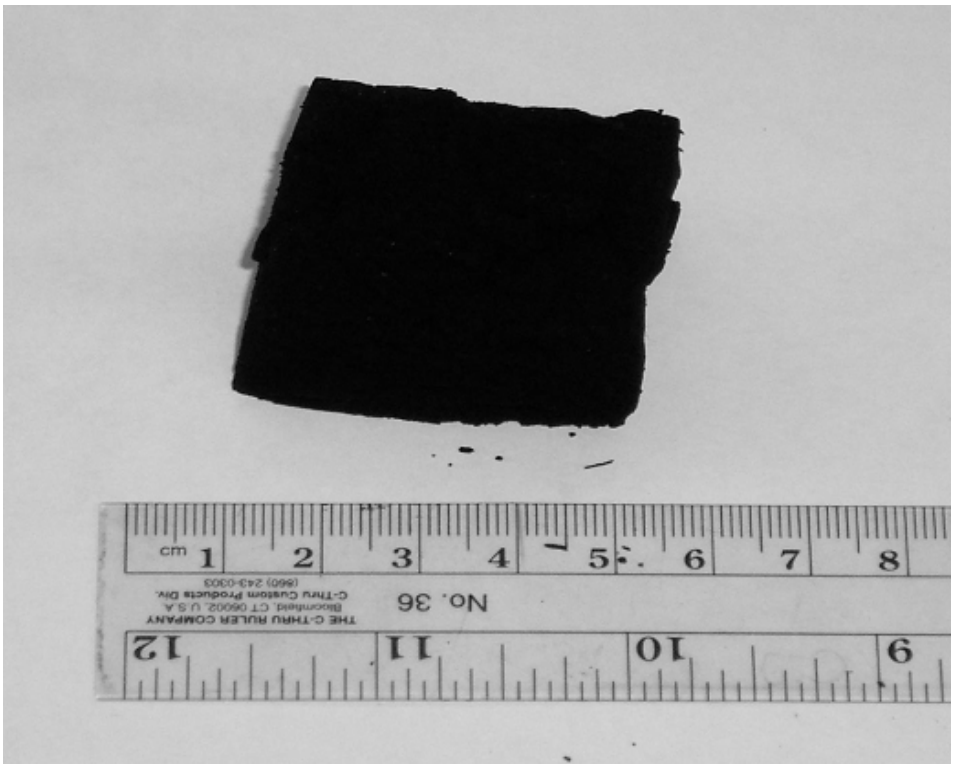

Figure 7.1: Carbon aerosol gel, density = 2.5 mg/cm^3.

When the chamber was opened within a minute or less after the explosion, however, we observed that it was completely filled with a very delicate aerosol gel which usually collapsed,

like a “falling” cake, to yield the deposits on the bottom and walls. Sometimes, when the chamber was opened after the explosion, the air convection from the removal of the lid caused chunks of aerosol gel several centimeters in size to fly out of the chamber. A series of top view pictures in Fig. 7.2 demonstrates the gravitationally collapsing aerosol gel network from acetylene in the chamber. Picture (a), taken 2 minutes after creating the aerosol and 5 seconds after opening the lid, shows the gel filled almost to the top of the 24 cm wide 37 cm deep chamber. The aerosol gel collapsed somewhat 30 sec after the lid was opened (Picture (b)). Picture (c) indicates that the gel collapsed by more than half the depth of the chamber 1 min after opening the lid. Further collapsing was relatively slow. Pictures (d) and (e) were taken 1.5 min and 2 min, respectively, after opening the chamber. Finally, picture (f) taken 20 min after the chamber was opened shows a completely collapsed gel to about 2 cm thick layer on the bottom of the chamber.

These pictures graphically demonstrate that a macroscopic, three dimensional gel can form from the aggregation of an aerosol. During the aggregation, the mean cluster size of the aerosol has grown from the monomer size of about 50 nm to the container size of nearly 0.5 meter, a change of seven orders of magnitude!

In other work we used a thin cylindrical disc chamber with circular glass windows on both ends of the cylinder. The internal space of the chamber was 51mm diameter wide and 10mm thick. This chamber was used for light scattering studies from the gelling aerosol reported in chapter 5 section 5.2. and chapter 6. After acetylene gas was exploded in this chamber, we initially observed an unresolved aerosol that coarsened with time until a volume spanning gel network formed within ca. 100 seconds (see Fig. 6.1).

From a broad perspective this aerosol gel we collect from the bottom and walls of the chamber was a result of an aerosol gelation process likely involving Brownian motion during the major growth period, then convection, wall deposition and gravitational settling.

With success in producing the aerosol gels from different liquid and gaseous hydrocarbon fuels we concentrated mostly on detail studies of the aerosol gel from acetylene and some other gaseous hydrocarbons.

Figure 7.2: A series of top view pictures of gravitationally collapsing acetylene aerosol gel in the 24 cm wide 37 cm deep chamber. (a) The gel was found to fill almost to the top 2 minutes after creating the aerosol and 5 seconds after opening the lid. (b) The aerosol gel collapsed somewhat 30 sec after the lid was opened. (c) The gel collapsed by more than half the depth of the chamber 1 min later. Relatively slow collapsing was observed afterwards. (d) 1.5 min later. (e) 2 min later. (f) Gel collapsed completely to about a 2 cm thick layer 20 min later.

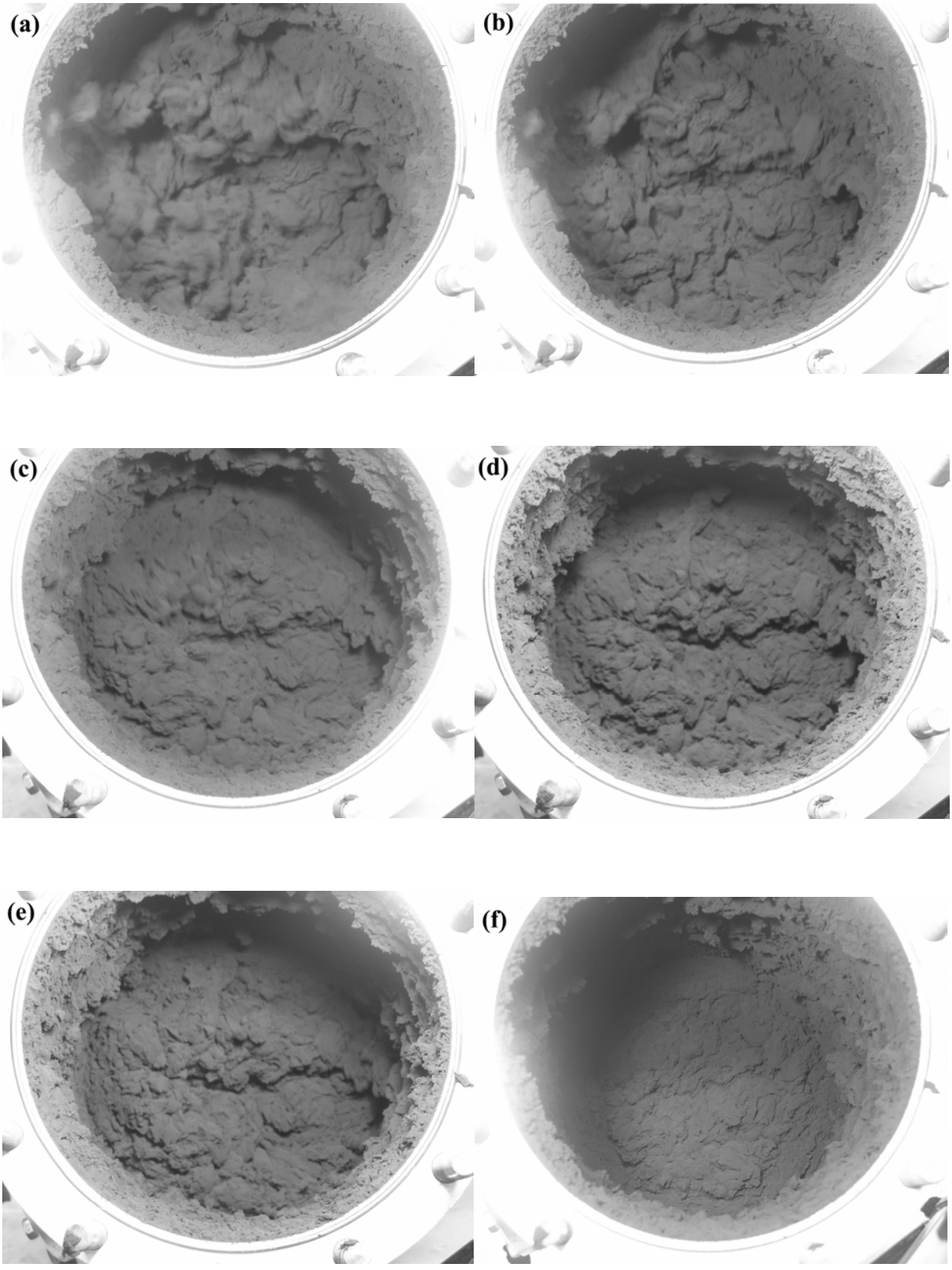
(a)
(b)
(c)
(d)
(e)
(f)

7.2.2.1. Density Measurement

The density of the carbon aerosol gel was determined by measuring the mass of a known volume of the sample using an electronic balance with sensitivity of 1 mg. Table 7-1 lists the densities of the carbon aerosol gels produced from the various hydrocarbons. The aerosol gel density is measured as low as 2.0 mg/cm^3, which is extraordinarily low. This density is less than twice the density of dry air at STP and is lower than any known solid or liquid material. The density measurements were qualitatively double checked by measuring the time taken by a roughly spherical aerosol gel to fall in air through a known height under the influence of gravity. Although the aerosol gel is delicate and fragile, it is still found capable to withstand a weight about 20 times itself without being crushed.

The aerosol gel was compressed by hand to examine the change in its density. Although the pressure involved in this process was unknown, the process was good enough to produce a homogeneous product for density measurement and to show how the specific surface area and electrical conductivity behave as a function of density (see subsections 7.2.2.2. and 7.2.2.4.). The density was found to be about 300 mg/cm^3, an order of magnitude lower than graphite, even after grinding by hand in a mortar and pestle and then tightly compressing into a 5 cm long circular tube with 8 mm internal diameter. This shows that there are still voids preserved even after applying high pressures. The rigid bond between the primary particles could be the reason for not being able to be close packed. It was noticed that the compressed aerosol gel expands back to some extent when the compressing force is removed showing elastic behavior.

Table 7-1: Aerosol gel densities for numerous synthesis runs obtained for selected fuels.

Hydrocarbon Fuels	Density		
	Lowest (mg/cm^3)	Highest (mg/cm^3)	Average (mg/cm^3)
Gaseous Fuels			
Acetylene	3.5	6.5	5.0
Ethylene	2.3	3.5	2.9
Propane	2.1	3.3	2.7
Liquid Fuels			
Pentane	2.4	8.6	5.1
Hexane	4.7	5.4	4.9
Isooctane	2.3	11.2	5.8

Note: Pure Graphite has density of 2.25 g/cm^3.

7.2.2.2. Specific Surface Areas and Surface Porosity

The specific surface areas and surface porosity of the black carbon aerosol gels were determined using the Brunauer-Emmett-Teller (BET) analysis technique (Kruk and Jaroniec, 2001) with nitrogen gas as an adsorbate. The results for both uncrushed and crushed samples are listed in Table 7-2. The acetylene and ethylene aerosol gels are found to have a high specific surface area of 350 m^2/g while propane aerosol gel is found to have a lower specific surface area of 130 m^2/g for uncrushed samples. If we assume the material density within a primary particle to be equal to that of graphite the BET results suggest an effective primary particle size, assumed to be spherical, of about a = 10 nm for propane aerosol gels and a = 4 nm for acetylene and ethylene aerosol gels, respectively. Acetylene aerosol gels are found to have a large specific mesopore volume of 0.56 cm^3/g for pores smaller than 135 nm diameter at relative pressure 0.986. The average pore diameter for this aerosol gel is measured to be 11.8 nm.

Table 7-2: Listing of the BET results averaged over different runs. The densities are about 10 mg/cm^3, higher than as prepared, due to some crushing during sample preparation.

	Uncrushed Aerosol Gel		Crushed Aerosol Gel	
	Sample Density (mg/cm^3)	Specific Surface Area (m^2/g)	Sample Density (mg/cm^3)	Specific Surface Area (m^2/g)
Acetylene Aerosol Gel	10	350	160	150
Ethylene Aerosol Gel	10	350	50	200
Propane Aerosol Gel	10	130	100	100

7.2.2.3. Microscopic Structure of the Carbon Aerosol Gel

Figs. 7.3a, 7.3b and 7.3c show transmission electron microscopy (TEM) pictures for acetylene, ethylene and propane aerosol gels, respectively. These pictures show that the aerosol gels are ramified fractal structures with pores trapped inside. Primary particles with typical size a = 38 nm are found for both acetylene and ethylene aerosol gels. Propane aerosol gels have a smaller primary particle of typical size a = 10 nm. The primary particles of acetylene and propane aerosol gels are more or less polygonal in structure. In the Ethylene aerosol gel the primary particles are not well defined. Instead the structure looks like a thin ribbon with thick borders. From these TEM images it appears that the primary particles of the aerosol gels from acetylene and ethylene have graphitic layer planes a few nanometers thick around the surface with their planer orientation parallel to the particle surfaces forming a shell-like structure. What appear to be encapsulated inside this shell are either voids or amorphous carbon with more random crystallite orientation. These graphitic layer planes are quasi-crystalline and can be referred to as nanocrystals. In the case of the primary particles of the aerosol gel from propane the graphitic layer planes are not distinct. Fig. 7.4 shows a high resolution TEM image of acetylene aerosol gel primary particles in which the graphitic layer planes are clearly visible.

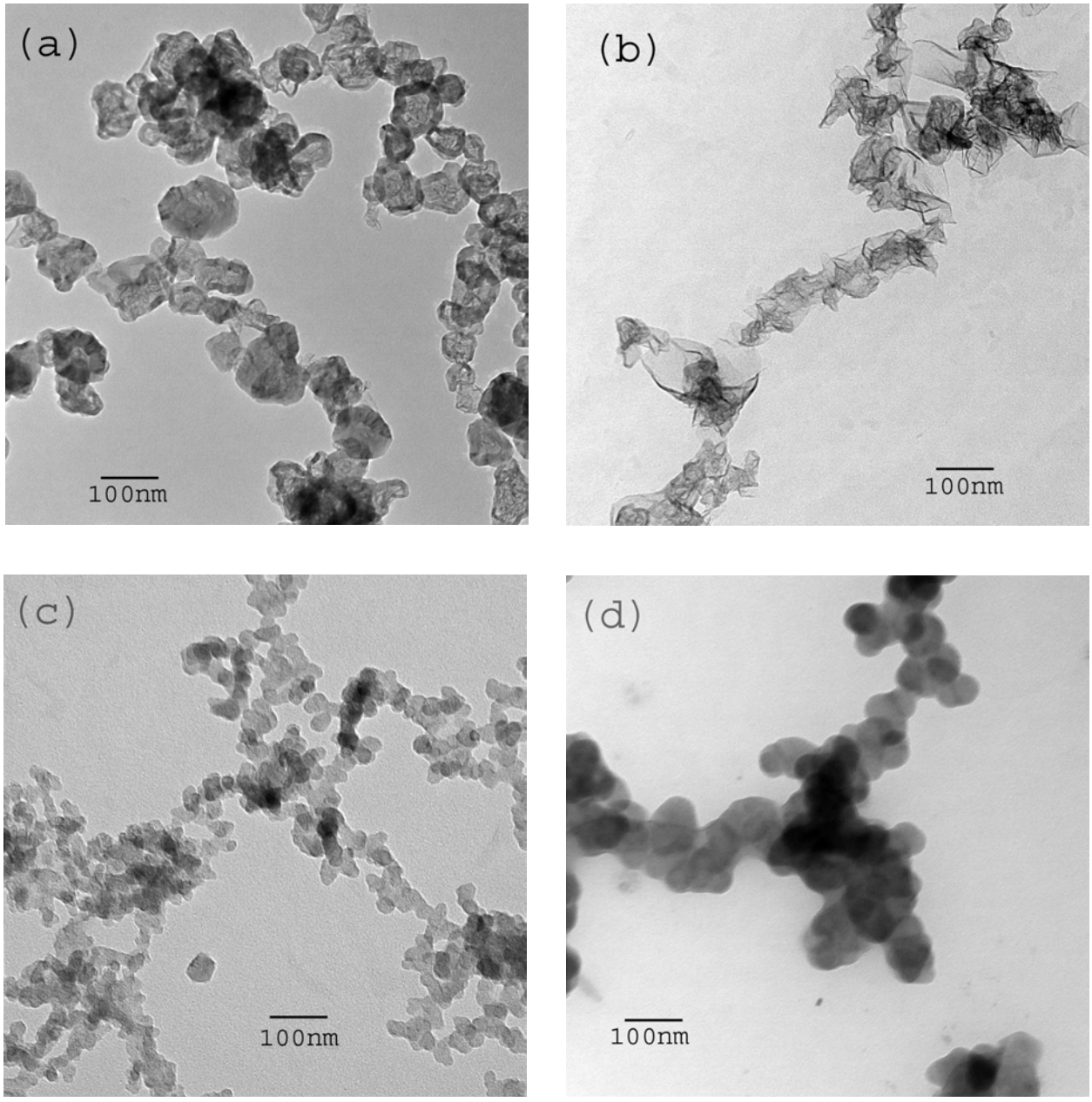

Figure 7.3: TEM pictures of (a) an acetylene aerosol gel (b) an ethylene aerosol gel (c) a propane aerosol gel and (d) an acetylene open flame soot.

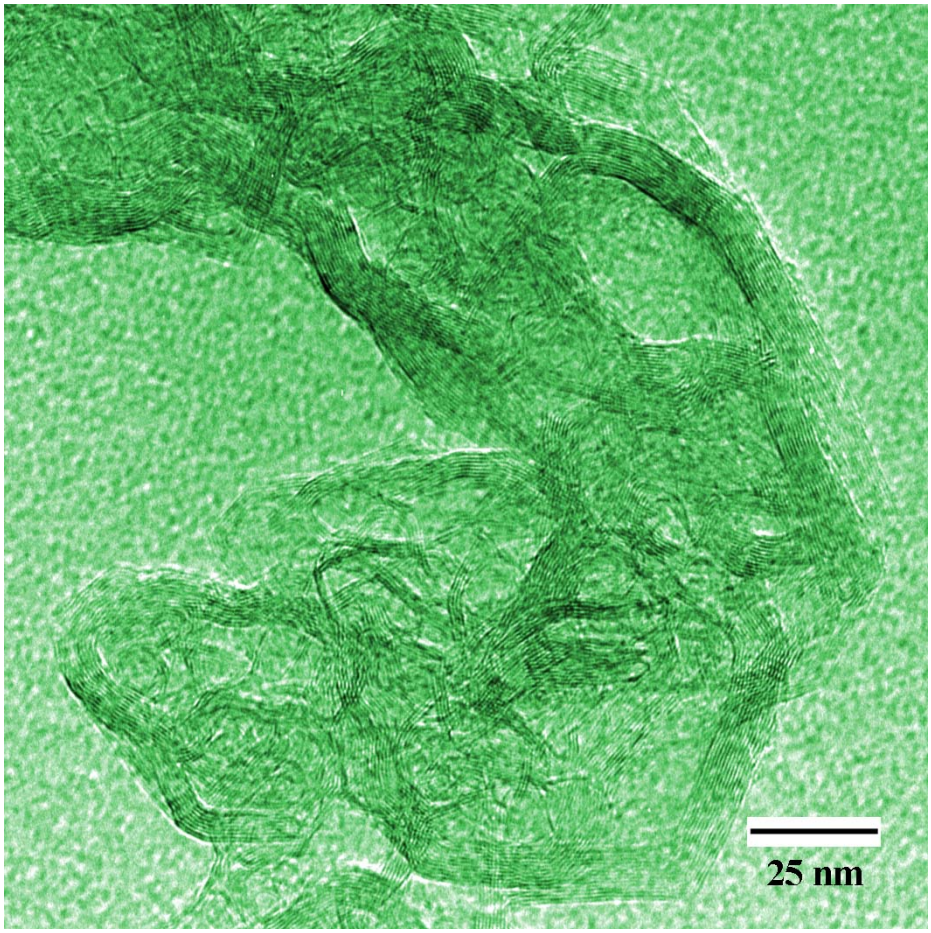

Figure 7.4: A high resolution TEM pictures of an acetylene aerosol gel. The graphitic layer planes are clearly visible and appear to extend only over the surface of the primary particles of the aerosol gel.

The X-ray diffraction (XRD) patterns with distinct peaks also exhibit the crystalline property of the aerosol gel primary particles. Fig. 7.5 shows the XRD patterns for the aerosol gels from acetylene, ethylene and propane. This figure also includes the XRD pattern from an open flame acetylene soot for comparison purpose. An effective sizes of the nanocrystals were determined by Scherrer broadening (Cullity, 1978), i.e. the size is inversely related to the angular width of the (002) diffraction peak. Among the three different aerosol gels investigated, propane aerosol gel has the broadest and acetylene aerosol gel has the narrowest diffraction peaks. From the Scherrer broadening measurement we found the crystallite size to be about 3 nm for acetylene and ethylene aerosol gels and about 2 nm for propane aerosol gel. A careful observation of these XRD patterns also revealed the fact that the (002) peak shifts towards larger

angle as we go from propane to acetylene aerosol gels. This indicates that the graphitic layer plane separation is largest for propane and smallest for acetylene aerosol gels. A range of lattice spacing within a soot monomer has been observed and reported in literature (Franklin, 1950, Palotas et al., 1996, Palotas et al., 1996, Palotas et al., 1998). These graphitic plane separations are found to be 3.59, 3.51 and 3.47 A^o for propane, ethylene and acetylene aerosol gels respectively. The (101) peak observed in the XRD pattern, however, shifts towards smaller angle as we go from propane towards acetylene aerosol gels.

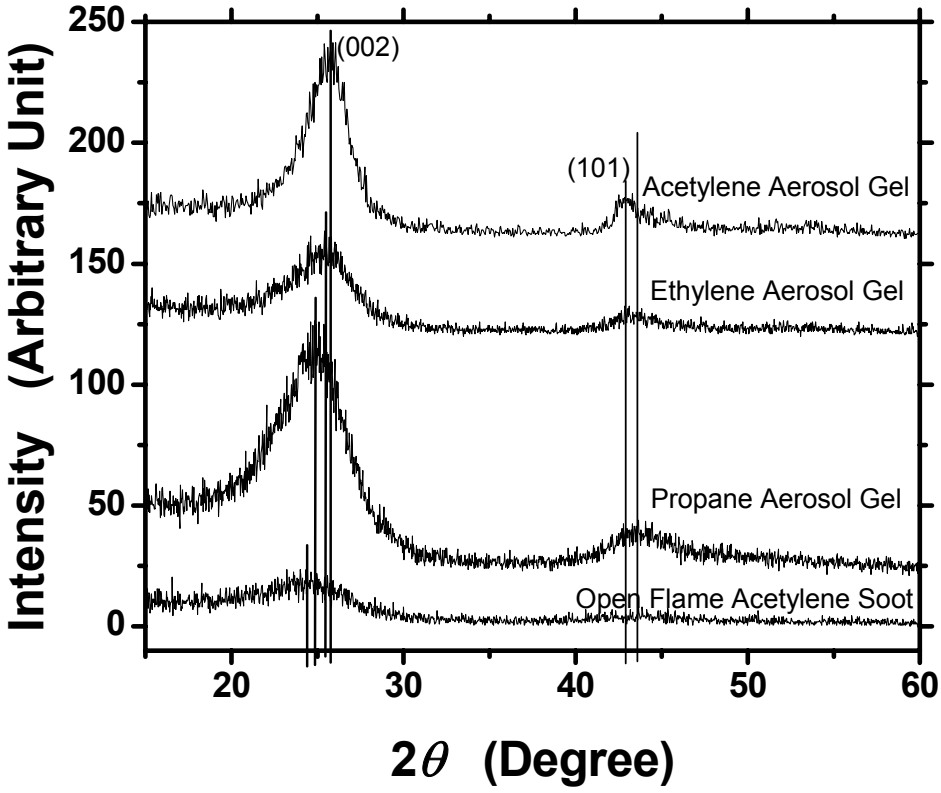

Figure 7.5: X-ray diffraction of the compressed carbon aerosol gels and open flame acetylene soot. The vertical lines indicate the positions of the corresponding diffraction peaks.

The primary particle sizes for acetylene and ethylene aerosol gels as measured from the TEM pictures are bigger compared with those determined from the BET and XRD results. This suggests that these primary particles are multicrystalline and porous. However, the propane

aerosol gel primary particles have sizes measured from TEM images and BET analysis approximately matching suggesting non-porosity. Monomeric particle sizes were measured with a reticle magnifier at roughly ten to twenty locations in the TEM micrographs. This led us to monomer size measurements accurate to 10 to 20 % which we warranted as good enough given the nonspherical, rather polygonal structure of the monomers. Indeed, in many cases the monomers seem to blend from one to the other. Given these morphological challenges, a more accurate determination with concomitant statistical analysis is not warranted. However, comparison to size scales inferred from BET, whatever these scales may be, is of value because they are much different in the cases of acetylene and ethylene precursors.

Thermal Gravimetric Analysis (TGA) showed that there is no significant change, less than 1% in the mass of the carbon aerosol gels, after heating from room temperature up to 600^{o}C (Fig. 7.6). This implied that there are no volatile substances present in the carbon aerosol gels.

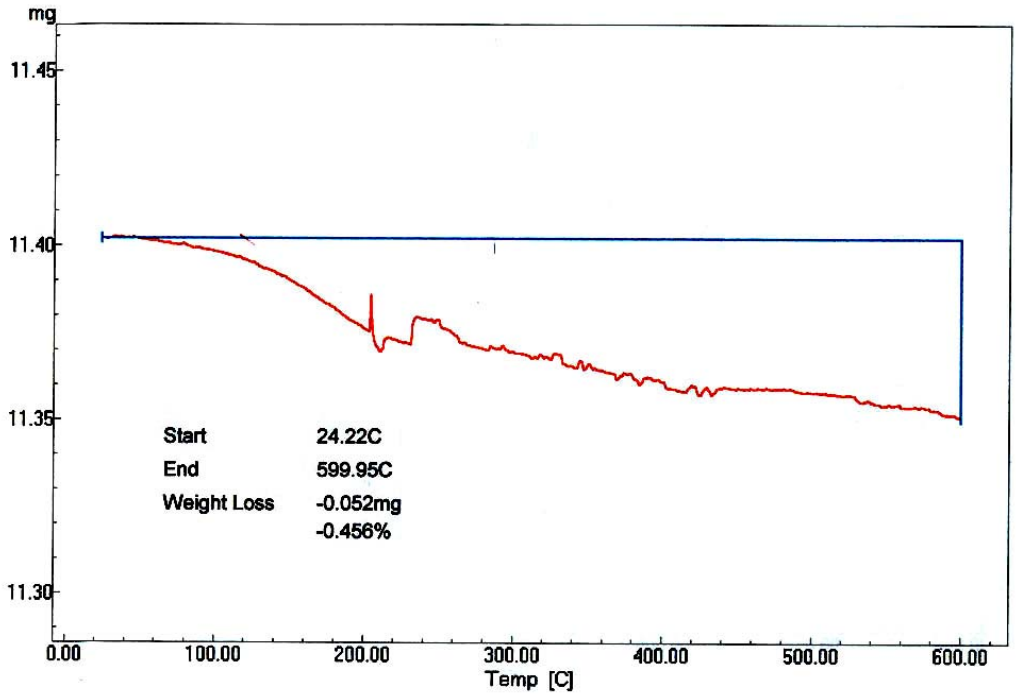

Figure 7.6: Thermal Gravimetric Analysis (TGA) showing less than 1% change in the total mass of the carbon aerosol gels after heating from room temperature up to 600^{o}C. This is an indication of the absence (or negligible presence) of volatile substances in the carbon aerosol gels.

The existence of elemental composition in the aerosol gel was also examined using Energy Dispersive X-ray spectroscopy (EDS).The characteristic X-rays are produced when the material is bombarded with electrons in an electron beam. Detection of these X-rays was accomplished by using an energy dispersive spectrometer, which is a solid-state device that discriminates among X-ray photon energies. The result from Energy Dispersive X-ray spectroscopy (Fig. 7.7) shows only the peak corresponding to the elemental carbon present in the aerosol gel revealing that it does not consist of any other higher elemental composition.

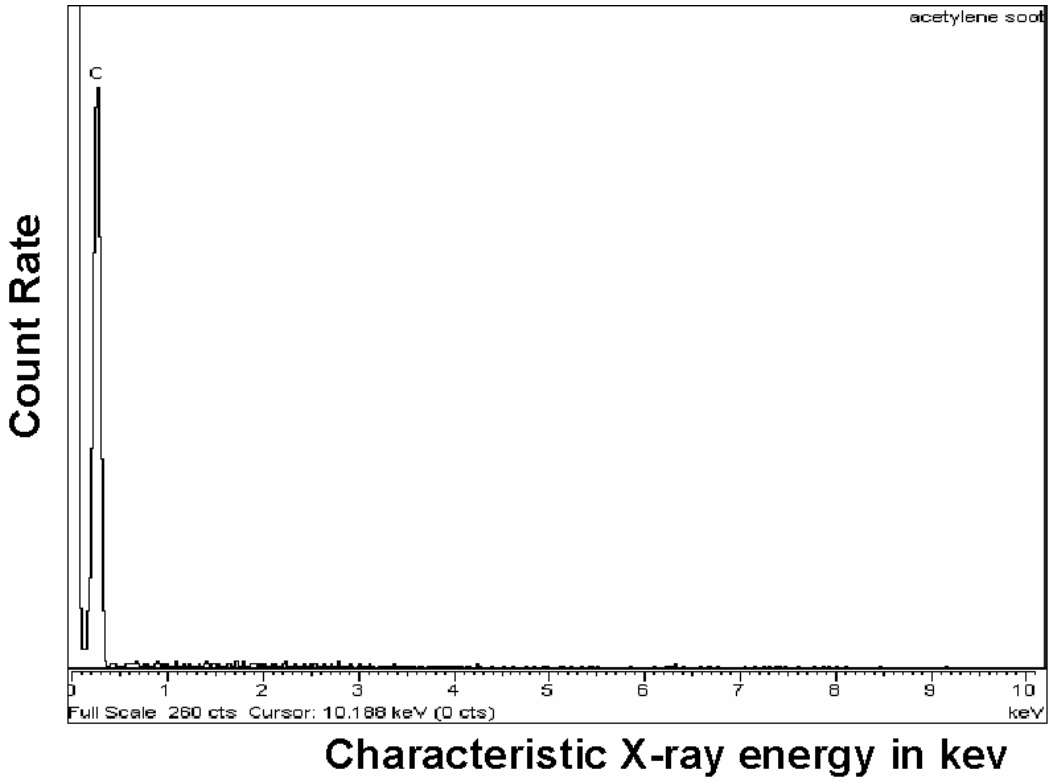

Figure 7.7: Energy Dispersive X-ray spectroscopy (EDS) result showing only the peak corresponding to the elemental carbon present in the carbon aerosol gel.

7.2.2.4. Electrical Conductivity of the Carbon Aerosol Gel

The aerosol gel is found to be a good conductor of electricity with its conductivity increasing quadratically with increase in its density. This is unusual since most materials have a linear dependence. The aerosol gel was packed in an 8 mm internal diameter 5 cm long glass tube capped with brass terminals to measure the electrical conductivity. Figure 7.8 shows the conductivity versus density plot for acetylene aerosol gel. This plot also includes the conductivity for graphite (density 2250 mg/cm^3), which is 142.86 Ω^{-1}cm^{-1}. As is clear from the plot, the conductivity for the carbon soot with density 4.0 mg/cm^3 is 2.86 x 10^{-4} Ω^{-1}cm^{-1}, which is comparable to those of semiconductors.

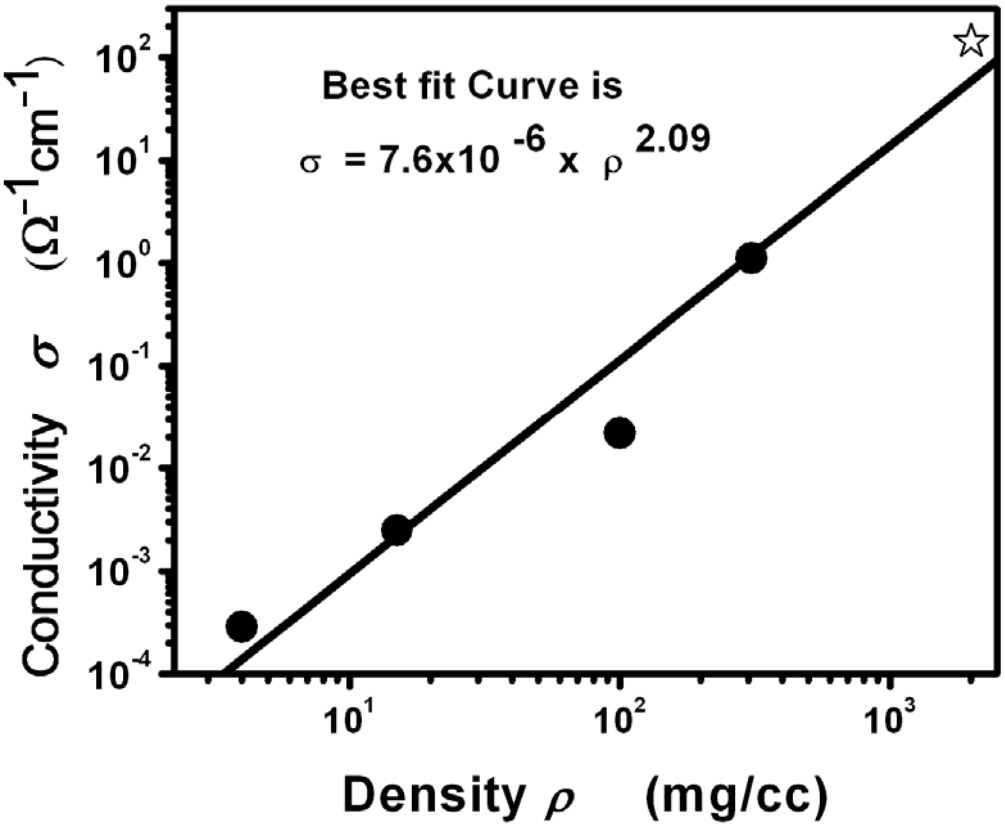

Figure 7.8: Log-log plot of conductivity vs density at room temperature for acetylene aerosol gel. Quadratic variation of conductivity with density is observed. The data final point indicated by a star sign is for pure graphite.

7.2.2.5. Hydrophobicity of the Carbon Aerosol Gel

The carbon aerosol gel was also found to be highly hydrophobic. Fig. 7.9 demonstrates the hydrophobicity of a crushed aerosol gel with an almost spherical water droplet about 2 mm in size with a very high contact angle. The crushed aerosol gel surface showed a very low flow resistance for water. The degree of hydrophobicity was found to decrease in the case where sample was heavily crushed, e.g. by hammering. This property of hydrophobicity of the aerosol gel is interesting because the material of the aerosol gel, i.e. carbon, does not possess this character in itself. We explain this hydrophobic property of the aerosol gel as a result of the dendritic structure of the aerosol gel. A high degree of surface roughness often results in a substantial increase in the degree of hydrophobicity of the solid substrate (Krupenkin et al., 2004, Otten and Herminghaus, 2004).

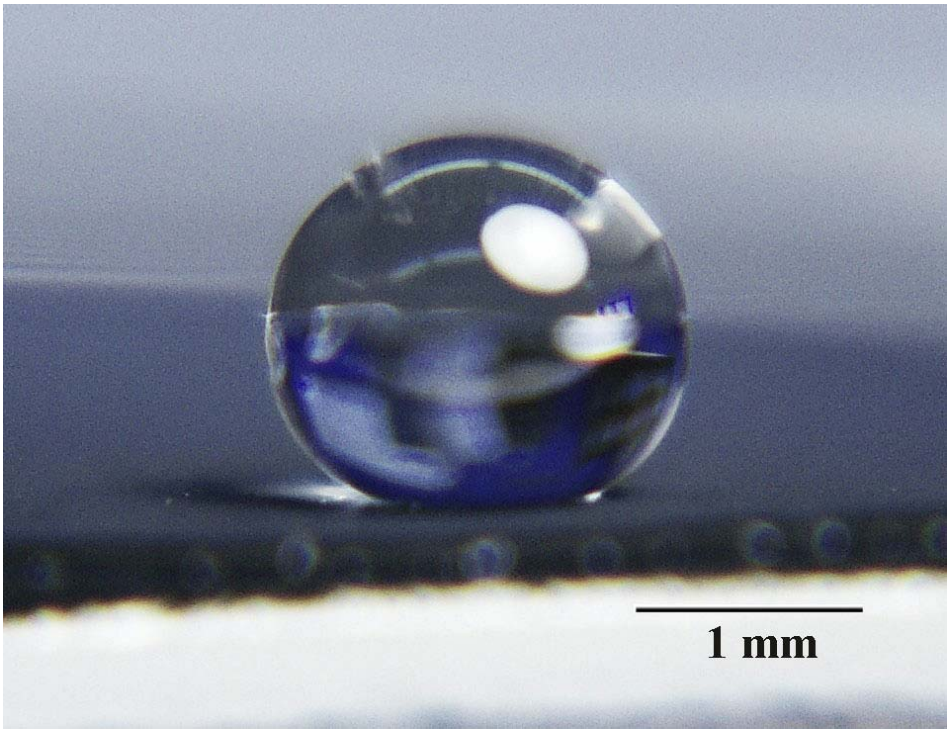

Figure 7.9: Almost spherical shaped water droplet, about 2 mm in diameter, sitting on the surface of a crushed carbon aerosol gel. A large contact angle demonstrates the hydrophobic behavior of the carbon aerosol gel.

7.2.2.6. Comparision with a Normal Open Flame Soot

The aerosol gel was compared with a normal open flame soot. The sample of an open flame soot was collected from an acetylene-air diffusion flame produced on a simple diffusion burner. The density of the open flame soot is found higher, ca. 13 mg/cm^3. Unlike the dark black aerosol gel, the open flame soot is dark gray in color. This indicates that the open flame soot might have contained hydrocarbons. A TEM comparison of the open flame soot shown in Fig. 7.3d to the aerosol gels shown in Figs 7.3a, 7.3b and 7.3c shows that the open flame soot monomers are more rounded in shape and uniform, without a noticeable graphitic nature, unlike the graphitic polygonal shaped crystalline aerosol gel monomers. The XRD pattern for the open flame acetylene soot (Fig. 7.5) shows a weak (002) and unnoticeable (101) peaks implying the amorphous nature unlike the aerosol gels. The position of (002) peak suggests the graphitic layer plane separation to be 3.66 nm, which is larger compare to those of the aerosol gels. The monomer diameter ($2a$) for an open flame soot is about 60 nm. The electrical conductivity of the open flame soot is found to be three orders of magnitude lower than that for the aerosol gel. However, two common characteristics were observed, i.e., both types of soot were hydrophobic and could be soaked with solvents like toluene. When crushed hard with a pestle, the aerosol gel became shiny showing its graphitic nature, but the open flame soot was still dull.

7.2.3. CONCLUSION

We have used a novel gelation of particles in the aerosols phase to create a new material that we have named aerosol gel. The nanoparticle aerosol was created by an explosion of a hydrocarbon/oxygen mixture. Aerosol gels have unusual properties including ultralow density and high specific surface area and thus are similar to well-known aerogel materials. We believe the aerosol gels have advantages over conventional aerogels made via the sol-gel process (Brinker and Scherer, 1990) in the sense that no supercritical drying step is required and thus complexities involved can be avoided. Though we have just produced carbon aerosol gels, our technique has the potential to lend itself to a wide class of materials, including those which have been developed into aerogels via the sol-gel process.

7.3. SILICA AEROSOL GEL

Aerosol gelation being a physical phenomenon, it should be possible to make aerosol gel of any material by aggregating particles provided the monomers are small enough (~10 nm) and monomer volume fraction f_v is high enough ($\geq 10^{-4}$). With this idea we extended our research successfully in making silica (SiO_2) aerosol gels after succeeding in making carbon aerosol gel. We chose SiO_2 among wide variety of materials since there is increasing interest in this material due to its immense potential applications. Silica aerosol gels were prepared by spontaneous explosive reaction of monosilane (SiH_4) with an oxidizing gas such as oxygen (O_2) or nitrous oxide (N_2O). These reactions were performed in the presence of an inert background gas such as nitrogen (N_2) or carbon dioxide (CO_2), but otherwise the procedure used was the same as that set forth in section 7.2. for the preparation of carbon aerosol gels.

We found that the resultant silica aerosol gels were very fluffy, translucent and bluish-white in color. Silica aerosol gels had low densities in the range 4 to 6 mg/cm^3 and specific surface areas as large as 500 m^2/g. These properties were closer to those of conventional silica aerogels. Silica aerogels are perhaps the best investigated material in inorganic chemistry traditionally produced via a base-catalyzed reaction of tetramethoxysilane (TMOS) or tetraethoxysilane (TEOS), usually with ammonia as the catalyst. Once gelation is complete, the resulting liquid in the wet gel foam is then removed via supercritical drying. The type and concentration of the precursors, the relative concentrations, the type of solvent, the temperature, and the pH of the sol-gel process all have a definitive effect on the resulting structure and properties of the silica aerogel.

We explain the details on experimental setup for preparing silica aerosol gels and the results in the following subsections.

7.3.1. EXPERIMENTAL SETUP

Even though SiH_4 is similar to CH_4 in chemical structure where C atom is replaced by Si atom, it, being a pyrophoric gas, spontaneously oxidizes to SiO_2 whenever it sees an oxidizer unlike CH_4. We were thus required to have a special arrangement for instant creation of an

aggregating system of SiO_2 monomers in a closed chamber by mixing and safely exploding silane with an oxidizing gas.

A schematic diagram of the experimental set up for creating silica aerosol gel is illustrated in Fig. 7.10. The explosion chamber was a thick walled aluminium chamber having a volume of 3.9 liters with 12.5 cm internal diameter and a 31.5 cm height. This explosion chamber was connected to two reservoirs, each through an electric solenoid valve and a one-way spring-loaded piston check valve. One of these reservoirs contained silane while the other contained an oxidizing gas. Arrangements were also made such that a vacuum can be pulled and an inert background gas (e.g., N_2, CO_2, He, etc.) could be introduced in the explosion chamber as well as the reservoirs. The silane gas cylinder was equipped with a cross purge system to handle the pyrophoric gas. We used N_2 as the purging gas. The whole arrangement was placed under an exhaust hood for the safety purpose. Fig. 7.11 shows a picture of this arrangement.

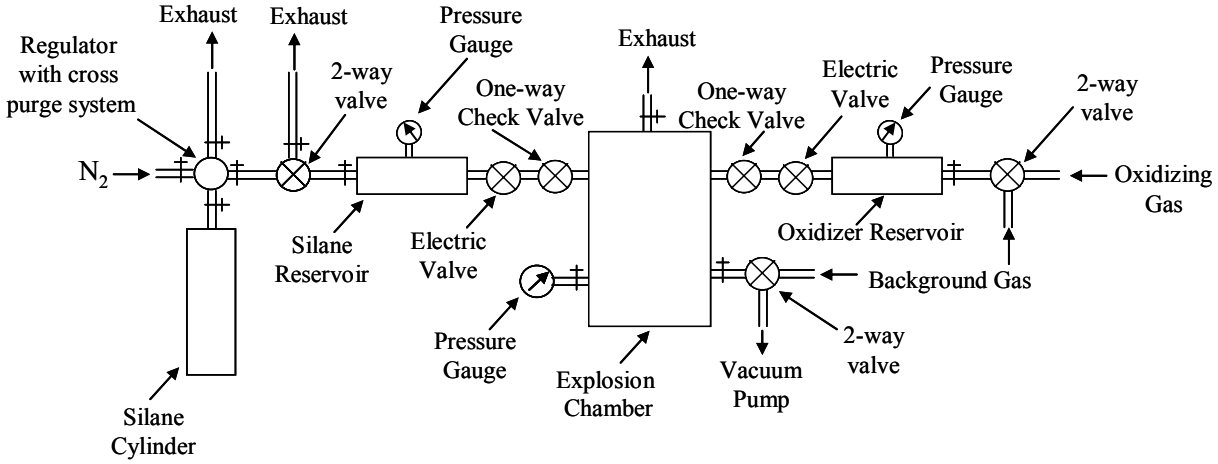

Figure 7.10: A schematic diagram of the experimental setup for making a silica aerosol gel.

We experimented making the silica aerosol gel by allowing silane and oxygen or nitrous oxide to mix in the explosion chamber in various ways. We studied the effect of simultaneous mixing of two gases, introducing an oxidizing gas to pre-existing silane in the explosion chamber and introducing silane to the pre-existing oxidizing gas in the chamber. We varied the amount of silane being introduced into the explosion chamber to change the silica monomer volume fraction. We also investigated the effect of the background gas partial pressure in the explosion chamber.

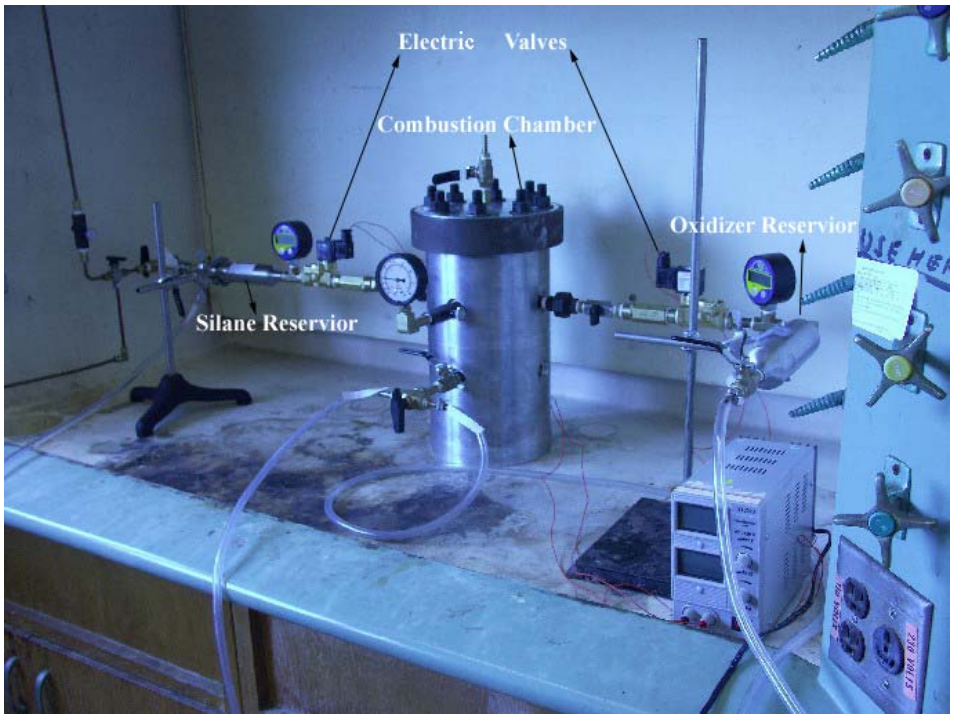

Figure 7.11: Experimental setup for making Silica Aerosol Gel. Apparatus arrangement under an exhaust hood. Different components are as labeled.

The silica aerosols were created by a violent oxidation of silane. The ideal stoichiometry for these chemical reactions with O_2 and N_2O are

$$SiH_4 + 2\,O_2 \rightarrow SiO_2 + 2\,H_2O \tag{7.2}$$

and

$$SiH_4 + 4\,N_2O \rightarrow SiO_2 + 2\,H_2O + 4\,N_2\,. \tag{7.3}$$

Safety precautions were exercised by remotely releasing the electric solenoid valve(s) using a wired electric switch. After hearing the explosion sound we waited several hours to allow aerosol aggregation and subsequent gelation before opening the explosion chamber. We explain our observations in the following subsection.

7.3.2. RESULTS AND DISCUSSION

We created low density, high specific surface area silica aerosol gels by allowing Brownian aggregation of ca. 20 nm size silica nanoparticles in the closed explosion chamber (Fig. 7.12). The silica aerosol gels were found to have very low density of 4 - 6 mg/cm^3 and high specific surface area of 300 – 500 m^2/g. We used Brunauer-Emmett-Teller (BET) analysis technique with nitrogen gas as an adsorbate (Kruk and Jaroniec, 2001) to measure the specific surface area of an aerosol gel sample. The volume fraction of 10^{-4} or greater required to gel aerosol particles was successfully created by instantaneous oxidation of pyrophoric silane gas. The sudden and quick reaction of silane with oxygen allowed us to have a large number of ~ 20 nm size silica particles. We found that some inert background gas, up to at least two atmospheric partial pressure in the combustion chamber, is necessary for quick thermal quenching of freshly formed molten silica particles. Without a background gas, the molten silica particles were found to die on the chamber wall forming a white paint instead of forming aerosol gel.

Figure 7.12: Silica aerosol gel prepared using oxygen as the oxidizer and nitrogen as a background gas.

We discuss the results, observed by varying the wide variety of parameters, in more detail in the following subsections.

7.3.2.1. Role of the Background Gas

Silica has a melting point of ~1650^{o}C which is much smaller compare to > 3500^{o}C melting point for carbon. Silica nanoparticles created during the explosion of silane thus takes much longer time to quench below its melting point compare to the quenching of carbon nanoparticles created during the explosion of a hydrocarbon. It was believed that the thermal quenching time for silica nanoparticles were long enough such that these nanoparticles, after their creation, move balistically in the absence of an inert background gas and "splash" on the chamber walls. This explains our finding of a white paint on the inner walls of the explosion chamber when we used no background gas. Fig. 7.13 shows a picture of such silica paint scrapped out from the inner wall of the explosion chamber.

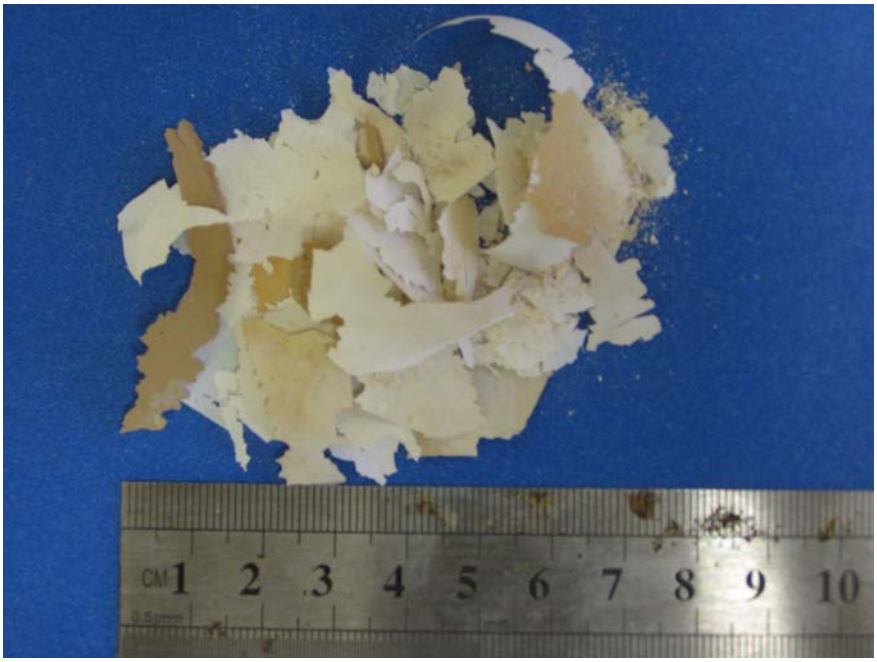

Figure 7.13: Silica paint scrapped out from the inner walls of the chamber when no background gas was used.

We next tried using nitrogen as the background gas. The role of the inert background gas was to help in quickly absorbing initial high momentum and quenching the fresh silica nanoparticles below the melting temperature thereof and before they collide with the chamber walls or each other. We found different results with use of different amount of nitrogen as the

background gas. We premixed 0.016 to 0.019 moles of silane with nitrogen in the explosion chamber before introducing oxygen as an oxidizer to observe the effect of the amount of the background. Silane in this mole range in the explosion chamber was enough to produce a silica monomer volume fraction of ~10^{-4}, which was large enough for a quiescent aggregating aerosol system to gel under gravitational field. Increasing the partial chamber pressure due to the background gas resulted in more fluffy and bluish aerosol gel. Lower density and higher specific surface area aerosol gel was yielded in larger amount when a background gas pressure was greater than 2 atmospheres. Further increasing the background gas partial pressure produced no further improvement. Lower pressure yielded whiter and denser aerosol gel in lesser amount. Fig. 7.14 shows pictures of silica aerosol gels in the explosion chamber when amounts of nitrogen were used as the background gas.

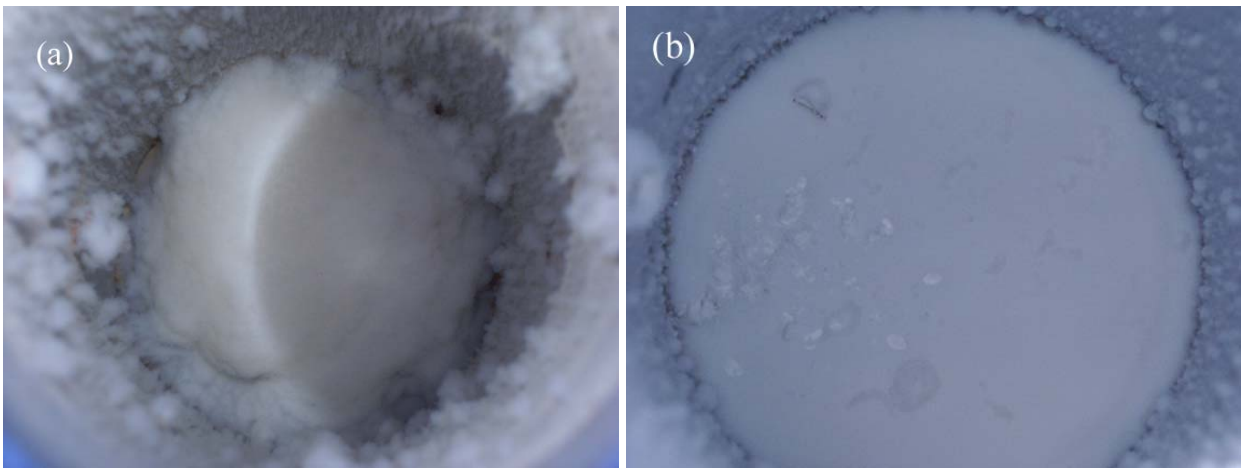

Figure 7.14: View, looking down into the reaction chamber, of (a) light fluffy silica aerosol gel formed when the N_2 gas up to 2.5 atmospheric pressure was used as the background gas and (b) comparatively denser silica aerosol gel formed when the N_2 gas up to 1.5 atmospheric pressure was used as the background gas.

Besides N_2, we also investigated the effect using carbon dioxide (CO_2), helium (He), sulphur hexafluoride (SF_6) and xenon (Xe) as the background gas. This list covers a wide range of molar mass starting from 4 g/mol for He up to 146 g/mol for SF_6. We believe use of heavier background gas with higher thermal conductivity will result in quicker absorption of the initial (at the time of their formation during the explosive reaction) kinetic and thermal energy of the silica nanoparticles.

We found no distinguishable difference between the silica aerosol gels using nitrogen and carbon dioxide. The silica aerosol gels in both cases had similar appearance (as shown in Fig. 7.12), densities in the range 4 - 6 mg/cm^3, specific surface area in the range 300 – 500 m^2/g and similar monomer sizes and distribution. Figs. 7.15 show TEM images of silica aggregates from silica aerosol gels with N_2 and CO_2 as the background gas at partial pressure of more than 2.5 atmospheres. The monomers in both cases appear to be more or less rounded with ~25 nm diameter and almost monodisperse in the size distribution.

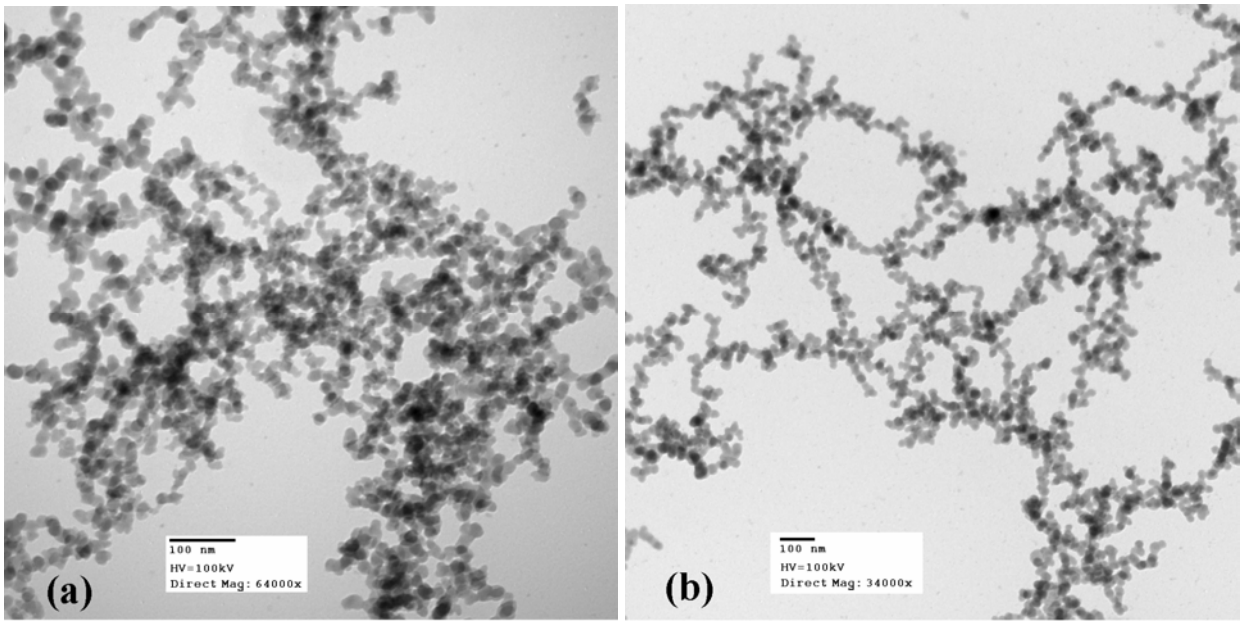

Figure 7.15: TEM images of silica aerosol gels prepared using (a) nitrogen and (b) carbon dioxide as the background gas. These images show no significant difference between the two cases.

Use of He, which has the lowest molar mass in the list, as the background gas yielded a dense looking white colored silica aerosol gel in lesser amount. We also noticed a thin silica paint layer on the inner wall of the chamber. TEM images of silica clusters in this case indicated the silica monomers to have more spherical shape but with non-uniform size distribution (Fig. 7.16). With such results we concluded that decreasing the molecular weight of the background gas caused slower absorption of the initial kinetic and thermal energies of the silica nanoparticles.

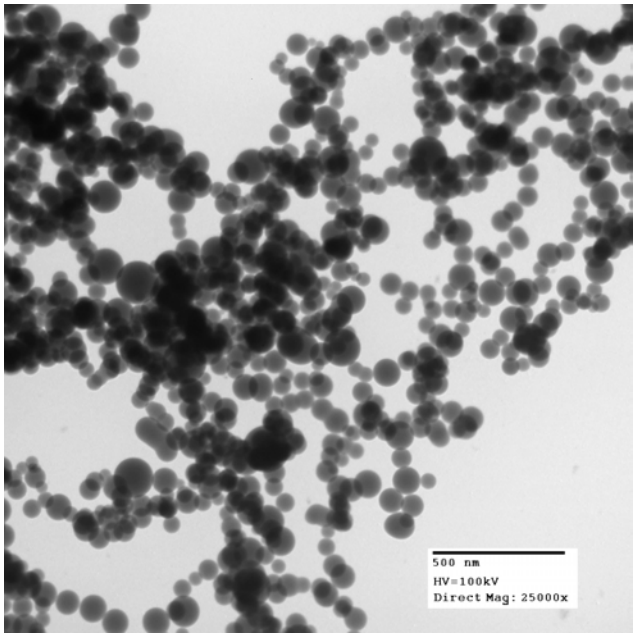

Figure 7.16: TEM picture of Silica aerosol gel prepared using oxygen as the oxidizer and helium as a background gas.

We performed experiments using SF_6 as the background gas. However, to our surprise, the explosive reaction of silane with oxygen in such experiments resulted in formation of no aerosol. An observation of no significant change in the chamber gas pressure before and after the explosion indicated a conversion of gas to gas during the chemical reaction. We believe SF_6 was also participating undesirably during the explosion. The octahedral covalent bond structure of SF_6 may break down during extreme situation like that of an explosion although it is considered chemically inert in normal conditions.

In our experiments we tried to introduce enough oxygen according to the stoichiometric requirement (Eq. (7.2)) to combust the silane premixed with the background gas in the explosion chamber. Inadequate supply of oxygen produced undesired results (see the following section). However, such attempts sometimes failed as the explosion in the chamber would shut the one-way valve early in time preventing the desired quantity of oxygen to enter the explosion chamber. In case of such failures we simply repeated our experiments. However, we could not repeat the experiment in the case of Xe as the background gas due to its limited supply. Our single attempt of using Xe as the background gas unfortunately went unsuccessful due to such incomplete oxygen supply.

7.3.2.2. Premixing and Amount of Silane/Oxidizer in the Background Gas

We experimented premixing either silane or oxidizer with the background gas in the explosion chamber. We used oxygen as the oxidizer and nitrogen as the background gas. Premixing silane with the background gas in the explosion chamber yielded fluffier and bluish white aerosol gel (Fig. 7.14a). When oxygen is premixed with the background gas in the combustion chamber instead, a dense (13 mg/cm^3) bright white silica aerosol gel was yielded (Fig. 7.17).

Figure 7.17: Dense (13mg/cm^3) bright white silica aerosol gel formed when O_2 was premixed with the background N_2 gas.

Brown aerosol gels formed (Fig. 7.18) when the silane/molecular oxygen ratio was more than stoichiometric of 1:2. We believe that this brown color was due to the presence of free silicon (Si). Use of 0.016 ± 0.001 to 0.019 ± 0.001 moles of silane premixed with the background gas in the 3.9 liter explosion chamber yielded the largest amount of lighter bluish white silica

aerosol gel (Fig. 7.12). Use of higher moles of silane resulted in brown aerosol gel since sufficient amount of oxygen failed to enter the chamber while use of lower moles of silane produces smaller monomer volume fraction and thus the system hardly gelled.

Figure 7.18: Brown silica aerosol gel prepared when SiH_4/O_2 ratio was more than stoichiometric.

7.3.2.3. Hydrophilic and Hydrophobic Silica Aerosol Gels

We were successful in producing both hydrophilic and hydrophobic silica aerosol gels by switching from one oxidizer to another. The silica aerosol gel made using oxygen as the oxidizing gas was found to readily absorb water showing its hydrophilic property. However, when we used nitrous oxide or a mixture of nitrous oxide (greater than 90%) and oxygen (less than 10%), white colored silica aerosol gels were formed which were hydrophobic in nature. These results were for 0.016 to 0.019 moles of silane premixed with nitrogen in the explosion chamber. Fig. 7.19 shows a picture of such a hydrophobic silica aerosol gel taken several months after floating the gel on the top of water.

Figure 7.19: A picture of a hydrophobic silica aerosol gel taken several months after floating the gel on the top of water. N_2O was used as the oxidizer to prepare this silica aerosol gel.

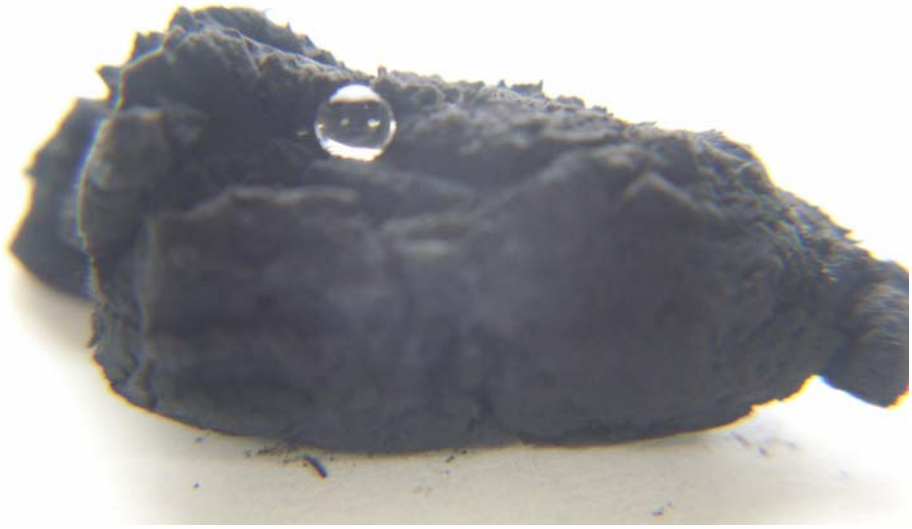

Figure 7.20: Carbon coating on hydrophilic silica aerosol gel turns it into a hydrophobic silica aerosol gel. In the picture is shown a water drop (~ 3mm diameter) sitting on the aerosol gel showing its hydrophobic nature.

It was also demonstrated that a hydrophilic silica aerosol gel could be turned to a hydrophobic one after uniformly depositing carbon by heating the silica aerosol gel at 500^{o}C in the presence of a hydrocarbon. Fig. 7.20 shows a picture of such a carbon coated silica aerosol gel which acquired a hydrophobic property after heat treatment in the presence of a hydrocarbon. The initial aerosol gel was prepared using oxygen as an oxidizer and had hydrophilic property.

7.3.2.4. Microscopic Structure of the Silica Aerosol Gel

The TEM pictures of the silica aerosol gels (Figs. 7.15 and 7.16) show that the gels consisted of clusters with ramified fractal structures. When 0.016 to 0.019 moles of silane, premixed with 2.5 atmosphere of nitrogen or carbon dioxide in the explosion chamber, were oxidized with oxygen, the resulting silica monomers were found to be more or less uniform in size distribution with ~25 nm diameter (Figs. 7.15). The monomers also appeared to be more or less rounded in shape with necking along the chain.

We compared the X-ray diffraction (XRD) patterns for the silica aerosol gel and amorphous silica powder (Fig. 7.21). The matching peak positions confirmed that the material of the monomers is definitely silica. Also the fairly broad diffraction peak indicated low degree of crystalline for silica monomers.

A comparison of the electron diffraction patterns from the monomers of our silica aerosol gel and those of commercial silica aerogel is shown in Figs. 7.22. Comparatively more distinct diffraction patterns for the silica aerosol gel implied more crystalline monomers for the silica aerosol gel compare to those of the commercial silica aerogel. A TEM picture of the commercial silica aerogel, shown in Fig. 7.23, indicated much small (~10 nm diameter), however, non distinct monomers.

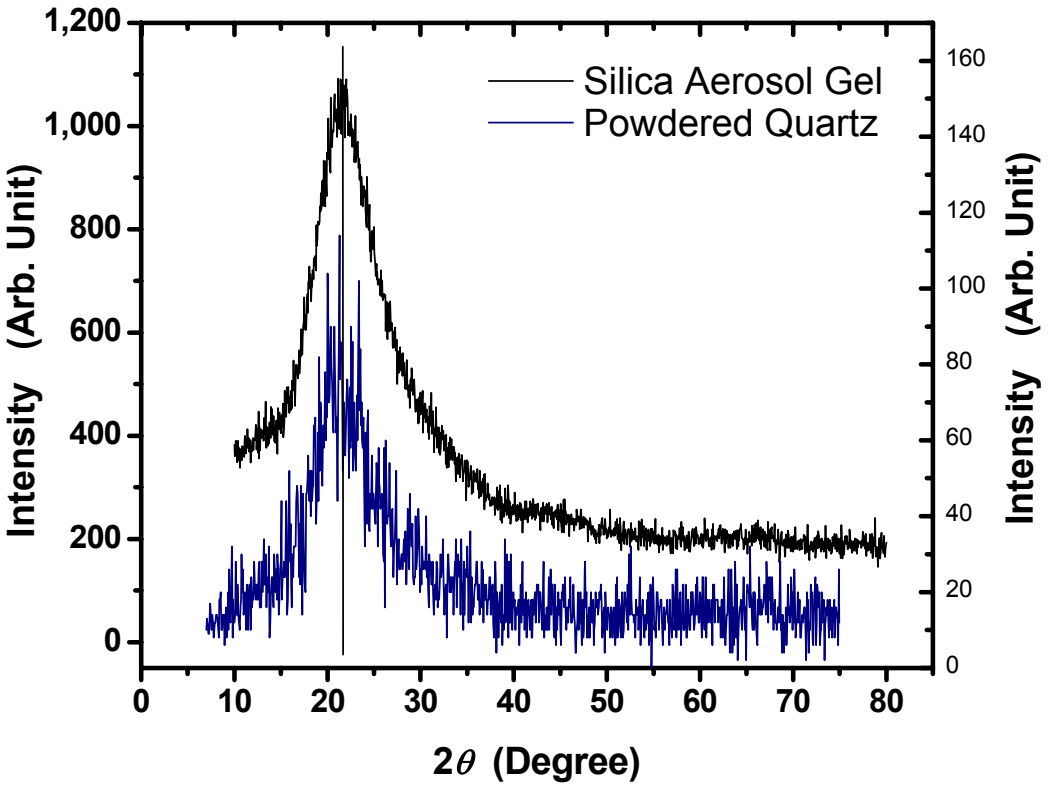

Figure 7.21: X-ray diffraction patterns for the silica aerosol gel and powdered amorphous silica. Matching of the peaks confirmed the material of the aerosol gel to be definitely silica. Broad peak indicated low degree of crystalline for the silica aerosol gel.

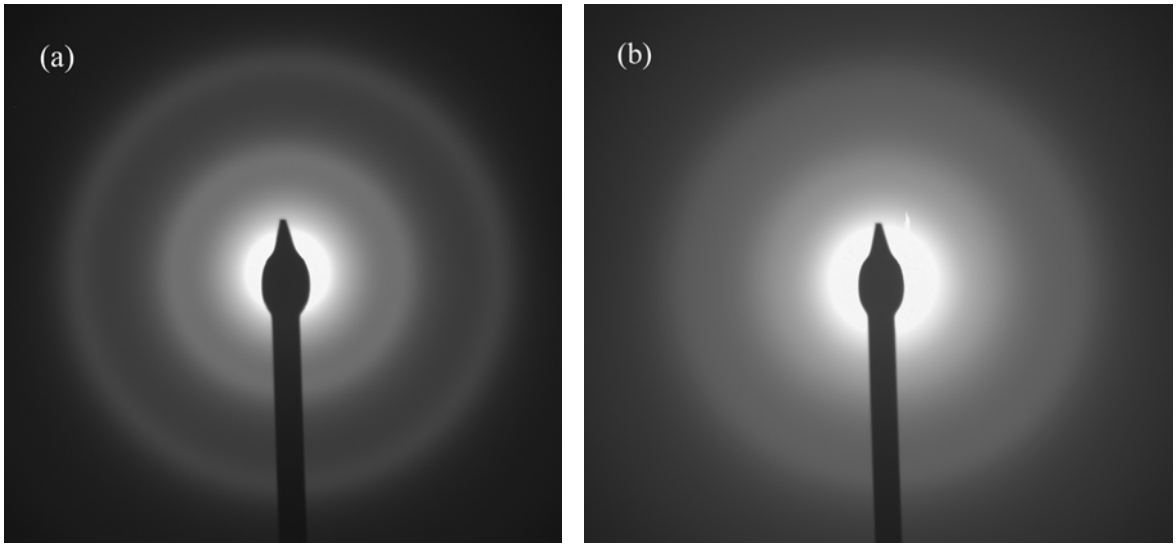

Figure 7.22: (a) Electron diffraction pattern from the silica aerosol gel. (b) Electron diffraction pattern from the commercial silica aerogel. The more distinct diffraction pattern for the silica aerosol gel implies that its monomers are more crystalline compare to those of commercial silica aerogel.

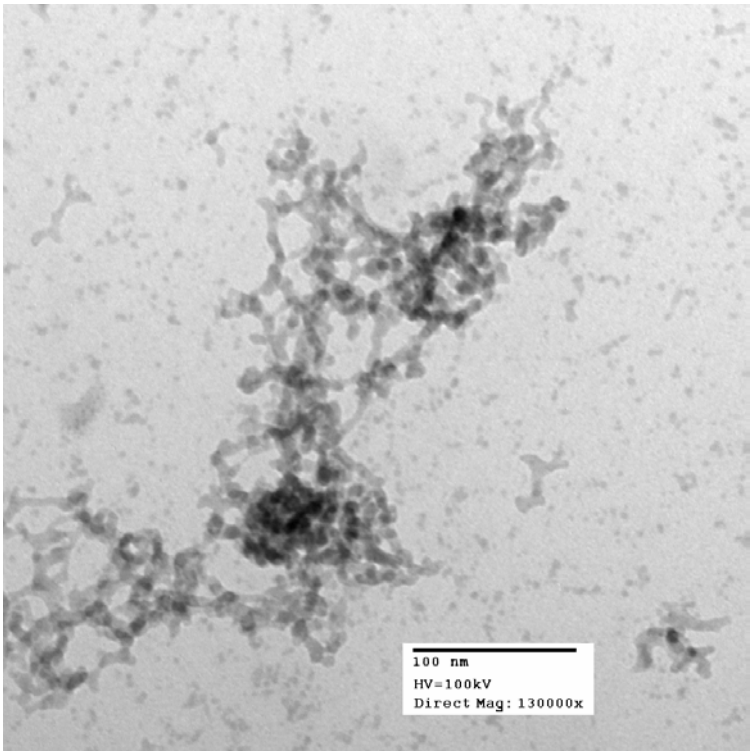

Figure 7.23: TEM image of the commercial silica aerogel. The monomers, ~10 nm in diameter, do not appear distinctly.

7.3.2.5. Morphology of the Silica Aggregates

The morphology of the silica aggregates in the aerosol gel was studied by performing neutron scattering at NIST Center for Neutron Research (NCNR). We prepared a sample of silica aerosol gel in our laboratory using 0.018 moles of silane, premixed with 2.5 atmosphere of nitrogen in the 3.9 liter explosion chamber and oxygen as the oxidizer. The sample was then shipped to NCNR where we collected both ultra small angle neutron scattering (USANS) and small angle neutron scattering (SANS) data from the sample. USANS and SANS can together provide q-range of approximately 5 x 10^3 cm^{-1} to 1 x 10^7 cm^{-1}.

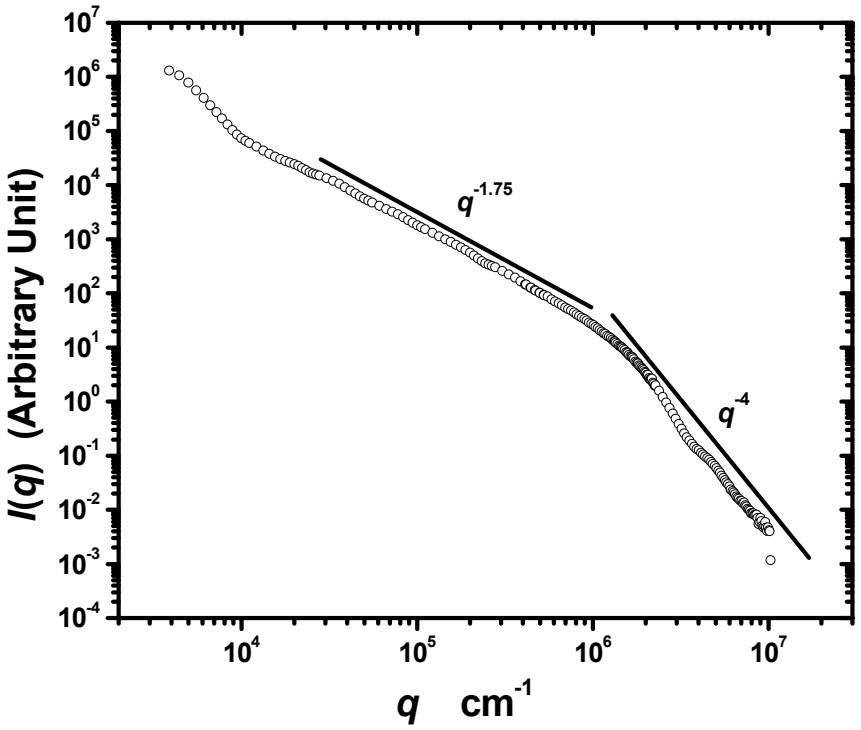

Figure 7.24: Combined USANS and SANS result from a collapsed silica aerosol gel sample. Scattered neutron intensity $I(q)$ is plotted versus the scattering wave vector q. One clearly see power-law regimes; $\sim q^{-1.75}$ at intermediate q indicative of a mass fractal aggregate and $\sim q^{-4}$ at high-q indicative of 3-d monomer structure. Stronger power law decay of scattered intensity at low-q can be explained as an artifact of the collapsing of the aerosol gel. Collapsing caused a compact 3-d structure to form at large length scales.

The aerosol gel sample was collapsed while shipping to NCNR and handling for the neutron scattering. However, this collapse was expected not to affect the structure below a micron or less length scale. Fig. 7.24 shows the USANS and SANS combined data from the collapsed silica aerosol gel. We clearly see a power law regime of $\sim q^{-1.75}$ at intermediate q (corresponding to a length scale range of 25 – 500 nm) indicative of a mass fractal aggregate with a fractal dimension of $D_f = 1.75$. This fractal dimension is matching with the DLCA value. At high-q (length scales below 10 nm), $\sim q^{-4}$ power law (Porod regime) was observed which was indicative of 3-d monomer structure. A weak ripple observed in the Porod regime suggested a narrow size distribution for monomers. The TEM pictures (Figs. 7.15) showing uniform monomer size distribution supported this observation. Stronger power law decay of scattered intensity at low-q can be explained as an artifact of the collapsing of the aerosol gel. Collapsing caused a compact 3-d structure to form at large length scales.

7.3.3. CONCLUSION

We created a silica aerosol gel by allowing Brownian aggregation of ca. 20 nm size silica nanoparticles in a closed chamber. With this we demonstrated that gelation is a physical phenomenon such that an aggregation process in a system with a large number of very tiny particles (~10 nm radius) can proceed from cluster dilute to cluster dense and finally gel. The volume fraction of 10^{-4} or greater required to gel aerosol particles was successfully created by instantaneous oxidation of pyrophoric silane gas.

The silica aerosol gels were found to have very low density of 4 - 6 mg/cm^3 and high specific surface area of 300 – 500 m^2/g. We found that some inert background gas, up to at least two atmospheric partial pressure in the combustion chamber, was necessary for quick thermal quenching of freshly formed molten silica particles.

CHAPTER 8- Light Scattering Study of Cluster Dynamics in Dense, Gelling Aerosols

8.1. INTRODUCTION

In this chapter we present the results of our dynamic light scattering experiments over our aggregating system of carbon nanoparticles which transited from a cluster dilute to a cluster dense situation and finally gelled forming a volume spanning network in the available space of the system. The importance of this study lies in the fact that even though there are numerous publications on the cluster dynamics in colloidal gelation we found none in aerosol gelation. To our knowledge, this report is the first study of the diffusional behavior of the clusters in a dispersed system gelling in the aerosol phase.

Dynamic light scattering (DLS) measurements can give us insights of the cluster dynamics during the cluster dilute to cluster dense transition and finally gelation. This is a non-invasive technique appropriate for the study of the *in situ* study of the relaxation behavior of clusters in both aerosol and colloidal systems (see section 4.2.5.). In DLS experiments we determine the scattered intensity correlation function $g^{(2)}(\tau)$ given by Eq. (4.74). This scattered intensity correlation function $g^{(2)}(\tau)$ is related to the scattered field correlation function $g^{(1)}(\tau)$ for homodyne and heterodyne detections as given by Eqs. (4.77) and (4.89) respectively.

For an aggregating system in continuum regime, we expect the clusters to exhibit Stoke-Einstein (Brownian) type of diffusion as long as the system is in cluster dilute regime. Rotational diffusion effect can be negligible compare to that of the translational diffusion at length scales q^{-1} larger than the average hydrodynamic (mobility) radius of the clusters. Once the system enters cluster dense regime and gel network starts developing, the cluster diffusion becomes restricted within the cage like structure of the gel network. The gel network acts like a static scatterer. Thus deviation from the Brownian type relaxation in the intensity or field correlation function is expected. The relation between the intensity and the field correlation functions in such case can

be given by Eq. (4.89) as in case of heterodyne detection. Close to the gel point the clusters become large (few tens of microns) such that chosen length scale q^{-1} can be small enough to detect the internal fluctuations within a cluster.

8.2. EXPERIMENTAL METHODS

For DLS study we created an aggregating system of carbon nanoparticles instantaneously by exploding a mixture of acetylene and oxygen gases (in 2:1 molar ratio) inside a closed optical chamber. Thus created dense aerosols aggregated and gelled within few minutes. The description of this optical chamber has been presented in the section 5.3.1.1. The same section also describes the filling procedure with the gas mixture for this optical chamber.

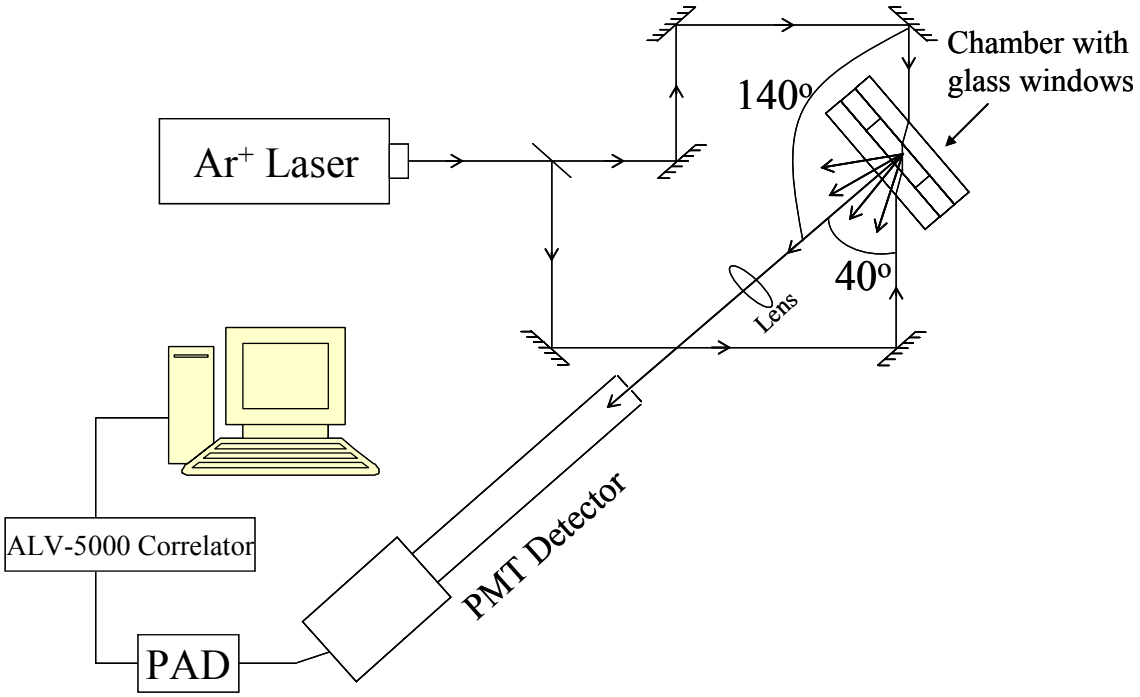

Figure 8.1: Schematic diagram of the experimental set up for the DLS experiments. Counter propagating beams allowed quick measurements of the intensity correlation at 40^{o} and 140^{o} scattering angles by blocking one beam at a time.

The charged optical chamber was positioned in the set up for the DLS experiment as shown in Fig. 8.1. A vertically polarized argon ion laser bean, operating at $\lambda = 488$ nm, was split into two such that counter propagating beams passed through the optical chamber. The scattering

path length inside the chamber was decreased to 1.5 mm to avoid the multiple scattering effect (see section 5.3.2.2.). A photomultiplier tube (PMT) detector was placed at an angle of 40^o relative to one of these two counter propagating beams such that, blocking one beam at a time, we could do scattered intensity measurement at 40^o and 140^o scattering angles. These 40^o and 140^o scattering angles corresponded to scattering wave vectors q of 8.81 μm^{-1} and 24.20 μm^{-1} respectively. Blocking one among two counter propagating beams could be quickly switched from one to another. With this arrangement we were able to make quick measurements at two different angles using a single detector. The PMT detector was coupled to ALV5000 correlator through a pulse amplifier and discriminator (PAD) device. The intensity correlation data were then stored in a personal computer.

A set of intensity correlation $g^{(2)}(\tau)$ data was taken at various times up to the first 30 minutes starting right after the creation of carbon nanoparticles inside the optical chamber. Intensity correlation was measured in the correlation time range between few microseconds and few hundred milliseconds. To ensure the reliability of the scattered intensity measurements on the scatterers inside the optical chamber, we first performed DLS experiments on a dilute non-aggregating system of 24 nm diameter polystyrene colloidal particles in the optical chamber at various q-values. The polystyrene colloidal particles were undergoing Brownian diffusion and thus the intensity correlation could be given by Eq. (4.78). This meant the characteristic correlation time τ_c should follow q^{-2} dependence. Fig. 8.2 shows that the τ_c determined from the measured intensity correlation did follow q^{-2} dependence as expected. This observation verified the reliability of the measurements on the scatterers inside the optical chamber.

From the measured intensity correlation $g^{(2)}(\tau)$ we computed the field correlation $g^{(1)}(\tau)$ using Eqs. (4.90) and (4.91).

$$g^{(2)}(\tau) = A + B\phi(\tau)\,. \qquad \text{(Eq. (4.90))}$$

$$\phi(\tau) = \left(\frac{1}{1+x}\right)^2 \left|g^{(1)}(\tau)\right|^2 + \frac{2x}{(1+x)^2}\left|g^{(1)}(\tau)\right|. \qquad \text{(Eq. (4.91))}$$

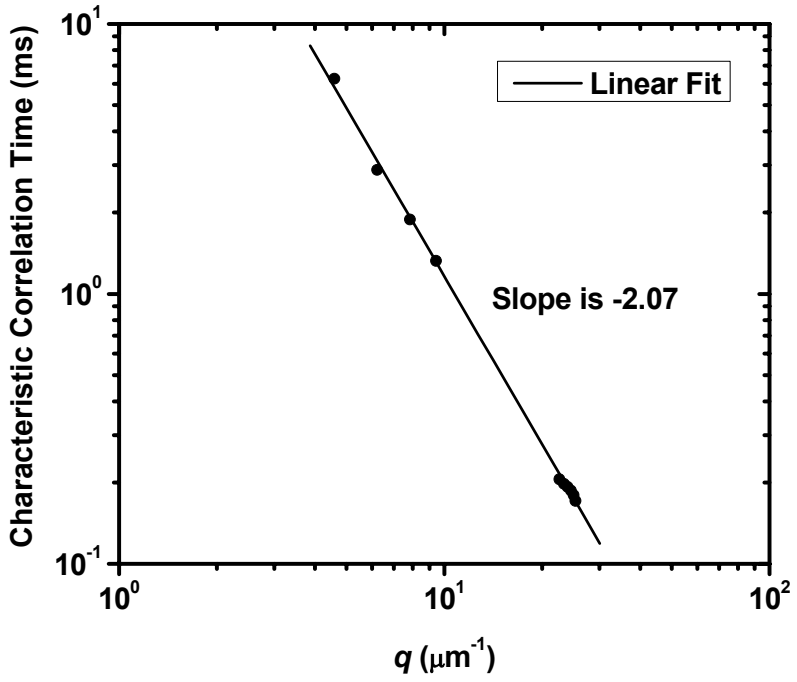

Figure 8.2: The characteristic correlation time τ_c for a dilute system of 24 nm diameter polystyrene colloidal particles inside the optical chamber plotted versus the scattering wave vector q. The observed q^{-2} dependence of τ_c verified that the measurements on the scatterers inside the optical chamber were reliable.

We determined the instrumental factors A and B by assuming that initially all the scatterers in the system were Brownian scatterers such that the field correlation function $g^{(1)}(\tau)$ could be given by Eq. (4.73). For such initial condition, x, which was the ratio of the mean scattered intensity from the diffusing scatterer I_s and the static scattering from the static structure in the scattering volume I_s, was equal to zero. We fitted Eq. (8.1) to the measured intensity correlation $g^{(2)}(\tau)$ data and found the factors A and B.

$$g^{(2)}(\tau) = A + B\exp(-\tau/\tau_c) \tag{8.1}$$

where $\tau_c = \left(2q^2D\right)^{-1}$ is the characteristic correlation time for the scatterers in the scattering volume.

When a gel network was formed x no longer remained equal to zero. Using $g^{(1)}(0) = 1$ feature of the field correlation function in Eq. (4.91) we can write

$$\phi_0 = \frac{2x+1}{(1+x)^2}\,. \tag{8.2}$$

Here $\phi_0 = \phi(\tau = 0)$. Solving for x we find,

$$x = \frac{(1-\phi_0)^{1/2}}{1-(1-\phi_0)^{1/2}}\,. \tag{8.3}$$

Using Eq. (8.3) we can solve Eq. (4.91) for the field correlation function $g^{(1)}(\tau)$ as

$$g^{(1)}(\tau) = \frac{[\phi(\tau)+(1-\phi_0)]^{1/2} - (1-\phi_0)^{1/2}}{1-(1-\phi_0)^{1/2}}\,. \tag{8.4}$$

The term $\phi(\tau)$ in Eq. (8.4) is directly related to $g^{(1)}(\tau)$ as

$$\phi(\tau) = \frac{1}{B}\left[g^{(2)}(\tau) - A\right]. \tag{8.5}$$

We used Eqs. (8.4) and (8.5) to compute the field correlation function from the measured intensity correlation in our DLS experiments.

8.3. RESULTS

For a system with a monomer volume fraction of ~ 8 x 10^{-5} or higher we observed that the decay in correlation function was exponential initially for up to about first 30 sec or less and then crossed over to stretched exponential. Any monomer volume fraction below ~8 x 10^{-5} was not of our interest since at such low volume fractions the aggregating system would gravitationally settle down before transiting from a cluster dilute to a cluster dense regime.

Figs. 8.3 and 8.4 show the plots of the field correlation function $g^{(1)}(\tau)$, at the scattering wave vectors q equal to 8.81 μm^{-1} and 24.20 μm^{-1} respectively, at different time t after the creation of ~9 x 10^{-5} monomer volume fraction of carbon soot aerosols inside the optical

chamber. A quick transition was observed from an exponential to a stretched exponential decay of the correlation function at both q values. This quick transition indicated a fast evolution of the aggregating system from a cluster dilute to a cluster dense stage and the consequent development of the gel network restricting the clusters from the Brownian type diffusional motion. We fitted a stretched exponential function of the form given by Eq. (8.6) on the field correlation data. Solid lines are the stretched exponential curves fitted in Figs. 8.3 and 8.4.

$$g^{(1)}(\tau) = \exp\left[-\delta\left\{1 - e^{-(\tau/\tau_c)^{\beta}}\right\}\right] \approx \exp\left[-\delta(\tau/\tau_c)^{\beta}\right]. \tag{8.6}$$

In Eq. (8.6) the exponent δ is a function depending on both, the type of the diffusional motion of the scatterers and the scattering wave vector q.

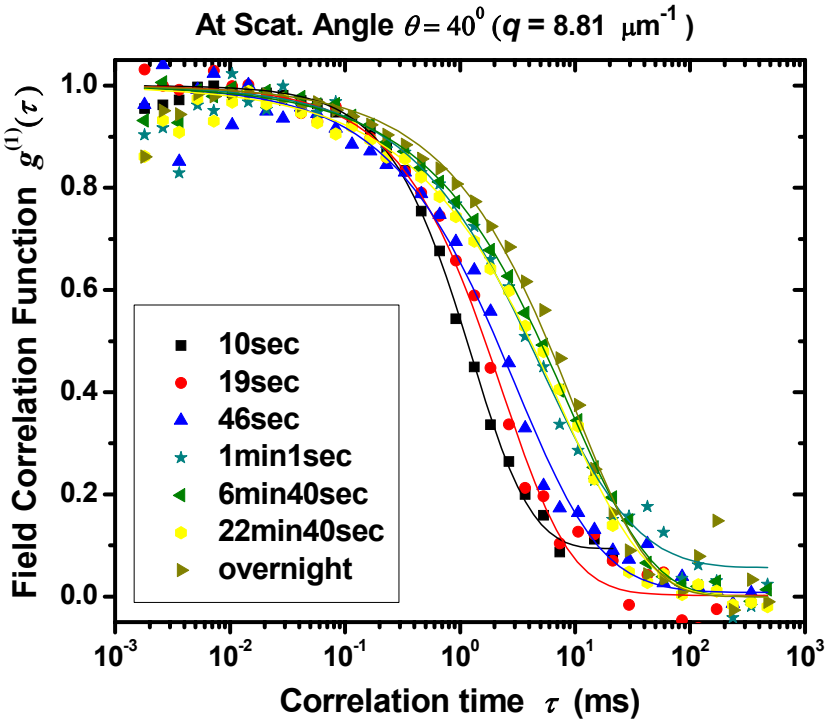

Figure 8.3: Field correlation function $g^{(1)}(\tau)$ at q = 8.81 μm^{-1} at various time t after the creation of carbon soot aerosols inside the optical chamber. A quick transition was observed from an exponential to a stretched exponential decay of the correlation function at both q values. Solid lines are the stretched exponential curves fitted.

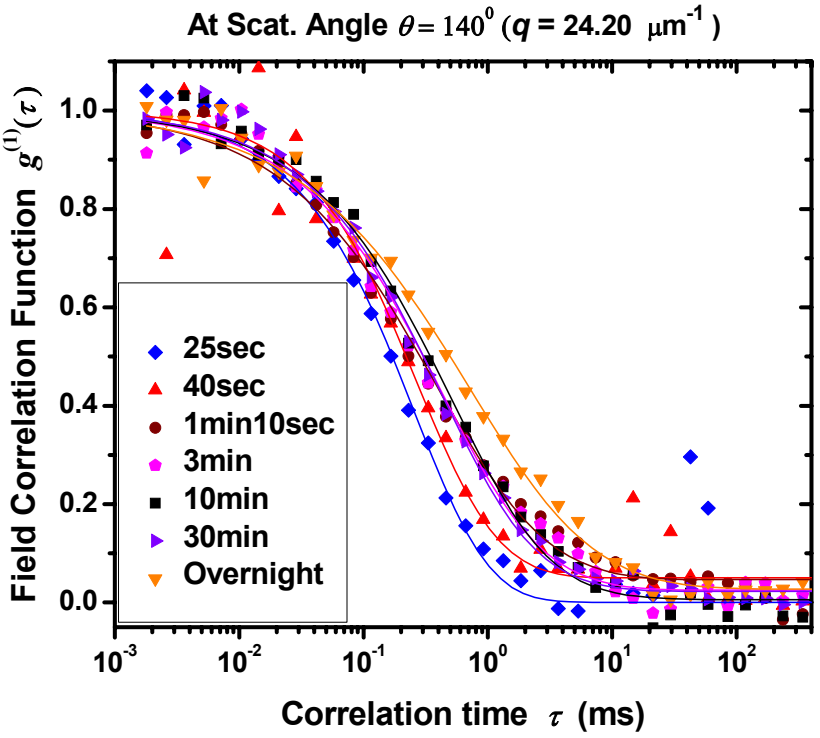

Figure 8.4: Field correlation function $g^{(1)}(\tau)$ at q = 24.20 μm^{-1} at various time t after the creation of carbon soot aerosols inside the optical chamber. A quick transition was observed from an exponential to a stretched exponential decay of the correlation function at both q values. Solid lines are the stretched exponential curves fitted.

Figs. 8.5 and 8.6 show the time evolutions of the decay exponent β and the characteristic correlation time $\tau_c^{'} = \tau_c / \delta^{1/\beta}$ at the scattering wave vectors q equal to 8.81 μm^{-1} and 24.20 μm^{-1} respectively. At q = 8.81 μm^{-1} it was observed that $\beta \approx 0.60$ and $\tau_c^{'} \approx 7.50$ ms once the aerosol gelled. Fig. 8.5 shows that the evolutions of β and $\tau_c^{'}$ at q = 8.81 μm^{-1} were fast and almost saturate in first 70 seconds. Likewise at q = 24.20 μm^{-1}, we observed $\beta \approx 0.65$ and $\tau_c^{'} \approx 0.45$ ms once the system gelled. Fig. 8.6 indicates that the time evolution in β was fast such that the saturation value was almost attained by the end of the first 60 sec after the creation of the aggregating aerosol system. The characteristic correlation time $\tau_c^{'}$ showed no or negligible evolution.

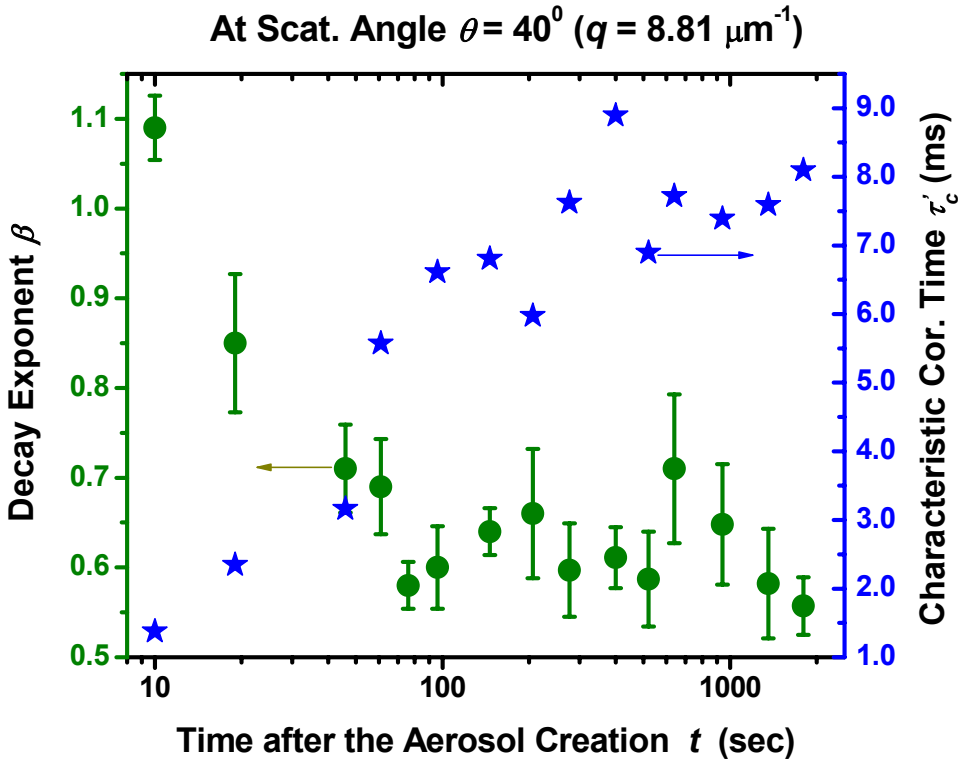

Figure 8.5: Plot of the decay exponent β and the characteristic correlation time $\tau_c^{'} = \tau_c / \delta^{1/\beta}$ versus time t. The time evolutions in β and $\tau_c^{'}$ were fast such that the saturation values were almost attained by the end of the first 70 sec after the creation of the aggregating aerosol system.

The field correlation functions at different q values (corresponding to 40^o and 140^o scattering angles), when plotted versus the scaled correlation time $\left(\tau/\tau_c^{'}\right) = \delta\left(\tau/\tau_c\right)^{\beta}$, fell on a single master curve showing the dynamics is well described by a stretched exponential decay of the correlation function (Eq. (8.6)). Fig. 8.7, in which field correlation functions at a certain time t corresponding to 40^o and 140^o scattering angles are plotted versus $\left(\tau/\tau_c^{'}\right)$, illustrates this behavior. Fig. 8.8 shows the same correlation functions plotted versus the correlation time τ.

When an aggregating system gels the clusters become static in the gel network. However these clusters can still possess internal thermal and acoustic fluctuations which will give rise to some relaxation modes in the field correlation function. The results reported here on DLS from

gelling aerosols are only preliminary results. More work is essential to explain the details of the dynamics of a gelling aerosol system.

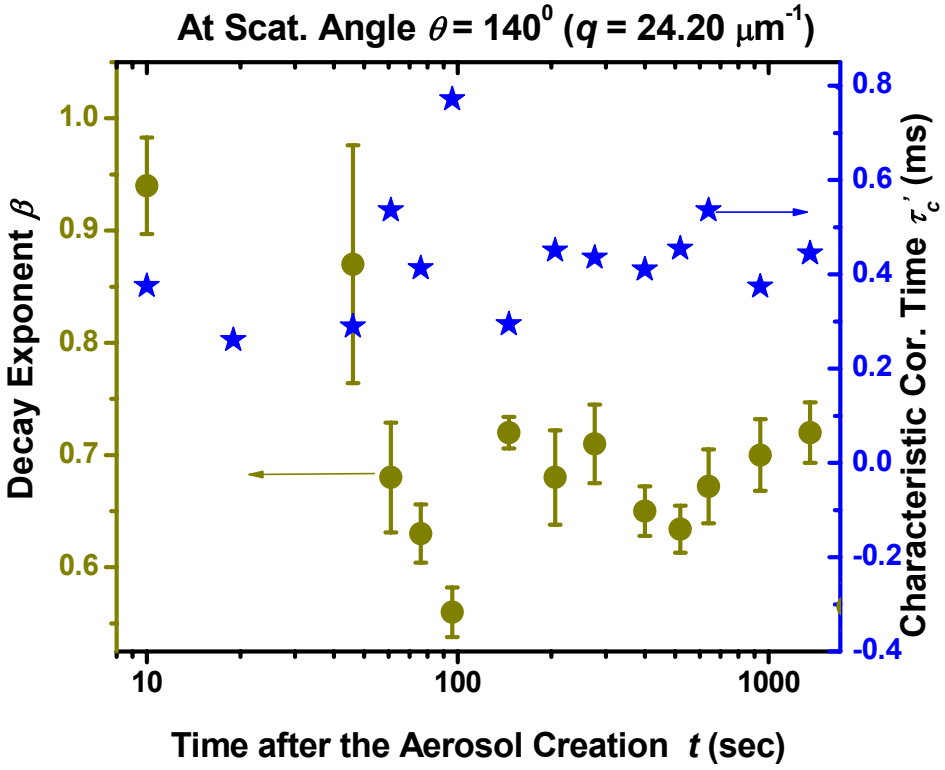

Figure 8.6: Plot of the decay exponent β and the characteristic correlation time $\tau_c^{'} = \tau_c / \delta^{1/\beta}$ versus time t. The time evolution in β was fast such that the saturation value was almost attained by the end of the first 60 sec after the creation of the aggregating aerosol system. The characteristic correlation time $\tau_c^{'}$ showed no or negligible evolution.

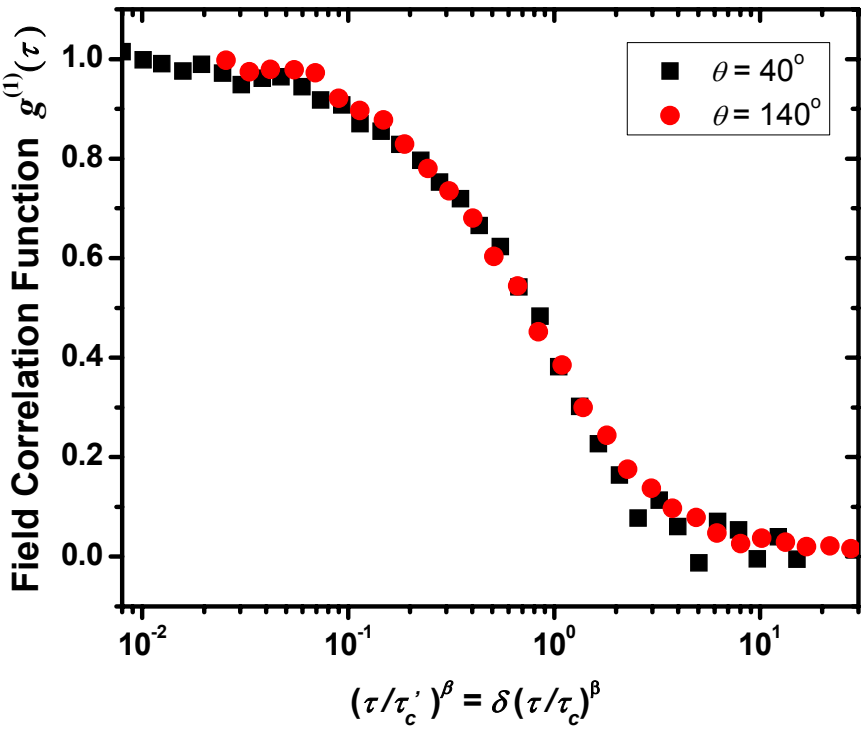

Figure 8.7: Field correlation functions at a certain time *t* corresponding to 40^{o} and 140^{o} scattering angles plotted versus (τ/τ_c'). The two correlation functions fall under the same master curve illustrating that the dynamics is well described by a stretched exponential decay of the correlation function (Eq. (8.6)).

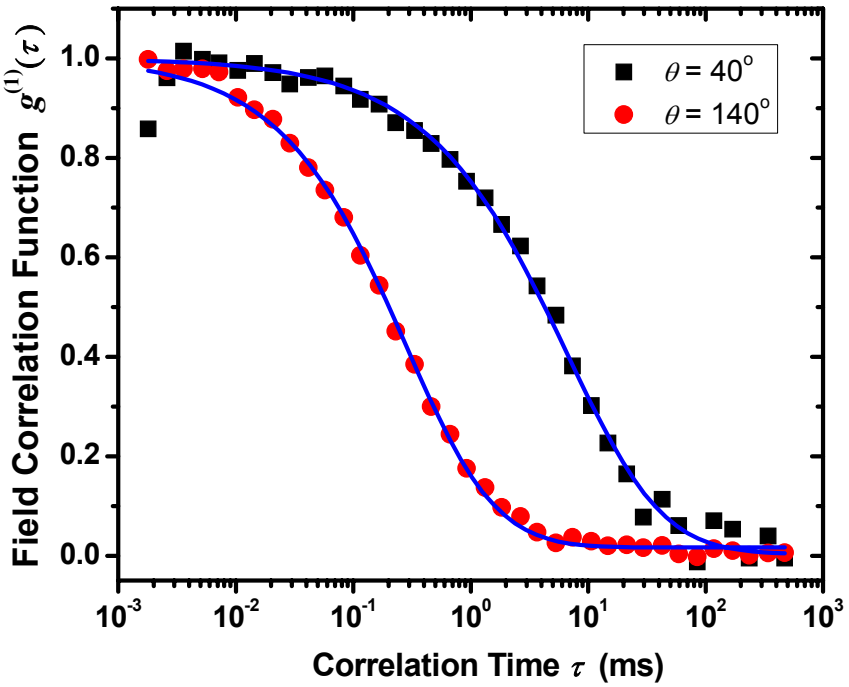

Figure 8.8: The same correlation functions as in Fig. 8.7 plotted versus the correlation time τ.

8.4. CONCLUSION

Intensity correlation function was measured using ALV5000 correlator for the aerosol system created inside an optical chamber by exploding a mixture of a hydrocarbon (Acetylene) and oxygen. The observations were taken at two q (scattering wave vector) values 8.81 μm^{-1} and 24.20 μm^{-1}, which for $\lambda = 488$ nm correspond to scattering angles 40^{o} and 140^{o} respectively. The aggregating aerosols showed exponentially decaying dynamic structure factor when the scatterers can exhibit free Brownian diffusional motion before gel network was formed. Transition from the exponential decay to a stretched exponential decay was quickly observed. This transition was a result of the restricted diffusional motion of the scatterers within the static gel structure.

CHAPTER 9- Summary

We summarise the results of our experimental study on aggregation of a dense aerosol system in this chapter.

The cluster morphology of aerosol soot particles was determined using both small angle static light scattering (SASLS) and image analysis techniques. Carbon nano-particles created by exploding C_2H_2 and O_2 mixture in a closed chamber served as the aggregating aerosol system in our experimental investigation. We observed a morphological crossover in the aggregating clusters from a homogeneous, DLCA fractal morphology at earlier time to a hybrid superaggregate morphology, DLCA at small scales and percolation at large scales, at later time during the aggregation process. These results also imply universality in superaggregates with hybrid DLCA and percolation morphologies consistent with previous results for gelation in simulations (Fry et al., 2004) and in flames (Kim et al., 2004, Kim et al., 2006, Sorensen et al., 2003).

By employing the SASLS technique we also investigated the aggregation kinetics of an aggregating aerosol system at different monomer volume fractions. We found $z \approx 1$ (and $\lambda \approx 0$) consistent with the cluster dilute, DLCA case at lower monomer volume fractions f_v. With increasing monomer volume fraction f_v, z (and λ) was also found to increase up to 1.9 (and λ up to 0.4) indicating the enhanced aggregation kinetics functionality. This result is consistent with simulation results in our laboratory (Fry et al., 2002) indicating the transition of the aggregating system from cluster dilute to cluster dense limit. Our exploration was limited in the monomer volume fraction f_v range extended only between 1×10^{-5} and 1×10^{-4}. This was because gravitational settling was affecting lower f_v systems while higher f_v systems were too turbid for the light scattering purpose. We also found the measured values of $K(s_2, s_2)$ to lie in the range 1.5×10^{-15} to 5.0×10^{-15} m^3/sec and to increase slightly with f_v which indicated the speeding up of aggregation kinetics as f_v was increased.

Next, we demonstrated a novel gelation of particles in the aerosols phase to create a new material that we have named aerosol gel. A high monomer volume fraction of 10^{-4} or greater is required for an aerosol system to gel. We created carbon and silica aerosol gels separately by allowing Brownian aggregation of corresponding aerosol particles in a closed chamber. With this we demonstrated that gelation is a physical phenomenon such that an aggregation process in a system with a large number of very tiny particles (~10 nm radius) can proceed from cluster dilute to cluster dense and finally gel. The carbon aerosol was created by an explosion of a hydrocarbon/oxygen mixture, while the silica aerosol was successfully created by instantaneous oxidation of pyrophoric silane gas.

Aerosol gels have unusual properties including ultralow density and high specific surface area and thus are similar to well-known aerogel materials. We believe the aerosol gels have advantages over conventional aerogels made via the sol-gel process (Brinker and Scherer, 1990) in the sense that no supercritical drying step is required and thus complexities involved can be avoided.

We also attempted to study the dynamics of the dense aerosol aggregation. Intensity correlation function was measured using ALV5000 correlator for the aerosol system created inside an optical chamber by exploding a mixture of a hydrocarbon (Acetylene) and oxygen. The observations were taken at two q (scattering wave vector) values 8.81 μm^{-1} and 24.20 μm^{-1}, which for $\lambda = 488$ nm correspond to scattering angles 40^{o} and 140^{o} respectively. The aggregating aerosols showed exponentially decaying dynamic structure factor when the scatterers can exhibit free Brownian diffusional motion before gel network was formed. Transition from the exponential decay to a stretched exponential decay was quickly observed. This transition was a result of the restricted diffusional motion of the scatterers within the static gel structure.

Appendix A

We show that $\left(\frac{d\sigma_{scat}}{d\Omega}\right)_{RDG} \approx \left(\frac{d\sigma_{scat}}{d\Omega}\right)_{Ray}$ as $qa \to 0$.

From Eq. (4.14) we have

$$\left(\frac{d\sigma_{scat}}{d\Omega}\right)_{RDG} = \left(\frac{d\sigma_{scat}}{d\Omega}\right)_{Ray}\left[\frac{9}{(qa)^6}\{\sin(qa) - qa\cos(qa)\}^2\right] \tag{A.1}$$

We have

$$\sin x - x\cos x \approx \left(x - \frac{x^3}{3!}\right) - x\left(1 - \frac{x^2}{2!}\right) \quad \text{as } x \to 0. \tag{A.2}$$
$$= \frac{x^3}{3}$$

Squaring Eq. (A.2) and replacing x by qa, we get

$$(\sin qa - qa\cos qa)^2 \approx \frac{(qa)^6}{9} \quad \text{as } qa \to 0. \tag{A.3}$$

Using Eq. (A.3) in Eq. (A.1) we find

$$\left(\frac{d\sigma_{scat}}{d\Omega}\right)_{RDG} \approx \left(\frac{d\sigma_{scat}}{d\Omega}\right)_{Ray} \quad \text{as } qa \to 0. \tag{A.4}$$

Appendix B

We show that $S(q) = 4\pi \int_{-\infty}^{\infty} g(r) \frac{\sin(qr)}{qr} r^2 dr$.

From Eq. (4.36) we have

$$S(q) = \int_{-\infty}^{\infty} e^{i\vec{q}.\vec{r}} g(r) d\vec{r} . \tag{B.1}$$

We can rewrite Eq. (B.1) as

$$S(q) = \int_{-\infty}^{\infty} \int_{-1}^{1} \int_{0}^{2\pi} \{\cos(qr\cos\theta) + i\sin(qr\cos\theta)\} g(r) r^2 dr\, d(\cos\theta)\, d\phi$$

$$= 2\pi \int_{-\infty}^{\infty} dr\, r^2 g(r) \int_{-1}^{1} d(\cos\theta) \{\cos(qr\cos\theta) + i\sin(qr\cos\theta)\}$$

$$= 2\pi \int_{-\infty}^{\infty} dr\, r^2 g(r) \left[\frac{\sin(qr\cos\theta)}{qr} \Big|_{\cos\theta=-1}^{1} - i \frac{\cos(qr\cos\theta)}{qr} \Big|_{\cos\theta=-1}^{1} \right]$$

$$= 2\pi \int_{-\infty}^{\infty} dr\, r^2 g(r) \left[\frac{2\sin(qr)}{qr} \right]$$

Hence

$$S(q) = 4\pi \int_{-\infty}^{\infty} g(r) \frac{\sin(qr)}{qr} r^2 dr . \tag{B.2}$$

Appendix C

We show that $4\pi \int_{-\infty}^{\infty} r^2 g(r) dr = 1$.

From Eq. (4.35) we have

$$g(r) = \int_{-\infty}^{\infty} n(\vec{r} - \vec{r}\,')n(\vec{r}\,')d\vec{r}\,' \tag{C.1}$$

for an isotropic system.

Also from Eq. (4.30) we have

$$n(\vec{r}\,') = \frac{1}{N}\sum_{i=1}^{N} \delta(\vec{r}\,' - \vec{r}_i)\,. \tag{C.2}$$

But

$$\delta(\vec{r}\,' - \vec{r}_i) = \frac{1}{r'^2}\delta(r' - r_i)\sum_{l=0}^{\infty}\sum_{m=-l}^{l} Y^*_{l,m}(\theta_i, \phi_i)Y_{l,m}(\theta', \phi')\,. \tag{C.3}$$

Since the system is isotropic where $l = m = 0$, Eq. (C.3) simplifies to

$$\delta(\vec{r}\,' - \vec{r}_i) = \frac{1}{4\pi}\frac{1}{r'^2}\delta(r' - r_i) \tag{C.4}$$

because

$$Y^*_{0,0}(\theta_i, \phi_i) = Y_{0,0}(\theta', \phi') = \frac{1}{\sqrt{4\pi}}\,. \tag{C.5}$$

Using Eq. (C.4) in Eq. (C.2) we get

$$n(\vec{r}\,') = \frac{1}{4\pi N}\sum_{i=1}^{N}\frac{1}{r'^2}\delta(r' - r_i)\,. \tag{C.6}$$

Likewise we can also write

$$n(\vec{r}-\vec{r}') = \frac{1}{4\pi N}\sum_{i=1}^{N}\frac{1}{r^2}\delta\big((r-r')-r_i\big) = \frac{1}{4\pi N}\sum_{i=1}^{N}\frac{1}{r^2}\delta\big(r-(r'+r_i)\big) \quad . \tag{C.7}$$

Using Eqs. (C.6) and (C.7) in Eq. (C.1) we get

$$g(r) = \frac{1}{(4\pi N)^2}\sum_{i=1}^{N}\sum_{j=1}^{N}\int_{-\infty}^{\infty}\frac{1}{r^2}\delta\big(r-(r'+r_i)\big)\frac{1}{r'^2}\delta\big(r'-r_j\big)4\pi\, r'^2\, dr'$$

$$g(r) = \frac{1}{4\pi N^2}\sum_{i=1}^{N}\sum_{j=1}^{N}\int_{-\infty}^{\infty}\frac{1}{r^2}\delta\big(r-(r'+r_i)\big)\delta\big(r'-r_j\big)dr' \,. \tag{C.8}$$

Now we use Eq. (C.8) and rewrite the expression $4\pi\int_{-\infty}^{\infty} r^2 g(r)dr$ as

$$4\pi\int_{-\infty}^{\infty} r^2 g(r)dr = \frac{1}{N^2}\sum_{i=1}^{N}\sum_{j=1}^{N}\int_{-\infty}^{\infty}dr'\,\delta\big(r'-r_j\big)\int_{-\infty}^{\infty}dr\,\delta\big(r-(r'+r_i)\big)$$

$$= \frac{1}{N^2}\left[\sum_{j=1}^{N}\int_{-\infty}^{\infty}dr'\,\delta\big(r'-r_j\big)\right]\left[\sum_{i=1}^{N}\int_{-\infty}^{\infty}dr\,\delta\big(r-(r'+r_i)\big)\right]$$

$$= \frac{1}{N^2}\;N\,N$$

Hence

$$4\pi\int_{-\infty}^{\infty} r^2 g(r)dr = 1 \,. \tag{C.9}$$

Appendix D

We show that $2\pi \int_{-\infty}^{\infty} r^4 g(r) dr = R_g^2$ for an isotropic system.

For an isotropic system, we can rewrite $2\pi \int_{-\infty}^{\infty} r^4 g(r) dr$ as

$$\begin{aligned} 2\pi \int_{-\infty}^{\infty} r^4 g(r) dr &= \frac{1}{2} \int_{-\infty}^{\infty} r^2 g(\vec{r})\, 4\pi\, r^2 dr \\ &= \frac{1}{2} \int_{-\infty}^{\infty} r^2 g(\vec{r})\, d\vec{r} \end{aligned} \quad . \tag{D.1}$$

Using Eq. (4.35) for $g(\vec{r})\,(= g(r))$ Eq. (D.1) becomes

$$2\pi \int_{-\infty}^{\infty} r^4 g(r) dr = \frac{1}{2} \int_{-\infty}^{\infty} r^2 \left(\int_{-\infty}^{\infty} n(\vec{r} - \vec{r}\,') n(\vec{r}\,') d\vec{r}\,' \right) d\vec{r}$$

$$= \frac{1}{2} \int_{-\infty}^{\infty} d\vec{r}\,' n(\vec{r}\,') \left(\int_{-\infty}^{\infty} d\vec{r}\; r^2 n(\vec{r} - \vec{r}\,') \right) . \tag{D.2}$$

In Eq. (D.2) we replace $\vec{r} - \vec{r}\,'$ by $\vec{r}$, i.e., $\vec{r} - \vec{r}\,' = \vec{r}$, such that $(\vec{r} - \vec{r}\,')^2 = r^2$. Then

$$2\pi \int_{-\infty}^{\infty} r^4 g(r) dr = \frac{1}{2} \int_{-\infty}^{\infty} d\vec{r}\,' n(\vec{r}\,') \left(\int_{-\infty}^{\infty} d\vec{r}\, (\vec{r} - \vec{r}\,')^2 n(\vec{r}) \right)$$

$$= \frac{1}{2} \int_{-\infty}^{\infty} d\vec{r}\,' n(\vec{r}\,') \left(\int_{-\infty}^{\infty} d\vec{r}\; r^2 n(\vec{r}) + r'^2 \int_{-\infty}^{\infty} d\vec{r}\; n(\vec{r}) - 2\vec{r}\,' \cdot \int_{-\infty}^{\infty} d\vec{r}\; \vec{r}\; n(\vec{r}) \right)$$

$$2\pi \int_{-\infty}^{\infty} r^4 g(r)dr = \frac{1}{2}\left(\int_{-\infty}^{\infty} d\vec{r}\; r^2 n(\vec{r}) \right)\left(\int_{-\infty}^{\infty} d\vec{r}'\, n(\vec{r}') \right) + \frac{1}{2}\left(\int_{-\infty}^{\infty} d\vec{r}\; n(\vec{r}) \right)\left(\int_{-\infty}^{\infty} d\vec{r}'\, r'^2\, n(\vec{r}') \right)$$

$$- \left(\int_{-\infty}^{\infty} d\vec{r}\; \vec{r}\; n(\vec{r}) \right) \cdot \left(\int_{-\infty}^{\infty} d\vec{r}'\, \vec{r}'\, n(\vec{r}') \right)$$

$$= \left(\int_{-\infty}^{\infty} d\vec{r}\; r^2 n(\vec{r}) \right)\left(\int_{-\infty}^{\infty} d\vec{r}'\, n(\vec{r}') \right) - \left(\int_{-\infty}^{\infty} d\vec{r}\; \vec{r}\; n(\vec{r}) \right)^2 . \qquad \text{(D.3)}$$

In Eq. (D.3) we have

$$\int_{-\infty}^{\infty} d\vec{r}'\, n(\vec{r}') = 1 \qquad \text{by definition} \qquad \text{(D.4)}$$

and

$$\int_{-\infty}^{\infty} d\vec{r}\; \vec{r}\; n(\vec{r}) = \vec{r}_{CM} \qquad \text{(radius vector for the center of mass).} \qquad \text{(D.5)}$$

Hence Eq. (D.3) reduces to

$$2\pi \int_{-\infty}^{\infty} r^4 g(r)dr = \int_{-\infty}^{\infty} d\vec{r}\; r^2 n(\vec{r}) - r_{CM}^2$$

$$= \int_{-\infty}^{\infty} d\vec{r}\left(r^2 - r_{CM}^2 \right) n(\vec{r})$$

$$= \int_{-\infty}^{\infty} d\vec{r}\left(r^2 + r_{CM}^2 - 2r_{CM}^2 \right) n(\vec{r})$$

$$= \int_{-\infty}^{\infty} d\vec{r}\left(r^2 + r_{CM}^2 - 2\,\vec{r}\cdot\vec{r}_{CM} \right) n(\vec{r})$$

$$= \int_{-\infty}^{\infty} d\vec{r}\left(r - \vec{r}_{CM} \right)^2 n(\vec{r}) . \qquad \text{(D.6)}$$

But from definition of radius of gyration R_g we have

$$R_g^2 = \int_{-\infty}^{\infty} d\vec{r}\,\left(r - \vec{r}_{CM}\right)^2\, n(\vec{r})\,. \tag{D.7}$$

Hence we prove

$$2\pi \int_{-\infty}^{\infty} r^4 g(r) dr = R_g^2\,. \tag{D.8}$$

Appendix E

We show that

$$R_{gz}^2 = a^2 k_0^{-2/D_f} \frac{M_{2+2/D_f}}{M_2} = a^2 k_0^{-2/D_f} s_2^{2/D_f} \frac{m_{2+2/D_f}}{m_2} \text{ and}$$

$$C_p = \frac{M_1}{M_2}\left(\frac{M_{2+2/D_f}}{M_2}\right)^{D_f/2} = \frac{m_1}{m_2}\left(\frac{m_{2+2/D_f}}{m_2}\right)^{D_f/2}.$$

From Eq. (4.51) we have

$$S_{eff}(q) = \frac{\int_0^\infty N^2 n(N) S[q, R_g(N)] dN}{\int_0^\infty N^2 n(N) dN}. \tag{E.1}$$

For the Guinier regime ($qR_g \le 1$) we can use $S[q, R_g(N)] \approx 1 - \frac{1}{3}\left(qR_g\right)^2$ (Eq. (4.50b)) in Eq. (E.1) to obtain

$$S_{eff}(q) = 1 - \frac{1}{3} q^2 \frac{\int_0^\infty N^2 n(N) R_g^2 dN}{\int_0^\infty N^2 n(N) dN}. \tag{E.2}$$

Comparing Eq. (E.2) with Eq. (4.52b) we have

$$R_{gz}^2 = \frac{\int_0^\infty N^2 n(N) R_g^2 dN}{\int_0^\infty N^2 n(N) dN}. \tag{E.3}$$

Using Eq. (3.3) for R_g, Eq. (E.3) becomes

$$R_{gz}^2 = a^2 k_0^{-2/D_f} \frac{\int_0^\infty N^{2+2/D_f} n(N) dN}{\int_0^\infty N^2 n(N) dN}. \tag{E.4}$$

Using the definition of the moment of the size distribution (Eq. (3.86)), Eq. (E.4) reduces to

$$R_{gz}^2 = a^2 k_0^{-2/D_f} \frac{M_{2+2/D_f}}{M_2}. \tag{E.5}$$

Eq. (E.5) can also be presented in terms of the moment of the scaling distribution using Eq.(3.89) as

$$R_{gz}^2 = a^2 k_0^{-2/D_f} s_p^{2/D_f} \frac{m_{2+2/D_f}}{m_2}. \tag{E.6}$$

If we use $S[q, R_g(N)] = C\left(qR_g\right)^{-D_f}$ (Eq. (4.50c)) in Eq. (E.1) we find

$$S_{eff}(q) = C\left[\frac{\int_0^\infty N^2 n(N) R_g^{-D_f} dN}{\int_0^\infty N^2 n(N) dN}\right] q^{-D_f}. \tag{E.7}$$

We can rewrite Eq. (E.7) as

$$S_{eff}(q) = C\left[R_{gz}^{D_f} \frac{\int_0^\infty N^2 n(N) R_g^{-D_f} dN}{\int_0^\infty N^2 n(N) dN}\right] \left(qR_{gz}\right)^{-D_f}. \tag{E.8}$$

Comparing Eq. (E.8) with Eq. (4.52c) we see

$$C_p = R_{gz}^{D_f} \frac{\int_0^\infty N^2 n(N) R_g^{-D_f} dN}{\int_0^\infty N^2 n(N) dN}. \tag{E.9}$$

Using Eq. (E.5) for R_{gz} and Eq. (3.3) for R_g in Eq. (E.9) we find

$$C_p = \left(\frac{M_{2+2/D_f}}{M_2} \right)^{D_f/2} \frac{\int_0^\infty N n(N) dN}{\int_0^\infty N^2 n(N) dN}. \tag{E.10}$$

Now using the definition of the moment of the size distribution (Eq. (3.86)), Eq. (E.10) becomes

$$C_p = \frac{M_1}{M_2} \left(\frac{M_{2+2/D_f}}{M_2} \right)^{D_f/2}. \tag{E.11}$$

Again using Eq.(3.89), Eq. (E.11) can be given in terms of the moment of the scaling distribution as

$$C_p = \frac{m_1}{m_2} \left(\frac{m_{2+2/D_f}}{m_2} \right)^{D_f/2}. \tag{E.12}$$

References

MD Allen, OG Raabe, Slip Correction Measurements of Spherical Solid Aerosol-Particles in an Improved Millikan Apparatus, Aerosol Science and Technology. 4 (1985) 269-286.

C Aubert, DS Cannell, Restructuring of Colloidal Silica Aggrregates, Physical Review Letters. 56 (1986) 738.

G Beaucage, Small-Angle Scattering from Polymeric Mass Fractals of Arbitrary Mass-Fractal Dimension, Journal of Applied Crystallography. 29 (1996) 134.

MJ Berg, CM Sorensen, A Chakrabarti, Patterns in Mie Scattering: Evolution when Normalized by the Rayleigh Cross Section, Applied Optics. 44 (2005) 7487.

BJ Berne, R Pecora, Dynamic Light Scattering: With Application to Chemistry, Biology and Physics. 2000.

MV Berry, IC Percival, Optics of Fractal Clusters such as Smoke, Optica Acta. 33 (1986) 577-591.

J Bibette, TG Mason, H Gang, DA Weitz, Kinetically Induced Ordering in Gelation of Emulsions, Physical Review Letters. 69 (1992) 981.

VA Bogoyavlenskiy, Mean-Field Diffusion-Limited Aggregation: A "Density" Model for Viscous Fingering Phenomena, Physical Review E. 64 (2001) 066303.

CF Bohren, DR Huffman, Absorption and Scattering of Light by Small Particles, Wiley, New York, 1983.

TC Bond, RW Bergstrom, Light Absorption by Carbonaceous Particles: An Investigative Review, Aerosol Science and Technology. 40 (2006) 1-41.

M Born, E Wolf, Principles of Optics, Cambridge University Press, Cambridge, 1999.

R Botet, Clustering of Clusters Processes above their Upper Critical Dimensionalities, Journal of Physics A-Mathematical and General. 18 (1985) 847.

CJ Brinker, GW Scherer, Sol-Gel Science: The Physics and Chemistry of Sol-Gel, Academic Press, San Diego, 1990.

JR Brock, Theory of Thermal Forces Acting on Aerosol Particles, Journal of Colloid Science. 17 (1962) 768.

ML Broide, RJ Cohen, Experimental-Evidence of Dynamic Scaling in Colloidal Aggregation, Physical Review Letters. 64 (1990) 2026.

WD Brown, RC Ball, Computer-Simulation of Chemically Limited Aggregation, Journal of Physics A-Mathematical and General. 18 (1985) L517.

GC Bushell, YD Yan, D Woodfield, J Raper, R Amal, On Techniques for the Measurement of the Mass Fractal Dimension of Aggregates, Advances in Colloid and Interface Science. 95 (2002) 1-50.

J Cai, NL Lu, CM Sorensen, Analysis of Fractal Cluster Morphology Parameters - Structural Coefficient and Density Autocorrelation Function Cutoff, Journal of Colloid and Interface Science. 171 (1995) 470-473.

M Carpineti, F Ferri, M Giglio, Salt-induced Fast Aggregation of Polystyrene Latex, Physical Review A. 42 (1990) 7347.

BD Cullity, Elements of X-ray Diffraction, 2nd Ed., Addison-Wesley Publishing Company 1978.

R Dhaubhadel, F Pierce, A Chakrabarti, CM Sorensen, Hybrid Superaggregate Morphology as a Result of Aggregation in a Cluster-Dense Aerosol, Physical Review E. 73 (2006).

RA Dobbins, CM Megaridis, Absorption and Scattering of Light by Polydisperse Aggregates, Applied Optics. 30 (1991) 4747.

PGJ v Dongen, MH Ernst, Dynamic Scaling in the Kinetics of Clustering, Physical Review Letters. 54 (1985) 1396.

F Family, DP Landau, Kinetics of Aggregation and Gelation, North Holland, Amsterdam, 1984.

F Ferri, Use of a Charge Coupled Device Camera for Low-Angle Elastic Light Scattering, Review of Scentific Instruments. 68 (1997) 2265-2274.

R Finsy, Particle Sizing by Quasi-Elastic Light-Scattering, Advances in Colloid and Interface Science. 52 (1994) 79.

SR Forrest, TA Witten, Long-Range Correlations in Smoke-Particle Aggregates, Journal of Physics A-Mathematical and General. 12 (1979) L109-L117.

RE Franklin, On the Structure of Carbon, Journal De Chimie Physique Et De Physico-Chimie Biologique. 47 (1950) 573-575.

T Freltoft, JK Kjems, SK Sinha, Power-Law Correlations and Finite-Size Effects in Silica Particle Aggregates Studied by Small-Angle Neutron-Scattering, Physical Review B. 33 (1986) 269.

SK Friedlander, CS Wang, Self-Preserving Particle Size Distribution for Coagulation by Brownian Motion, Journal of Colloid and Interface Science. 22 (1966) 126-132.

SK Friedlander, Smoke, Dust and Haze, Oxford University Press, New York, 2000.

D Fry, A Chakrabarti, W Kim, CM Sorensen, Structural Crossover in Dense Irreversibly Aggregating Particulate Systems, Physical Review E. 69 (2004).

D Fry, Aggregtion in Dense Particulate Systems, Ph.D. Thesis, Kansas State University, 2003.

D Fry, T Sintes, A Chakrabarti, CM Sorensen, Enhanced Kinetics and Free-Volume Universality in Dense Aggregating Systems, Physical Review Letters. 89 (2002).

NA Fuchs, The Mechanics of Aerosols, Revised and enlarged Ed., Pergamin Press Ltd., New York, 1964.

CS Gerving, Production of Low Density Aero-Gels through the Controlled Detonation of Hydrocarbon Fuels, M.S. Thesis, Kansas State University, 2004.

JC Gimel, D Durand, T Nicolai, Transition between Flocculation and Percolation of a Diffusion-Limited Cluster-Cluster Aggregation Process Using 3-Dimensional Monte-Carlo Simulation, Physical Review B. 51 (1995) 11348-11357.

JC Gimel, T Nicolai, D Durand, 3D Monte Carlo Simulations of Diffusion Limited Cluster Aggregation up to the Sol-Gel Transition: Structure and Kinetics, Journal of Sol-Gel Science and Technology. 15 (1999) 129-136.

O Glatter, Small Angle X-Ray Scattering, Academic Press, New York, 1982.

AE Gonzalez, Universality of Colloid Aggregation in the Reaction Limit - the Computer-Simulations, Physical Review Letters. 71 (1993) 2248-2251.

A Guinier, G Fournet, CB Walker, KL Yudowitch, Small-angle Scattering of X-rays, Wiley, New York, 1955.

A Guinier, La Diffraction Des Rayons X Aux Trespetits Angles: Application a L'etude de Phenomes Ultramicroscopiques, Ann. Phys. 12 (1939) 161-237.

A Hasmy, Aerogelation Process Simulation by a Cluster-Cluster Aggregation Algorithm, Journal of Sol-Gel Science and Technology. 15 (1999) 137-146.

A Hasmy, E Anglaret, R Thouy, R Jullien, Fluctuating Bond Aggregation: A numerical Simulation of Neutrally-Reacted Silica Gels, Journal De Physique I. 7 (1997) 521-542.

A Hasmy, R Jullien, Percolation in Cluster-Cluster Aggregation Processes, Physical Review E. 53 (1996) 1789-1794.

A Hasmy, R Jullien, Sol-Gel Process Simulation by Cluster-Cluster Aggregation, Journal of Non-Crystalline Solids. 186 (1995) 342-348.

E Hecht, Optics, 4th Ed., Addison Wesley 2002.

HJ Herrmann, M Kolb, Irreversible Aggregation of Clusters at High-Density, Journal of Physics A-Mathematical and General. 19 (1986) 1027-1031.

WC Hinds, Aerosol Technology: Properties, Behavior, and Measurements of Airborne Particles, 2nd Ed., Wiley, New York, 1998.

HC van de Hulst, Light Scattering by Small Particles, Dover, New York, 1981.

AJ Hurd, WL Flower, Insitu Growth and Structure of Fractal Silica Aggregates in a Flame, Journal of Colloid and Interface Science. 122 (1988) 178-192.

JN Israelachvili, Intermolecular and Surface Forces, Elsevier, London, 1992.

JD Jackson, Classical Electrodynamics, 3rd Ed., John, Wiley & Sons Inc., New York, USA, 1998.

TJC Jacob, The Relationship between Cataract, Cell Swelling and Volume Regulation, Progress in Retinal and Eye Research. 18 (1999) 223-233.

R Jullien, M Kolb, Hierarchical Model for Chemically Limited Cluster Cluster Aggregation, Journal of Physics A-Mathematical and General. 17 (1984) L639.

R Jullien, R Botet, Aggregation and Fractal Aggregates, World Scientific Publication 1987.

R Jullien, R Thouy, F Ehrburgerdolle, Numerical Investigation of 2-Dimensional Projections of Random Fractal Aggregates, Physical Review E. 50 (1994) 3878.

M Kerker, The Scattering of Light and Other Electromagnetic Radiation, Physical Chemistry: a Series of Monographs. 16 (1969) 666.

W Kim, CM Sorensen, A Chakrabarti, Universal Occurrence of Soot Superaggregates with a Fractal Dimension of 2.6 in Heavily Sooting Laminar Diffusion Flames, Langmuir. 20 (2004) 3969-3973.

W Kim, CM Sorensen, D Fry, A Chakrabarti, Soot Aggregates, Superaggregates and Gel-Like Networks in Laminar Diffusion Flames, Journal of Aerosol Science. 37 (2006) 386-401.

M Kolb, HJ Herrmann, The Sol-Gel Transition Modeled by Irreversible Aggregation of Clusters, Journal of Physics A-Mathematical and General. 18 (1985) L435-L441.

M Kolb, R Botet, R Jullien, Scaling of Kinetically Growing Clusters, Physical Review Letters. 51 (1983) 1123.

M Kolb, R Jullien, Chemically Limited Versus Diffusion Limited Aggregation, Europhysics Letters. 45 (1984) L977.

DE Koppel, Analysis of Macromolecular Polydispersity in Intensity Correlation Spectroscopy – Method of Cumulants, The Journal of Chemical Physics. 57 (1972) 4814.

MRH Krebs, GL Devlin, AM Donald, Protein Particulates: Another Generic Form of Protein Aggregation?, Biophysical Journal. 92 (2007) 1336-1342.

M Kruk, M Jaroniec, Gas Adsorption Characterization of Ordered Organic-Inorganic Nanocomposite Materials, Chemistry of Materials. 13 (2001) 3169-3183.

TN Krupenkin, JA Taylor, TM Schneider, S Yang, From Rolling Ball to Complete Wetting: The Dynamic Tuning of Liquids on Nanostructured Surfaces, Langmuir. 20 (2004) 3824.

SK Kumar, JF Douglas, Gelation in Physically Associating Polymer Solutions, Physical Review Letters. 87 (2001) 18188301.

FS Lai, SK Friedlander, J Pich, GM Hidy, Self-Preserving Particle Size Distribution for Brownian Coagulation in the Free-Molecule Regime, Journal of Colloid and Interface Science. 39 (1972) 395-405.

M Lattuada, H Wu, M Morbidelli, Estimation of Fractal Dimension of Colloidal Gels in the Presence of Multiple Scattering, Physical Review E. 6406 (2001).

M Lattuada, H Wu, M Morbidelli, Experimental Investigation of Colloidal Gel Structures, Langmuir. 20 (2004) 4355-4362.

C Léger, L Servant, JL Bruneel, F Argoul, Growth Patterns in Electrodeposition, Physica A. 263 (1999) 305.

XM Lin, GM Wang, CM Sorensen, KJ Klabunde, Formation and Dissolution of Gold Nanocrystal Superlattices in a Colloidal Solution, Journal of Physical Chemistry B. 103 (1999) 5488-5492.

XM Lin, HM Jaeger, CM Sorensen, KJ Klabunde, Formation of Long-Range-Ordered Nanocrystal Superlattices on Silicon Nitride Substrates, Journal of Physical Chemistry B. 105 (2001) 3353-3357.

MY Lin, HM Lindsay, DA Weitz, RC Ball, R Klein, P Meakin, Universal Reaction-Limited Colloid Aggregation, Physical Review A. 41 (1990) 2005-2020.

MY Lin, HM Lindsay, DA Weitz, RC Ball, R Klein, P Meakin, Universality in Colloid Aggregation, Nature. 339 (1989) 360-362.

WT Liu, Nanoparticles and their Biological and Environmental Applications, Journal of Bioscience and Bioengineering. 102 (2006) 1.

AA Lushnikov, AE Negin, AV Pakhomov, Experimental-Observation of the Aerosol Aerogel Transition, Chemical Physics Letters. 175 (1990) 138-142.

AA Lushnikov, Evolution of Coagulating Systems, Journal of Colloid and Interface Science. 45 (1973) 549-556.

AA Lushnikov, Exact kinetics of the Sol-Gel Transition, Physical Review E. 71 (2005) 046129.

BB Mandelbrot, Fractals Form, Chance, and Dimension, W.H. Freeman, San Francisco, 1977.

JE Martin, BJ Ackerson, Static and Dynamic Scattering from Fractals, Physical Review A. 31 (1985) 1180-1182.

JE Martin, JP Wilcoxon, D Schaefer, J Odinek, Fast Aggregation of Colloidal Silica, Physical Review A. 41 (1990) 4379-4391.

P Meakin, A Historical Introduction to Computer Models for Fractal Aggregates, Journal of Sol-Gel Science and Technology. 15 (1999) 97-117.

P Meakin, Aggregation Kinetics, Physica Scripta. 46 (1992) 295-331.

P Meakin, B Donn, Aerodynamic Properties of Fractal Grains – Implications for the Primordial Solar Nebula, The Astrophysical Journal. 329 (1988) L39.

P Meakin, Computer-Simulation of Cluster Cluster Aggregation using Linear Trajectories - Results from 3-Dimensional Simulations and a Comparison with Aggregates Formed using Brownian Trajectories, Journal of Colloid and Interface Science. 102 (1984a) 505-512.

P Meakin, Diffusion-Controlled Cluster Formation in 2-6-Dimensional Space, Physical Review A. 27 (1983a) 1495.

P Meakin, Diffusion-Controlled Cluster Formation in 2-Dimension, 3- Dimension, and 4-Dimension, Physical Review A. 27 (1983b) 604.

P Meakin, Effects of Cluster Trajectories on Cluster-Cluster Aggregation - a Comparison of Linear and Brownian Trajectories in Two-Dimensional and 3-Dimensional Simulations, Physical Review A. 29 (1984b) 997-999.

P Meakin, F Family, Structure and Dynamics of Reaction-Limited Aggregation, Physical Review A. 36 (1987) 5498-5501.

P Meakin, F Family, Structure and Kinetics of Reaction-Limited Aggregation, Physical Review A. 38 (1988) 2110-2123.

P Meakin, Formation of Fractal Clusters and Networks by Irreversible Diffusion-Limited Aggregation, Physical Review Letters. 51 (1983) 1119-1122.

P Meakin, Fractal Aggregates, Advances in Colloid Interface Science. 28 (1988) 249-331.

P Meakin, T Vicsek, F Family, Dynamic Cluster-Size Distribution in Cluster-Cluster Aggregation - Effects of Cluster Diffusivity, Physical Review B. 31 (1985) 564-569.

RE Meyer, Theory of Dispersed Multiphase Flow, Academic Press, New York, 1983.

T Mokhtari, CM Sorensen, A Chakrabarti, Multiple-Scattering Effects on Static Light-Scattering Optical Structure Factor Measurements, Applied Optics. 44 (2005) 7858-7861.

T Mokhtari, Studies of the Effect of Shear on Colloidal Aggregation and Gelation using Small-Angle Light Scattering, Ph.D. Thesis, Kansas State University, 2007.

RD Mountain, GW Mulholland, Light-Scattering from Simulated Smoke Agglomerates, Langmuir. 4 (1988) 1321-1326.

MSDS (Material Safety Data Sheet), The Occupational Safety and Health Act of 1970, (1970).

GW Mulholland, RJ Samson, RD Mountain, MH Ernst, Cluster Size Distribution for Free Molecular Agglomeration, Energy Fuels. 2 (1988) 481-486.

CB Murray, CR Kagan, MG Bawendi, Self-Organization of Cdse Nanocrystallites into 3-Dimensional Quantum-Dot Superlattices, Science. 270 (1995) 1335-1338.

J Nelson, Test of a Mean Field-Theory for the Optics of Fractal Clusters, Journal of Modern Optics. 36 (1989) 1031-1057.

T Nicolai, D Durand, JC Gimel, Static Structure Factor of Dilute-Solutions of Polydisperse Fractal Aggregates, Physical Review B. 50 (1994) 16357-16363.

C Oh, CM Sorensen, Light Scattering Study of Fractal Cluster Aggregation near the Free Molecular Regime, Journal of Aerosol Science. 28 (1997) 937-957.

A Otten, S Herminghaus, How Plants Keep Dry: A Physicist's Point of View, Langmuir. 20 (2004) 2405.

AB Palotas, LC Rainey, AF Sarofim, JB Vander Sande, RC Flagan, Where did that Soot Come From?, Chemtech. 28 (1998) 24-30.

AB Palotas, LC Rainey, AF Sarofim, JB VanderSande, P Ciambelli, Effect of Oxidation on the Microstructure of Carbon Blacks, Energy Fuels. 10 (1996) 254-259.

AB Palotas, LC Rainey, CJ Feldermann, AF Sarofim, JB VanderSande, Soot Morphology: An Application of Image Analysis in High-Resolution Transmission Electron Microscopy, Microscopy Research Technique. 33 (1996) 266-278.

RW Pekala, ST Mayer, JL Kaschmitter, FM Kong, Carbon Aerogels: An Update on Structure, Properties and Applications: In YA Attia (ed.), Sol-Gel Process. Appl. (Proc. Int. Symp. Adv. Sol-Gel Process. Appl.) (1994) 369-377.

F Pierce, Aggregation in Colloids and Aerosols, Ph.D. Thesis, Kansas State University, 2007.

F Pierce, CM Sorensen, A Chakrabarti, Computer Simulation of Diffusion-Limited Cluster-Cluster Aggregation with an Epstein Drag Force, Physical Review E. 74 (2006) 021411.

G Porod, Die Rontgenkleinwinkelstreuung Von Dichtgepackten Kolloiden Systemen.1, Kolloid-Zeitschrift Zeitschrift für Polymere. 124 (1951) 83.

PN Pusey, JG Rarity, R Klein, DA Weitz, Comment on "Hydrodynamic Behavior of Fractal Aggregates, Physical Review Letters. 59 (1987) 2122-2122.

DJ Rader, Momentum Slip Correction Factor for Small Particles in 9 Common Gases, Journal of Aerosol Science. 21 (1990) 161-168.

S Ren, A Dynamic Light Scattering Study of the Relaxation Dynamics in Aqueous Polymer Gelatin Solutions and Gels, Ph.D. Thesis, Kansas State University, 1992.

GAM Reynolds, MS Dresselhaus, RW Pekala, A Brief Overview of Structure-Property Relations in Carbon Aerogels. Recent Advances in the Chemistry and Physics of Fullerences and Related Materials. 3 (1996) 740-748.

SN Rogak, RC Flagan, Coagulation of Aerosol Agglomerates in the Transition Regime, Journal of Colloid and Interface Science. 151 (1992) 203-224.

M Rottereau, JC Gimel, T Nicolai, D Durand, Monte Carlo Simulation of Particle Aggregation and Gelation: I. Growth, Structure and Size Distribution of the Clusters, European Physical Journal E. 15 (2004) 133-140.

WB Russel, DA Saville, WR Schowalter, Colloidal Dispersions, Cambridge University Press, Cambridge, UK, 1999.

PG Saffman, JS Turner, On the Collision of Drops in Turbulent Clouds, Journal of Fluid Mechanics. 1 (1956) 16.

RJ Samson, GW Mulholland, JW Gentry, Structural Analysis of Soot Agglomerates, Langmuir. 3 (1987) 272-281.

Y Sawada, S Ohta, M Yamazaki, H Honjo, Self-Similarity and a Phase-Transition-Like Behavior of a Random Growing Structure Governed by a Non-Equilibrium Parameter, Physical Review A. 26 (1982) 3557.

DW Schaefer, JE Martin, Fractal Geometry of Colloidal Aggregates, Physical Review Letters. 52 (1984) 2371.

DW Schaefer, KD Keefer, Structure of Random Porous Materials - Silica Aerogel, Physical Review Letters. 56 (1986) 2199.

K Schatzel, Single-Photon Correlation Techniques. In: W Brown (ed.), Dynamic Light Scattering: The Method and Some Applications, Clarendon Press, Oxford, 1993, pp. 76-148.

PW Schmidt, Modern Aspects of Small-Angle Scattering, Kluwer Academic, Dordrecht, 1995.

NA Seaton, ED Glandt, Percolation and Conduction in Colloidal Dispersions, Physicochemical Hydrodynamics. 9 (1987) 369-378.

JH Seinfeld, Atmospheric Chemistry and Physics of Air Pollution, Wiley, New York, 1986.

D Shi, Experimental Studies of the Optical Structure Factor of Soot Clusters in a Heavily Sooting Acetylene Flame, M.S. Thesis, Kansas State University, 2001.

M v Smoluchowski, Mathematical Theory of the Kinetics of the Coagulation of Colloidal Solutions, Z. Phys. Chem. 92 (1917) 129.

CM Sorensen, B Hageman, TJ Rush, H Huang, C Oh, Aerogelation in a Flame Soot Aerosol, Physical Review Letters. 80 (1998) 1782-1785.

CM Sorensen, D Shi, Guinier Analysis for Homogeneous Dielectric Spheres of Arbitrary Size, Optics Communications. 178 (2000) 31-36.

CM Sorensen, D Shi, Patterns in the Ripple Structure of Mie Scattering, Journal of the Optical Society of America A-Optics Image Science and Vision. 19 (2002) 122.

CM Sorensen, DJ Fischbach, Patterns in Mie Scattering, Optics Communications. 173 (2000) 145-153.

CM Sorensen, GC Roberts, The Prefactor of Fractal Aggregates, Journal of Colloid and Interface Science. 186 (1997) 447-452.

CM Sorensen, GM Wang, Size Distribution Effect on the Power Law Regime of the Structure Factor of Fractal Aggregates, Physical Review E. 60 (1999) 7143-7148.

CM Sorensen, J Cai, N Lu, Light-Scattering Measurements of Monomer Size, Monomers Per Aggregate, and Fractal Dimension for Soot Aggregates in Flames, Applied Optics. 31 (1992) 6547-6557.

CM Sorensen, J Cai, N Lu, Test of Static Structure Factors for Describing Light-Scattering from Fractal Soot Aggregates, Langmuir. 8 (1992) 2064-2069.

CM Sorensen, Light Scattering by Fractal Aggregates: A Review, Aerosol Science and Technology. 35 (2001) 648-687.

CM Sorensen, Scattering and Absorption of Light by Particles and Aggregates. In: KS Birdi (ed.), Handbook of Surface and Colloid Chemistry, 2nd Ed., CRC Press, 2003.

CM Sorensen, W Kim, D Fry, D Shi, A Chakrabarti, Observation of Soot Superaggregates with a Fractal Dimension of 2.6 in Laminar Acetylene/air Diffusion Flames, Langmuir. 19 (2003) 7560-7563.

HE Stanley, N Ostrowsky, On Growth and Form: Fractal and Non-Fractal Patterns in Physics, NATO Advanced Science Institutes Series E: Applied Sciences, 1986, pp. 308.

D Stauffer, A Aharony, Introduction to Percolation Theory, Taylor & Francis, London, 1985.

PN Strenski, S Kirkpatrick, Scaling Behavior of Percolation Surfaces in 3 Dimensions, Physical Review Letters. 66 (1991) 1330.

DN Sutherland, I Goodarzn, Floc Simulation - Effect of Collision Sequence, Chemical Engineering Science. 26 (1971) 2071.

J Teixeira, Experimental Methods for Studying Fractal Aggregates. In: HE Stanley, N Ostrowsky (eds.), On Growth and Form Fractal and Non-Fractal Patterns in Physics, Martinus Nijhoff, Boston, 1986, pp. 145-162.

M Tence, JP Chevalier, R Jullien, On the Measurement of the Fractal Dimension of Aggregated Particles by Electron-Microscopy - Experimental-Method, Corrections and Comparison with Numerical-Models, Journal de Physique. 47 (1986) 1989.

HH Tsai, Understanding the Biophysical Mechanisms of Protein Folding, Misfolding, and Aggregation at Molecular Level, Huaxue. 63 (2005) 601-612.

C Urban, P Schurtenberger, Characterization of Turbid Colloidal Suspensions Using Light Scattering Techniques Combined with Cross-Correlation Methods, Journal of Colloid and Interface Science. 207 (1998) 150-158.

T Vicsek, F Family, Dynamic Scaling for Aggregation of Clusters, Physical Review Letters. 52 (1984) 1669-1672.

T Vicsek, Fractal Growth Phenomena, World Scientific, Singapore, 1989.

JM Victor, JP Hansen, Liquid-Gas Transition in Charged Colloidal Dispersions, Journal De Physique Lettres. 45 (1984) L307-L312.

L Waldmann, KH Schmitt, Thermophoresis and Diffusiophoresis of Aerosols, Academic Press, London, 1966.

GM Wang, CM Sorensen, Aggregation Kernel Homogeneity for Fractal Aggregate Aerosols in the Slip Regime, Aerosol Science and Technology. 34 (2001) 297-306.

GM Wang, CM Sorensen, Diffusive Mobility of Fractal Aggregates over the Entire Knudsen Number Range, Physical Review E. 60 (1999) 3036-3044.

DA Weitz, JS Huang, MY Lin, J Sung, Limits of the Fractal Dimension for Irreversible Kinetic Aggregation of Gold Colloids, Physical Review Letters. 54 (1985) 1416-1419.

DA Weitz, M Oliveria, Fractal Structures Formed by Kinetic Aggregation of Aqueous Gold Colloids, Physical Review Letters. 52 (1984) 1433.

JP Wilcoxon, JE Martin, DW Schaefer, Limits of the Fractal Dimension for Irreversible Kinetic Aggregation of Gold Colloids - Comment, Physical Review Letters. 58 (1987) 1051-1051.

TA Witten, Diffusion-Limited Aggregation at Multiple Growth Sites, Physical Review B. 28 (1983) 5632.

TA Witten, LM Sander, Diffusion-Limited Aggregation, a Kinetic Critical Phenomenon, Physical Review Letters. 47 (1981) 1400-1403.

HX Zhang, CM Sorensen, ER Ramer, BJ Olivier, JF Merklin, In situ Optical Structure Factor Measurements of an Aggregating Soot Aerosol, Langmuir. 4 (1988) 867-871.

Dr. Chris Sorensen and his research group.

From left: Brandon Lohman, Rajan Dhaubhadel, Hao Yan, Matthew Berg, Dr. Chris Sorensen, Dr. Xueying (Sharon) Qin, Dr. Tahereh Mokhtari and Elizabeth Gilbertson. The aluminum chamber seen in the picture was used for making carbon aerosol gel reported in this thesis. This picture was taken on October 2007.